# Magnetic Properties of $NiCr_2O_4$ and $MnCr_2O_4$ Based Spinel Chromites

*A Thesis Submitted*

*By*

**Junmoni Barman**

**Roll No: 126121013**

*In Partial Fulfillment of the Requirements for the Award of the Degree of*

*Doctor of Philosophy in Physics*


***Department of Physics***
***Indian Institute of Technology Guwahati***
***Guwahati-781039, India***

***August, 2017***

# *Statement*

The work contained in the thesis entitled **"Magnetic Properties of $NiCr_2O_4$ and $MnCr_2O_4$ Based Spinel Chromites"** has been carried out by me under the supervision of Prof. S. Ravi, Department of Physics, Indian Institute of Technology Guwahati. This work has not been submitted elsewhere for the award of any degree.

11th August, 2017

(Junmoni Barman)
Department of Physics
Indian Institute of Technology Guwahati
Guwahati – 781039, India

# *Certificate*

It is certified that the work contained in the thesis entitled **"Magnetic Properties of $NiCr_2O_4$ and $MnCr_2O_4$ Based Spinel Chromites"** by Ms. Junmoni Barman, a Ph. D. student of the Department of Physics, Indian Institute of Technology Guwahati, for the award of the degree of *Doctor of Philosophy* has been carried out under my supervision. This work has not been submitted elsewhere for the award of any degree.

11th August, 2017

(S. Ravi)
Professor, Department of Physics
Indian Institute of Technology Guwahati
Guwahati – 781 039, India

*Dedicated*

*to*

*My Family*

# *Acknowledgements*

It has been a wonderful experience to spend last five years in IIT Guwahati, carrying out my thesis work. Direct or indirect support of many people have made this whole journey successful and made this thesis possible. At the end of this journey, it is a great pleasure to have the opportunity to thank those people whom I will be forever grateful.

First of all, I wish to express my sincere gratitude to my research supervisor Prof. S. Ravi, for giving me the opportunity to conduct my doctoral research under his guidance and providing a well established experimental lab. His thoughtful guidance and encouragements have truly defined for me what a supervisor should be like and without him this work would have never been completed. His cool and down to earth behavior also inspired me a lot. He has enlightened me through his wide knowledge of physics and material science mainly experimental techniques, magnetism, *etc*.

I would like to thank my doctoral committee (DC) members, Prof. A. Perumal (Chairman), Dr. D. Pal and Prof. S. Kanagaraj for generously sharing their time, advice and support which helped me to improve the quality of my work.

I would like to thank my research collaborator Dr. P. D. Babu from UGC-DAE Consortium for Scientific Research, Mumbai Centre, Bhabha Atomic research center (BARC) for high field magnetization measurements.

It is also a great pleasure to thank all my lab mates whose presence has created a pleasant working environment. So, in no particular order, I offer my thanks to former and present research group members, Dr. Manoranjan Kar, Dr. Pramoda Kumar Nayak, Dr. Sandeep Kumar Srivastava, Dr. B. Samantaray, Dr. Sunita Mohanty, Dr. Tribedi Bora, Bipul Deka, Ranganadha Gopalarao, Bibhuti Bhushan Dash, Pratap Behera, Aakansha, Mahananda Brahma and Ritupan Bora for their assistance, advice and cooperation.

I am indeed grateful to the present and past Heads of department of physics for their help towards departmental facility. I am also thankful to all the faculty members of this department. My special thanks go to Dr. Sidananda Sarma for helping me to carry out

different experiments and Mr. Basab Bijoy Purakayasthya for interfacing of instruments by Lab View Program. I am thankful to other staff members of my department.

I am thankful to Central Instrumental Facility (CIF), IIT-Guwahati, for enabling me to avail several sophisticated instruments to perform the experiments during my PhD tenure. I am also thankful to Department of Science and Technology for facilitating Vibrating Sample Magnetometer and TTRAX III diffractometer.

My special thanks to all my batch mates for having good friendship. I am thankful to my department seniors Dr. Padam Rajender, Dr. Akhilesh Kr. Singh, Dr. P.C. Shyni, Dr. Ranjan Bhuyan, Dr. T. Santosh Kumar, Dr. P. Mahesh, Dr. Bhargab Deka and Bhagban Kishan for their help and support. I am also thankful to all other research scholars of department of physics for pleasant memories had with them.

I am grateful to my family members and relatives for their constant well wishes, love and moral support. Special gratitude must go to my parents and my husband for their supportive, tolerance and understanding behavior for which I could reach the present stage.

Last but not the least, I am grateful to CSIR New Delhi [03(1253)/12/EMR-11], UGC-DAE-CSR Mumbai (CSR/AO/MUM/CRS-M-150/09/467) and Department of Science and Technology (DST) New Delhi (Ref.No. SR/S2/CMP-0078/2010) for giving me the financial support through research project to carry out the present thesis work.

Lastly, word cannot express my gratitude to Almighty God for giving me the strength to believe my passion and pursue my dreams.

**Junmoni Barman**

**IIT Guwahati, India, 11th August, 2017**

# Abstract

Magnetism is a vast area that has been studied from centuries after their earliest discovery in mineral lodestone. The numerous worldwide research on magnetism and magnetic materials goes on to discover and develop new and improved magnetic materials so that they can meet the technological applications and to further unravel their fundamental properties. In recent years, two magnetic phenomena namely exchange bias (EB) and magnetization reversal (MR) have attracted intensive research interest due to their applications in several spintronics devices such as spin valves, magnetic tunnel junctions, thermomagnetic switches, thermally assisted magnetoresistive random access memory (TAMRAM) devices, *etc*. Various materials are found to exhibit these behaviors but research is still going on so as to explore these behaviors near room temperature. In order to carry forward the research in this field, our studies are focused on spinel compounds. Spinel compounds (general formula $AB_2O_4$) with ferrimagnetic (FIM) behavior have been proved as one of the most fascinating magnetic materials. They have been studied for decades because of their interesting fundamental magnetic properties and applications in many areas such as switching devices, sensors, recording media and read-write heads, magnetic refrigeration, magnetically controlled transport of anti-cancer drugs, contrast enhancement in magnetic resonance imaging, microelectronics, magneto-electric devices, spintronics, *etc*. Out of several spinel compounds, chromites have been studied extensively due to their rich magnetic phase diagram and strong correlations among spin, charge and lattice degree of freedom. Such correlations induce magnetoelastic, magnetodielctric and magnetoelectric multifferoic properties in spinel chromites. In addition, EB and MR behaviors have been noticed recently in some of the spinel chromites. Existence of EB and MR in multiferroic materials add to multi-functionality and enhance their potential for niche applications in spintronics.

Chromium based spinel compounds, $ACr_2O_4$, with magnetic A site ions (A= Mn, Fe, Co, Ni, Cu, *etc*.) exhibit cubic structure with $Fd\bar{3}m$ space group at high temperatures. They are normal spinels with $A^{2+}$ ions forming a diamond lattice with tetrahedral coordination of oxygen ions and $Cr^{3+}$ ions forming a pyrochlore lattice with octahedral oxygen ions. A Jahn-Teller distortion induced structural transition from cubic to tetragonal symmetry is observed

for the chromites with A = $Ni^{2+}$, $Cu^{2+}$, and $Fe^{2+}$ having orbital degeneracy. In spinels, the superexchange interactions exist through A – O – B, B – O – B and A – O – A networks. In case of magnetic A site ions, the negative superexchange interaction through A – O – B networks is the strongest one and controls the ferrimagnetic nature of the samples. $ACr_2O_4$ with A = Mn, Co, Fe are also reported to show ferroelectricity and electric polarization.

In this present thesis work, the two spinel compounds namely $NiCr_2O_4$ and $MnCr_2O_4$ are taken for extensive study. $NiCr_2O_4$ is an interesting normal spinel oxide having rich structural and magnetic properties. It is known to undergo structural transition at around $T_t$ = 320 K from cubic spinel at high temperature to tetragonal structure at low temperatures. $NiCr_2O_4$ undergoes FIM transition around $T_C$ = 75 K followed by an antiferromagnetic (AFM) ordering at $T_S$ = 29 K. Tomiyasu and Kagomiya [J. Phys. Soc. Jpn. 73 (2004) 2539] worked out the magnetic structure of $NiCr_2O_4$ and according to them, two A sites are grouped into single sublattice with longitudinal and transverse components and four B sites are grouped into two sublattices with each having longitudinal and transverse components of magnetic moments. Thus $NiCr_2O_4$ exhibits rich structural and magnetic behavior and its isothermal magnetic behavior at different temperature are yet to be understood. Recently, multiferroicity has been observed in $NiCr_2O_4$. A few authors have also observed EB behavior in some composite and nanoparticles of $NiCr_2O_4$ and also in pristine bulk $NiCr_2O_4$ sample but the detailed studies with temperature are lacking.

$MnCr_2O_4$ is another interesting normal spinel but unlike $NiCr_2O_4$, this compound does not undergo any structural transition and the crystal structure remains cubic down to low temperature. Similar to $NiCr_2O_4$, $MnCr_2O_4$ also exhibit non collinear FIM below 45 K. However, in addition to that it undergoes a short range spiral magnetic ordering at $T_S$ = 18 K due to geometrical magnetic frustration. This compound is known to exhibit multiferroic property below $T_S$ like in the $CoCr_2O_4$ compound. Several reports are available till date on the magnetic, magnetodielectric and magnetoelastic properties of pristine $MnCr_2O_4$.

All the exciting magnetic properties of both $NiCr_2O_4$ and $MnCr_2O_4$ compounds are very sensitive to the A – O – B and B – O – B superexchange interactions and therefore their magnetic properties can be easily tuned by substituting different elements either in A or B site. Although there are many reports available on the magnetic properties of both the parent

compounds, systematic study of the effect of substitution in their magnetic properties are still lacking. Therefore study of the basic magnetic properties, investigation of EB and MR phenomenon on the substitutionsl series of these compounds are the main objectives of the present thesis work.

In the present thesis work we have focused on the following four series

i. $Ni(Cr_{1-x}Fe_x)_2O_4$ ($x$ = 0 to 0.60)
ii. $Ni(Cr_{1-x}Al_x)_2O_4$ ($x$ = 0 to 0.50)
iii. $Mn(Cr_{1-x}Fe_x)_2O_4$ ($x$ = 0 to 0.50)
iv. $Mn(Cr_{1-x}Al_x)_2O_4$ ($x$ = 0 to 0.30)

Since $Fe^{3+}$ ($3d^5$) ions possess stronger magnetic moment of 5 $\mu_B$ compared to 3 $\mu_B$ of $Cr^{3+}$ ($3d^3$) ions, substitution of Fe in Cr site may enhance the magnetization and strengthen the superexchange interactions of the system thereby increasing the magnetic transition temperature. Consequently there may be a possibility of enhancing the value of EB field and may also initiate MR phenomenon due to different site preferences of Fe ions. Therefore we have preferred Fe substitution in the Cr site of $NiCr_2O_4$ and $MnCr_2O_4$. According to some earlier reports on similar type of spinel chromites, not only the magnetic ions but non magnetic ions substitution also highly influence their magnetic property. Therefore we are also keen to examine the influence of non magnetic ions substitution in the magnetic properties of these two pristine compounds. In the present thesis work non magnetic Al ions have been chosen for substitution in both $NiCr_2O_4$ and $MnCr_2O_4$.

For the convenience of the readers, the complete thesis work on the above mentioned series will be subdivided into 6 chapters as follows

1. Introduction

2. Experimental Techniques

3. $Ni(Cr, Fe)_2O_4$ Series

4. $Ni(Cr, Al)_2O_4$ Series

5. Fe and Al Substituted $MnCr_2O_4$ Series.

6. Conclusions

**Chapter 1** presents the basic aspects of magnetism and a brief discussion on spinel compounds with special emphasis on its structural and magnetic properties. Starting with various types of magnetic exchange interactions responsible for magnetic ordering, different types of magnetic orderings are described. Types of magnetic anisotropy that plays a major role in different magnetic properties is also discussed. The crystal structure of spinel compounds is introduced along with the effect of crystal field and Jahn-Teller distortion. The influence of geometrical magnetic frustration (GMF) on magnetic properties of spinel compounds is discussed. MR and EB behavior are the limelight of the present thesis work. So subsequently a special focus is given to the discovery of MR and EB behavior and their origin in spinel as well as in other magnetic systems. Review of the past works on $NiCr_2O_4$ and $MnCr_2O_4$ based compounds highlighting their structural and magnetic properties are also presented. As a final point we have discussed concisely the main motivation of the present thesis work.

**Chapter 2** contains the details of different experimental techniques used in the present thesis work. First and foremost need of an experimental research is the sample preparation and this chapter briefly describes the preparation method and various equipments used for this. The structural and magnetic characterization of the prepared samples were carried out by using various experimental tools such as X-Ray diffractometer, Raman spectroscopy, field effect scanning electron microscope, vibrating sample magnetometer, *etc*. The working principle of these sophisticated instruments is discussed in a few sentences.

The preparation of Fe substituted $NiCr_2O_4$ samples and comprehensive study of their structural and magnetic properties are presented in **Chapter 3.** Single phase samples of $Ni(Cr_{1-x}Fe_x)_2O_4$ ($x$ = 0 – 0.60) were prepared by using the standard sol-gel route. Rietveld refinement of the X-ray diffraction pattern of the parent $NiCr_2O_4$ at room temperature reveals the tetragonal structure of the sample with $I4_1/amd$ space group. Magnetization measurement shows a FIM transition with $T_C$ = 73 K. $NiCr_2O_4$ itself shows EB behavior and the detailed investigation of the EB behavior shows that the EB field decay exponentially with increase in temperature from a maximum value of 312 Oe. Origin of the EB in this sample can be explained by considering the anisotropic exchange interaction between the FIM and the AFM

components of magnetic moment. The temperature dependence of coercive field could be explained based on the empirical relation $H_C^{eff} = H_C^{eff}(0)[1-(T/T_C')^2]$.

Fe substitution at Cr site of $NiCr_2O_4$ leads to the structural transition into cubic form ($Fd\bar{3}m$ space group) as per the analysis of XRD patterns at room temperature. Temperature variation of magnetization measurements show that all the prepared samples exhibit FIM transition and the transition temperature ($T_C$) is also found to increase systematically with increase in Fe concentration due to the strengthening of the super-exchange interaction. The Fe substituted samples with $x$ = 0.02, 0.04 and 0.10 exhibit negative EB field as observed for the parent compound but with a higher magnitude and in a wide temperature range. This is due to the enhanced magnetic interaction in Fe doped samples and the corresponding increase in $T_C$ and exchange anisotropy. Fe substitution leads the $NiCr_2O_4$ system to a magnetic compensation behavior ($M$ = 0) for $x$ = 0.06, 0.30 0.40 and 0.50 samples with a sign reversal of magnetization across the compensation temperature. Their magnetic compensation temperature ($T_{comp}$) is found to be in the range of 49 K to 396 K, *i.e.* even above room temperature which is observed for the first time. MR is explained by considering different site occupancies (A and B sites) of the Fe ions and the different temperature dependence of the magnetic moments of different sublattices. Study of EB behavior in these samples having MR reveals that the EB field also undergoes a sign reversal across the $T_{comp}$. Most interestingly such tunable positive and negative EB fields for $x$ = 0.30, 0.40 and 0.50 samples have been observed close to the room temperature. Such tunable EB behavior is explained in terms of change in domination of one sublattice moment over the other as the temperature is varied. For the first time we have demonstrated the bipolar switching of magnetization at room temperature for $x$ = 0.30 and 0.40 samples by just varying the magnitude of magnetic field without changing its direction.

We have carried out the similar structural and magnetic properties in non magnetic Al substituted $NiCr_2O_4$ samples. The preparation and analysis of $Ni(Cr_{1-x}Al_x)_2O_4$ ($x$ = 0 – 0.50) samples are elaborated in **Chapter 4**. We have prepared the single phase samples of $Ni(Cr_{1-x}Al_x)_2O_4$ ($x$ = 0 – 0.50) by using sol-gel route. As observed in Fe doped series, here also the Rietveld refinement of the room temperature XRD patterns reveals a structural transformation from tetragonal ($I4_1/amd$ space group) to cubic ($Fd\bar{3}m$ space group) phase

with Al doping. The lattice parameter of Al doped samples is found to decrease with increase in Al concentration. All the samples show FIM behavior and the transition temperature is found to decrease with increase in Al concentration due to the weakening of the superexchange interaction. Here the dramatic reversal of magnetization below $T_{comp}$ is observed for $x$ = 0.10 sample and the compensation temperature is found to be 40 K. This phenomenon is explained considering different temperature dependences of the magnetic moment of two sublattices of the sample. Considerable EB field is observed for $x$ = 0.15 sample which can also be explained by considering the anisotropic exchange interaction between the FIM and the AFM components of magnetic moment similar to that of Fe substituted samples. The exchange bias field of $x$ = 0.15 sample is found to be only negative while similar to Fe substituted samples, tunable positive and negative exchange bias field is observed across $T_{comp}$ = 40 K for $x$ = 0.10 sample. This is due to the change in domination of magnetic moment of one magnetic sublattice over the other with variation in temperature. Both normal and inverse magnetocaloric effects are observed for $x$ = 0.10 sample.

$MnCr_2O_4$ is another interesting spinel chromite and here also we have substituted magnetic (Fe) and non magnetic (Al) ions in the Cr site. The investigation of structural as well as detailed magnetic properties of Fe and Al substituted $MnCr_2O_4$ samples are presented in **Chapter 5**.

We have successfully prepared the single phase samples of Fe substituted $MnCr_2O_4$ [$Mn(Cr_{1-x}Fe_x)_2O_4$ with $x$ = 0 – 0.50] samples by sol-gel method. Unlike the Fe doped $NiCr_2O_4$ series, the room temperature XRD patterns of these samples do not show any signature of structural transformation. Rietveld refinement of the XRD patterns confirms that all the samples crystallize in cubic structure with $Fd\bar{3}m$ space group. The lattice constant is found to increase with increase in Fe concentration up to $x$ = 0.30 sample and beyond that no appreciable variation is seen. Such variation of lattice parameter and the Raman peak broadening as well as shifting indicates the formation of inverse type of structure for $x$ > 0.30 samples. The FIM transition temperature is found to increase from 46 K for $x$ = 0 to 402 K for $x$ = 0.50 due to the strengthening of the superexchange interaction between A and B site ions. Saturation magnetization ($M_s$) values were determined by analyzing the magnetization data using the law of approach to saturation model and they are found to decrease with

increase in Fe concentration and approach the magnetic compensation at $x$ = 0.40. This composition driven compensation behavior is explained by considering the substitution of $Fe^{3+}$ ions in one of the $Cr^{3+}$ sites. The higher value of coercivity at the compensation point is observed due to poor response of magnetic energy as a result of very small magnetization of each domain. In addition to composition induced magnetic compensation, we have also observed temperature induced magnetic compensation for $x$ = 0.40 with a compensation temperature of 267 K. This is explained by considering different temperature dependence of the two sublattice moments.

$Mn(Cr_{1-x}Al_x)_2O_4$ ($x$ = 0 – 0.30) samples are also found to crystallize in cubic spinel structure and the lattice constant is found to decrease from $a$ = 8.4396 Å for $x$ = 0 to $a$ = 8.3801 Å for $x$ = 0.30. The substitution of Al at Cr site is confirmed from the blue shift of Raman modes. Magnetization measurements and analysis show all the prepared samples exhibit FIM transition with transition temperature in the range of 46 K for $x$ = 0 to 33 K for $x$ = 0.30. The saturation magnetization ($M_s$) and the estimated effective anisotropy constant ($K$) show an anomalous behavior up to $x$ = 0.10 and beyond that they decrease monotonously. They are explained by considering different site preferences of $Al^{3+}$ ions as the doping concentration is increased. The theoretical and experimental effective magnetic moment values of the samples are found to be comparable and they decrease with increasing Al concentration.

**Chapter 6** is devoted to the overall summary of the results obtained from the four series of samples based on $NiCr_2O_4$ and $MnCr_2O_4$. Fe substitution in the Cr site of $NiCr_2O_4$ greatly influences the magnetic properties compared to the Al substitution due to its high magnetic moment. Fe substitution improves the EB field and also initiates the MR behavior with enhanced magnetic compensation temperature. For $x$ = 0.30, 0.40 and 0.50 samples, the reversal in magnetization and EB field coexists near room temperature. Bipolar switching of magnetization is achieved at room temperature for $x$ = 0.30 and 0.40 samples. Al Substitution in $NiCr_2O_4$ also kicks off the MR behavior but with a lower compensation temperature. In both the cases these behaviors are explained by considering different temperature dependence of the two sublattice moments and change in their domination at different temperature range. Fe substituted $MnCr_2O_4$ series exhibits a composition dependent magnetic

compensation behavior at $x = 0.40$ and also gives rise to temperature induced compensation for this sample. These behaviors are explained by different site occupancy of Fe ions and different temperature dependences of the two sublattice moments. On the contrary to Fe substituted $NiCr_2O_4$ series, here magnetic compensation is observed without a reversal in magnetization which may be due to the low anisotropy of the sample. Al substituted samples show decrease in transition temperature as well as the magnetization.

Thus the Fe substituted samples yield superior magnetic properties compared to that of non magnetic Al inclusion in both $NiCr_2O_4$ and $MnCr_2O_4$. They show compensation behaviors close to room temperature. As per our knowledge, this is the first time that a coexistence of reversal in magnetization and exchange bias field is observed in bulk sample near room temperature. Bipolar switching of magnetization at room temperature is also obtained for the first time. Therefore the Fe substituted series with these interesting behaviors close to room temperature may become a suitable candidate for applications in magnetic data storage (memory) and switches. Moreover, there is a lot of future research scope on these series in order to know further basic properties and also to study them from application point of view. Various future scopes in this area are also discussed briefly.

# *Table of Contents*

**Content** **Page No.**

**Acknowledgements** ..... **v**

**Abstract** ..... **vii**

**List of Abbreviations used in this Thesis** ..... **xviii**

**List of Figures** ..... **xx**

**List of Tables** ..... **xxviii**

***Chapter 1*: Introduction** ..... **1**

1.1 Crystal Structure ..... 2

1.2 Origin of Magnetism ..... 5

1.3 Crystal Field Effect ..... 6

1.3.1 Orbital Quenching ..... 8

1.3.2 Jahn-Teller Distortion ..... 9

1.4 Magnetic Exchange Interactions ..... 11

1.4.1 Direct Exchange Interaction ..... 11

1.4.2 Superexchange Interaction ..... 12

1.4.3 Double Exchange Interaction ..... 14

1.4.4 RKKY Interaction ..... 15

1.4.5 Anisotropic Exchange Interaction ..... 16

1.5 Magnetic Orderings ..... 17

1.5.1 Diamagnetic Materials ..... 17

1.5.2 Paramagnetic Materials ..... 18

1.5.3 Ferromagnetic Materials ..... 19

1.5.4 Antiferromagnetic Materials ..... 20

1.5.5 Ferrimagnetic Materials ..... 20

1.6 Magnetic Anisotropy ..... 22

1.6.1 Magnetocrystalline Anisotropy ..... 23

1.6.2 Shape Anisotropy ..... 24

1.6.3 Stress Anisotropy .....25
1.6.4 Exchange Anisotropy .....25
1.7 Magnetization Reversal .....26
1.7.1 Magnetization Reversal in Ferrimagnetic materials ..... 26
1.7.2 Magnetization Reversal in Spin Canted Antiferromagnets and Weak Ferromagnets .....28
1.7.3 Intermetallic Alloys and Ferromagnetic/Antiferromagnetic Interfaces .....29
1.8 Exchange Bias..... 29
1.8.1 Tunable Exchange Bias .....34
1.9 Geometrical Magnetic Frustration ..... 37
1.10 Review of $NiCr_2O_4$ Based Spinel Compounds .....38
1.10.1 Crystal and Magnetic Structure .....39
1.10.2 Other Salient Properties..... 40
1.11 Review of $MnCr_2O_4$ Based Spinel Compounds .....42
1.11.1 Crystal and Magnetic Structure .....42
1.11.2 Other Salient Properties..... 44
1.12 Motivation of the Present Thesis Work .....45

***Chapter 2*: Experimental Techniques .....47**

2.1. Sample Preparation ..... 47
2.1.1 Sol-gel Method .....47
2.1.2 High Temperature Furnaces..... 50
2.2 Measurement Techniques ..... 52
2.2.1 X-ray Diffraction .....52
2.2.2 Raman Spectroscopy..... 55
2.2.3 Field Emission Scanning Electron Microscope .....58
2.2.4 Energy Dispersive X-ray Spectroscopic Technique ..... 60
2.2.5 Vibrating Sample Magnetometer .....61

***Chapter 3*: Ni(Cr, Fe)$_2$O$_4$ Series .....67**

3.1 Introduction .....67

3.2 Structural Properties ....68
3.3 Temperature and Field Dependent Magnetic Properties ....76
3.4 Magnetization Reversal .... 80
3.5 Bipolar Switching of Magnetization ....87
3.6 Exchange Bias Behavior ....89
3.7 Training Effect .... 109
3.8 Conclusions ....111

*Chapter 4*: **Ni(Cr, Al)$_2$O$_4$ Series** ....**113**

4.1 Introduction ....113
4.2 Structural Properties ....114
4.3 Temperature and Field Dependent Magnetic Properties ....121
4.4 Magnetization Reversal ....129
4.5 Exchange Bias Behavior .... 130
4.6 Magnetocaloric Effect ....136
4.7 Conclusions .... 138

*Chapter 5*: **Fe and Al Substituted MnCr$_2$O$_4$ Series** .... **141**

5.1 Introduction ....141
5.2 Fe Substituted MnCr$_2$O$_4$ Series ....142
5.2.1 Structural Properties ....143
5.2.2 Magnetic Properties of Mn(Cr$_{1-x}$Fe$_x$)$_2$O$_4$ .... 154
5.2.3 Temperature Induced Magnetic Compensation ....164
5.3 Al Substituted MnCr$_2$O$_4$ Series ....170
5.3.1 Structural Properties ....170
5.3.2 Magnetic Properties of Mn(Cr$_{1-x}$Al$_x$)$_2$O$_4$ .... 178
5.4 Conclusions .... 183

*Chapter 6*: **Conclusions** .... **187**

**References** .... **193**

**Publications** .... **205**

# *List of Abbreviations used in this Thesis*

**AFM** Antiferromagnetic

**BSE** Back scattered electrons

**CCD** Charge couple device

**CEP** Conduction electron polarization

**CW** Curie-Weiss

**DM** Dzyaloshinsky-Moriya

**EB** Exchange bias

**EDS** Energy dispersive X-ray spectroscopy

**FC** Field cooled

**FE** Field emission

**FESEM** Field emission scanning electron microscope

**FIM** Ferrimagnetic

**FM** Ferromagnetic

**FMR** Ferromagnetic resonance

**FWHM** Full width at half maximum

**GMF** Geometrical magnetic frustration

**JTD** Jahn-Teller distortion

**LAS** Law of approach to saturation

**LKDM** Lyons, Kaplan, Dwight and Menyuk

**MCE** Magnetocaloric effect

**MR** Magnetization reversal

**NMR** Nuclear magnetic resonance

**NN** Nearest neighbour

**NNN** Next nearest neighbour

**OSPE** Octahedral site preference energy

**PM** Paramagnetic

**RKKY** Ruderman, Kittel, Kasuya and Yosida

**SEM** Scanning electron microscope

**SG** Spin glass

**SPD** Single point detection

**TAMRAM** Thermally assisted magnetoresistive random access memory

**VSM** Vibrating sample magnetometer

**XRD** X-ray diffraction

**ZFC** Zero field cooled

# *List of Figures*

**Page No.**

## *Chapter 1:*

**Figure 1.1:** Spinel crystal structure showing $BO_6$ octahedra and $AO_4$ tetrahedra. Blue spheres represent oxygen anions, yellow spheres represent B site cations and green spheres represent A site cations. .....3

**Figure 1.2:** Schematic representation of (a) orbiting electron around the nucleus and (b) electron spinning around its own axis and their corresponding magnetic moments. .....6

**Figure 1.3:** The electronic distribution of *3d* orbitals. In the cubic crystal field, this fivefold degeneracy is lifted and separated into two $e_g$ levels ( $d_{x^2-y^2}$ and $d_{Z^2}$ ) and three $t_{2g}$ levels ($d_{xy}$, $d_{yz}$ and $d_{zx}$) (Reproduced from Tokura *et al.* [47]) .....7

**Figure 1.4:** Energy level diagram in octahedral and tetrahedral environments. .....8

**Figure 1.5:** Further splitting of both the $t_{2g}$ and $e_g$ states in ions with $d^4$ configuration due to the JTD. ..... 10

**Figure 1.6:** Schematic diagram of (a), (b) AFM and (c) FM superexchange interactions [53]. ..... 13

**Figure 1.7:** (a) Sketch of double exchange interaction which involves two Mn ions and one O ion. (b) The mobility of $e_g$ electrons improves if the localized spins are polarized and parallel to each other. .....15

**Figure 1.8:** Schematic curves of spontaneous magnetizations of the A and B sublattices, and the resultant saturation magnetizations for ferrimagnet showing compensation behavior [63]. .....22

**Figure 1.9:** Temperature dependence of magnetization of $Co_2VO_4$ in an external field of 700 Oe [16]. .. ..... 27

**Figure 1.10**: Hysteresis loops of Co nanoparticles coated with CoO at 77 K under both zero field cooled (dotted line) and field cooled (solid line) conditions [64]. .....30

**Figure 1.11**: Schematic diagram of the spin configuration of an FM-AFM couple at different stages of a shifted hysteresis loop for a system with large AFM magnetic anisotropy [68]. ..32

**Figure 1.12**: Schematic diagram of the spin configuration of an FM-AFM couple at different stages of a hysteresis loop for a system with low AFM magnetic anisotropy [94]. ... ..... 33

**Figure 1.13**: Temperature dependence of the (a) effective coercive field, $H_C^{eff}$ and (b) the EB field $H_{EB}$ in a single crystalline $Nd_{0.75}Ho_{0.25}Al_2$. (c) Schematic diagram of the orientation of different sub-components of magnetization with respect to the applied field for $Nd_{0.75}Ho_{0.25}Al_2$ single crystal at $T > T_{comp}$ and $T < T_{comp}$ [91]. .....36

**Figure 1.14:** (a) Corner sharing tetrahedra formed by B ($Cr^{3+}$) sublattice in the spinel structure. (b) Strong GMF in antiferromagnetically coupled $Cr^{3+}$ in the corner sharing tetrahedra formed by it [24]. .....38

**Figure 1.15:** (a) Heat capacity of $NiCr_2O_4$ [18]. Schematic diagram of (b) longitudinal FIM and (c) transverse AFM components of group of A ($Ni^{2+}$) and B ($Cr^{3+}$) sublattices [54]. .....40

**Figure 1.16:** Mean FIM spiral order of $MnCr_2O_4$ estimated by Tomiyasu *et al*. from neutron scattering experiments [118]. ..... 43

## *Chapter 2:*

**Figure 2.1:** Different stages of sintering process [164]. ..... ..... 49

**Figure 2.2:** Block diagram of the furnace with maximum operating temperature of 1200 °C. .....51

**Figure 2.3:** Schematic diagram of Bragg's X-ray diffraction. .....53

**Figure 2.4**: Ray diagram of X- ray diffractometer. .....53

**Figure 2.5:** Diagram of Rayleigh and Raman scattering process. ..... 56

**Figure 2.6**: Schematic diagram of Raman spectrometer. .....57

**Figure 2.7:** Schematic view of FESEM. .....59

**Figure 2.8**: (a) Electrons and photons emanating from tear-shaped interaction volume during electron beam impingement on specimen surface, and (b) Energy spectrum of electrons emitted from the specimen surface. .....59

**Figure 2.9:** Block diagram of the VSM. ..... 62

**Figure 2.10:** High temperature oven. .....65

## *Chapter 3:*

**Figure 3.1:** XRD patterns of $Ni(Cr_{1-x}Fe_x)_2O_4$ compounds for $x = 0 – 0.50$. .....70

**Figure 3.2:** Rietveld refinement of the XRD patterns of (a) $x$ = 0 and (b) $x$ = 0.02 samples. The red open circles are the experimental data and the black solid lines are the fitted data. The bottom line shows the difference between experimental and refined data. …..... 71

**Figure 3.3:** Rietveld refinement of the XRD patterns of (a) $x$ = 0.20 and (b) $x$ = 0.50 samples. The red open circles are the experimental data and the black solid lines are the fitted data. The bottom line shows the difference between experimental and refined data. .....72

**Figure 3.4:** FESEM images recorded for (a) $x$ = 0, (b) $x$ = 0.20 and (c) $x$ = 0.50 samples along with EDS spectrum [(d), (e) and (f) respectively]. .....74

**Figure 3.5:** Grain size distribution of (a) $x$ = 0, (b) $x$ = 0.06, (c) $x$ = 0.20 and (d) $x$ = 0.50 samples..... 75

**Figure 3.6:** Temperature dependent magnetization of $Ni(Cr_{1-x}Fe_x)_2O_4$ ($x$ = 0 – 0.50) samples under ZFC and FC conditions..... 77

**Figure 3.7:** Temperature dependent magnetization of $Ni(Cr_{1-x}Fe_x)_2O_4$ ($x$ = 0 – 0.50) samples under ZFC condition in expanded scales. .....78

**Figure 3.8:** *M–H* loops of $Ni(Cr_{1-x}Fe_x)_2O_4$ ($x$ = 0 – 0.50) samples measured at 45 K after cooling the samples under zero field condition. .....79

**Figure 3.9:** *M–H* loops of $Ni(Cr_{1-x}Fe_x)_2O_4$ ($x$ = 0 – 0.50) samples measured at a temperature just below their respective FIM $T_C$. .....80

**Figure 3.10:** Temperature dependence of FC magnetization for $x$ = 0.06, 0.30, 0.40 and 0.50..... 81

**Figure 3.11:** Temperature dependence of FC magnetization at different fields for $x$ = 0.06, 0.30, 0.40 and 0.50..... 82

**Figure 3.12:** Temperature dependence of FC magnetization for $x$ = 0.30 sample measured at $H = \pm$ 200 Oe. .....83

**Figure 3.13:** Schematic block diagram of the magnetic configurations in two temperature regions $T_{comp} < T < T_C$ *and* $T < T_{comp}$. .....85

**Figure 3.14:** Temperature variation of FC magnetization for $x$ = 0.60 sample. .....86

**Figure 3.15:** Bipolar switching of magnetization at 100 K for (a) $x$ = 0.30 and (b) $x$ = 0.40 samples at room temperature. .....89

**Figure 3.16:** *M–H* loops for (a) $x$ = 0, (b) $x$ = 0.02, (c) $x$ = 0.04 and (d) $x$ = 0.10 samples at different temperatures after cooling the samples under a field of 3000 Oe. .....91

**Figure 3.17:** Temperature variation of $H_{EB}$, $M_{EB}$ and $H_C^{eff}$ for (a) – (c) $x = 0$, (d) – (f) $x = 0.02$ and (g) – (i) $x = 0.04$, respectively along with the theoretical fit. Insets of (c), (f) and (i) show the linear behavior of $H_C^{eff}$ versus $T^2$ plot for $x = 0$, 0.02 and 0.04, respectively. .....93

**Figure 3.18:** The linear behavior of $H_C^{eff}$ versus $T^2$ plot. Inset shows the linear behavior of (111) peak intensity of neutron diffraction (obtained from reference [54]) versus $T^2$. .....96

**Figure 3.19:** *M–H* loops for $x = 0.06$ sample at different temperatures after cooling the samples under a field of 3000 Oe. .....97

**Figure 3.20:** Temperature variation of $H_{EB}$ for (a) $x = 0.06$ and (c) $x = 0.10$ samples. $M_{EB}$ versus temperature plots for these samples are shown in (b) and (d), respectively. .....98

**Figure 3.21:** *M–H* loops for $x = 0.30$ sample at different temperatures after cooling the samples under a field of 3000 Oe. .....99

**Figure 3.22:** *M–H* loops for $x = 0.30$ sample at different temperatures after cooling the samples under a field of 3000 Oe in an expanded scale. .....100

**Figure 3.23:** *M–H* loops for $x = 0.40$ sample at different temperatures after cooling the samples under a field of 3000 Oe. .....101

**Figure 3.24:** *M–H* loops for $x = 0.50$ sample at different temperatures after cooling the samples under a field of 3000 Oe. ..... 102

**Figure 3.25:** Temperature variation of $H_{EB}$ for (a) $x = 0.30$, (c) $x = 0.40$ and (e) $x = 0.50$ samples, respectively. Temperature variations of $H_C^{eff}$ for these samples are shown in (b), (d) and (f), respectively. .....104

**Figure 3.26:** Schematic block diagram of the magnetic configuration of $x = 0.30$ sample in the two temperature range $T_{comp} < T < T_C$ and $T < T_{comp}$ under the field cooling condition in order to explain the EB behavior. .....107

**Figure 3.27:** $d^2M/dH^2$ versus $H$ plots for $x = 0$, 0.02, 0.04 and 0.10 samples at a particular temperature. .....108

**Figure 3.28:** $dM/dH$ versus $H$ plots for $x = 0.30$, 0.40 and 0.50 samples at two particular temperatures above and below $T_{comp}$. .....109

**Figure 3.29:** Consecutive *M-H* loops with index $n = 1$ to $n = 9$ in expanded scale for $x = 0$ sample. .....110

**Figure 3.30:** (a) $H_{EB}$ and (b) $M_{EB}$ as a function of $n$ for $x = 0$ sample. Insets show the same data as a function of $1/\sqrt{n}$. The red solid lines represent the fitted data. .....111

## *Chapter 4:*

**Figure 4.1:** XRD patterns of $Ni(Cr_{1-x}Al_x)_2O_4$ compounds for $x = 0 – 0.50$. .....115
**Figure 4.2:** Rietveld refinement of the XRD patterns of (a) $x = 0$ and (b) $x = 0.05$ samples. The red open circles are the experimental data and the black solid lines are the fitted data. The bottom line shows the difference between experimental and refined data. .....116
**Figure 4.3:** Rietveld refinement of the XRD patterns of (a) $x = 0.20$ and (b) $x = 0.30$ samples. The red open circles are the experimental data and the black solid lines are the fitted data. The bottom line shows the difference between experimental and refined data. .....117
**Figure 4.4:** Variation of lattice parameter '$a$' with Al concentration '$x$'. .....118
**Figure 4.5:** FESEM images recorded for (a) $x = 0.10$ and (b) $x = 0.20$ samples along with EDS spectrum [(c) and (d), respectively]. .....120
**Figure 4.6:** Grain size distribution of (a) $x = 0.10$ and (b) $x = 0.20$ samples. .....120
**Figure 4.7:** Temperature dependent magnetization of $Ni(Cr_{1-x}Al_x)_2O_4$ ($x = 0 – 0.50$) samples under ZFC and FC conditions. .....123
**Figure 4.8:** Variation of $T_C$ with Al concentration '$x$'. .....123
**Figure 4.9:** Temperature dependent magnetization of $Ni(Cr_{1-x}Al_x)_2O_4$ ($x = 0 – 0.50$) samples under ZFC condition in an expanded scale. .....124
**Figure 4.10:** The Curie-Weiss fit in the PM region of $Ni(Cr_{1-x}Al_x)_2O_4$ ($x = 0 – 0.50$). .....126
**Figure 4.11:** Variation of experimental (circle) and theoretical (Square) effective magnetic moment '$\mu_{eff}$' with Al concentration '$x$'. .....126
**Figure 4.12:** *M-H* loops at 30 K for $Ni(Cr_{1-x}Al_x)_2O_4$ ($x = 0 – 0.50$) samples under ZFC condition. .....128
**Figure 4.13:** Variation of saturation magnetization '$M_s$' with Al concentration '$x$'. .....128
**Figure 4.14:** Temperature dependence of FC magnetization for $x = 0.10$ sample (a) at an applied field of 500 Oe and (b) at different applied fields. .....130
**Figure 4.15:** FC ($H = 3000$ Oe) *M–H* loops of $x = 0.10$ at different temperatures in expanded scales. .....132

**Figure 4.16:** FC ($H$ = 3000 Oe) $M$–$H$ loops of $x$ = 0.15 at different temperatures in expanded scales. .....133
**Figure 4.17:** Temperature variation of $H_{EB}$ and $M_{EB}$ for $x$ = 0.10 (a, b) and $x$ = 0.15 (c, d) samples. .....135
**Figure 4.18:** $d^2M/dH^2$ versus $H$ plots for $x$ = 0.15 sample at 30 K. .....136
**Figure 4.19:** Temperature variation of magnetic entropy change ($-\Delta S_M$) for $x$ = 0.10 sample. .....138

## *Chapter 5:*

**Figure 5.1**: XRD patterns of $Mn(Cr_{1-x}Fe_x)_2O_4$ compounds for $x$ = 0 – 0.50. .....144
**Figure 5.2:** Rietveld refinement of the XRD patterns of (a) $x$ = 0 and (b) $x$ = 0.40 samples. The red open circles are the experimental data and the black solid lines are the fitted data. The bottom line shows the difference between the experimental and the fitted data. .....145
**Figure 5.3:** (a) Enlarged view of the high intense (311) peak for $x$ = 0 – 0.50 samples and (b) Variation of lattice parameter with Fe concentration '$x$'. . ..... 146
**Figure 5.4:** (a) Variation of B – O – B and A – O – B bond angles and (b) variation of B – O and A – O bond lengths as a function of $x$, the concentration of Fe. . ..... 148
**Figure 5.5:** Raman spectra of $Mn(Cr_{1-x}Fe_x)_2O_4$ samples at room temperature along with the fitted data. .....150
**Figure 5.6:** (a) Peak position and (b) FWHM of various Raman modes of $Mn(Cr_{1-x}Fe_x)_2O_4$ samples at room temperature as a function of Fe concentration '$x$'. .....151
**Figure 5.7:** (a) **–** (d) FESEM images and (e) – (h) grain size distribution of $x$ = 0, 0.20, 0.40 and 0.50 samples of $Mn(Cr_{1-x}Fe_x)_2O_4$. .....152
**Figure 5.8:** EDS spectrum of $x$ = 0, 0.20, 0.40 and 0.50 samples. .....153
**Figure 5.9:** Temperature dependent magnetization of $Mn(Cr_{1-x}Fe_x)_2O_4$ ($x$ = 0 – 0.50) samples under ZFC and FC conditions. .....155
**Figure 5.10:** $M$-$H$ loops of $Mn(Cr_{1-x}Fe_x)_2O_4$ compounds at 25 K. .....156
**Figure 5.11:** Expanded scale view in the sign reversal region of the $M$-$H$ loops of $Mn(Cr_{1-x}Fe_x)_2O_4$ compounds at 25 K. .....157

**Figure 5.12:** Initial magnetization curves for (a) $x = 0$, (b) $x = 0.10$, (c) $x = 0.20$, (d) $x = 0.30$, (e) $x = 0.40$ and (f) $x = 0.50$ samples along with the fitted data to the law of approach to saturation. .....158

**Figure 5.13:** Variation of experimental (at 25 K) and calculated saturation magnetization ($M_s$) as a function of Fe concentration. Inset shows variation of $M_s$ with Fe concentration at 30, 35 and 40 K. .....160

**Figure 5.14:** (a) Variation of anisotropy constant and (b) coercivity at 25, 30, 35 and 40 K as a function of Fe concentration '*x*'. .....162

**Figure 5.15:** Variation of (a) saturation magnetization and (b) coercivity with temperature. .....164

**Figure 5.16:** (a) Magnetization as a function of temperature for $x = 0.40$ sample under FC condition for different cooling fields. Schematic block diagram of the magnetic configurations in two temperature regions (b) $T > T_{comp}$ and (c) $T < T_{comp}$. .....166

**Figure 5.17:** FC (H = 3000 Oe) *M–H* loops of $x = 0.40$ sample at different temperatures in an expanded scale. .....168

**Figure 5.18:** Variation of saturation magnetization ($M_s$), remanent magnetization ($M_r$) and coercive field ($H_C$) with temperature for $x = 0.40$ sample. .....169

**Figure 5.19:** XRD patterns of $Mn(Cr_{1-x}Al_x)_2O_4$ compounds for $x = 0 – 0.30$. ..... 171

**Figure 5.20:** Rietveld refinement of the XRD patterns of (a) $x = 0$ and (b) $x = 0.30$ samples. The red open circles are the experimental data and the black solid lines are the fitted data. The bottom line gives the difference between experimental and theoretical data. .....172

**Figure 5.21:** (a) Enlarged view of the high intense (311) peak for $x = 0 – 0.30$ samples and (b) Variation of lattice parameter with Al concentration. The solid line is just for guidance. .....173

**Figure 5.22:** Raman spectra of $Mn(Cr_{1-x}Al_x)_2O_4$ samples at room temperature along with the fitted data. ..... 176

**Figure 5.23:** (a) & (b) FESEM images and (c) & (d) grain size distribution of $x = 0.10$ and 0.30 samples. .....177

**Figure 5.24:** EDS spectrum of $x = 0.10$ and 0.30 samples. .....178

**Figure 5.25:** Temperature dependent magnetization of $Mn(Cr_{1-x}Al_x)_2O_4$ ($x = 0 – 0.30$) samples under zero ZFC and FC conditions. .....179

**Figure 5.26:** *M-H* loops of $Mn(Cr_{1-x}Al_x)_2O_4$ compounds at 25 K (for clearly distinguishing different plots, *M* values are restricted close to their saturation). .....180
**Figure 5.27:** Initial magnetization curves for (a) $x = 0$, (b) $x = 0.10$, (c) $x = 0.20$ and (d) $x = 0.30$ samples along with the fitted data to the law of approach to saturation. .....181
**Figure 5.28:** (a) variation of experimental (at 25 K) and theoretical saturation magnetization ($M_s$) and (b) variation of anisotropy constant at 25 K as a function of Fe concentration. ....182
**Figure 5.29:** Curie-Weiss law fit along with experimental data in the PM region of (a) $x = 0$ and (b) $x = 0.30$ samples. (c) Experimental (solid sphere) and theoretical effective magnetic moment '$\mu_{eff}$' (solid line) as a function of Al concentration '$x$'. .....183

# List of Tables

**Page No.**

## Chapter 3:

**Table 3.1:** Parameters obtained from the Rietveld analysis of XRD patterns for the samples $Ni(Cr_{1-x}Fe_x)_2O_4$ (0 – 0.50). $R_F$, $R_{Bragg}$, $R_P$ and $\chi^2$ are the reliability factors. .....73

**Table 3.2:** The cationic ratio determined from EDS analysis for $x$ = 0, 0.06, 0.20 and 0.50 samples. .....75

## Chapter 4:

**Table 4.1:** Parameters obtained from the Rietveld analysis of XRD patterns for the samples $Ni(Cr_{1-x}Al_x)_2O_4$ (0 – 0.50). $R_F$, $R_{Bragg}$, $R_P$ and $\chi^2$ are the reliability factors. .....119

## Chapter 5:

**Table 5.1:** Parameters obtained from the Rietveld analysis of XRD patterns for the samples $Mn(Cr_{1-x}Fe_x)_2O_4$ (0 – 0.50). $R_F$, $R_{Bragg}$, $R_P$ and $\chi^2$ are the reliability factors. .....147

**Table 5.2:** The cationic ratio determined from EDS analysis for $x$ = 0, 0.20, 0.40 and 0.50 samples. .....153

**Table 5.3:** Saturation magnetization ($M_s$), coercivity ($H_C$) and effective anisotropy constant ($K$) of the samples $Mn(Cr_{1-x}Fe_x)_2O_4$ at 25 K. .....163

**Table 5.4:** Parameters obtained from the Rietveld analysis of XRD patterns for the samples $Mn(Cr_{1-x}Al_x)_2O_4$ (0 – 0.30). $R_F$, $R_{Bragg}$, $R_P$ and $\chi^2$ are the reliability factors. .....174

# *Chapter 1*

# *Introduction*

Magnetism and magnetic materials is one of the core areas of condensed matter physics and material science due to its role on domestic, industrial, scientific and commercial applications. Some of their applications are in storage of digital and analogue information, accelerators, transportation, medical diagnosis, household appliances, *etc*. In some of the magnetic materials their electrical transport can easily be controlled by the application of magnetic field and they have potential application for Spintronics, *i.e.* Spin-electronics. Here in addition to the type and concentrations of charge carriers, the spin of the electrons is used as an additional degree of freedom in controlling the electrical transport. Addition of spin degree of freedom provides new effects, new capabilities and new functionalities to the conventional electronic devices. It is likely to improve the efficiency, miniaturization, reduction in power consumption, speed and non-volatile memory devices, *etc*. Spintronics is demonstrated in some of the discoveries like giant magneto resistance, colossal magneto resistance, tunneling magneto resistance, *etc*. and some of them are already being used in read/write heads and magnetic memory devices [1]. Recent research on magnetic materials and their properties suggest that exchange bias (EB) and magnetization reversal (MR) behaviors also play vital role in controlling the properties of spin valve and spintronic devices [1-3].

Materials exhibiting more than one ferroic ordering such as magnetic, ferroelectric and ferroelastic ordering, are called multiferroics. In such multiferroic materials, the strong coupling between magnetic and ferroelectric ordering offers additional lever in controlling the device functionalities such as electric control of magnetic properties or vice versa, electric control of EB, *etc*. [4, 5]. Therefore, the search for better multiferroics continues to

realize the above properties in different materials including single crystals, nanoparticles, multilayer thin films, and even in single phase bulk materials.

In the search for single phase materials with technologically advanced functional properties, one of the most studied structural families is that of the spinels. Magnetism itself was discovered in spinel compound, *i.e.* $Fe_3O_4$ based mineral lodestone. Investigation of spinels ($AB_2X_4$) was initiated by Bragg and Nishikawa in 1915, who determined their structure [6, 7]. Subsequently, various interesting phenomena were investigated in spinel compounds such as magnetoresistance [8, 9], superconductivity [10], Jahn-Teller distortion [11], metal insulator transition [12], multiferrocity [13], EB [14, 15], MR [16], *etc*.

Out of several spinel compounds, chromites ($ACr_2O_4$) are an intriguing class of materials that exhibit rich complex magnetic phase diagram and strong correlations among spin, charge and lattice degrees of freedom. Such correlations induce magnetoelastic, magnetodielctric and magnetoelectric multifferoic properties in spinel chromites [13, 17-25]. EB and MR behaviors have also been noticed recently in some of the spinel chromites [26-30]. Existence of EB and MR in multiferroic materials add to multi-functionality and enhanced their potential applications in spintronics [4, 5]. The present thesis work is dedicated to the study of EB and MR in spinel chromites. So, this introductory chapter is mainly devoted to the review of structural and physical properties of spinel chromites and, the EB and MR phenomena. We begin with a detailed discussion of the crystal structure of spinel compounds.

# 1.1 Crystal Structure

Spinel compounds have a general chemical formula of $AB_2X_4$, where A is a divalent element in a tetrahedral coordination with anions (X) and B is a trivalent transition metal ion in an octahedral coordination with anions, and X can be O, S, Se, or Te. Majority of the spinel compounds belong to the high symmetry $Fd\bar{3}m$ space group (No. 227) with the atomic positions of A, B and anion X in 8*a* (1/8, 1/8, 1/8), 16*d* (1/2, 1/2, 1/2) and 32*e* (*x*, *x*, *x*), respectively [31, 32]. The number of formula units ($AB_2X_4$) per unit cell is 8 [31]. Typical oxide spinel structure is shown in Fig. 1.1.

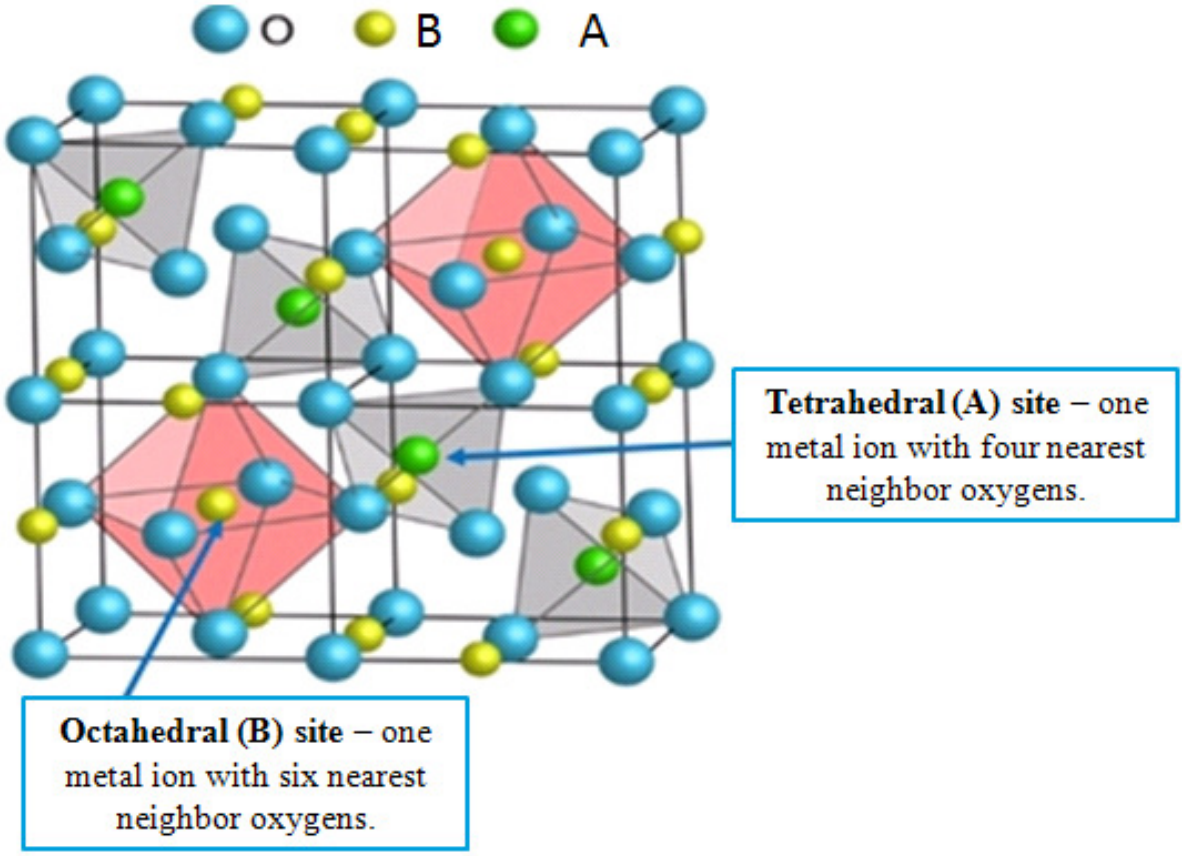


**Figure 1.1:** Spinel crystal structure showing $BO_6$ octahedra and $AO_4$ tetrahedra. Blue spheres represent oxygen anions, yellow spheres represent B site cations and green spheres represent A site cations.

Several transition metal ions can occupy the tetrahedral A and the octahedral B sites. Some commonly found A site and B site ions are respectively, A = $Zn^{2+}$, $Cu^{2+}$, $Co^{2+}$, $Fe^{2+}$, $Mn^{2+}$, $Ni^{2+}$, $Ga^{3+}$, *etc*. and B = $Cu^{2+}$, $Ni^{2+}$, $Co^{2+}$, $Co^{3+}$, $Fe^{2+}$, $Fe^{3+}$, $Mn^{3+}$, $Cr^{3+}$, $V^{3+}$, $Al^{3+}$, $Ti^{3+}$, *etc*. From these ions, it is noticeable that most of the ions have no overriding preference for either the octahedral or tetrahedral site, but they may occupy both the sites. Depending on the distribution of cations in the tetrahedral and the octahedral sites, three types of spinel compounds are possible. (i) Normal spinel: if all the 8 A cations occupy the tetrahedral sites and the 16 B cations occupy the octahedral site, then the spinel compound is called normal spinel. Generally, the spinel chromites with $Cr^{3+}$ in the octahedral sites ($CoCr_2O_4$, $NiCr_2O_4$, $MnCr_2O_4$, $CuCr_2O_4$, *etc*.) are normal spinel due to the large octahedral site preference energy (OSPE) of $Cr^{3+}$ [33]. (ii) Inverse spinel: if half (8) of the B cations occupy the tetrahedral

sites and the remaining half (8) of B and the 8 A cations occupy the octahedral sites then the resultant structure is an inverse spinel. Ferrites like $Fe_3O_4$, $NiFe_2O_4$, *etc*. are inverse spinel structure [34]. (iii) Mixed spinel: If A and B cations are randomly distributed among both tetrahedral and the octahedral sites and form intermediate compounds, *i.e.* neither normal nor inverse spinel, then the structure is called mixed spinel. Depending on the preparation conditions, $CoFe_2O_4$ is known to be in mixed spinel structure [34].

In spinel compounds, the distribution of nearest neighbor (NN) and the next nearest neighbor (NNN) for A and B site ions are such that, the A site ion consists of 4A NN, 12B NN, 12A NNN and 16B NNN ions, while the B site ion consists 6A NN, 6B NN, 8A NNN, and 12B NNN ions. The B site is more closely packed than the A site and hence the distance between the neighboring B – B ions is smaller than that of neighboring A – B ions. Distance between neighboring A – A ions is the longest one. In the spinel compound, the octahedrons are connected to each other by sharing their edges but the tetrahedrons and the octahedrons are attached through the corners. The angle between A site and B site ions (A – O – B) is around 120° whereas the B – O – B angle is around 90°. Due to large number of competing interactions between the ions in the two sites through different NN and NNN pathways, often the parent lattice broke down into a simpler model of interpenetrating sublattices. Then the atoms on the B site can be described as forming a pyrochlore lattice and the A sites constitute a diamond lattice of corner sharing tetrahedra [33].

At high temperatures, the spinel chromites $ACr_2O_4$ (A = Mn, Fe, Co, Ni, Cu) exhibit cubic structure with $Fd\bar{3}m$ space group. Here $A^{2+}$ ions form a diamond lattice with tetrahedral coordination of oxygen environment and $B^{3+}$ ions form a pyrochlore lattice with octahedral oxygen environment. $Cr^{3+}$ions in octahedral environment undergo splitting of 3*d* orbitals into low lying $t_{2g}$ triplet and higher energy $e_g$ doublet and they are inactive to Jahn-Teller distortion (JTD) [21]. In tetrahedral coordination, $t_{2g}$ orbitals are at higher energy state compared to $e_g$ orbitals and large JTD is expected for the orbitally degenerate $t_{2g}$ orbital, *i.e.* with electronic configurations $3d^3$ $(e_g^2 t_{2g}^1)$, $3d^4$ $(e_g^2 t_{2g}^2)$, $3d^8$ $(e_g^4 t_{2g}^4)$ and $3d^9$ $(e_g^4 t_{2g}^5)$ [35]. This distortion reduces the symmetry of the crystal from cubic to tetragonal. Orbitals in the same levels occupied by different number of electrons are called degenerate ground state. JTD induced structural transition is observed when A site is occupied by $Ni^{2+}$ or $Cu^{2+}$ ions in

spinel chromites [17, 36]. $FeCr_2O_4$ also exhibits such structural transition but at low temperature [37]. The crystal field effect and the JTD are discussed in detail in section 1.3.

The unit cell size, *i.e.* the lattice parameter ($a$) of the cubic spinel chromites at room temperature lies within the range of 8.30 Å to 8.45 Å. Reported value of $a$ for $MnCr_2O_4$ varies from 8.43 Å to 8.45 Å [23, 38, 39]. The lattice parameter of $CoCr_2O_4$, $MgCr_2O_4$ and $ZnCr_2O_4$ are almost comparable and it was reported to be around 8.33 Å [23, 39-42]. $FeCr_2O_4$ with room temperature cubic structure has $a$ = 8.38 Å [43]. The $NiCr_2O_4$ and $CuCr_2O_4$ compounds having JTD exhibit tetragonal structure at room temperature with $a$ = 5.84 Å and $c$ = 8.43 Å, and $a$ = 6.03 Å and $c$ = 7.78 Å, respectively [17].

Before investigating different magnetic properties of these materials, it is essential to understand some basic magnetic properties related to these materials. So the following sections will be devoted to some basic aspects of magnetism and magnetism in spinel compounds.

## 1.2 Origin of Magnetism

The origin of magnetism in materials arises from their atomic structure. In atomic scale, there are two types of electron motion that contribute magnetic moment. First one is the rotation of electrons in atomic orbitals which produces small magnetic field and hence a magnetic moment along the axis of rotation as shown in Fig. 1.2(a). Second one is the rotation (spin) of electron in its own axis generating a magnetic moment along the spin axis [Fig. 1.2(b)] [44-46]. Therefore, simply the moving of electrons can be considered as small electric current which produces a magnetic moment. The macroscopic magnetic properties of materials are the consequence of such magnetic moments of individual electrons. The overall magnetic moment of an atom is the sum of magnetic moments of each of the constituting electrons counting both orbital and spin contributions as well as considering the cancellation of moment in completely filled orbitals. Based on the magnetic moment of each atom or ion and its interaction with other neighbouring atoms or ions, the magnetic materials are broadly classified as: diamagnet, paramagnet, ferromagnet, antiferromagnet and ferrimagnet [45, 46]. Different type of magnetic interactions and their long range magnetic ordering are discussed in sections 1.4 and 1.5.

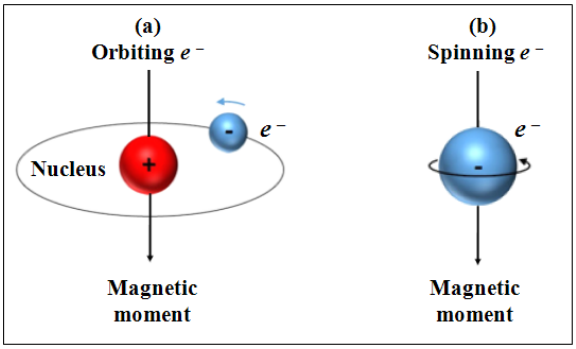


**Figure 1.2:** Schematic representation of (a) orbiting electron around the nucleus and (b) electron spinning around its own axis and their corresponding magnetic moments.

# 1.3 Crystal Field Effect

Atoms in a solid with a regular crystal structure are influenced by the electric field due to the neighboring atoms in the crystal. Average of such electric fields are called crystal field [46]. Crystal field depends upon the nature of the local environments such as nature of atomic co-ordination, *etc*. The magnetism in transition elements originates from their unfilled *d*-shell electrons. In general, the *d* orbital has five degenerate energy levels and is divided into two sub orbitals namely $t_{2g}$ ($d_{xy}$, $d_{yz}$ and $d_{zx}$) and $e_g$ ($d_{x^2-y^2}$ and $d_{Z^2}$) as shown in Fig. 1.3. But when ligands approach the *d* orbital from different directions, not all parts of *d* orbitals interact directly with the ligands and it results in unequal electrostatic repulsion between them. Such interaction creates a splitting of *d* orbital due to the electrostatic environment and the *d* orbital energy is no longer degenerate. For example, in octahedral environment, the crystal field arises mainly from the electrostatic repulsion from the negatively charged electrons in the surrounding oxygen 2*p* orbitals. The electronic configurations of 2*p* orbitals are oriented along *x*, *y* and *z* axes and are referred as $p_x$, $p_y$ and $p_z$, respectively. Therefore, in the octahedral environment the $e_g$ orbitals ($d_{x^2-y^2}$ and $d_{Z^2}$) which also point along *x*, *y* and *z* axes, overlap predominantly with neighboring *p*-orbitals of oxygen ion compared to those of $t_{2g}$ orbitals that points in between *x*, *y* and *z* axes. Consequently, the electrons in $e_g$ orbitals experience greater electrostatic repulsion and hence larger electrostatic energy. As a result $e_g$ levels are lifted up compared to those of $t_{2g}$ levels. But in the case of tetrahedral environment, the $e_g$ orbitals now maximally avoid the electronic charge density associated with the oxygen

atoms and hence the $e_g$ levels are now lowered in energy [46]. The energy level diagrams of octahedral and tetrahedral environments along with the respective figure of octahedral and tetrahedral coordinations are shown in Fig. 1.4.

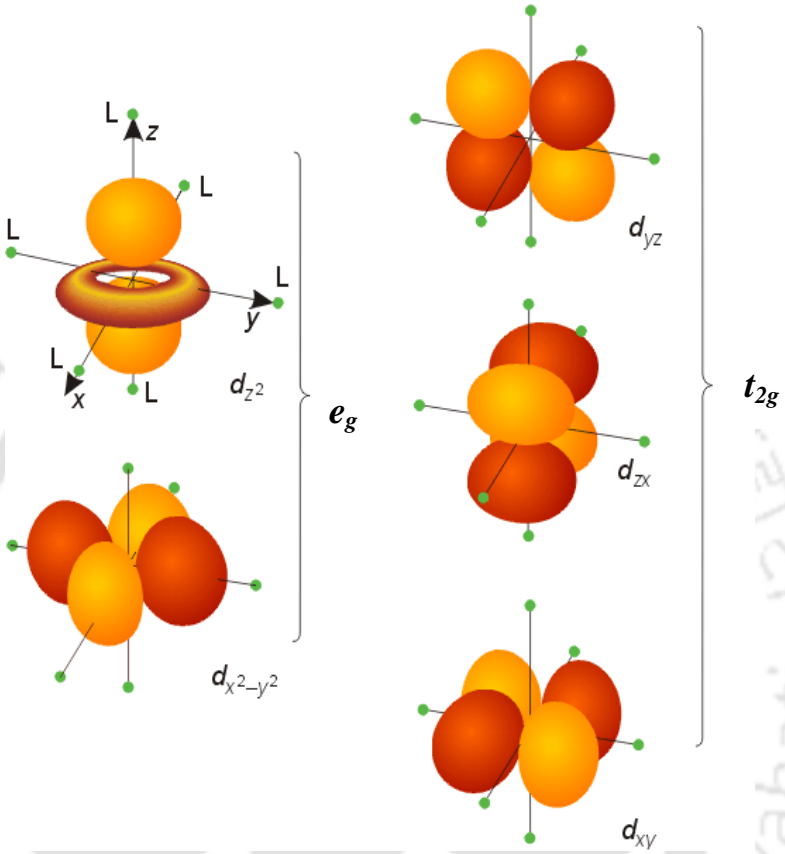


**Figure 1.3:** The electronic distribution of *3d* orbitals. In the cubic crystal field, this fivefold degeneracy is lifted and separated into two $e_g$ levels ($d_{x^2-y^2}$ and $d_{Z^2}$) and three $t_{2g}$ levels ($d_{xy}$, $d_{yz}$ and $d_{zx}$) (Reproduced from Tokura *et al.* [47]).

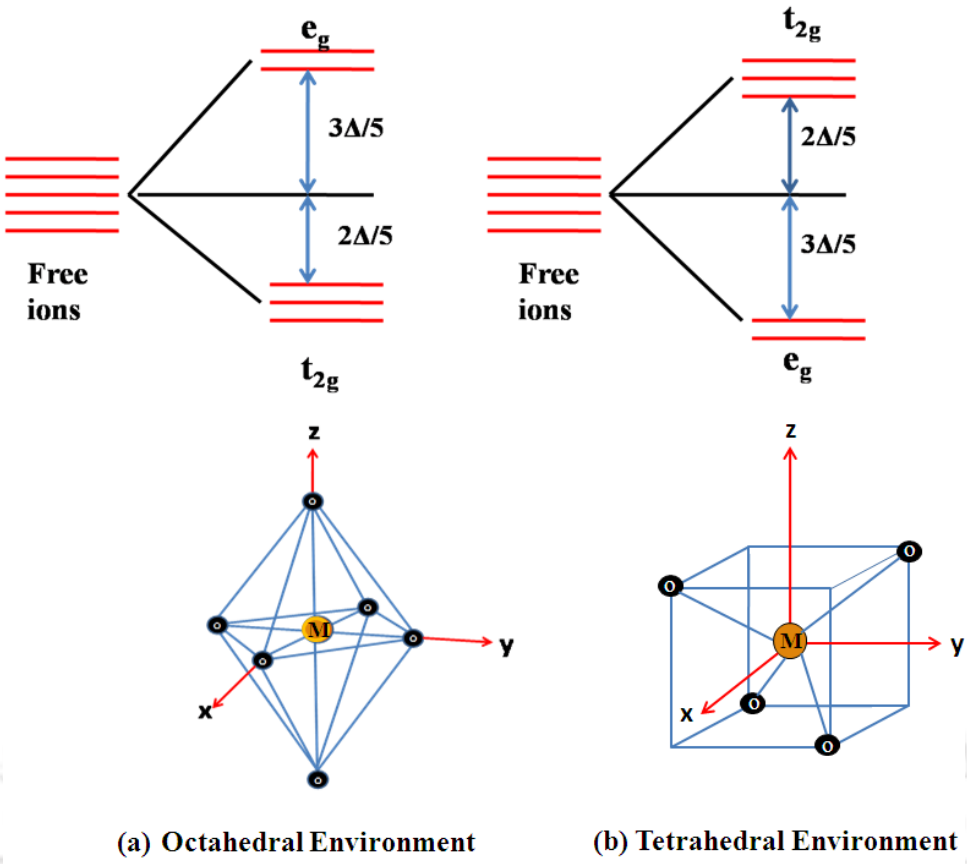


**Figure 1.4:** Energy level diagram in octahedral and tetrahedral environments.

## 1.3.1 Orbital Quenching

The crystal field effect is mainly observed in transition elements, where their *3d* valence electrons are close to the outermost shell and thus they are exposed to the electronic configuration of neighboring ions. In general, the effective magnetic moment ($\mu_{eff}$) of an ion can be calculated by using the relation $\mu_{eff} = g\sqrt{J(J+1)}$ in the unit of $\mu_B$ but it does not match with experimental values for most of the transition elements. This is due to the large crystal field effect, which dominates over the Hund's spin-orbit coupling energy in *3d* transition elements and hence the orbital angular momentum is quenched ($L = 0$). Hence, $\mu_{eff}$ is generally calculated using the relation $\mu_{eff}(\mu_B) = g\sqrt{S(S+1)}$. Here $J$ and $S$ refer quantum numbers corresponding to total and spin angular momentum of electrons, respectively. Another interesting series of elements having strong magnetic moments is rare earths, where the magnetism originates from *4f* shell. Unlike transition elements, here the *4f* levels are deep

inside from the outermost orbital, *i.e.* with negligible overlapping with the electronic configuration of neighboring ions and hence they do not show any crystal field effect. In this class of materials $\mu_{eff}$ can be calculated using the general relation, $\mu_{eff}(\mu_B) = g\sqrt{J(J+1)}$ [46].

## 1.3.2 Jahn-Teller Distortion

In some of the 3*d* transition elements for a specific valence state of an ion, electrons asymmetrically occupy the degenerate $t_{2g}$ or $e_g$ orbital leading to net larger electronic energy in the system. In order to reduce the overall energy, the system undergoes lattice distortion either by stretching or compressing their bonding such that degeneracy in the above orbitals is lifted. This distortion is known as the JTD [46]. The above process leads to overall reduction in the energy of the system.

In the octahedral environment, the most pronounced JTD is observed when an odd number of electrons occupy the $e_g$ orbitals, *i.e.* when the ion has an orbital degeneracy in the $e_g$ orbitals. However, ions with orbital degeneracy in the $t_{2g}$ orbitals show very weak JTD since these orbitals do not point directly towards the ligands (non bonding orbitals) and are lower in energy. High spin complexes with $d^4$, $d^9$ ($Mn^{3+}$, $Cu^{2+}$, *etc.*) electrons and low spin complexes with $d^7$ ($Co^{2+}$) electrons in octahedral environment undergo strong JTD. For example in case of $d^4$ configuration, three electrons occupy the $t_{2g}$ orbitals and the fourth electron has the orbital degereracy of $e_g$ ($d_{x^2-y^2}$ and $d_{Z^2}$) orbitals. In order to lift the orbital degeneracy, the JTD stretch the octahedra along z-direction and this process leads to smaller energy of $d_{Z^2}$ due to smaller overlapping with adjacent legands. So, the fourth electron occupies the $d_{Z^2}$ level and this process leads to overall reduction in energy. This process is shown in Fig. 1.5 [46]. Conversely in some system, the net energy is redudced by compressing the octahedra, where the $d_{x^2-y^2}$ orbital will be lowered and the fourth electron occupies this orbital rather than that of $d_{Z^2}$ level [48].

In tetrahedral environment, the $t_{2g}$ orbitals are closer to the distribution of electrons in the 2*p* orbitals of the ligands (oxygen) and directed to each other compared to the $e_g$ orbitals

and hence $t_{2g}$ orbitals are at higher energy level. So, here strong JTD occurs only for the configurations which are degenerate with respect to $t_{2g}$ orbital. High spin complexes with $d^3$, $d^4$, $d^8$, $d^9$ electrons and low spin complexes with $d^5$, $d^6$, $d^8$, $d^9$ electrons in tetrahedral environment undergo strong JTD. Spinel compounds having Jahn-Teller active ions, such as $Ni^{2+}$, $Cu^{2+}$ and $Fe^{2+}$ at the tetrahedral site cause a cubic to tetragonal distortion. For example, the spinel chromites $NiCr_2O_4$, $FeCr_2O_4$ and $CuCr_2O_4$ undergo a cubic to tetragonal distortion at 310 K, 140 K and 853 K, respectively as the temperature is decreased. In $NiCr_2O_4$ and $FeCr_2O_4$ the JTD is of elongation type while in $CuCr_2O_4$ it is compression type [11, 35, 48].

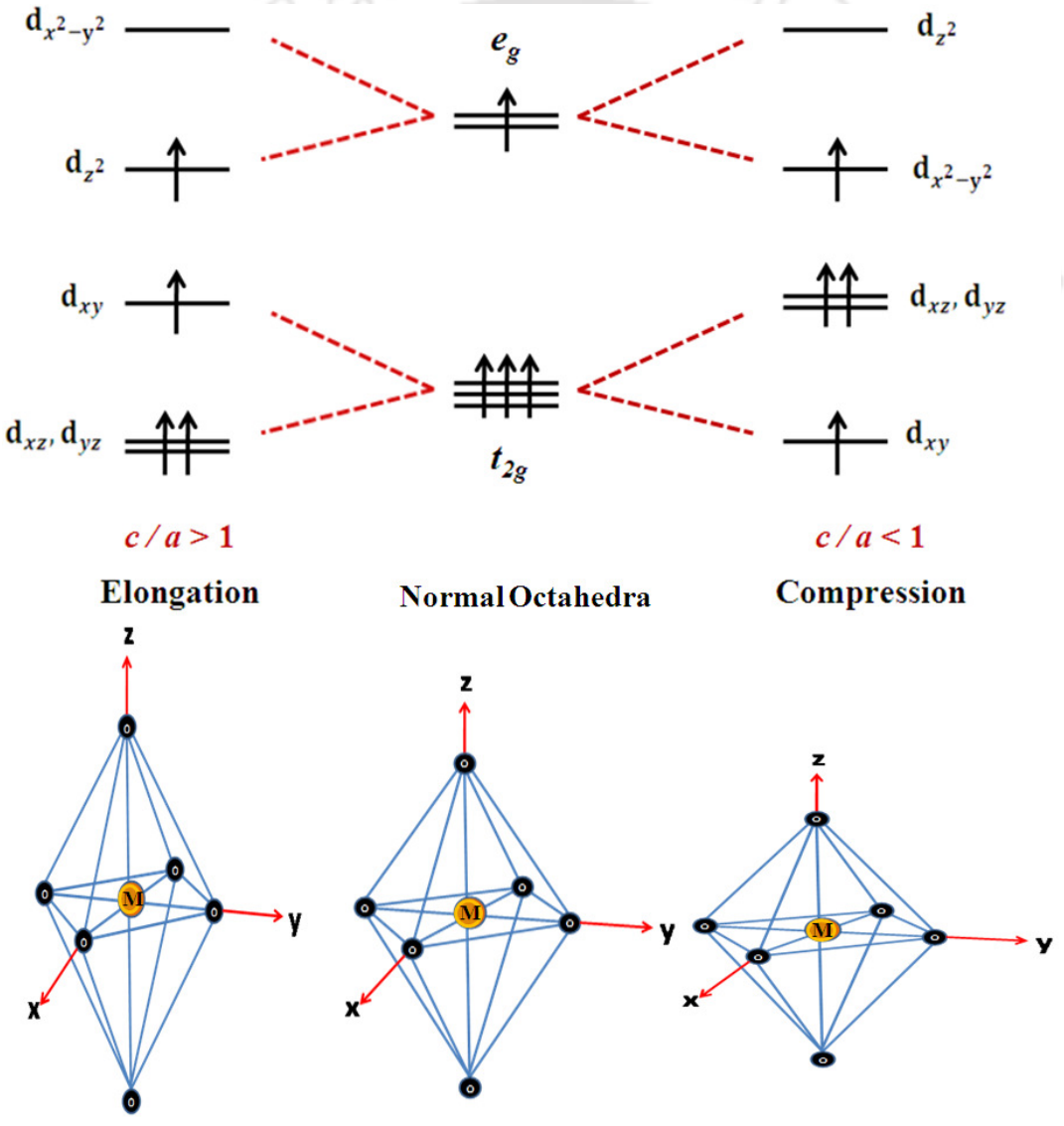


**Figure 1.5:** Further splitting of both the $t_{2g}$ and $e_g$ states in ions with $d^4$ configuration due to the JTD.

# 1.4 Magnetic Exchange Interactions

The spontaneous magnetization observed in ferromagnetic (FM) and ferrimagnetic (FIM) materials and the vanishing of net magnetization in antiferromagnetic (AFM) materials below their respective ordering temperature are explained based on various long range interactions among magnetic moments. Here the molecular field or the exchange field called Weiss molecular field is responsible for their magnetically ordered states. In 1928 Heisenberg explained this molecular field from quantum mechanical aspect and it was termed as exchange interaction [45]. The exchange interaction is driven by the coulomb interaction and the Pauli's exclusion principle. According to Heisenberg model, the energy of interaction between the atoms *i* and *j* having electron spins $S_i$ and $S_j$ is defined as

$$E_{exch} = -2\sum_{i>j} J_{ij} S_i . S_j \qquad (1.1)$$

where, $J_{ij}$ is the exchange integral related to the overlap of the charge distribution of the atoms *i* and *j*. For $J_{ij} > 0$, the parallel alignment (FM) of spin vectors is energetically favorable and lead to lower energy. On the other hand for $J_{ij} < 0$, the antiparallel alignment (AFM and FIM) of spins is energetically favorable [46]. Different types of magnetic interactions at microscopic scale are responsible for long range magnetic ordering. In this section some of the important magnetic exchange interactions are briefly described.

## 1.4.1 Direct Exchange Interaction

In direct exchange interaction, two neighboring magnetic atoms interact by the direct overlapping of their electronic wave functions. Thus it does not involve any intermediate ions and it generally operates between moments, which are close enough to have sufficient overlap of their wavefunctions. The Pauli's exclusion principle keeps the electrons with parallel spins away from each other to reduce the Coulomb repulsion. So, the direct exchange interaction mostly favors antiparallel spin configuration. In most of the materials due to insufficient direct overlapping of electronic wave functions of neighboring magnetic atoms, the direct exchange interaction is not an important mechanism in controlling their magnetic properties. Moreover, the wave functions of the magnetic '*d*' or '*f*' electrons decrease

exponentially in space. Therefore the overlapping of wave functions of magnetic ions is very small and hence it leads to very weak direct exchange interaction.

## 1.4.2 Superexchange Interaction

This is an indirect exchange interaction where the exchange interaction between two non-neighboring magnetic ions is mediated by means of a non-magnetic ion located between them. Superexchange interaction is a long range interaction. According to Kramers' model [49], interaction between cations having more than half filled *d*-shells gives rise to the AFM interaction, while such interaction among cations having less than half filled *d*-shells gives rise to FM interaction. On the other hand, Slater [50], Goodenough and Loeb [51, 52] proposed that the AFM interaction is also allowed among cations having less than half filled *d*-shell.

To understand the mechanism of superexchange interaction we have taken the example of interaction between two Mn - 3*d* orbitals. When core spins of magnetic cations are antiparallel to each other across an intermediate non-magnetic ion like oxygen, AFM interaction is facilitated due to the strong Hund's coupling. Following Hund's rule, each of the five 3*d* electrons of $Mn^{2+}$ occupy a different 3*d* orbital in order to align parallel to each other. If the left-most $Mn^{2+}$ ion has up-spin as shown in Fig. 1.6(a), the neighboring oxygen ion donates its down-spin 2*p* electron and form a partial covalent bond. This covalent bond is possible only when the oxygen ion donates its down spin electron; because all the $Mn^{2+}$ orbitals (left side) contain up-spin electrons already. Similarly the up spin electron left in the oxygen 2*p* orbital is donated to the next $Mn^{2+}$ ion in the chain. By the same argument, bonding can only occur if the electrons on the next $Mn^{2+}$ ion are down-spin. This oxygen-mediated interaction leads to an overall AFM alignment between the two $Mn^{2+}$ ions [53].

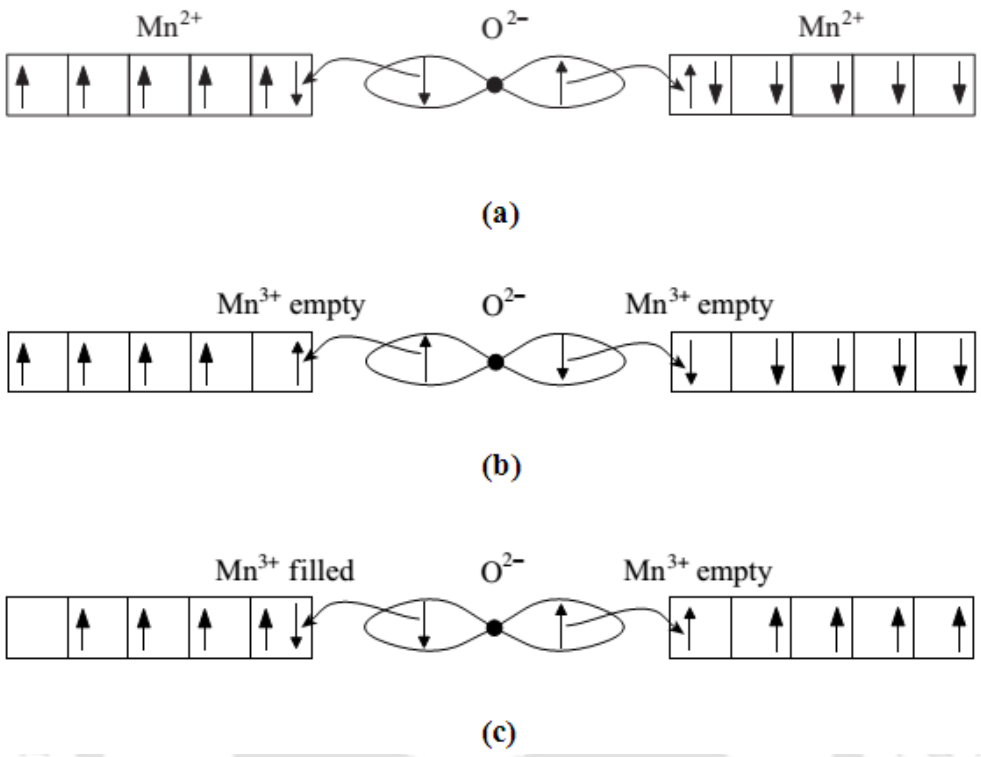


**Figure 1.6:** Schematic diagram of (a), (b) AFM and (c) FM superexchange interactions [53].

If the 3*d* orbital of Mn is less than half filled, the oxygen-mediated coupling between neighboring Mn ions can be either FM or AFM, depending upon whether the empty or the filled sub level of Mn - 3*d* orbitals points towards the electrons in oxygen 2*p* orbital. If $Mn^{3+}$ ions in both side of oxygen point their respective empty *d* orbital towards oxygen 2*p* orbital, then this leads to AFM interaction as shown in Fig. 1.6(b). On the other hand, if one of the $Mn^{3+}$ ions points the partially filled (*i.e.* with an electron) 3*d* - sub level towards oxygen 2*p* orbital while the other $Mn^{3+}$ ion pointing its empty 3*d* - sub level towards oxygen 2*p* orbital, then this arrangement will lead to FM coupling as shown in Fig. 1.6(c). Here in both cases, the coupling are permitted such that Hund's rule and Pauli's exclusion principle are not violated [53].

Superexchange can also be described by a Heisenberg Hamiltonian, in which the sign of $J_{ij}$ is determined by the metal – oxygen – metal bond angle and the *d* electron configuration on the transition metal. According to semi-empirical Goodenough – Kanamori – Anderson rules 180º metal – oxygen – metal angles between identical metal ions with both

orbitals either filled or empty lead to AFM interactions whereas 90º angle results in FM [53].

In spinel compounds, the cations in tetrahedral (A) and octahedral (B) sites are bonded via $O^{2-}$ ions. In spinels with magnetic ions in both A and B sites, superexchange interaction through A – $O^{2-}$ – B networks is the strongest one and gives rise to the FIM ordering. Interactions through other networks such as B – $O^{2-}$ – B and A – $O^{2-}$ – A are also possible. In ferrites, A – $O^{2-}$ – B angle is around 120° and it gives rise to AFM superexchange interaction. On the other hand, B – $O^{2-}$ – B angles are close to 90° and hence they interact ferromagnetically. In some spinel chromites AFM interaction also occurs through B – $O^{2-}$ – B networks due to spin canting. For example in $NiCr_2O_4$, AFM interaction exists within the B sites due to canting of the B site moments; but this interaction is weaker compared to that of between A and B site ions [54].

## 1.4.3 Double Exchange Interaction

Double exchange interaction occurs in mixed valent materials, *i.e.* in materials where the magnetic ions can exist in more than one oxidation states. It is also an indirect exchange interaction but with a transfer of electron from one magnetic ion to another magnetic ion through a non-magnetic intermediate ion and is popularly known as Zener double exchange interaction [55, 56]. Typical example of double exchange interactions between $Mn^{3+}$ and $Mn^{4+}$ ions through $O^{2-}$ ion is shown in Fig. 1.7(a). Here, $O^{2-}$ gives up its spin-up electron to $Mn^{+4}$ and this is followed by the transfer of a spin up electron from $Mn^{3+}$ to $O^{2-}$. At the end of the process $Mn^{4+}$ reduces to $Mn^{3+}$ and $Mn^{3+}$ oxidized to $Mn^{4+}$. Due to the two step process of exchange of electrons, it is called double exchange interaction. Zener model predicts that the carrier electrons can jump between two Mn ions only if their core electron spins are parallel to each other. If the Mn spins are not parallel, the electron transfer becomes difficult due to strong onsite Hund's coupling as shown in Fig. 1.7(b). The electron transfer is also more difficult if the Mn – O – Mn bond is considerably bent away from 180°. Such deviation of bond angles affects the overlapping of Mn - *d* and oxygen - 2*p* orbitals. Thus double exchange interaction always gives rise to ferromagnetism. The movement of electron can be shown as, $Mn^{3+}_{1\uparrow} O_{2\uparrow,3\downarrow} Mn^{4+} \rightarrow Mn^{4+} O_{1\uparrow,3\downarrow} Mn^{3+}_{2\uparrow}$, where the electron spins are labeled as

1, 2 and 3. Anderson and Hasegawa [57] presented the double exchange mechanism in detail by visualizing a second order process in which the electron transfer takes as follows $Mn^{3+}_{1\uparrow} O_{2\uparrow,3\downarrow} Mn^{4+} \rightarrow Mn^{3+}_{1\uparrow} O_{3\downarrow} Mn^{3+}_{2\uparrow} \rightarrow Mn^{4+} O_{1\uparrow,3\downarrow} Mn^{3+}_{2\uparrow}$.

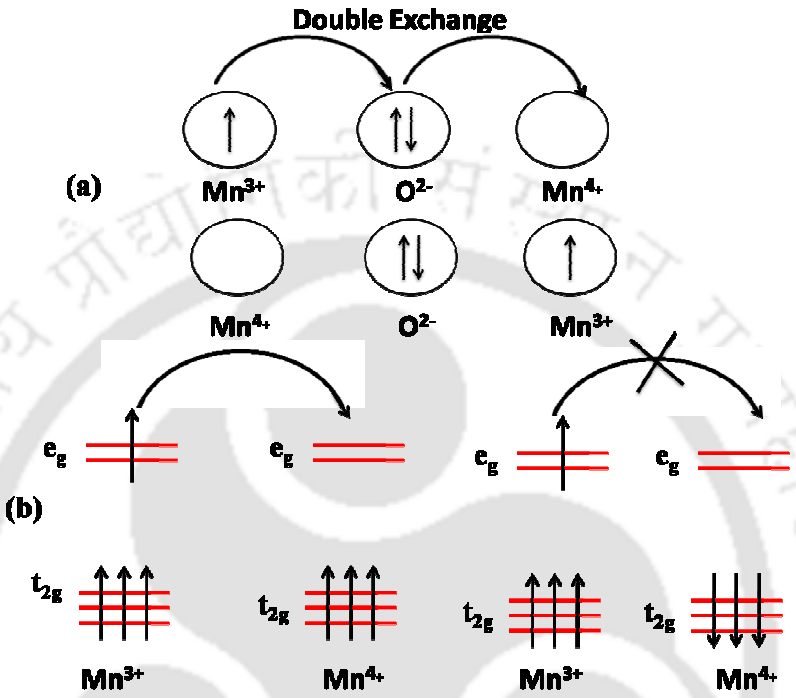


**Figure 1.7:** (a) Sketch of double exchange interaction which involves two Mn ions and one O ion. (b) The mobility of $e_g$ electrons improves if the localized spins are polarized and parallel to each other.

## 1.4.4 RKKY Interaction

The RKKY interaction occurs in metals with localized magnetic moments and the exchange interaction between the magnetic ions is mediated via conduction electrons. A localized magnetic moment of an ion, spin polarizes the conduction electrons and this polarization couples to the neighboring localized magnetic moment at a distance $r$ away. Since direct coupling between the magnetic moments do not takes place, this interaction is an indirect one. The coupling takes the form of an $r$-dependent exchange interaction $J_{RKKY}(r)$ given by [46]

$$J_{RKKY}(r)\alpha\frac{\cos(2k_F r)}{r^3} \tag{1.2}$$

where, $k_F$ is the radius of the spherical Fermi surface. This interaction has oscillatory dependence of the distance between the magnetic ions and it is in long range. Such interaction gives rise to either FM or AFM coupling depending on the distance between the magnetic ions.

## 1.4.5 Anisotropic Exchange Interaction

Anisotropic exchange interaction was proposed by Dzyaloshinsky-Moriya and hence it is also known as Dzyaloshinsky–Moriya (DM) interaction [58, 59]. This exchange mechanism leads to the tilting of the magnetic moments of antiparallel spins towards each other and hence gives rise to a net magnetic moment. However, such a canted spin arrangement is possible only if the magnetic crystal symmetry remains same as that of the original one having antiparallel spins. The exchange energy between the magnetic moments at this canted configuration can be written as follow,

$$H_{DM} = \vec{D}.\left(\vec{S}_1 \times \vec{S}_2\right) \tag{1.3}$$

Where $\vec{S}_1$ and $\vec{S}_2$ are the spins of two interacting magnetic ions and $\vec{D}$ is DM vector. Vector $\vec{D}$ vanishes when the crystal field has inversion symmetry with respect to the middle point connecting the two magnetic ions. Usually $\vec{D}$ lies either parallel or perpendicular to the line connecting the two spins, depending on the symmetry. The DM interaction tries to align $\vec{S}_1$ and $\vec{S}_2$ at right angle to each other in a plane perpendicular to $\vec{D}$. Its effect is therefore very often to cant (*i.e.* slightly rotate) the spins by a small angle. It commonly occurs in antiferromagnets and then results in a small FM component of the moments which is produced perpendicular to the spin-axis of the antiferromagnet. The effect is known as weak ferromagnetism. Some of the AFM crystals like α-$Fe_2O_3$, $Cr_2O_3$, $MnCO_3$, $CoCO_3$, *etc.* exhibit such weak FM behavior [46, 60].

# 1.5 Magnetic Orderings

The diamagnetic and paramagnetic (PM) materials can be described successfully by considering them as isolated magnetic moments. But as discussed above, the strong exchange interaction among magnetic moments of different ions/atoms in FM, AFM and FIM materials leads to collective magnetism and hence a magnetic ordering below a characteristic temperature known as the transition temperature. In the above section various magnetic interactions are discussed. So in this section different magnetic orderings caused by these magnetic interactions are presented.

## 1.5.1 Diamagnetic Materials

Diamagnetic materials hold no unpaired electrons and hence no permanent net magnetic moment per atom. Here, under the application of an external magnetic field, a magnetic moment is induced opposite to the direction of the applied field. Such behavior can be understood by considering the Lenz's law in electrodynamics. When a magnetic field is applied to a material having closed shell electronic configuration, the direction of orbital motion of electrons rearrange such a way that a magnetic moment is induced, which opposes the original applied magnetic field. The diamagnetic moment will persist as long as magnetic field is applied. Diamagnetism is an inherent property of all materials but it is often obscured by other types of magnetism [60].

The susceptibility of diamagnetic material was first explained by Langevin [61]. The Langevin's equation for a diamagnetic material having $N$ number of atoms per unit volume and $Z$ number of completely filled electrons per atom can be written as,

$$\chi = -\frac{\mu_0 NZe^2}{6m}\overline{r}^2 \tag{1.4}$$

where, $\mu_0$ is the permeability of free space, $e$ is the charge of electron, $m$ is the mass of the electron and $\overline{r}^2$ is the mean square radius of the electron orbit. The diamagnetic susceptibility is generally quite small and is of the order of $10^{-5}$ or $10^{-6}$ (cgs unit) and, is mostly independent of temperature. The only type of material known to exhibit strong diamagnetism

is superconductor. The other examples of diamagnetic substances are He, Ne, Ar, *etc.* having closed shell electronic configuration, polyatomic gases $H_2$, $N_2$, *etc*. with closed shell electrons due to the nature of molecule formation and ionic solids like, NaCl with closed shell electrons due to electron transfer during ionic bonding. Formation of covalent bonding leads to closed shell configuration in C, Si and Ge [45].

## 1.5.2 Paramagnetic Materials

In some of the materials, each atom or ion exhibit a magnetic moment due to their unpaired electronic configuration and the associated net spin and orbital momentum. However, in the absence of magnetic field, the magnetic moments orient in random directions such that they cancel each other; so the net magnetic moment is zero. As the magnetic field is applied, the magnetic moments tend to orient in the applied field direction. But thermal energy resists their complete orientation along the field direction. This results in a partial alignment of the moments along field direction and hence a small positive susceptibility. With increase in applied field or decrease in temperature, the degree of alignment increases and the net magnetic moment also increases. So, magnetization of PM material is directly proportional to *H/T* [46].

The PM susceptibility as per the classical approach (Langevin's equation) is given as,

$$\chi = \frac{\mu_0 N \mu^2}{3k_B T} \tag{1.5}$$

where, *N* is the number of magnetic dipoles (magnetic ions) per unit volume each having a magnetic moment of $\mu$. The Eq. (1.5) demonstrates that the magnetic susceptibility is inversely proportional to the temperature and is known as Curie Law [61].

The PM susceptibility at low magnetic field, by considering the quantum mechanical approach is given as,

$$\chi = \frac{N \mu_0 g^2 \mu_B^2 J\left(J+1\right)}{3k_B T} \tag{1.6}$$

where, $g$ is Landé $g$ factor which is written as

$$g = \frac{3}{2} + \frac{S(S+1) - L(L+1)}{2J(J+1)}$$

Salts of transition elements, salts and oxides of rare earths and the rare earth elements are strongly PM. Other examples of PM materials are platinum, aluminum, oxygen. In the salts of transition metals such as chlorides, sulphates and carbonates of manganese, chromium, iron and copper, the PM moments reside on $Cr^{3+}$, $Mn^{2+}$, $Fe^{2+}$ and $Cu^{2+}$ ions, respectively. [45].

## 1.5.3 Ferromagnetic Materials

In FM materials, the unpaired electron spins line up parallel to each other in a region called magnetic domain due to the presence of strong exchange forces (molecular field) between them. Hence FM materials exhibit spontaneous magnetization within a domain even in the absence of external magnetic field. But due to random orientation of different domains the net magnetization is zero. When a magnetic field is applied all domains align along the field direction and a large positive susceptibility is observed. This alignment tends to persists even after the removal of the magnetic field which gives rise to magnetic hysteresis [45].

According to the molecular field theory, the magnetic moments align parallel to each other due to the presence of molecular field $H_m = \lambda M$. Here, λ is a positive constant and $M$ is the magnetization of the material. Such FM behavior is observed below the transition temperature $T_C$. For $T > T_C$, mostly they behave like a paramagnet and follow the Curie-Weiss law,

$$\chi = \frac{C}{T - \theta_C} \tag{1.7}$$

where, $C$ and $\theta_C$ are Curie constant and Curie temperature, respectively. Here $C = \mu_o N g^2 \mu_B^2 J(J+1)/3k_B$ or $C = \mu_o N \mu^2 / 3k_B$. Fe, Ni and Co are common FM materials with typical $\theta_C$ values of 1043 K, 1394 K and 631 K, respectively [45].

## 1.5.4 Antiferromagnetic Materials

In an AFM substance, the magnetic moments of atoms/ions at particular crystallographic sites align antiparallel to each other such that the net magnetic moment becomes zero. Such behaviors are observed below certain temperature known as Néel temperature ($T_N$) and above that it behaves like a paramagnet. Under an applied magnetic field they give rise to a small positive susceptibility. The magnetic susceptibility in the PM region of such substance is written as,

$$\chi = \frac{C}{T + T_N} \tag{1.8}$$

Examples of AFM materials include $MnF_2$, MnO, CoO, FeO, $Cr_2O_3$, α-$Fe_2O_3$, *etc*. with respective Néel temperature of 67 K, 116 K, 292 K, 116 K, 307 K and 950 K [45].

## 1.5.5 Ferrimagnetic Materials

Ferrimagnetism is a special type of antiferromagnetism where the magnetic moments of atoms at particular crystallographic sites align antiparallel to each other but due to their different magnitudes the net magnetization is not zero. Unlike in AFM materials, different sublattice sites in FIM materials are crystallographically different. Therefore the molecular field in a FIM material differs at different sublattices. The temperature dependence of sublattice magnetizations also thus differs. In a FIM material with two sublattices A and B, the net magnetic moment is the difference between the two sublattice moments, *i.e.* $M = M_A - M_B$ [44, 45].

Most of the FIM materials are electrical insulators and they are useful for many of the practical applications. Cubic spinel ferrites with the general formula $AB_2O_4$ were the first class of materials of this type. Some other examples of FIM materials are hexagonal ferrites like $BaFe_{12}O_{19}$ and garnets such as $Y_3Fe_5O_{12}$ [45].

Since the different sublattices of FIM materials are crystallographically different, their molecular field is inherently more complicated compared to that of AFM material. This means that in a FIM material with two sublattices A and B, the A – A interaction will differ

from the B – B interaction, even though the ions involved are identical. According to Néel's theory, the local molecular fields at A and B sites are given by [45],

$$H_A = \gamma\left(\alpha M_A - M_B\right) \tag{1.9}$$

$$H_B = -\gamma\left(M_A - \beta M_B\right) \tag{1.10}$$

where, $M_A$ and $M_B$ are the magnetization of the A and B sub-lattice respectively, and γ is absolute value of the molecular field coefficient corresponding to the A – B magnetic exchange interaction. The $\alpha$ and $\beta$ are the molecular field coefficients for the intra sublattices A – A and B – B interactions normalized by the $\gamma$. The A and B sublattice magnetizations depend on the Brillouin function $B_S(x)$ with respect to temperature ($T$) and external magnetic field ($H$), and are given by

$$M_A = \lambda N g \mu_B S_A B_{S_A}\left(\frac{g\mu_B S_A\left(H + H_A\right)}{k_B T}\right) \tag{1.11}$$

$$M_B = \delta N g \mu_B S_B B_{S_B}\left(\frac{g\mu_B S_B\left(H + H_B\right)}{k_B T}\right) \tag{1.12}$$

where $N$ is total number of magnetic ions per unit volume and $S_A$ and $S_B$ are the spin angular momenta for the A and B sites, respectively. The $\lambda$ and $\delta$ are the molar fractions of the magnetic ions at the A and B sites such that $\lambda + \delta = 1$ [62].

The sublattice magnetizations given by Eq. (1.11) and Eq. (1.12) depend on the values of the parameters $\alpha$, $\beta$, $\lambda$, $\delta$, $S_A$, and $S_B$. The shape of the curve for A sublattice will thus usually differ from that of the B sublattice. Since the resultant magnetization curve is the difference between these two, therefore small changes in the shapes of the sublattice curves can yield quite unusual resultant magnetization curves. Due to such behaviors, FIM materials become a very interesting magnetic material where often the resultant magnetization vanishes below the transition temperature and then becomes negative. The temperature at which the resultant becomes zero is called the compensation temperature at which the opposing sublattice magnetizations are exactly balanced (Fig. 1.8). For temperatures above

and below the compensation temperature one of the sublattices magnetization dominates over the other [45, 62, 63].

All the spinel chromites, $ACr_2O_4$, with A sites occupied by magnetic ions falls into this category of magnetic materials.

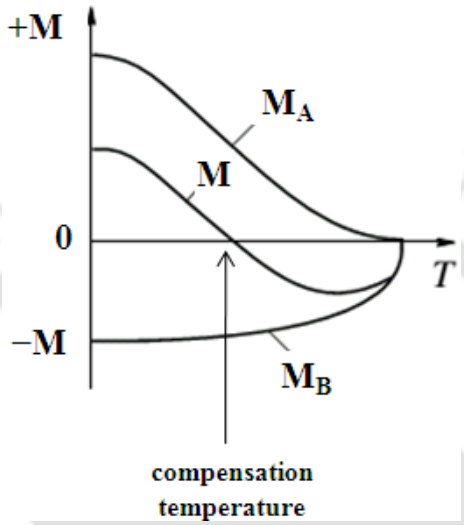


**Figure 1.8:** Schematic curves of spontaneous magnetizations of the A and B sublattices, and the resultant saturation magnetizations for ferrimagnet showing compensation behavior [63].

## 1.6 Magnetic Anisotropy

Magnetic anisotropy refers to the variation of magnetic properties depending on the direction of application of probing external field. The magnitude and type of magnetic anisotropy affect the shape of the magnetization curves including coercivity, remanent magnetization, saturation magnetization, *etc*. The anisotropy can be intrinsic to the material, as a result of its crystal chemistry or its shape, or it can be induced by careful choice of processing method. Different types of anisotropies are as follows:

I. Crystal anisotropy or magnetocrystalline anisotropy
II. Shape anisotropy
III. Stress anisotropy
IV. Exchange anisotropy

## 1.6.1 Magnetocrystalline Anisotropy

The phenomenon that causes the magnetization to align itself along a preferred crystallographic direction is called the magnetocrystalline anisotropy. The preferred direction is called the easy axis and it is easy to magnetize the sample to its full saturation value if the field is applied in this direction. The other crystallographic directions are then termed as hard axis. Spontaneous domain magnetization remains aligned along the easy direction in the absence of external field. Therefore crystal anisotropy is considered as a force which tends to hold the magnetization in certain equivalent crystallographic direction in a crystal. The energy associated in the crystal having magnetization orientation away from the easy axis is given as,

$$E_a = K_0 + K_1\left(\alpha_1^2\alpha_2^2 + \alpha_2^2\alpha_3^2 + \alpha_3^2\alpha_1^2\right) + K_2\left(\alpha_1^2\alpha_2^2\alpha_3^2\right) + \ldots\ldots\ldots \quad (1.13)$$

Here $K_0$, $K_1$ and $K_2$ are constants for a particular crystal at a particular temperature and, $\alpha_1$, $\alpha_2$ and $\alpha_3$ are the direction cosines of the magnetization with respect to crystallographic axes *a*, *b* and *c*. If $K_2$ is zero, the direction of easy magnetization can be determined from the sign of $K_1$. If $K_1$ is positive, then $E_{100}<E_{110}<E_{111}$ with <100> as the easy axis as observed in iron, cubic ferrite containing cobalt, *etc*. If $K_1$ is negative, $E_{111}<E_{110}<E_{100}$, here the easy axis is <111> and the examples are nickel, cubic ferrite, *etc*. If $K_2$ is not zero, then the direction of easy magnetization axis is determined by both $K_1$ and $K_2$ [45].

The anisotropy associated with a single crystallographic axis (which is the easy axis) is called uniaxal anisotropy and the anisotropy energy then will only the function of angle $\theta$ between the magnetization and the easy axis which can be written as,

$$E_a = K_0 + K_1 \sin^2\theta + K_2 \sin^4\theta + \ldots\ldots\ldots \quad (1.14)$$

If $K_1$ and $K_2$ are positive, then $E_a$ will be minimum when $\theta = 0$, *i.e.* for the magnetization lying along the easy axis and the examples are cobalt, barium ferrite and many rare earth transitional metal intermetallic compounds. If $K_1$ and $K_2$ are negative, then $E_a$ will be minimum when $\theta = 90^\circ$ so here magnetization lie in an easy plane which is perpendicular to the easy axis. The anisotropic energy is generally larger for low symmetric crystals. The

magnitude of crystal anisotropy sharply decreases with increase in temperature and it vanishes at Curie temperature. Anisotropy gives rise to the enhanced coercive field [45].

The origin of magnetocrystalline anisotropy is the spin-orbit coupling of electrons in magnetic materials. Electrons in a crystal are subjected to four different type of coupling namely spin-spin coupling, orbit-lattice, spin-orbit and spin-lattice coupling. The spin-spin coupling is very strong which forces the neighboring spins to be either parallel or antiparallel with each other. The energy associated with this coupling is isotropic and it depends on the angle between the spins rather than the crystallographic orientation. So, it does not contribute any crystal anisotropic energy. In most of the FM materials, orbital moments are quenched, so the orientations of the orbits are fixed with the crystal lattice, so the orbit-lattice interaction is very strong and even large applied magnetic field can't change them. The spin-orbit coupling is relatively weak, so when an external magnetic field is applied the spin and orbital moments of an electron try to align along the field direction but since the orbit is strongly coupled to the lattice, it resists the spin axis to rotate. The energy required to rotate the spin from its easy axis is called anisotropic energy [45, 53].

## 1.6.2 Shape Anisotropy

Even though most materials show some magnetocrystalline anisotropy, a polycrystalline material having no preferred orientation of its grains will have no overall crystalline anisotropy. If the sample is spherical in shape then the magnetization produced by the applied field will be uniform in all the directions. However, if the sample is not spherical then it will be easier to magnetize it along the longer axis due to the small demagnetization factor compared to the shorter axis. This shape dependent phenomenon is known as the shape anisotropy. The demagnetization field $H_d$ is created whenever magnetic poles are produced in the material. $H_d$ depends directly on the magnetization of the material and a shape and dimension dependent parameter known as demagnetization factor $N_d$. It is written as

$$\vec{H}_d = -N_d \vec{M} \tag{1.15}$$

The sum of the demagnetization factors along three orthogonal axes of an ellipsoid is a constant:

$$N_a + N_b + N_c = 1 \text{ (SI) } or \text{ } 4\pi \text{ (cgs)} \tag{1.16}$$

For spherical sample, all the three demagnetization factors are equal so, $N_{sphere} = 4\pi/3$ (cgs) or 1/3 (SI). The energy related with the demagnetization field of a specimen is called as magnetostatic energy ($E_{ms}$) and it can be written in the unit of J/m$^3$ as

$$E_{ms} = \frac{1}{2}\mu_0 N_d M^2 \tag{1.17}$$

## 1.6.3 Stress Anisotropy

Stress can change the domain structure of a material thereby creating one or more easy axis of magnetization. Therefore, when stress is present, stress anisotropy must be taken into account along with any other anisotropies. It is a uniaxial anisotropy and the stress anisotropy energy or magnetoelastic energy can be written as

$$E_\sigma = K_\sigma \sin^2\theta \tag{1.18}$$

where $K_\sigma$ is the stress anisotropy constant and $\theta$ is the angle between magnetization and the axis of stress. The axis of the stress behaves like easy axis if $K_\sigma$ is positive or hard axis if $K_\sigma$ is negative [45].

## 1.6.4 Exchange Anisotropy

Exchange anisotropy is generally created at the interface between a FM and an AFM layer. When a material having both FM and AFM layer is cooled through the Néel temperature ($T_N$) of the antiferromagnet in the presence of static magnetic field then anisotropy is developed at the interface between them and such anisotropy is called exchange anisotropy. Due to the exchange anisotropy, the center of hysteresis loops (*M–H* loops) shifts from the origin towards either negative or positive field axis. The above shifting of *M–H* loop is known as exchange bias (EB) phenomenon and is discussed in detail in section 1.8. The EB was first discovered by Meklejohn and Bean in 1956 in Co particle coated with CoO layer [64]. The pinning of the FM spins by the hard AFM spins at interface gives rise to unidirectional exchange anisotropy and its energy can be written as,

$$E = -K_u \cos\theta \tag{1.19}$$

where, $K_u$ is the unidirectional anisotropy constant and $\theta$ is the angle between the magnetization and the direction of cooling field.

# 1.7 Magnetization Reversal

Magnetization reversal (MR) is a phenomenon of change in sign of magnetization from positive to negative or vice versa without changing the direction of applied magnetic field but by just varying its magnitude or by varying the temperature. In the temperature dependent dc magnetization study, the temperature at which the magnetization becomes zero and reverses its sign thereafter is called the compensation temperature ($T_{comp}$). MR was first predicted by Néel in FIM material in 1948 [65]. Later, it was extended to other systems of canted AFM [66] and also in FM compounds [67]. It has many potential applications in spintronics devices such as spin valves, magnetic tunnel junctions, thermomagnetic switches, thermally assisted magnetoresistive random access memory (TAMRAM) devices, *etc.* [62, 68]

The MR is highly influenced by the crystal structure of a material, magnetic anisotropy, *etc*. Presence of a finite magnetic anisotropy is found to be necessary for the observation of MR. Otherwise only a magnetic compensation behavior will be observed without reversal of magnetization, *i.e.* without a negative magnetization; as observed in some rare earth garnets [69-71]. In the absence of magnetic anisotropy, the magnetization of the dominant component/sublattice (antiparallel to the applied field) below $T_{comp}$ rotates in the direction of the applied field and thus circumventing the MR. MR has been observed in several types of compounds but mechanism behind MR varies depending on the material. They are classified as follows.

## 1.7.1 Magnetization Reversal in Ferrimagnetic Materials

The MR in FIM materials such as in spinel ferrites was predicted by Néel way back in 1948 [65]. The different temperature dependence of antiferromagnetically coupled

sublattice magnetization gives rise to MR where one sublattice magnetization may dominate over the other and vice versa at above and below the $T_{comp}$.

Typical magnetization versus temperature ($M-T$) plot of cobalt vanadate ($Co_2VO_4$) exhibiting MR is shown in Fig. 1.9. Here Co ions are distributed at both tetrahedral (A) and octahedral (B) sites and thus forming an inverse spinel (*fcc*) structure. Menyuk *et al*. [16] have successfully explained the occurrence of negative magnetization in this compound below $T_{comp}$= 70 K by considering the different temperature dependences of magnetic moments of $Co^{2+}$ (A site) and $Co^{2+}/V^{4+}$ (B site) ions as per the Néel's hypothesis. Considering the similar argument with two/three magnetic sublattices, the MR behavior observed in many other spinel compounds such as $Li_{0.5}Cr_xFe_{2.5-x}O_4$ ($x$ = 0 – 2) [72, 73], $Fe_2MoO_4$ [74], $FeCr_{2-x}Al_xO_4$ [75], $NiFe_{2-x}Fe_xO_4$ [76], $Co_2TiO_4$ [77], *etc*. was successfully explained. Recently, the MR has been studied extensively in spinel $CoCr_2O_4$ based compounds such as $CoCr_{2-x}Fe_xO_4$ [28], $Co_{0.8}Cu_{0.2}Cr_2O_4$ [29], $Co(Cr_{1-x}Fe_x)_2O_4$ ($x$ = 0 – 0.125) [78], $Co(Cr, Mn)_2O_4$ [27], *etc*. Other than spinel compounds, some rare earth garnets, Prussian blue analogues (PBA), *etc*. also show MR behavior which can be explained with the help of mean field theory [62].

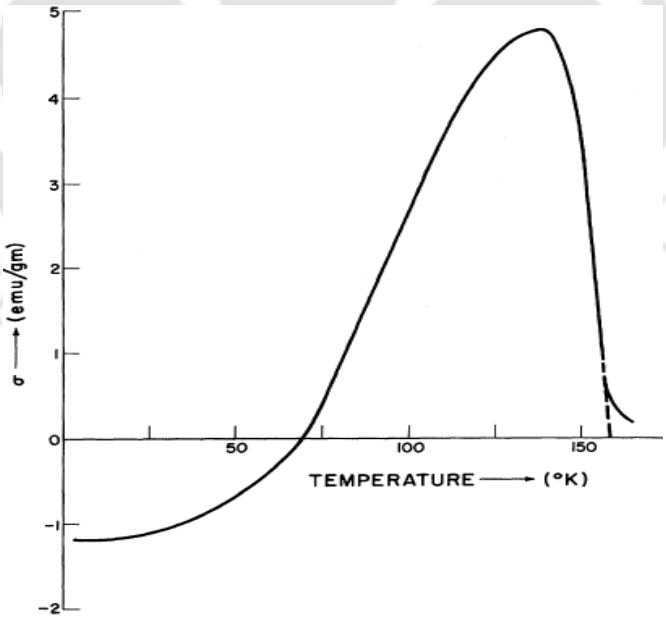


**Figure 1.9:** Temperature dependence of magnetization of $Co_2VO_4$ in an external field of 700 Oe [16].

## 1.7.2 Magnetization Reversal in Spin Canted Antiferromagnets and Weak Ferromagnets

Several spin canted antiferromagnets having weak ferromagnetism such as in orthovanadates, orthochromites, manganites, *etc.* exhibit MR. Here also, the mechanism differs depending on the nature of material. The MR observed at 138 K in $LaVO_3$ is explained in terms of structural transition from orthorhombic to monoclinic phase as the temperature is decreased [79]. This structural transition induces two different in-equivalent positions of V site having different level of quenching of orbital magnetic moments. Such inequality in magnetic moment having different temperature dependence gives rise to MR. The MR in AFM $YVO_3$ is explained in terms of competition between single ion anisotropy and DM interaction [80]. Similar behavior is observed in $NdVO_3$ [81].

In some orthochromite ($RCrO_3$) and Manganite ($RMnO_3$) systems**,** the MR is observed due to the competition between the spin canted AFM leading to weak FM component and the PM moment residing at different crystallographic sites. In such case, the PM atom at a crystallographic site experiences an effective negative internal molecular field due to the spin canted AFM ordering of other magnetic sublattice. For example in single crystal samples of $La_{1-x}Gd_xMnO_3$ ($x$ = 0.25, 0.5, and 0.75) [82], $Nd_{0.96}Ce_{0.04}MnO_3$ [83], $SmMnO_3$ [84], *etc.*, the FM moment arises due to the canting of the AFM ordered Mn moments. The substituted magnetic ions Gd, Ce and Sm behave like PM entity. The MR in these compounds results from the competition between the PM entities under the influence of negative internal magnetic field due to AFM ordered $Mn^{3+}$ ions and the weak FM component of $Mn^{3+}$ ions. An internal field of the order of 8 kOe was obtained. The orthochromite nanoparticles such as $La_{0.2}Ce_{0.8}CrO_3$ possess a core–shell type structure and show MR due to the competition between an AFM core of the $Cr^{3+}$ and $Ce^{3+}$ spins and a disordered surface shell with the uncompensated spins [85]. Later MR has been observed in polycrystalline samples of $La(Cr_{1-x}M_x)O_3$ samples with M = Mn, Fe, *etc.* [86, 87]. Similar MR has been reported in $NdCr_{1-x}Mn_xO_3$ (M = Mn, Fe) [88, 89].

### 1.7.3 Intermetallic alloys and Ferromagnetic/Antiferromagnetic Interfaces

The antiparallel arrangement between spin and orbital moments of an atom or ion residing at a given crystallographic site and their competition as a function of temperature can give rise to MR in a system. Some compounds having $AB_2$ type structure shows MR due to this reason. The MR observed in single crystal as well as polycrystalline FM alloys such as in $(Sm_{1-x}Gd_x)Al_2$ ($x$ = 0.01 – 0.026) [67, 90], $Nd_{0.75}Ho_{0.25}Al_2$ [91], *etc.* was explained by different temperature dependences of the spin and orbital moments of A site ions and the significance of moments due to the polarized conduction electrons. MR in polycrystalline samples of $Sm_2Al$, $Sm_{1.988}Gd_{0.012}Al$ [92], $SmNiAlH_{1.17}$ [93], *etc*. can be explained by the similar mechanism.

In some systems having different layers of FM, FIM, AFM, Weak FM, *et*c., MR is observed due to the different temperature dependence of the magnetization of the exchange coupled interfaces. Some examples of this category are Ni-$FeF_2$, Gd-Fe, Gd-Co, Gd-CoNi, $Fe_3O_4/Mn_3O_4$, *etc*. [62].

## 1.8 Exchange Bias

EB is a phenomenon associated with the exchange anisotropy at the interface between a FM and an AFM phase and this effect is seen as a shift in the magnetic hysteresis loop along the field axis. EB effect was discovered by Meiklejon and Bean in the year of 1956. They observed the shifting of magnetic hysteresis loop towards the negative field axis in FM Co nanoparticles coated with AFM CoO under field cooled condition through its Néel temperature ($T_N$) [64]. The shifted hysteresis loop of this system towards the negative field axis is shown in Fig. 1.10. The amount of shifting of the hysteresis loop can be quantitatively described in terms of the EB field ($H_{EB}$) using the relation,

$$H_{EB} = \frac{(H_+ + H_-)}{2} \tag{1.20}$$

Similarly, the vertical shift in magnetization ($M_{EB}$) can be expressed as

$$M_{EB} = \frac{(M_+ + M_-)}{2} \tag{1.21}$$

The effective coercive field, $H_C^{eff}$ can be obtained using the relation,

$$H_C^{eff} = \frac{(H_+ - H_-)}{2} \tag{1.22}$$

Here, $H_+$ and $H_-$ are the field values corresponding to the loop crossing the $M = 0$ axis during the ascending and descending branches of $M$–$H$ loop. Similarly $M_+$ and $M_-$ correspond to the values of magnetization at $H = 0$ in the descending and ascending branches of the loop, respectively.

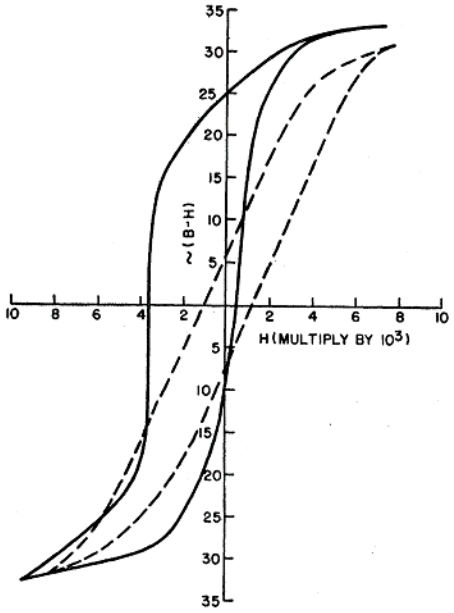


**Figure 1.10:** Hysteresis loops of Co nanoparticles coated with CoO at 77 K under both zero field cooled (dotted line) and field cooled (solid line) conditions [64].

The origin of EB is associated with the unidirectional exchange anisotropy developed at the interface between a FM and an AFM layer and it is generally described in presence of field cooled condition [68]. Fig. 1.11(a) and (b) show the schematic spin configurations in the FM and the AFM layers below and above the $T_N$. When a magnetic field is applied in a temperature $T_N < T < T_C$, the FM spins will align along the field direction but the spins in

AFM material remain random because they are in the PM state. When the system is cooled to $T < T_N$ in presence of the field, the spins of FM and AFM interact with each other at the interface such a way that the first layer of AFM spins align parallel to FM spins. So, there is a FM interaction at the interface, while the other spins deep inside the AFM simply follow the AFM order. When the field is reversed in order to record the hysteresis loop, the FM spins try to align along the reversed field direction as shown in Fig. 1.11(c). But due to sufficiently large AFM anisotropy, the AFM spins remain unchanged. Therefore, the interaction between the FM and the AFM spins at the interface resists the FM spins from rotating along the field direction. In other words, the AFM spins at the interface exert a microscopic torque on the FM spins to keep them in their original direction. Thus a unidirectional anisotropy develops at the interface and the FM spins have only one stable configuration. Therefore a larger negative field is required to align the FM spins compared to the case of isolated FM substance and to attain the stage shown in Fig. 1.11(d). Hence the coercive field in the negative field branch will increase. On the other hand, while changing the magnetic field in the positive direction, the FM spins will align easily along the direction of field because the anisotropy at the interface now exert a torque in the same direction as applied field [Fig. 1.11(e)]. Therefore the coercive field in the positive field branch will be reduced. The net effect will be shifting of the hysteresis loop along the magnetic field axis. In the above process we have considered FM coupling at the interface that gives rise to shifting of *M–H* loop along negative field axis. If the coupling at the interface is AFM, one would expect shifting of the loop along the positive field axis [68, 94].

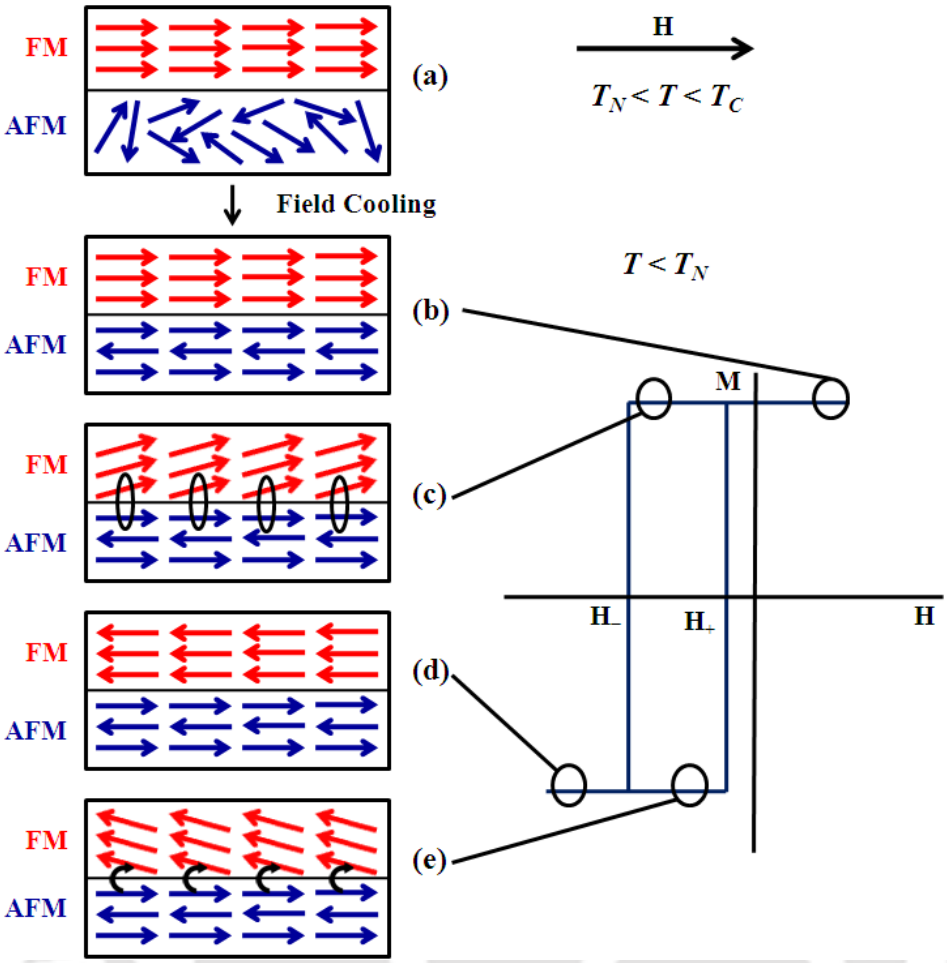


**Figure 1.11:** Schematic diagram of the spin configuration of an FM-AFM couple at different stages of a shifted hysteresis loop for a system with large AFM magnetic anisotropy [68].

However, if anisotropy of the AFM is low then shifting of the hysteresis loop will not be observed, only a hysteresis with large coercivity is observed. In this case, when field is reversed to measure the hysteresis loop, the FM spin starts to rotate and due to the low magnetic anisotropy the AFM spins also tend to align along the field direction [Fig. 1.12(b)]. The extra energy associated with the creation of an irreversible twist in the AFM structure translates into an enhanced coercivity. Analogous behavior is observed after the saturation in the negative field [Fig. 1.12(c) and (d)]. In this case, although no loop shift is observed, the magnetic field required to reverse magnetization in both positive and negative branches becomes larger, *i.e.* hysteresis loop becomes broader [94].

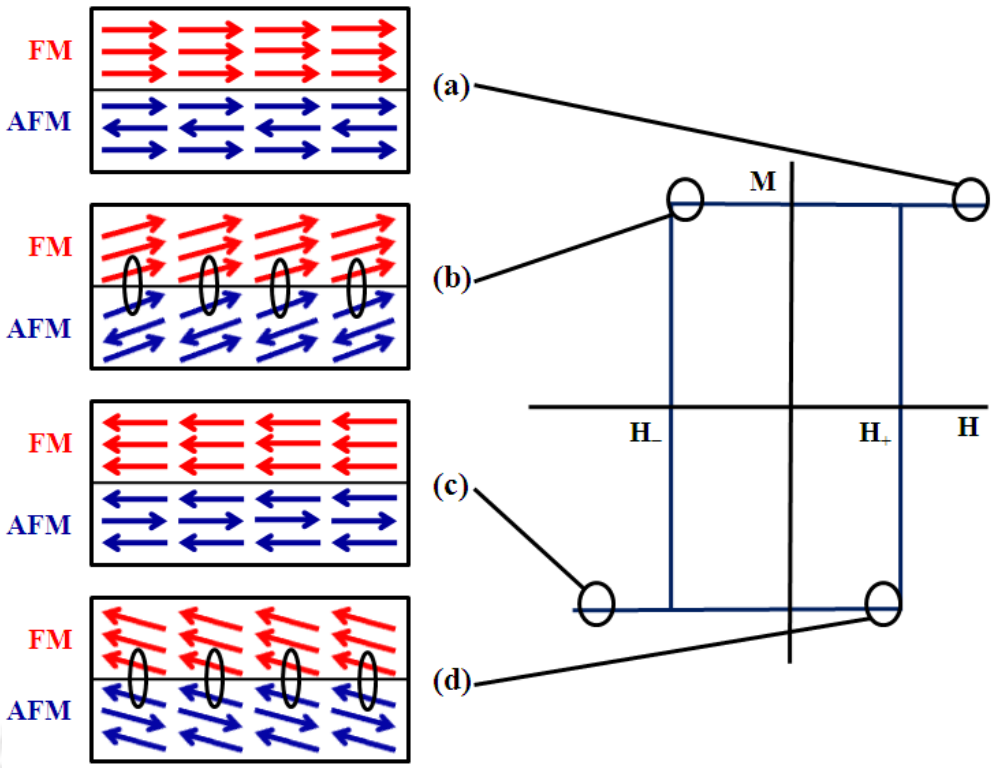


**Figure 1.12:** Schematic diagram of the spin configuration of an FM-AFM couple at different stages of a hysteresis loop for a system with low AFM magnetic anisotropy [94].

Systems having EB behavior are applicable in several spintronics devices. They are useful in read heads of recording devices for reading the stored information. Some other technological applications of EB are in magnetic random access memories (MRAM), magnetic field sensors, enhancement of the coercivity and energy product of permanent magnets and in overcoming the superparamagnetic limit of memory devices [2, 68, 94, 95]. Despite many advantages, the applications of EB systems are limited due to fact that in most of the systems it is observed much below the room temperature. Therefore it is an important ongoing research topic. Since the discovery of EB, it has been studied in wide variety of hetero-structured systems such as oxidized FM particles, bilayer and multilayer of FM/AFM, FM/Ferrimagnet, FM/spin-glass (SG), *etc*. [68]. It has also been observed in bulk materials like binary alloys, intermetallic alloys and oxide materials [68, 95].

There are many composites, thin films and nanoparticles of spinel oxides which are known to exhibit EB behavior. Composites like NiO/$NiMn_2O_4$ [96], $CoFe_2O_4$/$Co_2O_3$ [97],

$NiCr_2O_4/Cr_2O_4$ [98], *etc*. show EB behavior due to the exchange coupling between the FIM and the AFM phases. In nanoparticles of $CoCr_2O_4$, $NiCr_2O_4$, $CoFe_2O_4$, $NiFe_2O_4$, *etc*., the EB was explained by considering various aspects. In $CoCr_2O_4$, it is originated due to the presence of SG phase. When the sample is field cooled, the frozen spins of SG phase aligned along the field direction and during the *M–H* loop measurement, they provide a pinning force to the rotatable spins of SG phase leading to the appearance of considerable EB field [99]. Coupling between the surface spins of nanoparticles and the ferrimagnetically ordered core spins give rise to EB in $NiCr_2O_4$ [100]. In both the compounds the observed EB field is around 500 Oe. The nanoparticles of $CoFe_2O_4$ and $NiFe_2O_4$ exhibit a larger EB field of around 1500 Oe [15, 101]. Study of EB in bulk spinel oxides is very few. $CaV_2O_4$ [102] and $Co_2TiO_4$ [14] are reported to exhibit EB like behavior but its origin is not studied in detail. Origin of EB like nature observed in $Cu_{1-x}Zn_xCrO_4$ ($x$ = 0.10 – 0.42) was ascribed to the freezing effect of the local anisotropy in the cluster glass system [30, 103]. Noticable EB was observed only below the lock in transition temperatures of $Co(Cr_{1-x}Co_x)O_4$ ($x$ = 0 – 0.10), *i.e.* of the order of 150 Oe at 3 K and it was attributed to the presence of commensurate spin spiral which get locked to the lattice [104]. However, all these chromite samples exhibit appreciable value of EB field only at very low temperature (below around 30 K) and in a narrow temperature range.

## 1.8.1 Tunable Exchange Bias

In all the materials mentioned above, the hysteresis loops are found to shift along the negative field axis, *i.e.* opposite to the direction of the applied field. But bilayer systems such as Ni – $FeF_2$ (FM/AFM) [105] and Fe – $FeF_2$ [106] show the MR due to strong interfacial AFM coupling between the FM (Ni and Fe) and the AFM $FeF_2$ layer and they shift along both positive and negative field axes depending on the cooling field. The corresponding EB field here switches from negative values at low fields to positive values at higher cooling fields. For small cooling fields, the interfacial AFM coupling dominates over the Zeeman energy, and the uncompensated AFM moments orient opposite to the cooling field thus giving rise to a negative EB. On the other hand, for large cooling fields, the Zeeman energy is large enough to orient the AFM moments in the direction of the cooling field and results in a positive EB. Thus the observed coexistence of a positive and negative EB is quite different

from the conventional negative EB. Such coexistence is termed as the tunable EB behavior as the EB field can be tuned from positive to negative values either by changing the temperature or magnitude of the applied field. Generally, the materials that show temperature induced MR are expected to show tunable EB behavior.

Owing to the interesting physical properties and applications in memory devices, several types of materials including bilayers, intermetallic alloys, manganites, orthochromites were studied. A detailed study on the temperature induced tunable EB behavior was carried out by Kulkarni *et al.* in rare earth intermetallic system $Nd_{0.75}Ho_{0.25}Al_2$ [91]. It shows tunable positive and negative EB behavior across the $T_{comp}$ = 23.85 K as shown in Fig. 1.13(b). The occurrence of tunable EB field has been discussed in the light of various exchange coupling between the moments corresponding to conduction electron polarization (CEP) and two dissimilar rare-earth ions. Considering that CEP in this system is analogous to that of the FM layer of a FM/AFM multilayer, EB above and below $T_{comp}$ was discussed with the help of schematic diagram as shown in Fig. 1.13(c). The CEP aligns antiparallel to the field for $T > T_{comp}$. In the vicinity of $T_{comp}$, the contributions from the local magnetic moments of both the rare earth ions $Nd^{3+}$ and $Ho^{3+}$ are nearly compensated, and the role of CEP become significant. Thus here the CEP plays significant role in the existence of EB effect and its sign reversal across $T_{comp}$. Similar kind of tunable EB field is observed for other rare-earth intermetallic compounds $Sm_{0.98}Gd_{0.02}Al_2$ [107] and $Sm_{0.975}Gd_{0.025}Cu_4Pd$ [108]. Unlike the divergence of coercivity observed at the $T_{comp}$ in the multilayer films of $GdCo_2$ and Co [109], here a dramatic collapse of coercivity is observed at the $T_{comp}$.

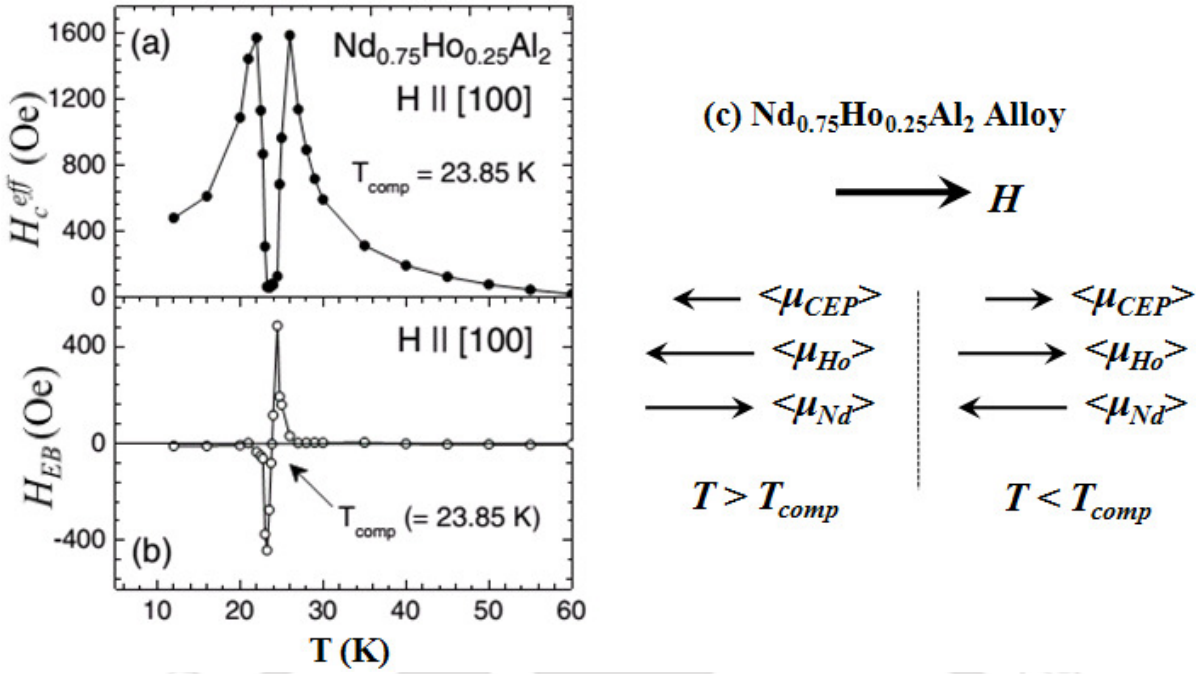


**Figure 1.13:** Temperature dependence of the (a) effective coercive field, $H_C^{eff}$ and (b) the EB field $H_{EB}$ in a single crystalline $Nd_{0.75}Ho_{0.25}Al_2$. (c) Schematic diagram of the orientation of different sub-components of magnetization with respect to the applied field for $Nd_{0.75}Ho_{0.25}Al_2$ single crystal at $T > T_{comp}$ and $T < T_{comp}$ [91].

Later the coexistence of temperature dependent sign reversal of magnetization and the EB field have been observed in core-shell type $La_{0.2}Ce_{0.8}CrO_3$ nanoparticles [85], bulk single phase oxide materials like $Sr_2YbRuO_6$ [110], $YFe_{0.5}Cr_{0.5}O_3$ [111], $NdMnO_3$ [112], orthochromites $La_{1-x}Pr_xCrO_3$ [113], $NdCr_{1-x}Fe_xO_3$ ($x$ = 0.05 – 0.20) [89], $LaCr_{0.85}Mn_{0.15}O_3$ [86], solid solutions of $BiFeO_3$ – $BiMnO_3$ [114], *etc*.

Very few reports are available on the study of tunable EB behavior in spinel compounds. In spinel $Co(Cr_{0.95}Fe_{0.05})_2O_4$ [26], sign reversal of both magnetization and EB field is first observed across the $T_{comp}$ = 43.8 K which was attributed to the flipping of the sign of the spins of Co, Cr and Fe without affecting the spin-spin exchange interaction between them. Wang *et al.* have reported the sign reversal of magnetization and a zero field cooled EB behavior in $Co_{0.8}Cu_{0.2}Cr_2O_4$ [29]. Nayak *et al*. [115] have reported the MR behavior with $T_{comp}$ = 27 K. They also found the polarity reversal of EB field across $T_{comp}$ under both ZFC and FC condition which they have explained through the exchange

interaction between the FIM and the spin glass ordering that arises from intrinsic anti-site disorder.

However, as per our knowledge all the above compounds exhibit the tunable positive and negative EB field well below the room temperature. So, search for new materials with higher $T_{comp}$ and tunable EB field across it is still continuing so as to fulfill their technological importance. Moreover, as we observed that the origin of such behaviors is not common to all the materials, therefore it increases the curiosity to explore new materials with similar behavior and search for their origin.

# 1.9 Geometrical Magnetic Frustration

Magnetic frustration arises in systems having competing interactions between local magnetic moments or spins that fail to satisfy the minimum energy condition of all pair wise magnetic interactions simultaneously and thus gives rise to large degeneracy of the system in the ground state. The emergence of frustration due to the geometry of the system is called geometrical magnetic frustration (GMF). Mainly GMF is observed in materials having antiferromagnetically coupled magnetic moments in geometric units such as triangles or tetrahedron [116, 117]. The B site of a spinel oxide forms a pyrochlore lattice (corner shared tetrahedra) and such arrangement leads to a strong GMF when the B sublattice is antiferromagnetically coupled. It is depicted in Fig. 1.14 for $ACr_2O_4$, *i.e.* with Cr in the B site. If both A and B site ions are magnetic in nature, strong magnetic interaction between A and B site ions offer an alternate way for the frustrated B site moments to satisfy the different magnetic exchange interactions simultaneously; thereby reducing GMF to some extent [118].

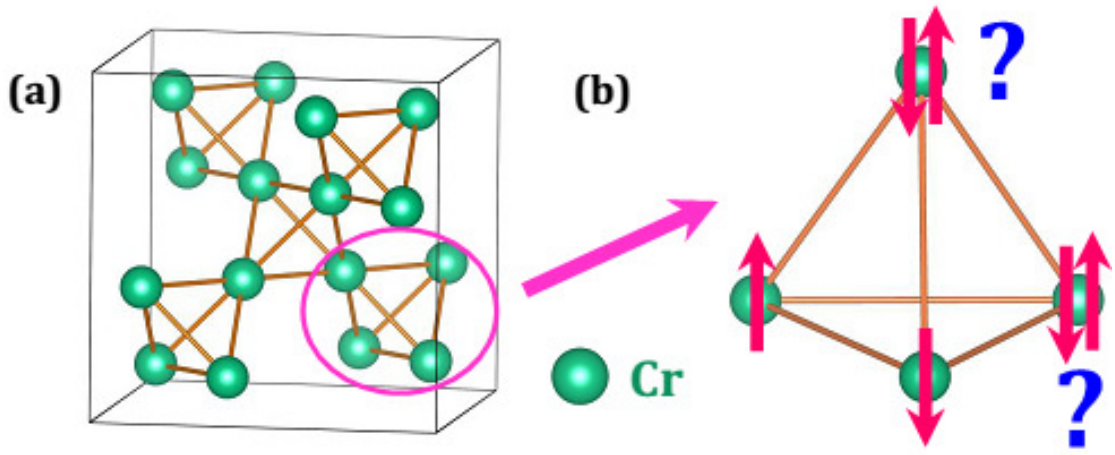


**Figure 1.14:** (a) Corner sharing tetrahedra formed by B ($Cr^{3+}$) sublattice in the spinel structure. (b) Strong GMF in antiferromagnetically coupled $Cr^{3+}$ in the corner sharing tetrahedra formed by it [24].

According to Lyons, Kaplan, Dwight and Menyuk (LKDM) theory [119], strength of the GMF can be estimated from the '*u*' parameter,

$$u = \frac{4J_{BB}S_B}{3J_{AB}S_A} \tag{1.23}$$

where, $J_{BB}$ & $J_{AB}$ are the nearest neighbor AFM superexchange integrals along the B – O – B & A – O – B pathways, and $S_A$ & $S_B$ are the magnitude of moments at the A & B sites, respectively. $u = \infty$ signifies large GMF [120], $\infty > u > 1.298$ signifies weak GMF and results in short range spin spiral order as observed in $MCr_2O_4$ (M = Co and Mn) [118], long range spiral configuration is observed for $1.298 \geq u \geq 8/9$ and Néel type collinear FIM or AFM ordering is observed for spinels with $u < 8/9$. Thus in spinels, particularly, in spinel chromites the non-collinear magnetic structure is due to the GMF in the pyrochlore B site.

## 1.10 Review of $NiCr_2O_4$ Based Spinel Compounds

Investigation of spinel oxide, $NiCr_2O_4$, began in 1950's. It has very complicated crystal and magnetic structures. Here we will review some of the earlier works based on this compound in order to know its different physical properties.

## 1.10.1 Crystal and Magnetic Structure

Lotgering in 1956 reported that $NiCr_2O_4$ is a normal spinel compound with Jahn-Teller active $Ni^{2+}$ ($3d^8$) ions in the tetrahedral site and $Cr^{3+}$ ($3d^3$) ions in the octahedral site. It undergoes a structural transition from cubic to tetragonal phase at 310 K and it is followed by the PM to FIM transition ($T_C$) at 80 K [121]. Low saturation magnetization ($M_s$) of about 0.3 $\mu_B$/f.u. for $NiCr_2O_4$ raises the question about its magnetic structure: is it a collinear FIM or a non-collinear FIM with triangular (canted) arrangement described by Yafet-Kittel theory? Large increase in net magnetization at high applied magnetic field provides the evidence for a non-collinear FIM arrangement, since such behavior is not expected for the Néel model of FIM. Jacobs [122] confirmed the non-collinear FIM structure in $NiFe_{2-t}Cr_tO_4$ series with $t >$ 1, *i.e.* in the chromite rich samples, but it was not confirmed by neutron diffraction study. Several authors have confirmed the JTD induced structural transition at around 310 K and the FIM transition in the range of 65 – 79 K by X-ray diffraction study and neutron diffraction study [17, 123-126]. Crottaz *et al*. [17] have studied the crystal structure of $NiCr_2O_4$ both above and below the structural transition temperature. At 353 K, $NiCr_2O_4$ is cubic ($Fd\bar{3}m$ space group) with lattice parameter, $a$ = 8.3155 Å while at 298 K it is tetragonal ($I4_1/amd$ space group) with $a = b$ =5.8369 Å and $c$ = 8.4301 Å. The respective atomic positions of Ni, Cr and O in tetragonal structure are reported to be 4*b* (0, 1/4, 3/8), 8*c* (0, 0, 0) and 16*h* (0, 0.506, 0.2387). In the year of 2002, Klemme *et al*. [18] discovered a new peak at 29 K in their heat capacity data [Fig. 1.15(a)]. This additional low temperature transition is later confirmed by Tomiyasu and Kagomiya ($T_S$ = 31 K) [54] from magnetization measurements and it is explained in terms of ordering of the AFM transverse components. In order to explain the low $M_s$ of $NiCr_2O_4$ (0.3 $\mu_B$ / f. u.), they also worked out its magnetic structure below $T_S$ from neutron diffraction measurement. According to them, the A sublattice is classified into A1-A2 pairs and B sublattice is classified into B1-B3 and B2-B4 pairs with each having longitudinal and transverse components such that the total longitudinal component of moment is 0.3 $\mu_B$ / f. u. The FIM and the AFM components are depicted in Fig. 1.15(b) & (c). Thus the total magnetization per formula unit can be written as $M = | \uparrow \mu_{A1\text{-}A2} + \uparrow \mu_{B1\text{-}B3} - \downarrow \mu_{B2\text{-}B4} |$, where $\uparrow \mu_{A1\text{-}A2}$, $\uparrow \mu_{B1\text{-}B3}$ and $\downarrow \mu_{B2\text{-}B4}$ are the longitudinal components of the magnetic moments of A1-A2, B1-B3 and B2-B4 sublattices, respectively along the field

direction. Ishibashi and Yasumi [127] performed the high resolution X-ray diffraction measurements using synchrotron radiation on $NiCr_2O_4$ and found that the FIM transition at $T_C$ = 74 K is associated with structural transition into orthorhombic phase from tetragonal at ambient pressure. This highlights the presence of important magneto-elastic behavior. The spin induced structural changes in $NiCr_2O_4$ was studied by Suchomel *et al*. [19] by recording the high resolution synchrotron X-ray powder diffraction as a function of temperature. They found that the structural transition from tetragonal to orthorhombic phase with *Fddd* space group occurs concurrently with the onset of FIM ordering and also found the evidence of further subtle structural changes at the AFM transition temperature (30 K).

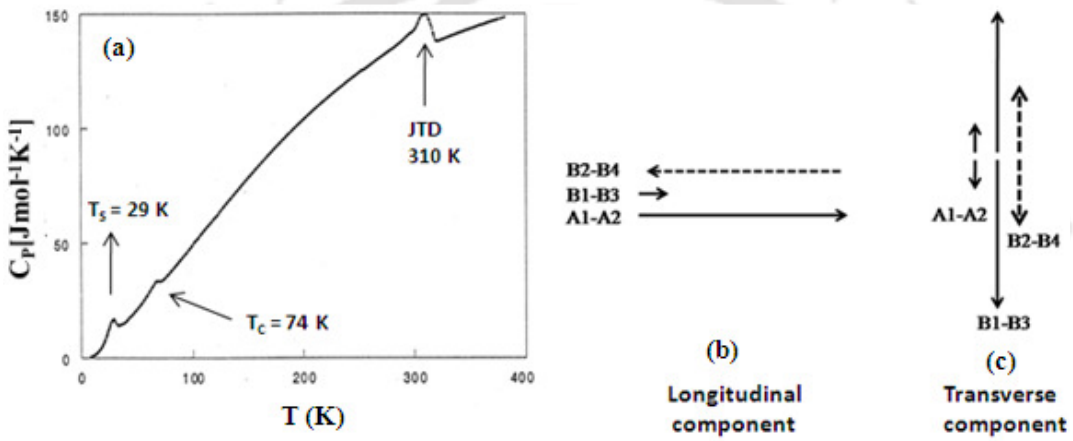


**Figure 1.15:** (a) Heat capacity of $NiCr_2O_4$ [18]. Schematic diagram of (b) longitudinal FIM and (c) transverse AFM components of group of A ($Ni^{2+}$) and B ($Cr^{3+}$) sublattices [54].

## 1.10.2 Other Salient Properties

After the discovery of crystal and magnetic structure of $NiCr_2O_4$, several authors have tried to explore its other exciting properties like magnetodielectric, magnetoelectric, magnetoelastic, EB, *etc*. Spinel chromites are generally known to have strong correlation between spin, charge and lattice degree of freedom. Mufti *et al*. [23] have studied the magnetodielectric coupling in the pollcrystalline samples of $NiCr_2O_4$ and observed a clear anomaly in the dielectric constant in the vicinity of $T_S$. The dielectric response in an applied magnetic field was found to scale with the square of the magnetization and thus they predicted that the magnetodielectric coupling originates from $P^2M^2$ term in the free energy. In the context of this magnetodielectric coupling, magnetocapacitance is also discussed in

this sample by Sparks *et al*. [128]. The magnetoelastic measurements are also shown to exhibit anomalies at different magnetic transitions of $NiCr_2O_4$ [21].

The coexistence of ferroelectric and magnetic properties in a single phase material is a subject of great interest from fundamental as well as application point of view. Frustrated magnets like $CoCr_2O_4$, $RMnO_3$ and $RMn_2O_5$ (R = Tb, Dy and Ho), exhibit multiferroic property with large magnetoelectric coupling, *i.e.* here the electric polarization (*P*) has magnetic origin and can be reversibly switchable by applying magnetic field [13, 129, 130]. In spinel oxides like $CoCr_2O_4$ [13], conical spiral magnetic ordering below $T_S$ = 26 K is responsible for the inversion symmetry breaking and hence the magnetically induced polarization. This process can be explained by combining spin current model and the inverse DM interaction [13, 131],

$$\vec{p} = a\vec{e}_{ij} \times \left( \vec{S}_i \times \vec{S}_j \right) \tag{1.24}$$

where $\vec{S}_i$ and $\vec{S}_j$ are the canted spin vector, $\vec{e}_{ij}$ denotes the vector connecting the two sites, and *a* is a proportionality constant. $NiCr_2O_4$ do not exhibit any spiral magnetic structure. But an evidence of electrical polarization below $T_C$ has been observed by Maignan *et al*. in $NiCr_2O_4$ [22]. They have attributed the existence of the polar state in $NiCr_2O_4$ due to its complex magnetic structure with different A – O – B, A – O – A, B – O – B magnetic interactions. Interaction through such different exchange pathways probably is responsible for local symmetry breaking and leads to electrical polarization in the system.

Existence of EB phenomenon in multiferroic materials enhances their multifunctionality and thus their potential for suitable applications in spintronics. Signature of EB (shifting of hysteresis loop) was observed in bulk $NiCr_2O_4$ sample which was explained due to the presence of some $Cr_2O_3$ impurity [132, 133]. But the detailed study by varying the temperature and field are not available. Later EB study has been carried out in $NiCr_2O_4$ nanoparticles where it was attributed to the coupling between surface spin and ferrimagnetically ordered spin [100]. EB was also observed in $NiCr_2O_4$ /NiO [134] and $NiCr_2O_4/Cr_2O_3$ [98] composites and was explained in terms of the exchange coupling between FIM $NiCr_2O_4$ and AFM NiO and $Cr_2O_3$.

Although lots of reports are available on different properties of parent $NiCr_2O_4$, very few studies have been carried out on the effect of substitutions at Ni or Cr site. Structural analysis were carried out in $M_{1-x}Ni_xCr_2O_4$ (M = Cu and Fe) [135], $Ni_{1-x}Cu_xCr_2O_4$ [136] and $Ni(Fe_{1-x}Cr_x)_2O_4$ [137] in order to understand the cooperative JTD. FIM behavior with increasing $T_C$ was reported in $Ni_{1-x}Cu_xCr_2O_4$ [138] and $NiCr_{2-x}Fe_xO_4$ [139]. The Neel temperature for $NiCr_{1.7}Fe_{0.3}O_4$ was reported to be 250 K and the Mössbauer spectra detected the distribution of $Fe^{3+}$ ions in the two sites of $Cr^{3+}$ [139, 140]. Strong orthorhombic distortions into *Fddd* space group was observed in $Ni_{1-x}Cu_xCr_2O_4$ due to competing Jahn-Teller activities between the $Cu^{2+}$ and $Ni^{2+}$ ions [141]. Multiferroic properties were studied recently in $Co_{1-x}Ni_xCr_2O_4$ ($x$ = 0.2, 0.4, 0.6) [142] and $Ni_{1-x}Zn_xCr_2O_4$ ($x$ = 0.05) solid solutions [143]. The remarkable multiferroic nature of $Ni_{0.95}Zn_{0.05}Cr_2O_4$ might originate from the DM interaction [143]. Recently, EB behavior was also evidenced in Mn doped $NiCr_2O_4$ sample ($NiCr_{1.90}Mn_{0.10}O_4$) [144].

# 1.11 Review of $MnCr_2O_4$ Based Spinel Compounds

$MnCr_2O_4$ is also an interesting compound with complicated magnetic phase diagram. First attempt to study this compound was made by Gorter [145]. Some of the early works are summarized below.

## 1.11.1 Crystal and Magnetic Structure

Gorter [145] attempted to explain the magnetic properties of Mn ferrite chromite as well as in pure $MnCr_2O_4$ on the basis of non-collinear spin structure as suggested by Yafet-Kittel [146]. He postulated that canting of B site moments is present in pure $MnCr_2O_4$ and chromium rich samples. Similar analysis was also carried out by Lotgering [121] and Edwards [147] and found presence of canting angles between Cr moments in the B sites. Some authors also argued that a good agreement between observed and calculated $M_s$ value can be obtained for a series of chromites and mixed ferrite chromites if some of the Cr moments in B sites are parallel to the A site moments, rather than being antiparallel [148]. Lyons and Kaplan [149] have found a conical spiral magnetic ground state where the axial components of spins on each sublattice are constant but the transverse components rotate in

discrete steps along a fixed direction in the crystal and translate to equivalent sites in other unit cells. LKDM provide the detailed picture of the conical structure of $MnCr_2O_4$ theoretically using classical Heisenberg exchange energy. Such conical spiral structure is detected in both A and B sites.

Later, the extensive neutron diffraction and NMR (Nuclear Magnetic Resonance) studies have been carried out in order to determine the cone angles for Mn, Cr(1) and Cr(2) in the conical FIM state. From neutron powder diffraction studies, Hastings *et al*. [150] have observed the cone angles of Mn, Cr1 and Cr2 as 24°, 76° and 28°, respectively with an approximate $u$ value of 1.6. On the other hand, some reports on NMR studies of $MnCr_2O_4$ reveal two different cone angles of 63° and 42° for Mn ion spins. These angles for Cr1 and Cr2 spins were reported to be 94° and 97°, respectively [151-153]. Recently, Tomiyasu *et al*. [118] have reported the values to be 28°, 85° and 11°, respectively with $u$ value of 1.5 from neutron diffraction study (Fig. 1.16). This magnetic structure results in the axial (FIM) components, $\mu_{Mn}$ = 4.41 $\mu_B$, $\mu_{Cr1}$ = 0.26 $\mu_B$ and $\mu_{Cr2}$ = 2.94 $\mu_B$ such that the macroscopic moment along $[1\bar{1}0]$ direction is 1.2 $\mu_B$ ($M_s$). Therefore the net moment here can be expressed as $M = |\uparrow \mu_A - \downarrow \mu_{B1} - \downarrow \mu_{B2}|$. This compound shows long range non-collinear FIM ordering with $T_C$ in the range of 41 to 51 K and a short range spiral magnetic ordering around $T_S$ = 14 – 18 K with a typical $u$ value of 1.5. Due to weak GMF, long range spiral magnetic ordering is not observed here [23, 38, 154-156].

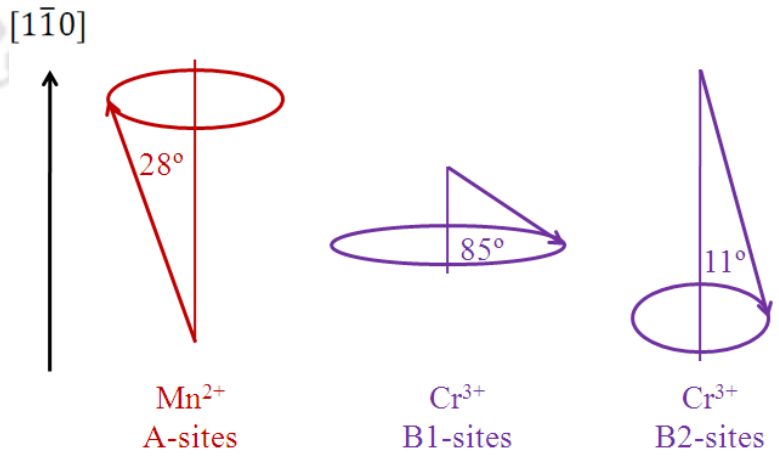


**Figure 1.16:** Mean FIM spiral order of $MnCr_2O_4$ estimated by Tomiyasu *et al*. from neutron scattering experiments [118].

Unlike $NiCr_2O_4$, $MnCr_2O_4$ does not undergo any structural transition because $Mn^{2+}$ in the tetrahedral site is not a Jahn-Teller active ion. It is known to crystallize in $Fd\bar{3}m$ space group in a wide temperature range, *i.e.* even down to $T_S$ (18 K). $MnCr_2O_4$ is a normal spinel with $Mn^{2+}$ ($3d^5$) ions in the tetrahedral A site and the $Cr^{3+}$ ($3d^3$) ions in the octahedral B site. Lattice parameter ranges from $a$ = 8.410 to 8.450 Å [24, 154, 155, 157].

## 1.11.2 Other Salient Properties

Like $NiCr_2O_4$, several authors have also studied the pristine $MnCr_2O_4$ in the light of magnetic, magnetodielectric, magnetoelectric and magnetoelastic properties. Many authors studied its magnetic properties across the FIM $T_C$ and the spiral magnetic ordering $T_S$ by magnetic as well as specific heat measurements [38, 155, 156]. Tobia *et al*. [156] have studied the low temperature magnetic phase of $MnCr_2O_4$ through dc magnetization and ferromagnetic resonance (FMR) spectroscopy. These experiments yield $T_C$ = 41 K and $T_S$ = 18 K. They also tried to define the easy direction of magnetization of $MnCr_2O_4$ from the FMR spectra below $T_C$. They modeled the FMR spectra by a cubic magnetocrystalline anisotropy to second order and found <110> direction as the easy direction of magnetization. While at low temperature [$1\bar{1}0$] direction was considered as the direction of propagation of the spiral arrange.

Spiral magnetic order driven ferroelectricity was detected below $T_S$ = 18 K by Dey *et al*. [24]. Zero-field- cooled memory effect and linear temperature dependence of magnetic entropy was observed below the spiral spin order suggesting the presence of reentrant spin-glass-like state. From synchrotron X-ray diffraction studies they also observed significant magnetoelastic coupling at FIM $T_C$ and $T_S$. Magnetocaloric properties of $MnCr_2O_4$ have also been simulated based on a phenomenological model by Hamad [158]. He used the simulation of magnetization as function of temperature to explore magnetocaloric properties such as magnetic entropy change, heat capacity change, and relative cooling power. Simulation results imply the magnetocaloric effect in the vicinity of Curie temperatures (38 – 44 K). Therefore, $MnCr_2O_4$ can be used as a promising practical material in the active magnetic regenerator cycle that cools hydrogen gas.

The study of effect of substitution of Mn and Cr sites in $MnCr_2O_4$ by other magnetic and nonmagnetic elements is quite limited. Effect of substitution of magnetic Fe and the nonmagnetic Zn ions at the Mn site on the structural and magnetic properties has been studied by a few authors [39, 159-161]. There are some reports on the substitution of Cr in the Fe site of $MnFe_2O_4$. But their magnetic properties were explained by considering the spin canting only in the B sublattice [145, 147, 162, 163].

## 1.12 Motivation of the Present Thesis Work

As per the literature review, we found that $NiCr_2O_4$ and $MnCr_2O_4$ have very rich magnetic phase diagram. The JTD near room temperature makes $NiCr_2O_4$ interesting structurally also. Non-collinear as well as spiral magnetic ordering in these compounds arises from GMF which is very sensitive to the A – O – B and B – O – B superexchange interactions. Therefore substitution of other elements either in tetrahedral or in the octahedral site may vary the strength of superexchange interaction and thus the corresponding magnetic properties. Although there are many reports available on the magnetic properties of both the parent compounds, systematic study of the effect of substitution in their magnetic properties are still lacking.

Recently EB has received a special attraction among the researchers due to its interesting underlying origin in different systems and numerous practical applications. If EB is observed in multiferroic compounds, it further enhances their technological potentials. Signature of EB was also observed in bulk $NiCr_2O_4$, but detailed study with magnetic field and temperature was not attempted in parent as well as in substituted systems.

In similar type of spinel compound, $CoCr_2O_4$, MR has been achieved by substitution of different elements at the Cr site [26-28]. Therefore, the substitutions in $NiCr_2O_4$ and $MnCr_2O_4$ are expected to induce MR due to their complicated magnetic structure. Moreover, the literature review shows that most of the compounds undergoing MR, the magnetic compensation temperature is quite low. Thus the corresponding tunable EB across $T_{comp}$ is also observed at very low temperatures. Careful selection of substituents may enhance the $T_{comp}$ and lead to tunable EB behavior near room temperature.

In order to achieve the above objectives we have chosen $Fe^{3+}$ with higher magnetic moment of 5 $\mu_B$ compared to 3 $\mu_B$ of $Cr^{3+}$ and $Al^{3+}$ with zero magnetic moment as the substituents. So, in the present thesis work we have focused on the following four series

i. $Ni(Cr_{1-x}Fe_x)_2O_4$ ($x$ = 0 to 0.60)
ii. $Ni(Cr_{1-x}Al_x)_2O_4$ ($x$ = 0 to 0.50)
iii. $Mn(Cr_{1-x}Fe_x)_2O_4$ ($x$ = 0 to 0.50)
iv. $Mn(Cr_{1-x}Al_x)_2O_4$ ($x$ = 0 to 0.30)

In order to study the above mentioned properties, these samples were characterized by using X-ray diffractometer (XRD), Raman spectroscopy, Field emission scanning electron microscope (FESEM), Energy dispersive X- ray spectroscopy (EDS) and Vibrating sample magnetometer (VSM). To determine the crystal structure, XRD patterns were recorded at room temperature by using the Rigaku make TTRAX III diffractometer. To understand the magnetic properties of these samples we have studied the dc magnetization as a function of temperature and field by using a Lakeshore make VSM of model no. 7410. The preparation method of the above samples and the working principle of these sophisticated instruments are briefly discussed in Chapter 2.

# *Chapter 2*

# *Experimental Techniques*

Experimental techniques are the fundamental part of experimental research. Therefore, before using an experimental tool and taking measurements it is essential to understand its working principle and operational details so that proper data can be collected and suitable informations can be extracted from them. During the course of my research work different types of experimental techniques were used. The samples for the current research were prepared by using sol-gel technique. Further heat treatments required for the complete sample preparation were done by using different types of furnaces such as homemade and commercial furnaces. The prepared samples were characterized by X-ray diffractometer (XRD) in order to check their phase purity and crystal structure. XRD patterns were refined by using Rietveld refinement method in order to determine the structural parameters like lattice parameter, atomic positions, bond angles, bond distances, *etc*. Raman spectra were recorded in order to check any structural transformations. Field emission scanning electron microscope (FESEM) and energy dispersive spectrometer (EDS) were used to study the microstructure and composition of the samples. Magnetization as a function of temperature and field were measured by using a vibrating sample magnetometer (VSM). The details of all the above mentioned experimental techniques are discussed in this chapter.

## 2.1 Sample Preparation

### 2.1.1 Sol-gel Method

In general polycrystalline samples are prepared by solid state or sol-gel routes. But in solid state reaction method sometime good chemical homogeneity is not obtained and also

very high temperature is needed to complete the reaction. Hence sol-gel method has been used to achieve molecular scale mixing of reactants at comparatively low temperatures. In sol-gel method, 'Sol' is a colloidal suspension of solid particles of ions in a solvent and 'Gel' is a semi rigid mass that forms when the solvent from the sol begins to evaporate and the particles or ions left behind begin to join together in a three dimensional continuous solid network. To prepare the sol, the starting compounds as per stoichiometric ratio are dissolved in either distilled water or nitric acid and then mixed together. (In general nitrates are mostly used as starting materials due to their solubility in water.) The resultant mixture is then kept under constant magnetic stirring at temperature of around 80 – 100 °C by placing it in a hot plate and proper amount of citric acid and ethylene glycol are added. Citric acid acts as a chelating agent which can bind up only metal ions and remove the non metallic ions. The added ethylene glycol helps to convert the solution into dense gel form. The resultant solution is kept under constant stirring for 3 – 4 hours to ensure the homogeneity and kept in the same temperature for several hours to completely evaporate the water and acid. Finally a metal citrate gel is obtained. The gel is then fired at high temperature to remove volatile components trapped in the pores of the gel, organic ligands, *etc*. and the final product thus obtained is a fine powder. Further heating treat is needed to crystallize the final product and to obtain the required particle sizes.

In general, at room temperature solids (in atomic scale) do not react with each other due to the lack of diffusion between the constituent elements, so the powder is heated at high temperatures by using high temperature furnaces in order to overcome the kinetic barriers. Heat treatment is done for several hours and it is repeated to get good homogeneity throughout the sample. Heat treatment can be divided into two stages: presintering and sintering. Presintering is a low temperature sintering step to facilitate handling and shaping of the powder material before the final high temperature sintering cycle. Here, the thermal energy initially decomposes the starting materials which are usually a single cation oxides, carbonates, nitrates or hydroxides and then supplies the energy required for reaction among the constituent atoms. Hence in presintering stage the starting materials start to react with each other and the product start forming. The better contact between surfaces of the reactants gives rise to fast reaction rate. Therefore, a thorough grinding before presintering is important to reduce the particle size so that the surface contact area increases. Grinding also

helps to achieve homogeneous mixture of the reactants. Further heating speeds up the reaction and for large enough temperature the reaction completes and finally results in a dense polycrystalline solid. This final heat treatment is called sintering. Before sintering samples are pressed in pellet form for good contact between the particles.

The sintering process mainly reduces the total interfacial energy. The total interfacial energy of compact powder can be expressed as $\gamma A$ where $\gamma$ is the specific surface (interface) energy and $A$ is the total surface (interface) area of the compact powder. The change in the interfacial energy can be written as [164]

$$\Delta(\gamma A) = A\Delta\gamma + \gamma\Delta A$$

where, the reduction of interfacial energy $\Delta\gamma$ is due to the densification and the reduction in the interfacial area $\Delta A$ is due to the expansion of grain size. In solid state sintering, the reduction of the interfacial energy $\Delta\gamma$ is related to the replacement of solid/vapour interfaces by solid/solid interfaces. Thus the reduction in total interfacial energy occurs via densification and grain growth. The schematic diagram of the sintering process is shown in Fig. 2.1

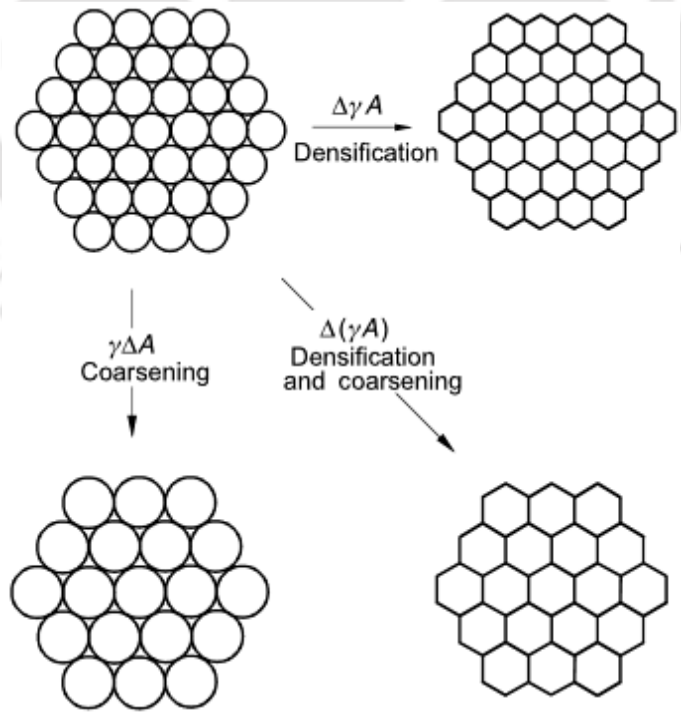


**Figure 2.1:** Different stages of sintering process [164].

The sintering process depends on the two types of variables: material variable and process variable. Material variable is related to the chemical composition of the material, powder size, powder shape, degree of powder agglomeration, *etc.* and such variables control the nature of grain growth and densification of the materials. The other variable is related to the sintering process such as temperature, time, atmosphere, heating and cooling rate of the samples, *etc.*

In this thesis work, the samples were prepared mainly by sol-gel technique. The starting compounds used for the preparation of the samples are nickel nitrate ($Ni(NO_3)_2.6H_2O$, 99%), chromium nitrate ($Cr(NO_3)_3.9H_2O$, 99%), ferric nitrate ($Fe(NO_3)_3.9H_2O$, 99%), manganese acetate ($C_4H_6MnO_4.4H_2O$, 99.5%) and aluminium nitrate( $Al(NO_3)_3.6H_2O$, 98%). The starting compounds as per stoichiometric ratio were weighed using an electronic balance supplied by Mettler Toledo of model no. AG135 with an accuracy of ± 0.01 mg. The precursor powders obtained after the sol-gel method were presintered at 600 ºC, 800 ºC and 1000 ºC for 12 h followed by intermediate grinding. These powders were then pressed into pellets by using a 13 mm cylindrical die and a hydraulic press supplied by Techno Search instruments, Thane, India with a maximum load of 6 Ton/cm$^2$. The final sintering in cylindrical pellet form was carried out at 1100 ºC for 24 h for $Ni(Cr_{1-x}M_x)_2O_4$ (M = Fe and Al) samples and for $Mn(Cr_{1-x}M_x)_2O_4$ (M = Fe and Al) samples it was carried out at 1200 ºC for 24 h. Different high temperature furnaces are used for presintering and sintering.

## 2.1.2 High Temperature Furnaces

High temperature furnaces were used for material preparation. Homemade muffle furnaces with a maximum operating temperature of 1200 ºC and commercial high temperature furnaces with the maximum operating temperature of 1400 ºC were used for sintering the samples. The commercial furnaces were supplied by N. R. Enterprises and Bysakh & Company, Kolkata, India. The furnace supplied by N. R. Enterprises was powered by a thyristor unit of 30 A rating. The temperature was controlled using Honeywell make PID programmable temperature controller model no. DC 1040 with 16 segment programming feature. The platinum versus platinum-rhodium (Platinum + 10 % Rh)

thermocouple was used for sensing the temperature. The heating elements were based on Si-carbide rods.

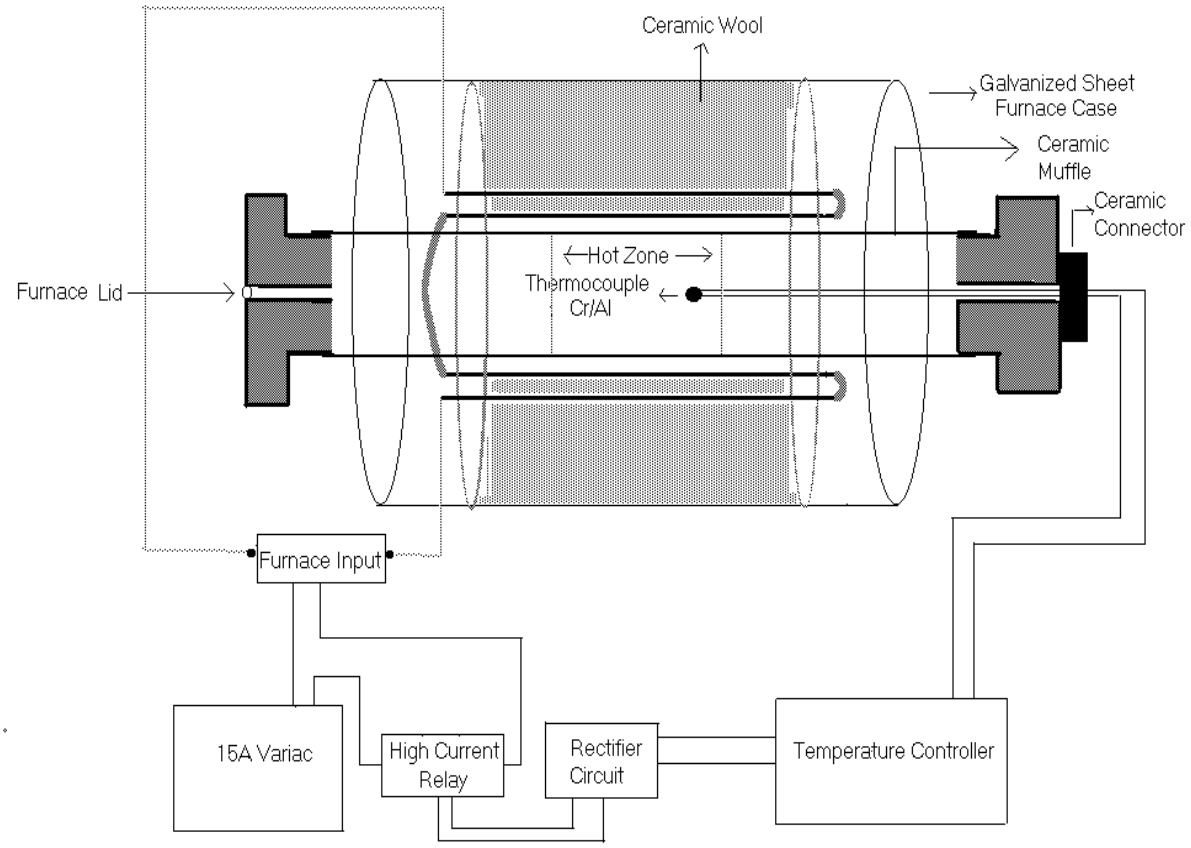


**Figure 2.2:** Block diagram of the furnace with maximum operating temperature of 1200 ºC.

The temperature was controlled to an accuracy of ± 1 ºC. The furnace could be operated up to a maximum temperature of 1400 ºC. The other furnace supplied by Bysakh & Co. contains (1) a thyristor unit with a rating of 35 A, (2) a PID programmable temperature controller (model no. PRC-300) with 16 segment programming feature, (3) a platinum versus platinum-rhodium (Platinum + 13 % Rh) thermocouple wire and (4) Si-carbide rods based heating elements. The maximum operating temperature is 1450 ºC.

The homemade furnace was fabricated using a cylindrical alumina muffle with an inner diameter of 5.8 cm and 50 cm length. Six Si-carbide rods of 45 cm length each are used as heating element. The muffle loaded with heating elements is housed in a cylindrical container of 50 cm diameter and 50 cm length and it is made up of galvanized aluminum

sheet. High temperature ceramic bricks and ceramic wools are used as thermal insulation. Chromel-Alumel (Cr-Al) thermocouple and a commercial on/off type temperature controller are being used for temperature measurement and controlling. The input power to the furnace is regulated using a variac (dimmerstat) of 15 A capacity. An external on/off relay (15 A capacity) controls the power supply to the heater wire. The relay is triggered using the temperature controller. The block diagram of the furnace is shown in Fig. 2.2. The furnace could be operated up to a maximum temperature of 1200 ºC. The temperature could be controlled with an accuracy of ± 5 ºC.

# 2.2 Measurement Techniques

## 2.2.1 X-ray Diffraction

The X-ray diffraction (XRD) pattern is the fingerprint of a crystalline material as this technique gives information on the phase, purity, and structure of a material. A powder may be composed of many small and finely ground crystals, known as crystallites. These crystallites are randomly oriented to one another. If a beam of monochromatic X-ray is allowed to incident on the polycrystalline powder sample then due to the comparable inter-atomic spacing and the X-ray wavelength, diffraction of X-ray takes place (Fig. 2.3). But the diffraction occurs only when the condition for constructive interference are fulfilled. In case of powder sample diffraction will occur only from the planes in those crystallites that are oriented at the correct angle to fulfill the Bragg condition,

$$2d \sin\theta = n\lambda \tag{2.1}$$

where, $\lambda$ is the wavelength of the X-ray beam, $d$ is the inter planer spacing, $n$ is the order of diffraction and $\theta$ is the glancing angle [61]. The diffracted X-rays are detected by a detector. When $\theta$ is changed, maximum intensity peaks are observed if different planes are exposed, otherwise no peak is observed. In this way XRD patterns are obtained as a function of $2\theta$ for all the possible ($h$, $k$, $l$) planes in the crystal.

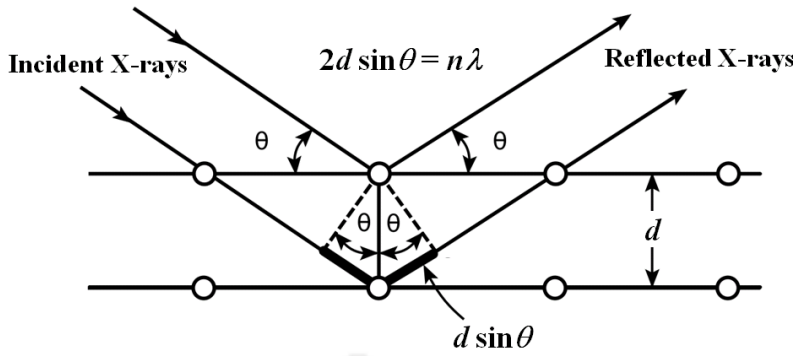


**Figure 2.3:** Schematic diagram of Bragg's X-ray diffraction.

In the present thesis work, in order to check the phase purity of the prepared samples and to reveal their crystal structure, room temperature powder XRD patterns were recorded by using Rigaku make TTRAX III ($\theta$ – $\theta$ Rotating Anode X-ray) diffractometer by employing Cu-Kα radiation of wavelength $\lambda$ = 1.54056 Å. In this powder X-ray diffractometer, the X-ray generator voltage and current were kept at around 50 kV and 200 mA, respectively to produce X-rays. The instrument is based on the principle of Bragg-Brentano geometry which is shown in Fig. 2.4. In Bragg-Brentano geometry, focus of the X-ray tube and receiving slit reside on the circle with the center positioned on the sample surface. In this geometry, both X-ray generator and detector are placed at equidistance from the sample holder. The data were collected by scanning the samples from 10º to 70º in $2\theta$ angle with a scan speed of 3º/min and the step size was maintained around 0.03º.

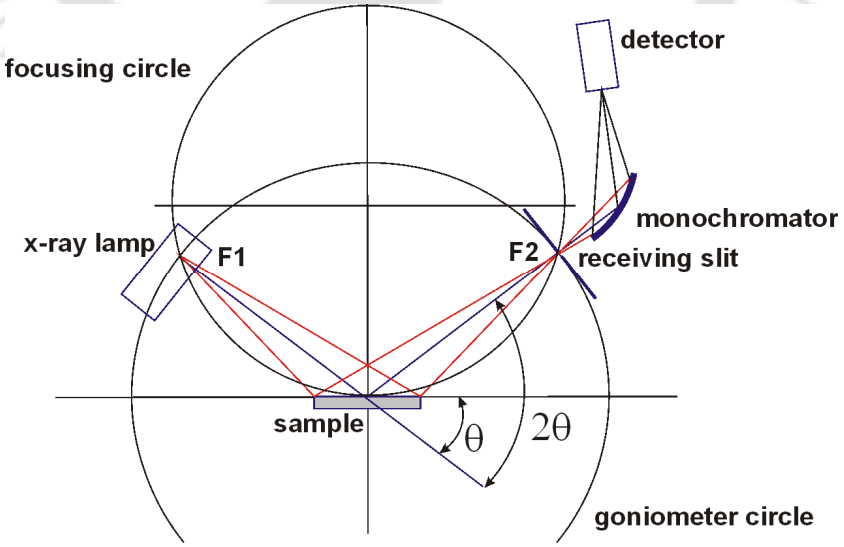


**Figure 2.4:** Ray diagram of X- ray diffractometer.

Analysis of the XRD patterns was carried out by employing the Rietveld refinement method using Fullprof software. Refinement probes phase purity of the samples and also gives the crystal structure information such as lattice parameters, atomic positions, occupancies, different bond lengths, bond angles, *etc*. Basically the Rietveld method is the one which refines user-selected parameters to minimize the difference between an experimental XRD pattern (observed data) and a model based on the hypothesized crystal structure and instrumental parameters (calculated pattern). It minimizes the difference using a non-linear least square method. In this method, the background was refined using a polynomial function. Pseudo-Voigt function was chosen for peak shape refinement. The global parameters, such as coefficients of background polynomial, scaling factor, half width parameters (*u*, *v*, *w*) and lattice parameters (*a, b, c*) were mainly varied during the refinement. In addition to that fractional atomic co-ordinates (*x*, *y*, *z*), isotropic displacement (temperature) parameters and occupancy values were varied. Here, occupancy is the chemical occupancy normalized to the multiplicity of the general position of the group. The occupancy of oxygen was taken as 1 for all the refinements and it was not varied during the refinement. The quality of the refinements are known based on the values of reliability factors such as, $R_p$, $R_{wp}$, $R_{exp}$, $R_{Bragg}$, $R_F$ and $\chi^2$ and they are defined as follows [165].

Profile factor,
$$R_p = 100\frac{\sum_{i=1,n}\left|y_i - y_{c,i}\right|}{\sum_{i=1,n} y_i} \qquad (2.2)$$

Here, $y_i$ is the observed point (experimental) and $y_{c,i}$ is the calculated point and $n$ represents the number of data points.

Weighted profile factor,
$$R_{wp} = 100\left[\frac{\sum_{i=1,n}\omega_i\left|y_i - y_{c,i}\right|^2}{\sum_{i=1,n}\omega_i y_i^2}\right]^{1/2} \qquad (2.3)$$

Here $\omega_i = \frac{1}{\sigma_i^2}$, $\sigma_i^2$ is the variance of observation $y_i$.

Expected weight factor,
$$R_{\exp} = 100\left[\frac{n-p}{\sum_{i=1,n}\omega_i y_i^2}\right]^{1/2} \quad (2.4)$$

Here $(n - p)$ is the number of degrees of freedom. $n$ is the total number of experimental points and $p$ is the number of refined parameters.

Reduced chi-square,
$$\chi^2 = \left[\frac{R_{wp}}{R_{\exp}}\right]^2 \quad (2.5)$$

Bragg factor,
$$R_B = 100\frac{\sum_h \left|I_{obs,h} - I_{calc,h}\right|}{\sum_h I_{obs,h}} \quad (2.6)$$

Here $h$ represents the particular hkl Bragg peak. The $I_{obs,h}$ is the observed integrated intensities and $I_{calc,h}$ is the calculated intensities.

Crystallographic $R_F$ factor,
$$R_F = 100\frac{\sum_h \left|F_{obs,h} - F_{calc,h}\right|}{\sum_h F_{obs,h}} \quad (2.7)$$

Here $F_{obs,h}$ and $F_{calc,h}$ are the observed and calculated structural factors, respectively.

Inter atomic distances (bond length) and bond angles were calculated using the refined fractional coordinates and lattice parameters by using Fullprof software.

## 2.2.2 Raman Spectroscopy

Raman scattering is a spectroscopic technique which is used to study the vibrational modes of molecules. Raman scattering was first observed experimentally by C. V. Raman in 1928 and for this discovery, he won the Nobel Prize in Physics in 1930.

The mechanism of Raman scattering is based on the change of the rotational or vibrational quantum states of molecules being illuminated. When a sample is irradiated with intense monochromatic light (energy $hv_0$), great majority of the scattering takes place with no

loss of energy and therefore no frequency change, this is known as elastic or Rayleigh scattering (Fig. 2.5). However, a very small fraction of incident photons transfer to or receive energy from the sample due to changes in the vibrational or rotational modes of sample molecules, causing a change in the energy and therefore the frequency of the scattered light. This inelastic scattering is known as Raman scattering. If $v_0$ is the frequency of the incident radiation and $v_s$ is that of the scattered light, then the Raman shift is defined as $\Delta v = v_0 - v_s$. If the incident photon gives up energy to the sample it is scattered with a red shifted frequency and referred to as stokes shift ($v_s < v_0$) (Fig. 2.5). If the molecule is already in an exited energy state, and gives energy to the scattered photon, the output has a blue-shifted frequency and is referred to as anti-stokes shift ($v_s > v_0$) (Fig. 2.5). Since the vibrational ground state is generally more populated than the excited states, stokes scattering intensities are generally higher than those of anti-Stokes. So, in most cases, the Raman scattering photons collected for analysis are the Stokes photons called stokes lines. However, it is the polarizability of the molecule during vibration which determines whether the Raman spectra will be observed or not. The molecule should be polarizable to different extents in different directions if it is to exhibit Raman scattering [166]. In a molecule having centre of symmetry, the asymmetric stretching and bending do not give rise to change in polarizability and hence such molecules are Raman inactive. While for symmetric stretching things will be just the opposite. However, for molecules without a center of symmetry, the vibrational mode could be either Raman active, infra-red active, both or neither.

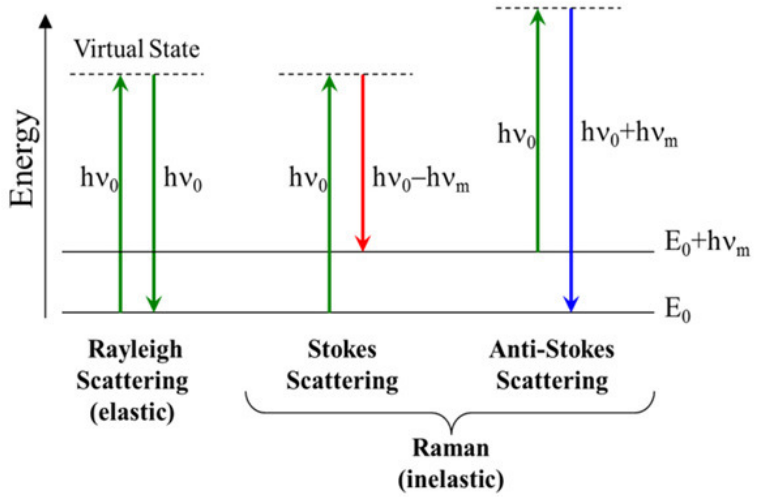


**Figure 2.5:** Diagram of Rayleigh and Raman scattering process.

The frequency shift or the Raman shift is a measure of the energy of the molecular vibrational modes. Hence, the Raman spectra provide valuable structural information about crystalline phases, strain, defect, distortion, *etc*. present in a material. Raman spectrometers for recording Raman spectra are based on one of two technologies: dispersive Raman and Fourier transform Raman. Fig. 2.6 shows a schematic diagram of dispersive Raman spectrometer. The HR800 is an integrated Raman system which is used for the study of Raman spectra of all the samples in the present thesis work. The microscope in this system is coupled confocally to an 800 mm focal length spectrograph equipped with two switchable gratings. The excitation photon generally can be supplied by using two sources namely He-Ne laser of 20 mW power (wavelength, $\lambda$ = 632.817 nm) and Argon laser ($\lambda$ = 488 nm and 514 nm). The laser beam from the source is totally reflected by the beam splitter, which splits the beam into two parts having equal wavelengths. When the beam was allowed to fall on the sample, both Rayleigh and Raman scattering occurs. The notch filter allows only the Raman scattered wavelength while it rejects the Rayleigh scattered wavelength. The inelastic scattered light was allowed to pass through the grating and etalon which in turn resolve the weak inelastic scattered wavelength coming from the sample more efficiently. Further the beam was allowed to enter into a charge couple device (CCD) where it detects the change in polarizability of the sample from the change in wave length and converts into the intensity. We could see intensity vs. wave number graph in the computer screen.

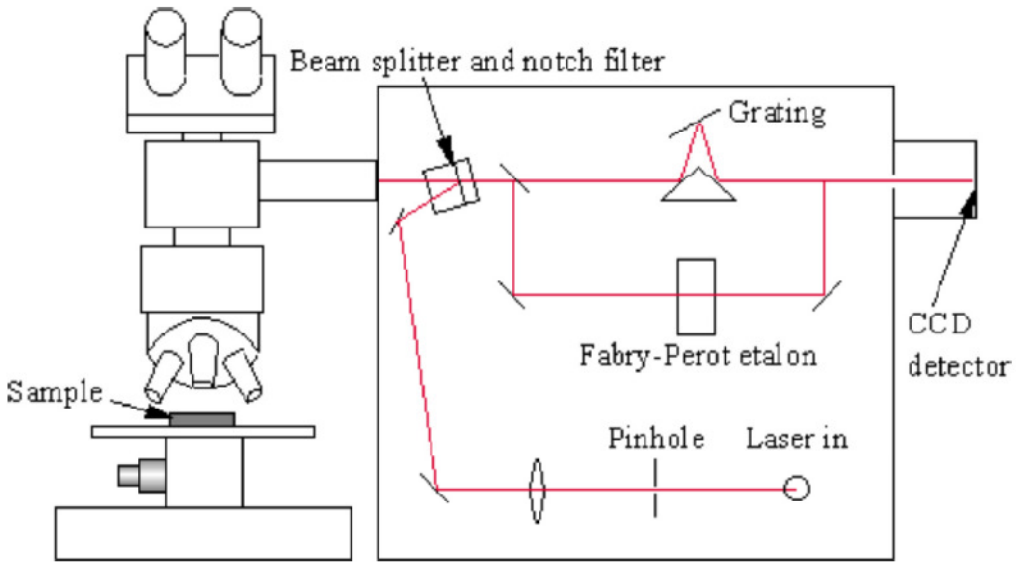


**Figure 2.6:** Schematic diagram of Raman spectrometer.

In the present thesis work, Raman spectra at room temperature were recorded using Horiba Jobin Yvon make Laser micro-Raman spectrometer of model LabRam HR800, in the wave number range of 100 to 1000 $cm^{-1}$ with excitation wavelength of 514 nm.

## 2.2.3 Field Emission Scanning Electron Microscope

Field emission scanning electron microscope (FESEM) is a scanning electron microscope (SEM) based technique which employs a beam of highly energetic electrons to study surface morphology, fractured components, foreign particles and residues, *etc.* on a very fine scale. There are two types of electron emission sources: thermionic emitter and field emitter. The type of electron emitter is the main difference between SEM and the FESEM. Thermionic emitters use electrical current to heat up a filament and when the heat is enough to overcome the work function of the filament material, the electrons can escape from the material. Thermionic sources have relatively low brightness, evaporation of cathode material and thermal drift during operation. Thermionic emitters are used in SEM. On the other hand, a Field emission (FE) source which is also called a cold cathode field emitter, does not heat the filament but it is placed in a huge electrical potential gradient to reach the electron emission. In FESEM such emitter is used and hence the name field emission SEM is adopted. FE avoids the problems of thermionic emitter while generating electrons.

The FE electron gun is basically a zirconium oxide coated tungsten ($ZrO_2$/W) emitter, which operates in a thermally assisted Schotky emission mode. This type of gun provides narrower probing beams as well as high electron energy, resulting in both improved spatial resolution and minimized sample charging and damage. In FESEM, electrons are liberated from the FE source under extreme vacuum and accelerated in a high electrical field gradient. The acceleration voltage between cathode (electron gun) and anode is commonly in the order of magnitude of 0.5 to 30 kV. The high vacuum allows the electrons to move along a column without scattering which helps to prevent discharges inside the instrument. Within the high vacuum column, these so-called primary electrons are focused and deflected by the electromagnetic lenses (Fig. 2.7) to produce a narrow scan beam that bombards the specimen. As a result of this bombardment different types of electrons are emitted from the specimen as shown in Fig. 2.8. Upon electron impingement on the surface, the interaction volume

assumes a tear shape. These dislodged electrons are known as secondary electrons. A high efficient annular in-lens ac-detector catches these secondary electrons and an image of the sample surface is constructed by comparing the intensity of these secondary electrons to the scanning primary electron beam. This process results in to image construction and this image is displayed on a monitor.

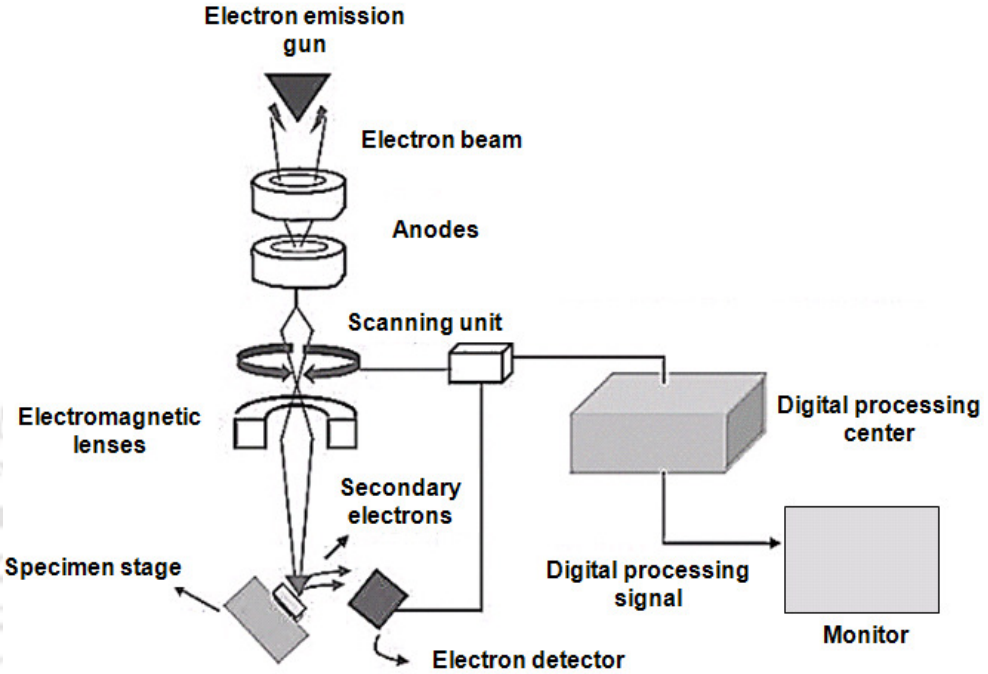


**Figure 2.7:** Schematic view of the FESEM.

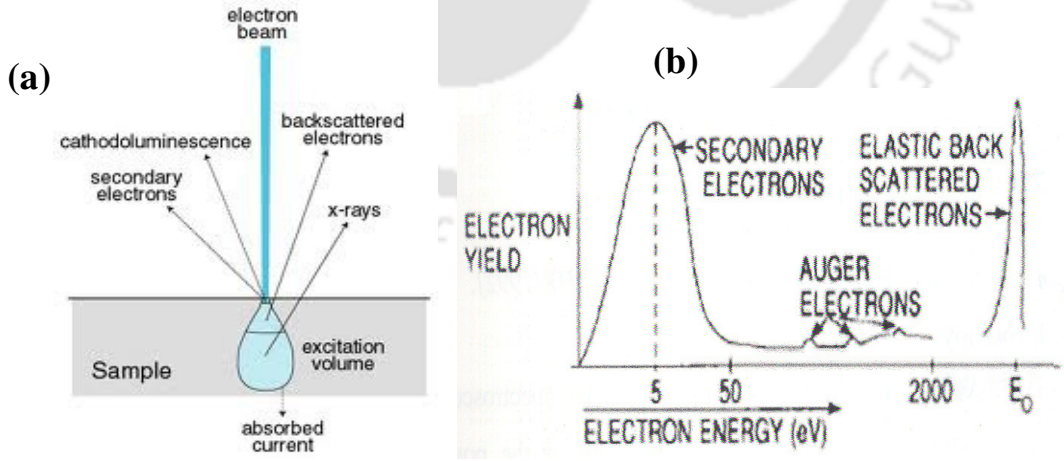


**Figure 2.8:** (a) Electrons and photons emanating from tear-shaped interaction volume during electron beam impingement on specimen surface, and (b) Energy spectrum of electrons emitted from the specimen surface.

Apart from secondary electrons, the back scattered electrons (BSE), characteristic X-rays, light (cathode-luminescence), specimen current and transmitted electrons are also emitted from the specimen surface. These types of signal require specialized detectors and all such detectors are not present in a single machine. The primary electron beam results in the emission of BSE from the specimen. BSE possess more energy than secondary electrons and have a definite direction. As such, they cannot be collected by a secondary electron detector, unless the detector is directly in their path of travel. All emissions above 50 eV are considered to be BSE. BSE imaging is useful in distinguishing one material from another, since the yield of the collected BSE increases monotonically with the specimen's atomic number $Z$ (~ 0.05 $Z^{1/2}$). Backscattered imaging can distinguish elements with atomic number difference of at least 3. In FESEM, one more detector, *i.e.*, solid state back scattered detector is used to detect the BSE.

The advantages of FESEM over SEM are as follows, (1) FESEM produces clearer, less electrostatically distorted images with spatial resolution down to 1 nm. That is 3 to 6 times better than conventional SEM; (2) smaller-area contamination spots can be examined at electron accelerating voltages compatible with Energy Dispersive X-ray Spectroscopy; (3) closer to the immediate material surface can be probed due to the reduced penetration of low kinetic energy electrons; (4) high quality, low voltage (0.5 to 30 kV) images are obtained with negligible electrical charging of samples.

In order to observe FESEM for objects, the sample should have electrically conducting. This can be done by coating them with an extremely thin layer (1.5 - 3.0 nm) of gold or carbon by using respective coater. In the present thesis work, the samples are insulating and hence were coated by gold to make electrically conducting. The surface morphology was then analyzed by ZEISS make FESEM (ΣIGMA).

## 2.2.4 Energy Dispersive X-ray Spectroscopic Technique

Energy dispersive X-ray spectroscopy (EDS) is an analytical technique used for the elemental analysis or chemical characterization of a sample. The equipment is attached to the FESEM to allow for elemental information to be gathered about the specimen under investigation. Its characterization capabilities originate from the fact that each element has a

unique atomic structure, which emits its unique characteristic X-ray. To stimulate the emission of characteristic X-rays from a specimen, a high energy beam of charged particles such as electrons or protons, or a beam of X-rays, is focused into the sample being studied. At rest, an atom within the sample contains ground state (or unexcited) electrons in discrete energy levels or electron shells bound to the nucleus. The incident beam may excite and eject an electron from an inner shell and it results in a hole or electron vacancy in the shell. An electron from an outer higher-energy shell then fills the hole, and the difference in energy between the higher-energy shell and the lower energy shell is released in the form of an X-ray. The atoms of every element releases X-rays with unique amounts of energy during the above process. Thus, by measuring the value of energy of X-rays being released by a specimen during electron beam bombardment, the identity of the atoms present in the specimen can be established. Thus, we get the EDS spectrum as an output and it is just a plot of how frequently an X-ray is received for each energy level. An EDS spectrum normally displays peaks corresponding to the energy levels for which the X-rays had been received. Each of these peaks is unique to an atom, and therefore corresponds to a single element. The intensity of the peaks depends on the concentration of the elements present.

In the present thesis work, EDS spectra of the samples were recorded by using ZEISS make FESEM (ΣIGMA) equipped with EDS facility.

## 2.2.5 Vibrating Sample Magnetometer

The vibrating sample magnetometer (VSM) has become a widely used instrument for measuring the magnetic properties of a large variety of magnetic materials. The VSM developed originally by Foner [167] has however, been the most successful for low/high temperature and high magnetic field studies of most of the magnetic materials. It has a flexible design and combines high sensitivity with ease of sample mounting and exchange. Samples can be changed rapidly even at any operating temperature. Using a VSM, one can measure the DC magnetic moment as a function of temperature, magnetic field and time. So, it allows performing susceptibility and magnetization studies. Magnetic moments as small as $5\times10^{-5}$ emu are measurable with a VSM [167].

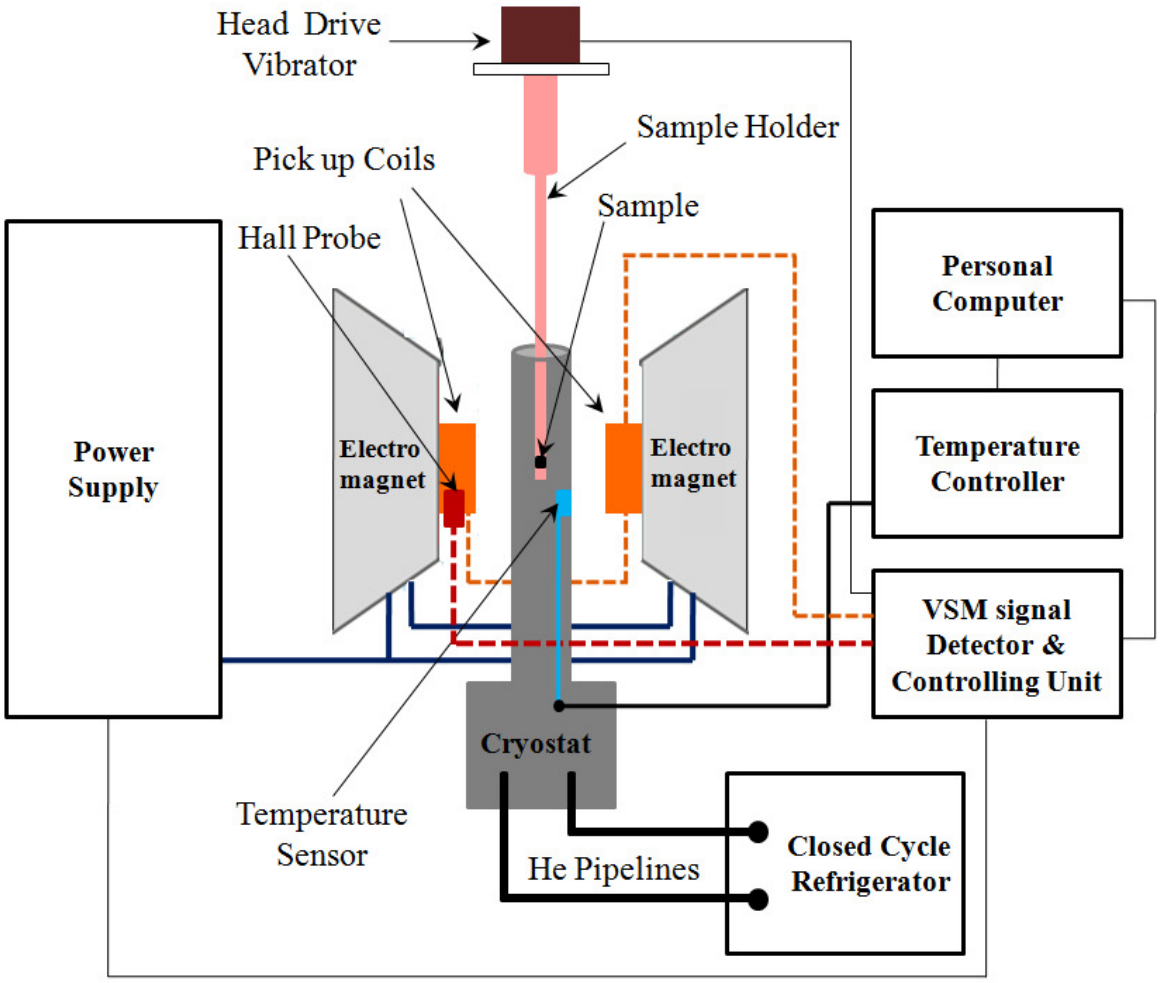


**Figure 2.9:** Block diagram of the VSM.

The VSM is based upon Faraday's law of induction, according to which an electromotive force (emf) is induced in a conductor or coil when there is a change in magnetic flux through the coil. A sample of any magnetic material is mounted on a long quartz rod such that the sample is positioned between the pole pieces of an electromagnet producing uniform magnetic field. As a result a dipole moment will be induced. If the sample vibrates with sinusoidal motion, *i.e.* up and down, with the help of a mechanical vibrator, there is some magnetic flux change. This induces a voltage in the pick-up coils mounted on the pole pieces of the electromagnet and this voltage is proportional to the magnetic moment of the sample. Voltage, $V(t)$ can be detected to a high resolution and accuracy by means of suitable VSM signal detector. Block diagram of the VSM is shown in Fig. 2.9 and, its important parts along with their functions are described below.

**(i) Water cooled electromagnet and power supply:**

A variable bipolar power supply gives power to the electromagnets. The electromagnets along with the power supply thus generate the constant external applied magnetic field which is used to magnetize the sample. Samples magnetization can be varied by changing the magnetic field produced by the electromagnet. The electromagnets and the power supply both are kept cool by circulating cold water using a water chiller so that they are not overheated due to the Jules heating in the coil and circuit components.

**(ii) Mechanical (head drive) vibrator and sample holder:**

The sample is mounted at the end of a long quartz rod, which is connected to the mechanical vibrator. The vibrator moves the sample up and down at a set frequency. The sample rod can be rotated to achieve the desired orientation of the sample to the constant magnetic field. There are also three knobs for controlling the x, y, and z positions of the sample.

For high temperature measurements, *i.e.* for measurements above room temperature, high temperature oven assembly with a ceramic sample holder is used. The sample is attached to the holder by using ceramic putty.

**(iii) Pick up coils:**

A pair of coils mounted in between the pole piece of the magnets picks up the induced emf due to the change in magnetic flux as a result of sample vibration. The emf induced in the pick up coils is proportional to the magnetic moment of the sampe.

**(iv) Hall probe:**

The magnetic field is measured by a Gauss-meter with analog output capabilities; its Hall probe is mounted between the magnetic pole pieces close to the sample position.

**(v) Lock in amplifier:**

The induced alternating voltage in the pick up coils is detected to a high resolution by means of a lock in amplifier and it gives a dc output which is proportional to the magnetic

moment. This amplifier is tuned to pick up only signals at the vibrating frequency. This eliminates noise from the environment.

**(vi) Computer interface:**

Various components of the instrument are interfaced to a personal computer so that they can be controlled easily by the software. Using the controlling and monitoring software, the system can tell how much the sample is magnetized and how its magnetization depends on the strength of the constant magnetic field. The data can be graphed and plotted on the computer.

**(vii) Temperature controller:**

For the temperature variation of magnetic measurements, both below and above the room temperature, a suitable temperature controller is used to control the temperature. A proportional, integral and derivative (PID) temperature controller facilitates temperature control over the range 20 K < T < 300 K and 300 K < T < 1273 K. The accuracy of the measured temperature is ± 0.01 K. The temperature was stabilized within ± 0.5 K. The temperature controller takes an input from a temperature sensor and has an output that is connected to a control element, *i.e.* a heater. The cooling is done with the help of a closed cycle Helium refrigerator cryostat.

**(Viii) Closed cycle Helium Refrigerator:**

Closed cycle Helium refrigerator cryostat along with a temperature controller is used to vary the temperature down to 20 K. The sample chamber is connected thermally to the cold head motor. The cold head motor is connected to Helium compressor. For a good thermal contact and temperature uniformity over the sample, dry Helium gas is allowed to continuously flow into the sample chamber. The temperature variation is achieved by using a heater wire connected to the temperature controller. The temperature is measured using a cernex sensor.

**(ix) High temperature oven:**

For high temperature measurements, the cryostat is replaced by a high temperature oven as shown in Fig. 2.10, with suitable temperature controller to vary the temperature. A heater is located inside the oven and the temperature is controlled by the temperature controller in the VSM control panel. During measurement, the oven was purged with Nitrogen/Argon gas to avoid oxidation of the samples at high temperature to avoid overheating of the flanges and for uniform temperature in the entire sample region. Temperature is measured using a type K thermocouple attached to the oven.

**Figure 2.10:** High temperature oven.

In the present thesis work, the temperature variations of zero field cooled (ZFC) and field cooled (FC) dc magnetization (*M*–*T*) and the hysteresis loops (*M*–*H*) were measured by using the Lakeshore make VSM of model no. 7410. In Lakeshore make VSM, the mechanical vibrator vibrates the sample at a frequency of 80 Hz. Before performing all the magnetic measurements, calibration was carried out by measuring the magnetic moment of standard Ni sphere sample. The measurement sequence is programmed as per the users'

choice using the software IDEASVSM, provided with the instrument. The temperature variation down to 25 K was achieved using an OXFORD make closed cycle refrigerator (CCR) cryostat (model M125) along with the temperature controller. The magnetic field was produced by using a $10^{//}$ electromagnet. The magnetization loop was measured by varying the magnetic field ($H$) up to 1.5 T. A high temperature oven with suitable temperature controller as described above is used to vary the temperature from room temperature to 1000 K.

# Chapter 3

# $Ni(Cr, Fe)_2O_4$ Series

## 3.1 Introduction

As discussed in the first chapter, $NiCr_2O_4$ is a normal spinel oxide having interesting structural, magnetic, magnetoelastic and magnetoelectric properties [22, 123, 126]. It undergoes a Jahn-Teller distortion (JTD) induced structural transition from cubic (space group $Fd\bar{3}m$) at above 320 K to tetragonal (space group $I4_1/amd$) structure at $T < 320$ K [11, 18]. $NiCr_2O_4$ consists of two magnetic sublattices at tetrahedral (A-site) and octahedral (B-site) positions with $Ni^{2+}$ ($e_g^4 t_{2g}^4$) ions occupying the A-site and $Cr^{3+}$ ($t_{2g}^3 e_g^0$) ions in the B-site. Two A sites in $NiCr_2O_4$ are grouped into a single sublattice and four B sites are grouped into two sublattices with each sublattice having both longitudinal and transverse components of magnetic moment [54]. Therefore, $NiCr_2O_4$ undergoes a ferrimagnetic (FIM) transition at 75 K and also an antiferromagnetic (AFM) transition at 29 K [18]. Due to the existence of different sublattice sites, substitution of other transition elements in this system may give rise to quite complicated cation distribution which may influence its structural property. Moreover, the magnetic properties of $NiCr_2O_4$ are very sensitive to the Ni – O – Cr and Cr – O – Cr superexchange interactions; therefore substitution of other cations on either Ni or Cr sites may affect its magnetic properties. The $Fe^{3+}$ ($3d^5$) ions possess stronger magnetic moment of 5 $\mu_B$ compared to 3 $\mu_B$ of $Cr^{3+}$ ($3d^3$) ions. Substitution of Fe in Cr site therefore may enhance the magnetization of the system. Strengthening of the superexchange interactions and hence increase in the magnetic transition temperature can also be expected. Further, due to complicated magnetic structure of $NiCr_2O_4$ it exhibits interesting exchange bias (EB) property. Even though EB is reported earlier by a few authors in some composite

and nanoparticles of $NiCr_2O_4$ based compounds [100, 132-134], to our knowledge no systematic study with temperature is available for the bulk system of both pristine and Fe doped $NiCr_2O_4$ systems. However, it is also interesting to study the possibility of enhancing the value of EB field by Fe doping. Moreover, different site preferences of the substituted Fe ions may also lead to a composition dependent magnetization reversal (MR) phenomenon. Recently Zhang *et al.* [27] have reported composition dependent MR in Mn doped $CoCr_2O_4$ system. According to our knowledge, there was no attempt on the study of MR phenomenon of Fe doped $NiCr_2O_4$ series.

This chapter deals with the preparation of $Ni(Cr_{1-x}Fe_x)_2O_4$ samples for $x = 0 – 0.60$ and the study of their structural; temperature, time and magnetic field dependent magnetization, EB and MR properties. Detailed analysis of these parameters is presented.

Polycrystalline samples of $Ni(Cr_{1-x}Fe_x)_2O_4$ for $x = 0 – 0.60$ were prepared by using the standard sol–gel method, which was discussed in Chapter 2. Stoichiometric ratio of high purity $Ni(NO_3)_2.6H_2O$ (99%), $Fe(NO_3)_3.9H_2O$ (99%) and $Cr(NO_3)_3.9H_2O$ (99%) were taken as the starting materials. The precursor powder obtained from sol-gel process was grinded and presintered at 600 °C, 800 °C and 1000 °C for 12 hours each. Final sintering was carried out at 1100 °C in pellet form for 24 hours. X-ray diffraction (XRD) patterns at room temperature were recorded by using Rigaku make TTRAX III X-ray diffractometer using Cu-Kα (λ = 1.54056 Å) radiation. Microstructure and composition analysis were carried out by using ZEISS make field emission scanning electron microscope (FESEM, ΣIGMA) equipped with energy dispersive X-ray spectroscopy (EDS) facility. Temperature and field dependent magnetization measurements were performed by using a Lakeshore make vibrating sample magnetometer (VSM) of model no. 7410 and Quantum Design made 9 Tesla physical property measurement system (PPMS) – VSM.

## 3.2 Structural Properties

The XRD patterns recorded at room temperature show that the parent and all the Fe doped $NiCr_2O_4$ samples are in single phase form. Fig. 3.1 shows the XRD patterns for $x = 0 – 0.50$ samples. A structural transition is clearly observed even for 2 atomic % of Fe substitution. To further confirm the phase purity and to obtain other structural information of

the samples, Rietveld refinement has been carried out on the XRD patterns of all the samples using Fullprof software. Rietveld analysis reveal that these compounds are in single phase form and the $x = 0$ sample crystallizes in tetragonal structure with $I4_1/amd$ space group while all the Fe doped samples crystallize in cubic structure with $Fd\bar{3}m$ space group. Typical XRD patterns along with Rietveld refinement for $x = 0$ and $x = 0.02$ samples are shown in Fig. 3.2 and the patterns for $x = 0.20$ and $x = 0.50$ samples are shown in Fig. 3.3. For $x = 0$, the lattice parameters are found to be $a = b = 5.828$ Å and $c = 8.415$ Å which are in good agreement with that reported earlier [17, 133]. The lattice parameters, reliability factors and unit cell volume of all the samples at room temperature are given in table 3.1. It is found that the substitution of Fe in $NiCr_2O_4$ drives the system into cubic from tetragonal structure at room temperature even with 2 atomic % of Fe substitution. Since in $NiCr_2O_4$, the tetragonal distortion occurs very close to the room temperature (320 K) as compared to other spinel chromites (*e.g.* for $CuCr_2O_4$ it is 853 K [19]), small amount of Fe may influence its crystal structure. Suppression of the tetragonal distortion therefore may be due to the occupation of some of the doped $Fe^{3+}$ ions at A site rather than occupying only the B site because $Fe^{3+}$ ions have low octahedral site preference energy (OSPE). Such substitution would reduce JTD as $Fe^{3+}$ ions at A site are not Jahn-Teller active and thus stabilize the cubic structure. As a result of above substitution, equivalent amount of $Ni^{2+}$ ions are expected to occupy B sites. This argument is further supported by the observed decrease in the lattice parameter of Fe doped samples with increase in Fe concentration. The ionic radius of $Cr^{3+}$ (oct) = 0.615 Å, $Fe^{3+}$ (oct) = 0.645 Å, $Fe^{3+}$ (tet) = 0.49 Å, $Ni^{2+}$ (tet) = 0.55 Å and $Ni^{2+}$ (oct) = 0.655 Å [137]. The size reduction due to $Fe^{3+}$ substitution at A site in place of $Ni^{2+}$ is quite dominant compared to the expected increase in size due to $Fe^{3+}$ substitution at B site in place of $Cr^{3+}$; so a net reduction in lattice constant is observed. In the above arrangement of ions no charge imbalance is expected in the compound. However, we could not quantitatively estimate the site occupation of doped Fe ions in A site due to comparable X-ray scattering factors of Ni, Cr and Fe. In the refinement of XRD patterns, the occupation factor of Fe was refined by taking its atomic position in the B site (Cr site).

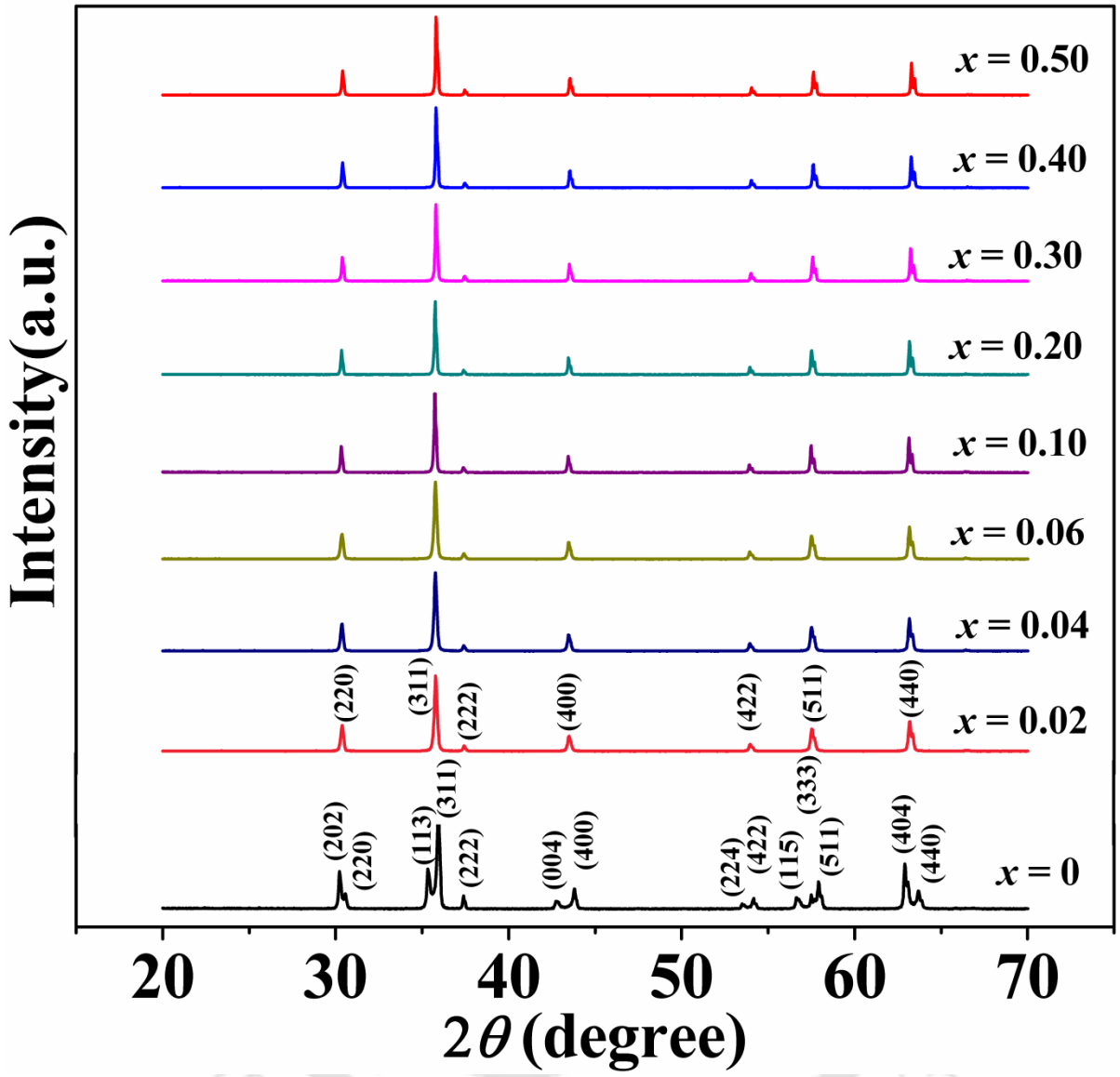


**Figure 3.1:** XRD patterns of Ni($Cr_{1-x}Fe_x$)$_2$O$_4$ compounds for $x$ = 0 – 0.50.

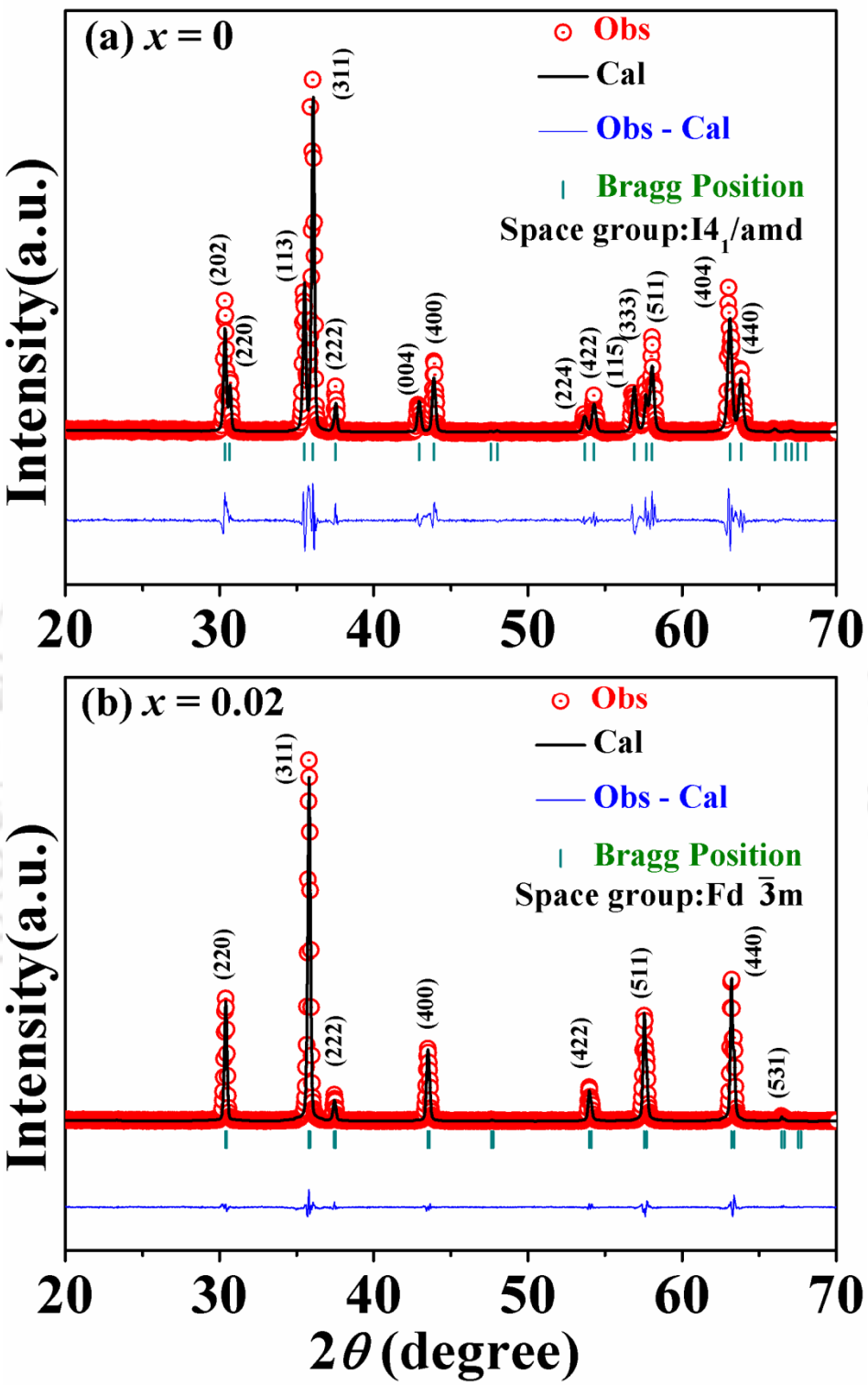


**Figure 3.2:** Rietveld refinement of the XRD patterns of (a) $x$ = 0 and (b) $x$ = 0.02 samples. The red open circles are the experimental data and the black solid lines are the fitted data. The bottom line shows the difference between experimental and refined data.

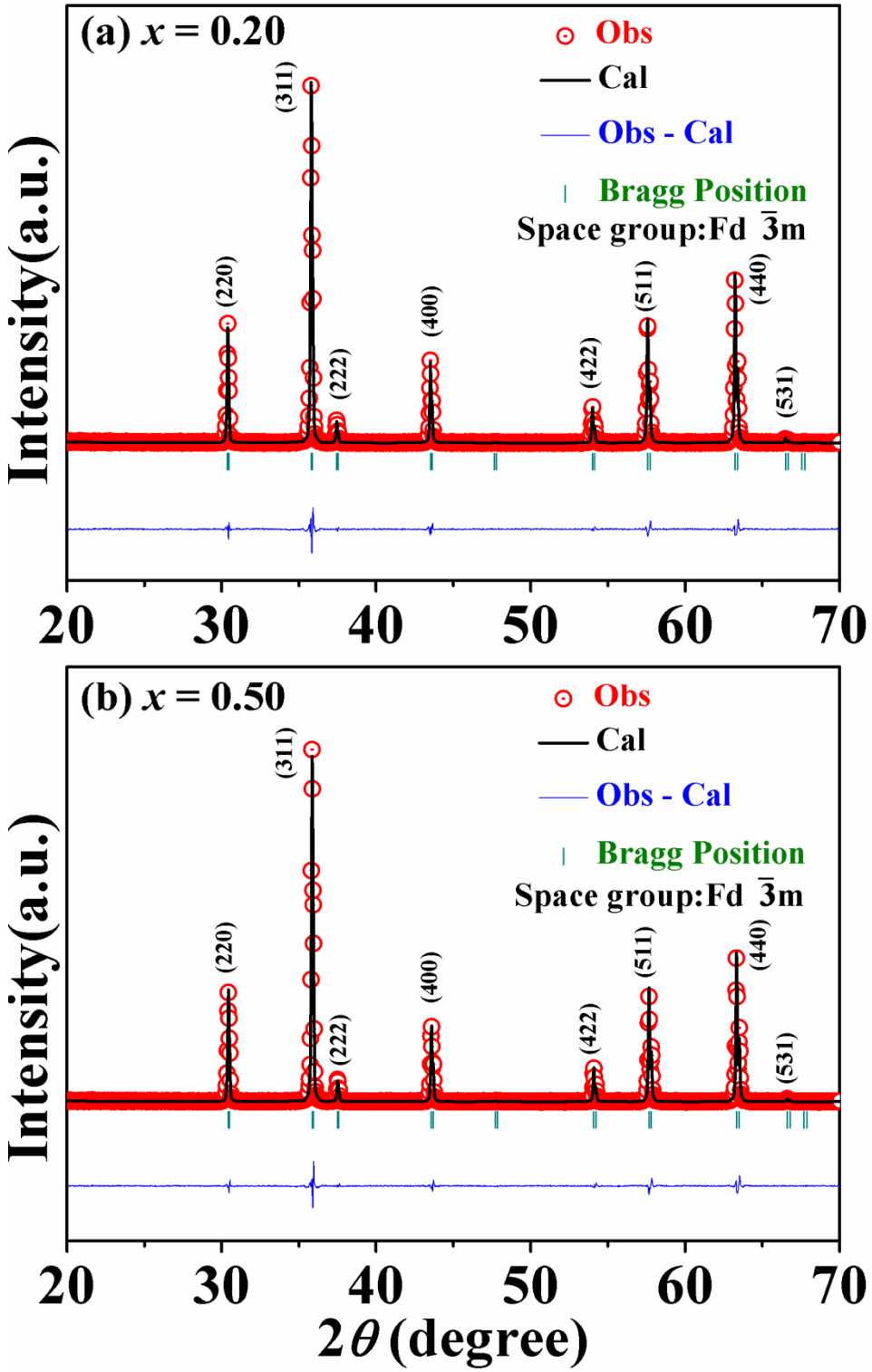


**Figure 3.3** Rietveld refinement of the XRD patterns of (a) $x = 0.20$ and (b) $x = 0.50$ samples. The red open circles are the experimental data and the black solid lines are the fitted data. The bottom line shows the difference between experimental and refined data.

**Table 3.1:** Parameters obtained from the Rietveld analysis of XRD patterns for the samples $Ni(Cr_{1-x}Fe_x)_2O_4$ (0 – 0.50). $R_F$, $R_{Bragg}$, $R_P$ and $\chi^2$ are the reliability factors.

| **Sample/ Parameters** | ***x* = 0** | ***x* = 0.02** | ***x* = 0.04** | ***x* = 0.06** | ***x* = 0.10** | ***x* = 0.20** | ***x* = 0.30** | ***x* = 0.40** | ***x* = 0.50** |
|---|---|---|---|---|---|---|---|---|---|
| **Space group** | $I4_1/amd$ | $Fd\bar{3}m$ | $Fd\bar{3}m$ | $Fd\bar{3}m$ | $Fd\bar{3}m$ | $Fd\bar{3}m$ | $Fd\bar{3}m$ | $Fd\bar{3}m$ | $Fd\bar{3}m$ |
| ***a* (Å)** | 5.8285 (0.0010) | 8.3166 (0.0008) | 8.3156 (0.0007) | 8.3154 (0.0007) | 8.3142 (0.0007) | 8.3104 (0.0007) | 8.3069 (0.0008) | 8.3012 (0.0007) | 8.2983 (0.0007) |
| ***c* (Å)** | 8.4156 (0.0015) | – | – | – | – | – | – | – | – |
| ***Volume* (Å$^3$)** | 285.89 (0.09) | 575.22 (0.01) | 575.02 (0.09) | 574.97 (0.09) | 574.73 (0.08) | 573.94 (0.09) | 573.21 (0.09) | 572.03 (0.08) | 571.43 (0.08) |
| **$R_F$ (%)** | 4.47 | 1.71 | 2.33 | 1.73 | 2.42 | 3.00 | 1.94 | 2.68 | 2.73 |
| **$R_{Bragg}$ (%)** | 6.25 | 1.50 | 1.66 | 1.45 | 2.70 | 3.00 | 2.39 | 3.22 | 3.04 |
| **$R_P$ (%)** | 16.7 | 7.40 | 6.82 | 6.71 | 9.43 | 8.09 | 7.68 | 7.97 | 7.93 |
| **$\chi^2$** | 7.75 | 5.82 | 5.28 | 5.13 | 4.00 | 4.97 | 4.15 | 5.51 | 6.07 |
| **Ni/Cr/Fe Occupancy** | 0.959 /2.005 /0.000 | 1.002 /1.960 /0.040 | 1.004 / 1.920 / 0.080 | 1.004 / 1.880 / 0.120 | 1.001 /1.801 /0.200 | 0.999 /1.600 /0.400 | 1.001 /1.400 /0.601 | 0.998 /1.196 /0.798 | 0.999 /1.001 /0.999 |

The typical microstructural images for $x$ = 0, 0.20 and 0.50 samples are shown in Fig. 3.4 along with the EDS spectrum (right column of the Fig. 3.4). The grain sizes of the samples were determined by using ImageJ software. The grain sizes of the samples are found to be distributed in a wide range. The grain size distribution for $x$ = 0, 0.06, 0.20, and 0.50 samples are shown in Fig. 3.5. The average grain size of each sample is obtained by fitting the size distribution histogram to log normal distribution function [168],

$$f(d,\mu,\sigma) = \frac{1}{d\sigma\sqrt{2\pi}} \exp\left(-\frac{(\ln d - \mu)^2}{2\sigma^2}\right) \qquad (3.1)$$

Where, $d$ is the cross-sectional length of the particle, $\mu$ is the logarithmic mean and $\sigma$ represents the standard deviation. The average grain size of the samples is found to be in the

range of 270 – 630 nm with a standard deviation in the range of 0.16 to 0.23 nm. However, the crystallite size ($D$) estimated from the XRD analysis as per Scherrer formula ($D = K\lambda/\beta\cos\theta$) is found to be in the range of 37 to 82 nm. This variation could be attributed to the agglomeration of several crystallites into particle. The chemical composition obtained as per the EDS analysis is found to be comparable to the nominal starting composition. The cationic ratios for $x$ = 0, 0.06, 0.20 and 0.50 samples are given in table 3.2.

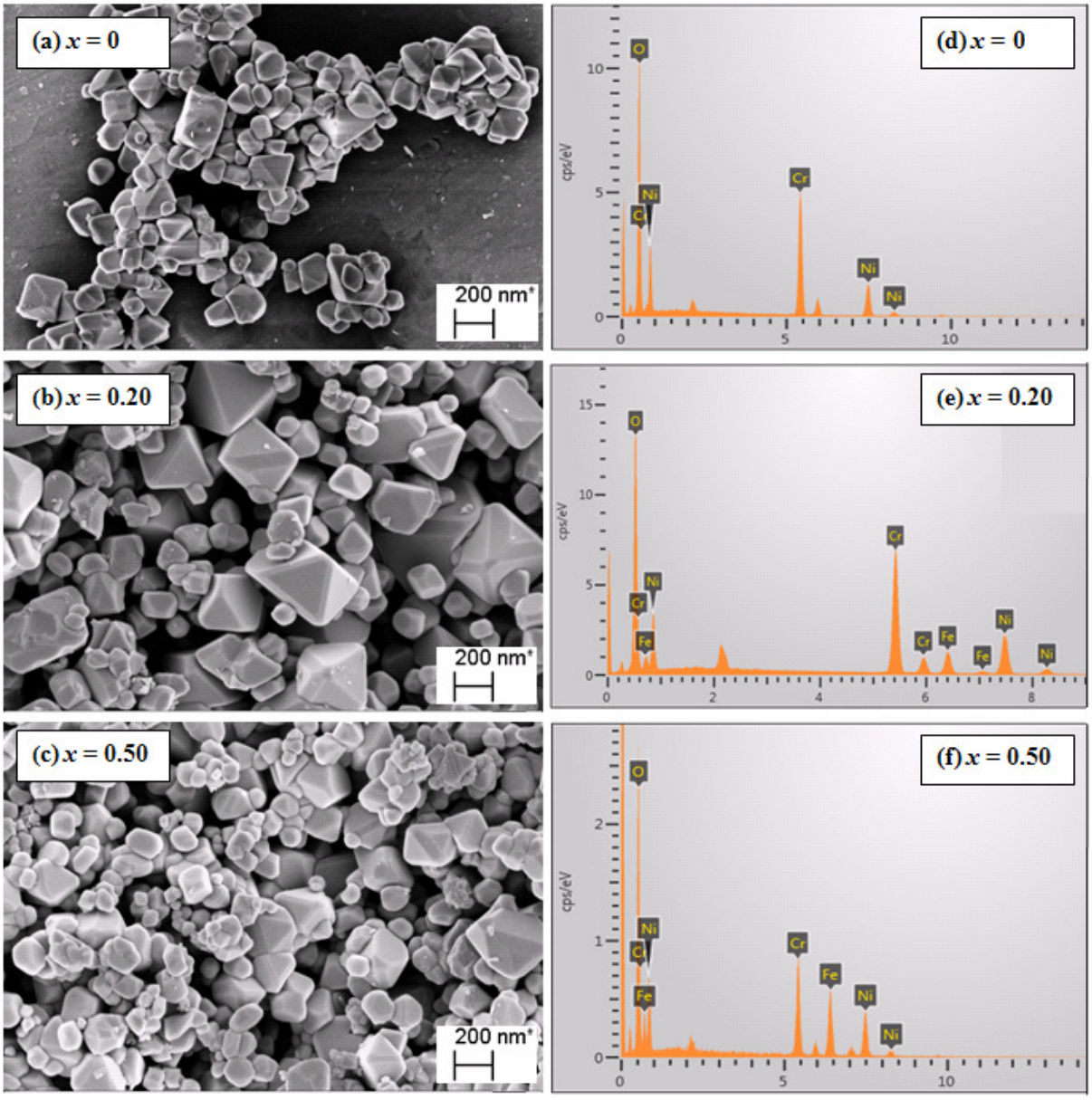


**Figure 3.4:** FESEM images recorded for (a) $x$ = 0, (b) $x$ = 0.20 and (c) $x$ = 0.50 samples along with EDS spectrum [(d), (e) and (f), respectively].

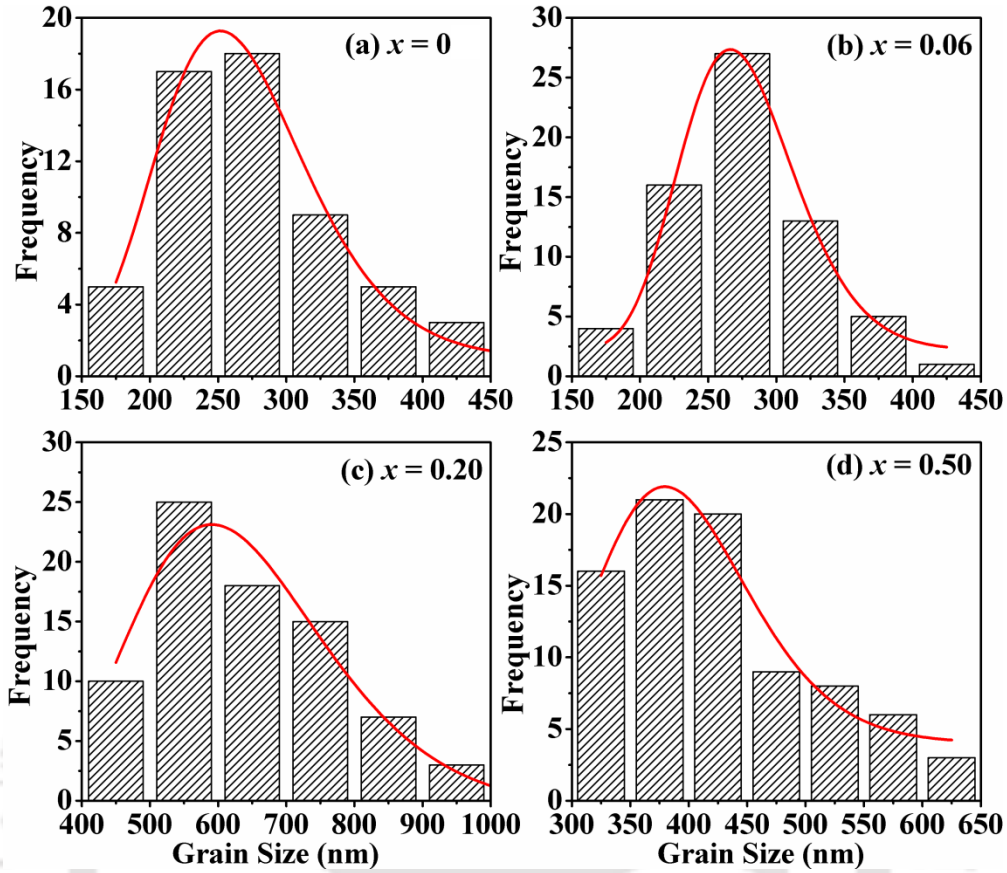


**Figure 3.5:** Grain size distribution of (a) $x$ = 0, (b) $x$ = 0.06, (c) $x$ = 0.20 and (d) $x$ = 0.50 samples.

**Table 3.2:** The cationic ratio determined from EDS analysis for $x$ = 0, 0.06, 0.20 and 0.50 samples.

| Samples | Calculated Cationic Ratio from EDS Analysis | | |
|---|---|---|---|
| | Ni | Cr | Fe |
| ***x* = 0** | 1.00 | 1.98 | 0.00 |
| ***x* = 0.06** | 0.95 | 1.90 | 0.13 |
| ***x* = 0.20** | 1.00 | 1.61 | 0.38 |
| ***x* = 0.50** | 0.97 | 1.01 | 0.99 |

## 3.3 Temperature and Field Dependent Magnetic Properties

Temperature dependent dc magnetization (*M–T*) of all Ni($Cr_{1-x}Fe_x$)$_2$O$_4$ samples was measured under zero field cooled (ZFC) and field cooled (FC) conditions for an applied field of *H* = 200 Oe. In ZFC condition the sample is initially cooled in zero field from 300 K to 25 K and then the data were recorded during warming by applying 200 Oe field. In FC condition, the sample is cooled to 25 K in a field of 200 Oe and then the data were recorded during warming keeping the field constant. Fig. 3.6 shows the *M–T* plots for $x = 0 - 0.50$ samples. The *M–T* plot under ZFC condition for each sample shows a peak highlighting the FIM transition. The transition temperature ($T_C$) of $x = 0$ sample determined from *dM/dT* versus *T* plot is found to be 73 K and it is found to increase quite sharply with increase in Fe concentration which is clear from the *M–T* plots shown in Fig. 3.6. Even for 2 atomic % of Fe substitution, $T_C$ is found to increase drastically to 101 K and it shifts beyond room temperature for $x = 0.20$ ($T_C$ = 314 K). It highlights that substituted Fe ions with higher magnetic moment of 5 $\mu_B$ are strengthening the superexchange interactions in the system. Strong irreversibility is observed at $T < T_C$ due to the presence of competing AFM interactions.

The ZFC magnetization value at 30 K is found to decrease slightly with increase in Fe concentration up to $x = 0.06$ and for further increase in Fe concentration it increases. Fig. 3.7 shows the ZFC magnetization plots for all the samples in expanded scale. As discussed in Chapter 1, the total magnetization per formula unit of $NiCr_2O_4$ can be written as

$$\mu = | \uparrow \mu_{A1\text{-}A2} + \uparrow \mu_{B1\text{-}B3} - \downarrow \mu_{B2\text{-}B4} | \qquad (3.2)$$

where, $\uparrow \mu_{A1\text{-}A2}$, $\uparrow \mu_{B1\text{-}B3}$ and $\downarrow \mu_{B2\text{-}B4}$ are the longitudinal components of the magnetic moments of A1-A2, B1-B3 and B2-B4 sublattices, respectively along the field direction [54]. Thus the initial decrease in magnitude of magnetization with increase in Fe concentration can be attributed to the Fe ions occupying only the B2-B4 site of the B site. For $x > 0.06$, comparatively more Fe ions may occupy the A sites thereby increasing the net magnetization. The FC magnetization also shows similar behavior as that of ZFC magnetization plots but

with larger magnetization at a given temperature. However for $x$ = 0.06, a sign reversal of magnetization is observed. When the temperature is varied, below $T_C$ the magnetization of this sample increases and attain a maximum value. Then it decreases to zero at a particular temperature called the compensation temperature ($T_{comp}$), below which negative magnetization is observed. The samples for $x$ = 0.30, 0.40 and 0.50 show similar behavior but with larger $T_{comp}$ even above room temperature. The phenomenon of MR will be explained in details in section 3.4.

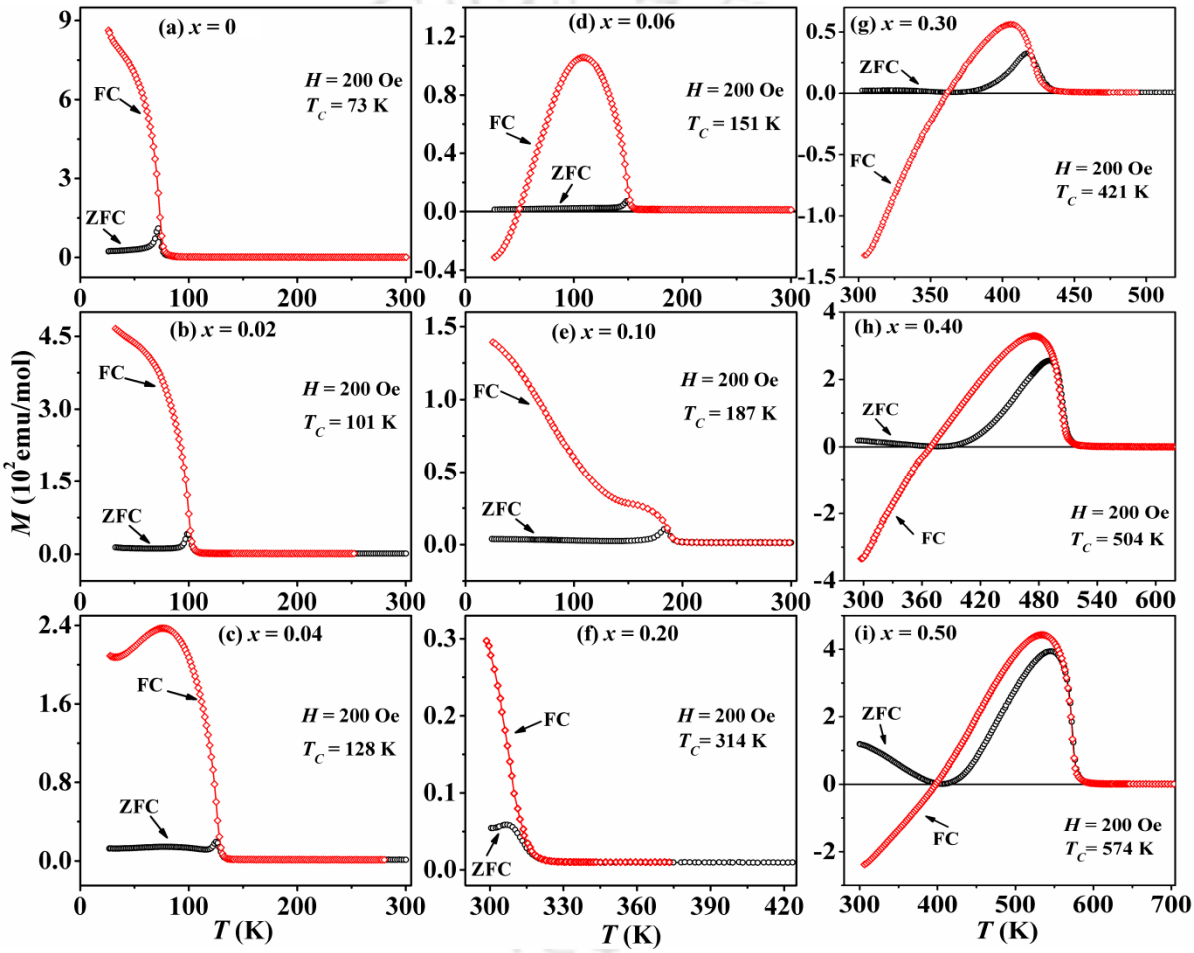


**Figure 3.6:** Temperature dependent magnetization of Ni(Cr$_{1-x}$Fe$_x$)$_2$O$_4$ ($x$ = 0 – 0.50) samples under ZFC and FC conditions.

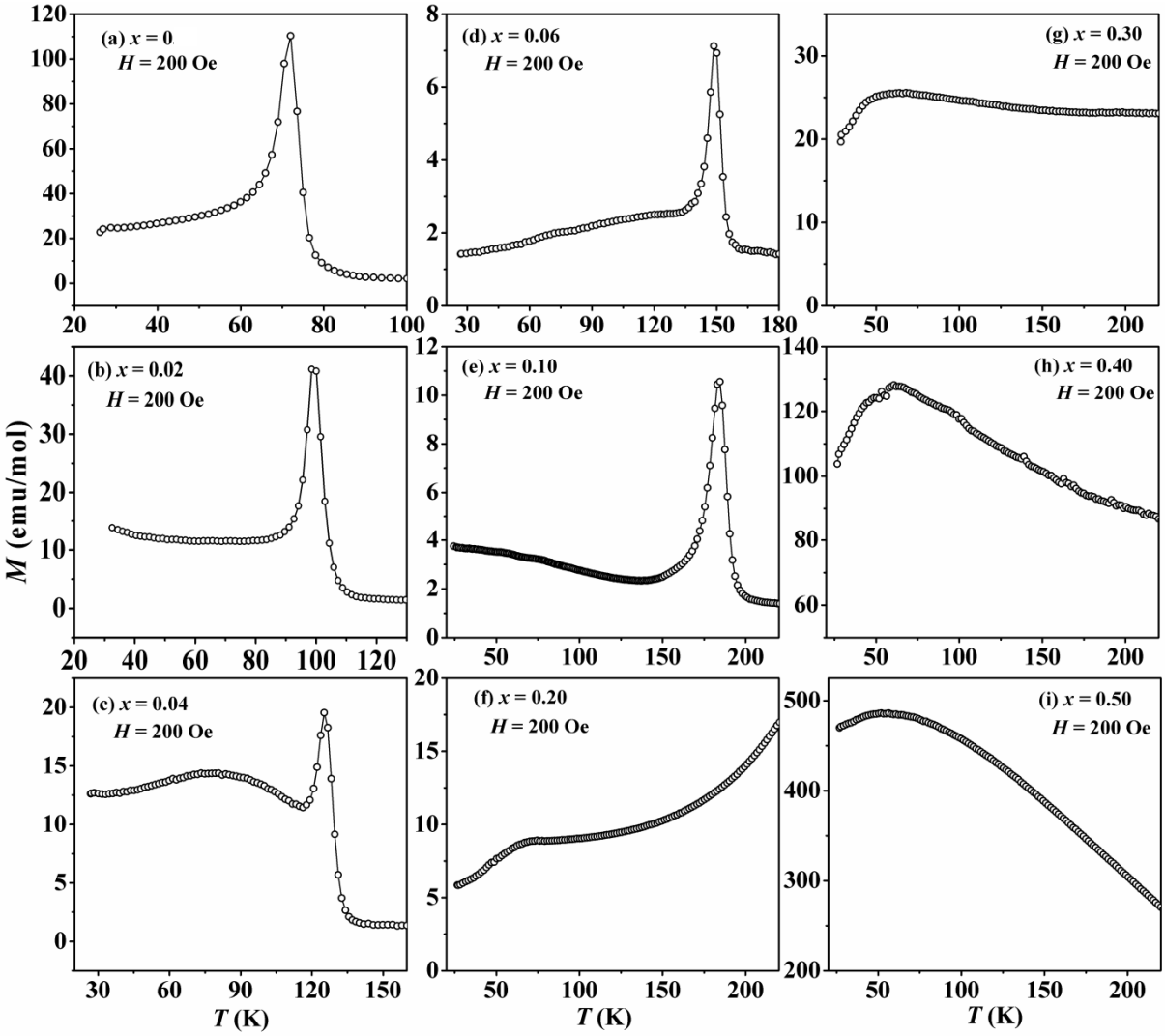


**Figure 3.7:** Temperature dependent magnetization of $Ni(Cr_{1-x}Fe_x)_2O_4$ ($x$ = 0 – 0.50) samples under ZFC condition in expanded scales.

The field dependent magnetization ($M$–$H$) loops for $Ni(Cr_{1-x}Fe_x)_2O_4$ recorded at 45 K are shown in Fig. 3.8. Large coercivity is observed for $x$ = 0 and 0.02 samples which can be attributed to the presence of competing AFM in addition to the existing long range FIM interaction. On the other hand for the intermediate compositions, *i.e.* $x$ = 0.04 to 0.10, almost linear loop is observed due to the dominant AFM interaction which completely overtakes the FIM [86, 100]. For these samples, FIM $T_C$ is quite large (> 128 K) and far away from 45 K**.** However in the vicinity of FIM $T_C$, these samples also exhibit FIM behavior with considerable coercive field comparable to that of $x$ = 0 sample. Fig. 3.9 shows the $M$–$H$ loops

of each sample at a temperature just below its FIM $T_C$. For further increase in Fe concentration, *i.e.* for $x \geq 0.20$, large coercivity and increase in magnetization value is observed at 45 K itself due to stronger FIM interaction through considerable concentration of $Fe^{3+} - O^{2-} - Fe^{3+}$ networks [169]. But the coercivity again decreases gradually for $x = 0.40$ and 0.50. With increase in Fe concentration, the magnetic structure of $Ni(Cr_{1-x}Fe_x)_2O_4$ is expected to be more close to $NiFe_2O_4$ which is a soft magnetic material and thus leads to decrease in coercivity. As discussed from ZFC *M–T* measurements, similar trend is also observed from *M–H* loop measurement; the magnitude of magnetization at the field of 15 kOe decreases with increase in Fe concentration up to $x = 0.06$ and thereafter it starts increasing with further increase in Fe concentration.

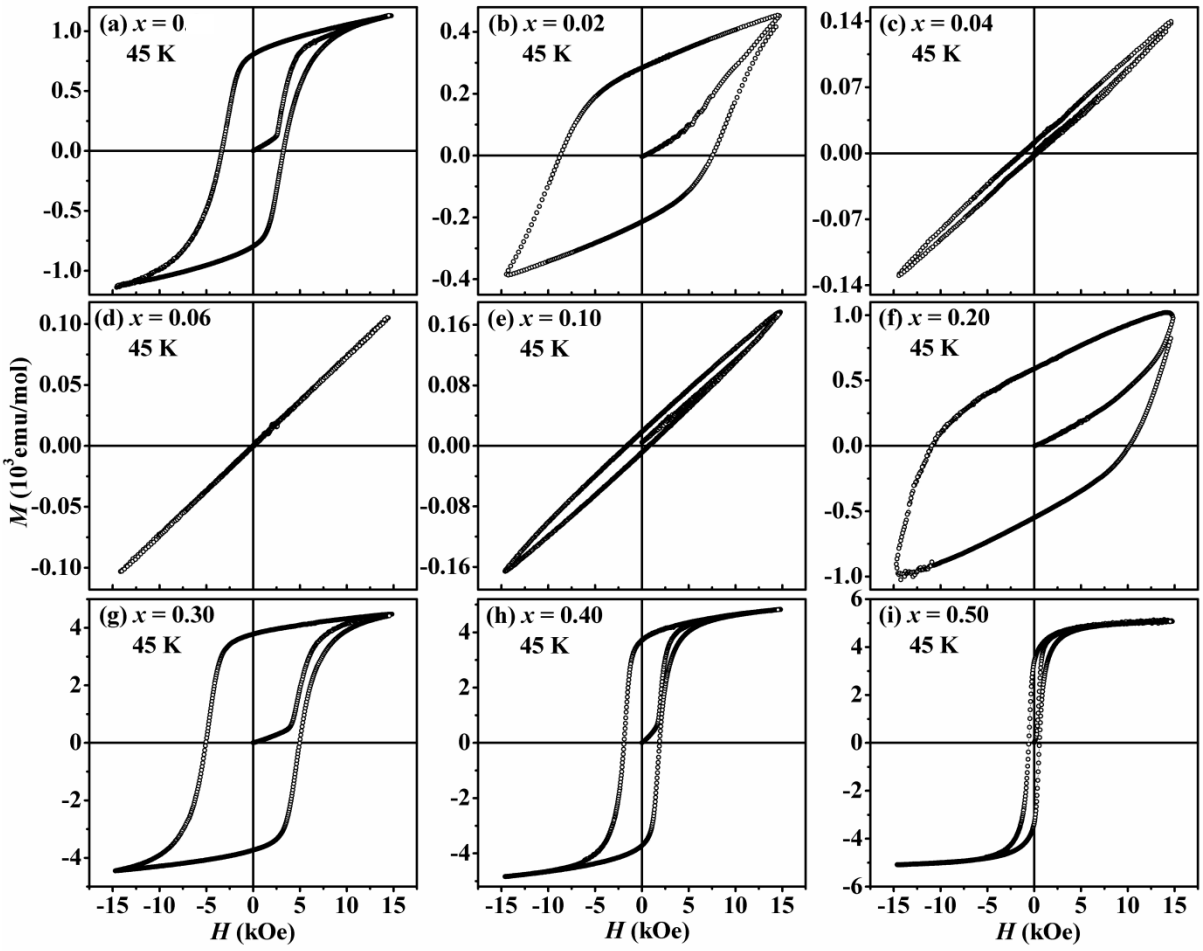


**Figure 3.8:** *M–H* loops of $Ni(Cr_{1-x}Fe_x)_2O_4$ ($x = 0 – 0.50$) samples measured at 45 K after cooling the samples under zero field condition.

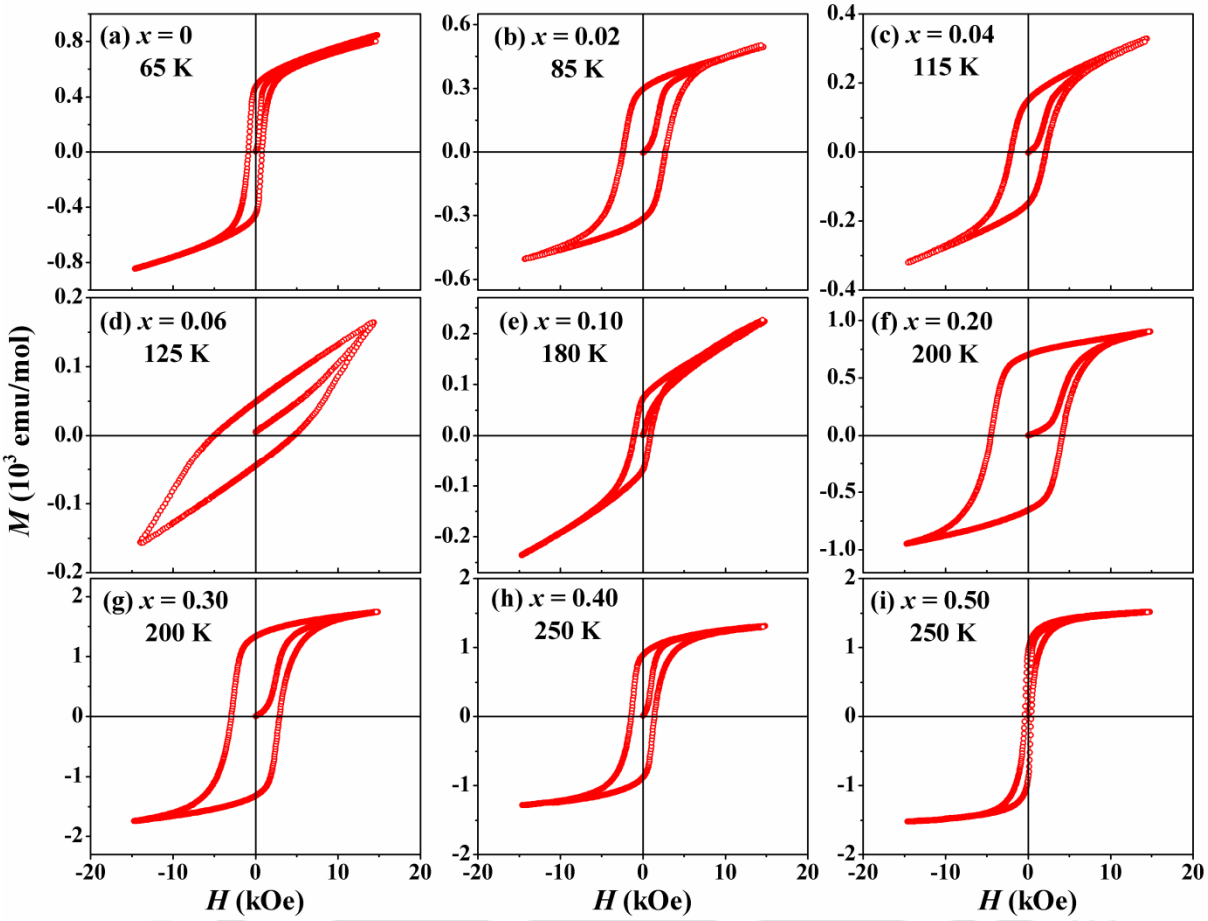


**Figure 3.9:** *M–H* loops of Ni(Cr$_{1-x}$Fe$_x$)$_2$O$_4$ ($x$ = 0 – 0.50) samples measured at a temperature just below their respective FIM $T_C$.

## 3.4 Magnetization Reversal

Temperature induced MR is observed for $x$ = 0.06, 0.30, 0.40 and 0.50 samples. Fig. 3.10 shows separately the FC *M–T* plots of these samples under an applied field of 200 Oe. The magnetic compensation temperature, $T_{comp}$ of $x$ = 0.06 sample is found to be 49 K. This $T_{comp}$ value is larger and near to room temperature for $x$ = 0.30, 0.40 and 0.50 samples due to the increase in corresponding $T_C$ which are found to be 358 K, 366 K and 396 K, respectively. In order to understand the magnetization behavior of these samples exhibiting magnetization reversal, we have carried out *M–T* measurements at different applied fields ranging from 200 to 4000 Oe. Increase in the applied magnetic field results in slight decrease of $T_{comp}$ value and finally for a particular applied field MR disappears and the magnetization

remains positive in all temperature range as depicted in Fig. 3.11. The $T_{comp}$ value is found to decrease from 49 K for $H$ = 200 Oe to 38 K for $H$ = 4000 Oe for $x$ = 0.06 sample. However, for $x$ = 0.30 and 0.40 samples the MR vanishes for $H \geq$ 2000 Oe and for $x$ = 0.50 it vanishes at $H \geq$ 500 Oe. The trend of $M$–$T$ curves remains same even for $H$ = 4000 Oe in case of $x$ = 0.06 sample. It suggests that no major change in the mechanism of magnetic interaction is observed with increase in $H$ value rather than shifting of the entire $M$–$T$ curve towards positive magnetization due to the field induced increase in canted FIM component. However, for $x$ = 0.30, 0.40 and 0.50 samples, an upturn in the magnetization is observed below $T_{comp}$ with increase in the $H$ value. This can be attributed to the reorientation of the B site moment along the field direction due to relatively large applied $H$, without affecting the original AFM interaction between the A and B site moments. Such spin reorientation and hence the upturn is much prominent for $x$ = 0.40 and 0.50 samples due to their comparatively low magnetic anisotropy which can be predicted from small coercivity of $M$–$H$ loops in Fig. 3.8.

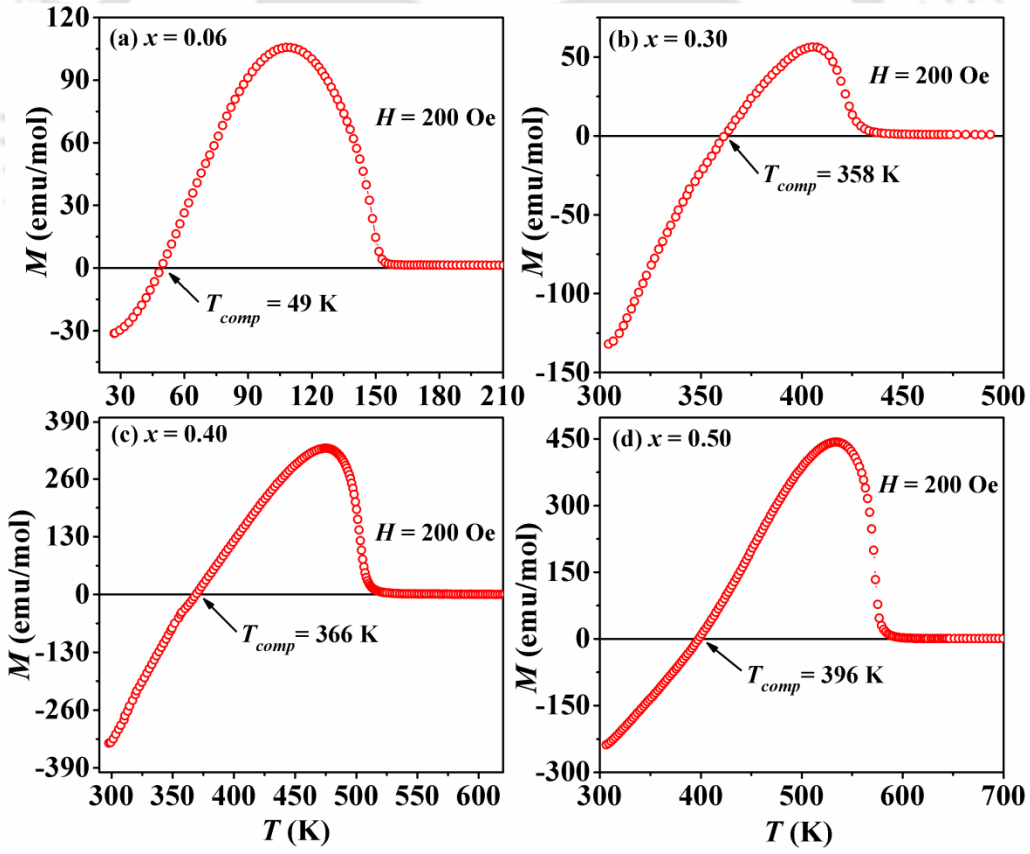


**Figure 3.10:** Temperature dependence of FC magnetization for $x$ = 0.06, 0.30, 0.40 and 0.50.

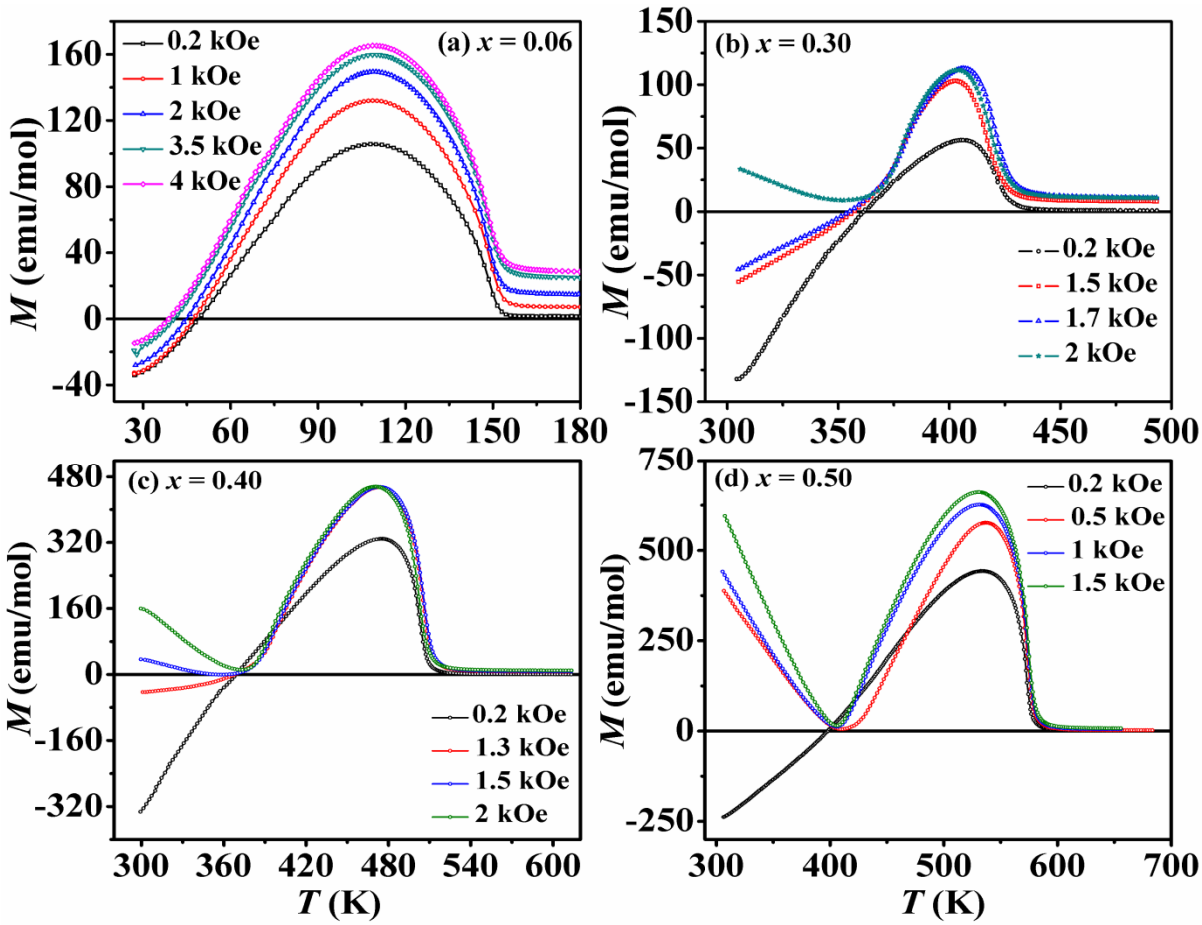


**Figure 3.11:** Temperature dependence of FC magnetization at different fields for $x$ = 0.06, 0.30, 0.40 and 0.50.

However, since the MR with $T_{comp}$ above room temperature is observed for the first time, in order to make sure that it is not due to any experimental artifact as a result of possible trapped negative field, we have recorded the $M$–$T$ curves both for $H_{FC}$ = + 200 Oe and – 200 Oe, and they are shown in Fig. 3.12 for $x$ = 0.30 sample. A mirror image is observed when the direction of cooling field is reversed, *i.e.* for $H$ = – 200 Oe and it confirms the observed MR phenomenon in the present sample. Because otherwise under negative applied field we would have observed only negative magnetization.

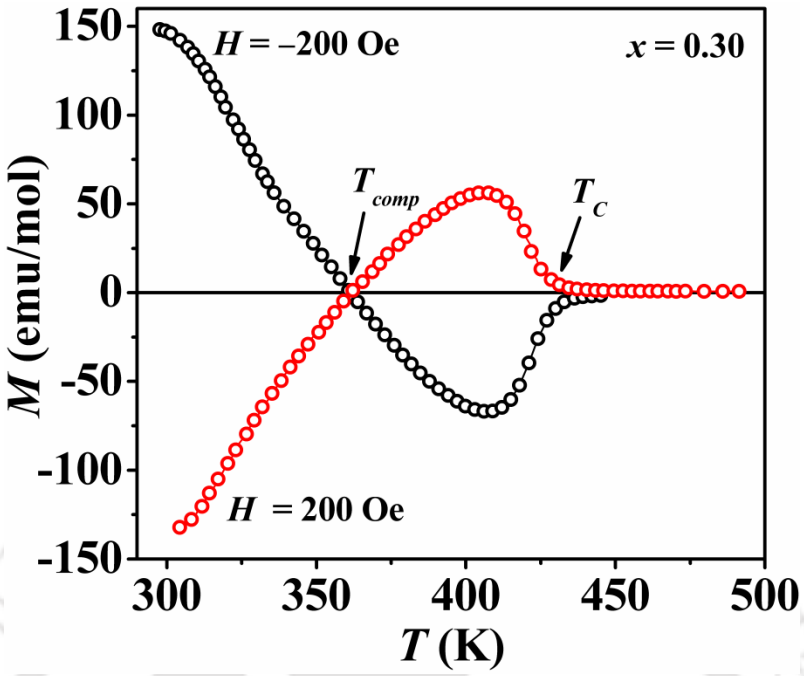


**Figure 3.12:** Temperature dependence of FC magnetization for $x$ = 0.30 sample measured at $H$ = ± 200 Oe.

Due to weak geometrical magnetic frustration (GMF) in the pyrochlore B sublattice, $NiCr_2O_4$ exhibit non-collinear FIM with three magnetic sublattices namely Ni, Cr1 and Cr2. The net B site (Cr1+Cr2) moment aligns opposite to that of A site (Ni) moment. Therefore, the occurrence of negative magnetization in $Ni(Cr_{1-x}Fe_x)_2O_4$ samples can be explained by considering different temperature dependences of the two sublattices (A and B). In order to avoid the intricacy in understanding, here we consider only the longitudinal components of magnetic moments of different sublattices in the compounds. At $T_{comp} < T < T_C$, for small applied field the A sublattice moment (Ni and Fe moments) is aligned along the field direction and the resultant magnetic moment of two B sites (Cr1, Cr2, Fe & Ni) align antiparallel to A site moment and in this arrangement A site moment dominates over net B site moment, *i.e.*, $\mu_A > \mu_B$ (= $\mu_{B1\text{-}B3} - \mu_{B2\text{-}B4}$). As the temperature is reduced, the net B site moment starts growing and at $T = T_{comp}$, it compensates A site moment. It results in a net zero magnetic moment at $T_{comp}$. For further decrease in temperature the B site moment continues to grow such that negative magnetization is observed below $T_{comp}$, where $\mu_A < \mu_B$ (= $\mu_{B1\text{-}B3} - \mu_{B2\text{-}B4}$). Schematic block diagram of the magnetic configurations in two temperature regions $T_{comp} < T < T_C$ *and* $T < T_{comp}$ for $x$ = 0.06 sample is shown in Fig. 3.13. Here, we

consider Ni also in the Cr site because as per XRD analysis small amount of Fe occupies the A site transferring same amount of Ni into the B site.

The above argument for MR can be substantiated from the reported saturation magnetization value (0.3 $\mu_B$ / f.u.) of the parent compound $NiCr_2O_4$, where net A site moment dominates over net B site moment down to low temperature, thereby without any MR [123]. Upon Fe substitution, initially Fe ions occupy the B2-B4 (Cr2) (as discussed in the earlier section) site and thus the B site moment gradually increases thereby reducing the net magnetic moment. Due to gradual increase in B site moment, for $x = 0.06$, both the sublattice moment become comparable. Hence, especially for $x = 0.06$, net B site moment is expected to dominate over A site moment for $T < T_{comp}$ and it results in MR. However for $0.06 < x \leq 0.20$, due to possible substitution of relatively larger concentration of Fe ions at A site compared to that of B site, A site moment becomes dominant. Hence, even when the temperature is lowered the B site moment cannot overcome the A site moment and no MR is observed. With further increase in Fe concentration, there will be considerable amount of $Fe^{3+}$ ions in both A and B sites which further strengthens the superexchange interaction between these sites owing to large number of $Fe^{3+} - O^{2-} - Fe^{3+}$ networks. Such strong interaction may remove the magnetic frustration in the B site significantly which in turn reduces the canting angles of the B site moment. Reduction in the canting angle of B2-B4 site may be rather large compared to that of B1-B3 due to $Fe^{3+}$ ions in this site. This will enhance the net FIM moment of B2-B4 site and it may be comparable to the A site moment in case of $x = 0.30$, 0.40 and 0.50 samples. It is clear from Fig. 1.15(b) in Chapter 1 that increase in FIM moment of B2-B4 site enhances the net B site moment and make it comparable to the net A site moment. Therefore for small applied field net B site moment may increase in opposite direction as the temperature is lowered and may lead to a magnetic compensation effect again for these samples. However, further increase in Fe concentration $NiCr_2O_4$ may tend to take complete collinear magnetic structure like $NiFe_2O_4$ (have no MR behavior) and therefore the magnitude of negative magnetization decreases for $x = 0.50$ and just for $H \geq 500$ Oe the magnetization become positive. For $x = 0.60$ MR completely disappears as observed from the FC *M–T* plot in Fig. 3.14.

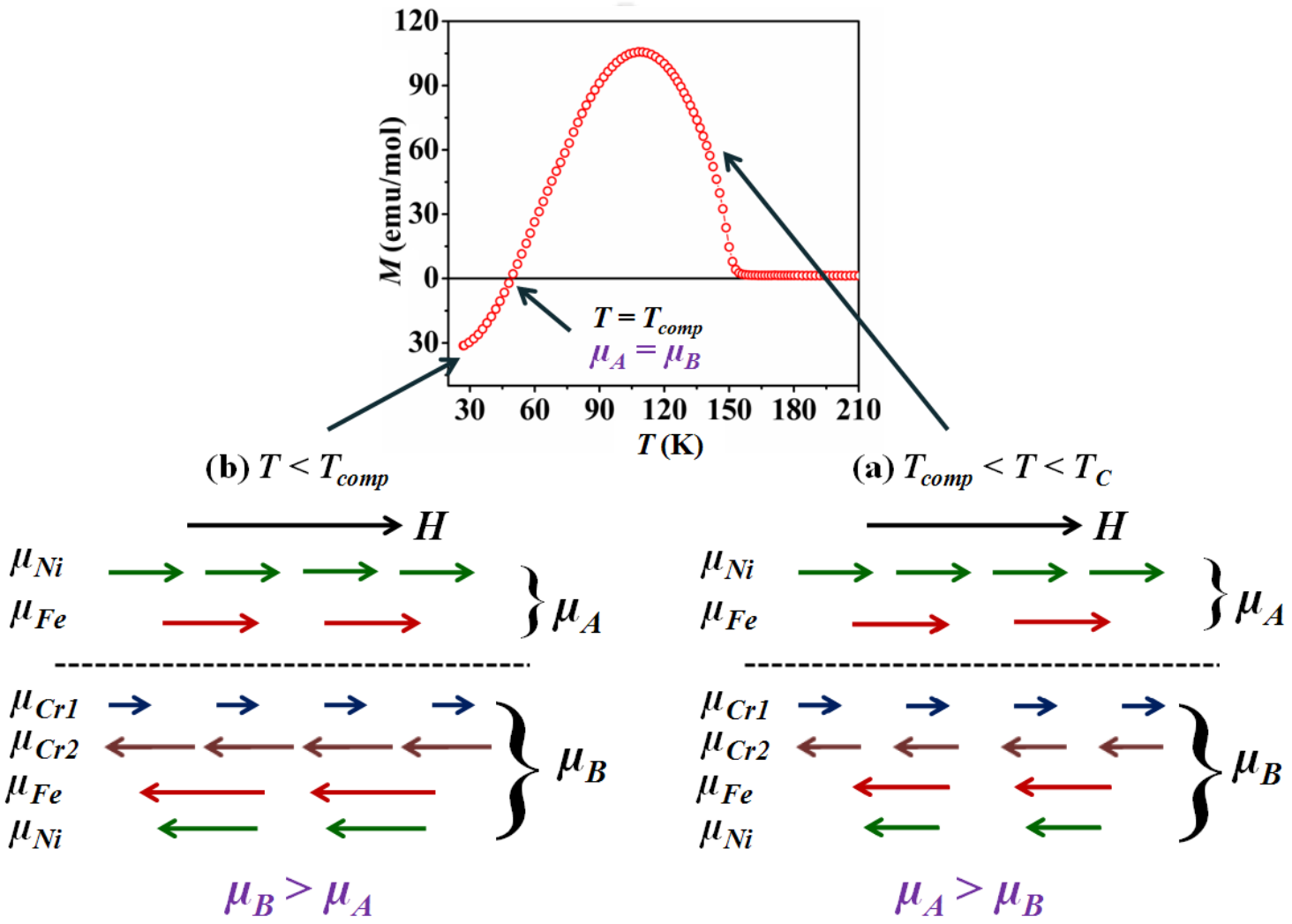


**Figure 3.13:** Schematic block diagram of the magnetic configurations in two temperature regions $T_{comp} < T < T_C$ *and* $T < T_{comp}$.

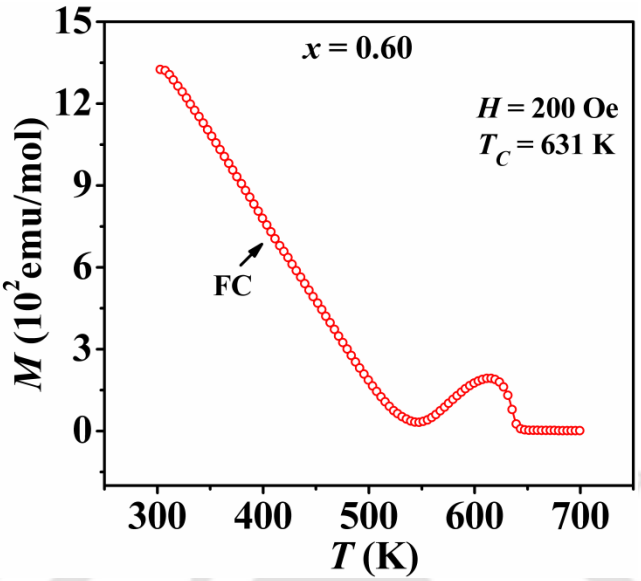


**Figure 3.14:** Temperature variation of FC magnetization for $x = 0.60$ sample.

The MR phenomenon has been studied extensively in different materials after its discovery in ferrites in the year of 1950. However, the mechanism of MR is different in different materials which were already discussed elaborately in Chapter 1. As in ferrites, MR in many other spinel compounds such as $Fe_2MoO_4$, $CoCr_{2-x}Fe_xO_4$, $FeCr_{2-x}Al_xS_4$, *etc*. is explained by considering different temperature dependences of the antiparallel magnetic moments of two/three sublattices. Antiparallel coupling among canted AFM (arises due to Dzyaloshinsky-Moriya (DM) antisymmetric exchange interaction) sublattices occupying different crystallographic sites may also give rise to MR. Origin of MR in orthovanadate $YVO_3$, orthoferrites $YFe_{0.5}Cr_{0.5}O_3$ and $BiFe_{0.5}Mn_{0.5}O_3$, *etc*. is due to such AFM interaction between single ion anisotropy and antisymmetric DM interaction. MR in $Gd_{1-x}Ca_xMnO_3$, $Dy_{1-x}Ca_xMnO_3$, $GdCrO_3$, $YbCrO_3$, $LaCr_{1-x}Mn_xO_3$, $NdCr_{1-x}Fe_xO_3$, *etc*. are explained considering negative exchange coupling among FM/canted AFM and paramagnetic (PM) sublattices. In intermetallic alloys like $(Sm_{1-x}Gd_x)Al_2$ and $SmNiAlH_{1.17}$, *etc*., MR is explained in terms of different temperature dependences of spin and orbital moments of different atoms/ions. The MR in $La_{0.2}Ce_{0.8}CrO_3$ nanoparticles was explained in terms of the core shell model. MR may also occur in systems having strong interfacial exchange coupling between FM and AFM phases such as in Ni–$FeF_2$, Gd–CoNi multilayer, *etc*. [62]. In the present set of samples, single ion anisotropy is unlikely to play a role in MR due to the cubic nature of the

crystal structure. Also, no PM moment is expected at $T < T_C$. The present oxide compounds are insulator and do not possess any conduction electron. It eliminates the role of imbalance of spin and orbital moments or conduction electron polarization (CEP) in the observed MR in present samples. We are dealing with bulk samples and as per FESEM analysis the particle size lies in micrometer range. Therefore MR due to core-shell structure can be ruled out. From XRD analysis the present set of samples are known to form in single phase form and thus the choice of MR due to interfacial exchange between different FM and AFM phases can be eliminated. Moreover, from the XRD analysis the lattice parameters are found to decrease systematically with increase in Fe concentration $x$ and the JTD is suppressed with Fe substitution. It supports the argument of Fe ions replacing the Cr ions in the B site and also in the A site without any phase segregation. Therefore possibility of MR due to any clustering of substituted Fe moments can be ruled out.

Thus the observed MR in the present samples is due to the different temperature dependences of the magnetic moments of A ($Ni^{2+}$) and B ($Cr^{3+}$) sublattices. Very recently, Zhang *et al.* [27] and Wang *et al.* [29] have reported MR in $CoCr_{2-x}Mn_xO_4$ and $Co_{0.8}Cu_{0.2}Cr_2O_4$ samples, respectively and explained the result on the basis of different temperature dependences of two sublattice moments. Zhang *et al.* [27] have effectively explained how the site preference of different ions gives rise to the magnetic compensation in $CoCr_{2-x}Mn_xO_4$ which resembles the behavior observed in the present set of samples.

## 3.5 Bipolar Switching of Magnetization

The magnetic field induced MR phenomenon, *i.e.*, the bipolar switching of magnetization without changing the direction of applied magnetic field is also studied for $x$ = 0.30 and 0.40 samples at room temperature which are shown in Fig. 3.15. Both the samples were cooled from $T > T_C$ to room temperature under an applied field of 200 Oe and magnetization was recorded for the same field for 200 sec. and it is found to be negative as shown in the Fig. 3.15. Since the negative magnetization vanishes above 2000 Oe for $x$ = 0.30 sample (Fig. 3.11), the magnitude of applied field is raised to 2050 Oe to switch the magnetization to positive value in case of the $x$ = 0.30 sample. The magnetization was then recorded for 200 sec. again. The process of cycling the magnetic field from + 200 Oe to +

2050 Oe and back to + 200 Oe was repeated several times and a simultaneous negative and positive magnetization is observed. Thus the bipolar switching of magnetization is possible for this sample. In case of $x$ = 0.40 sample, the field is cycled between + 200 Oe and +1850 Oe. However, for both the samples, at the end of the first cycle the original negative magnetization was not achieved. But for subsequent cycles, there is no change in the magnitude of negative magnetization. The magnitude of magnetization in this reproducible part is larger than that of $YFe_{0.5}Cr_{0.5}O_3$ for the applied field cycle in the range of 50 Oe to 1200 Oe at 200 K [170]. In the present case, at 300 K the net magnetization of the sample is negative under $H$ = 200 Oe (as observed in Fig. 3.10). But when the applied field is increased up to 2050 Oe for $x$ = 0.30, the magnetic moments in the B sublattice which were aligned opposite to the field may now tend to align along the field and magnetization becomes positive. This is also clear from Fig. 3.11. However, while the applied field is reversed back to 200 Oe, the irreversible part of negative magnetization could be due to field induced domain growth and associated stabilization of AFM transverse component of spins at the expense of longitudinal component due to large applied field. The phenomenon of bipolar switching of magnetization was studied in various materials [89, 170-173] but they are at temperatures well below the room temperature. Recently Yin *et al.* [174] and Mao *et al.* [175] have observed such phenomenon at a moderate temperature of around 240 K; but to our knowledge such phenomenon is not reported at room temperature. The observed bipolar switching of magnetization at room temperature in $Ni(Cr_{0.70}Fe_{0.30})_2O_4$ and $Ni(Cr_{0.60}Fe_{0.40})_2O_4$ compounds suggest that these materials can be one of the suitable candidate for applications in magnetic data storage (memory) and switches [173]. Here, the two magnetization states (positive and negative) are achieved by just varying the magnitude of magnetic field without changing its direction.

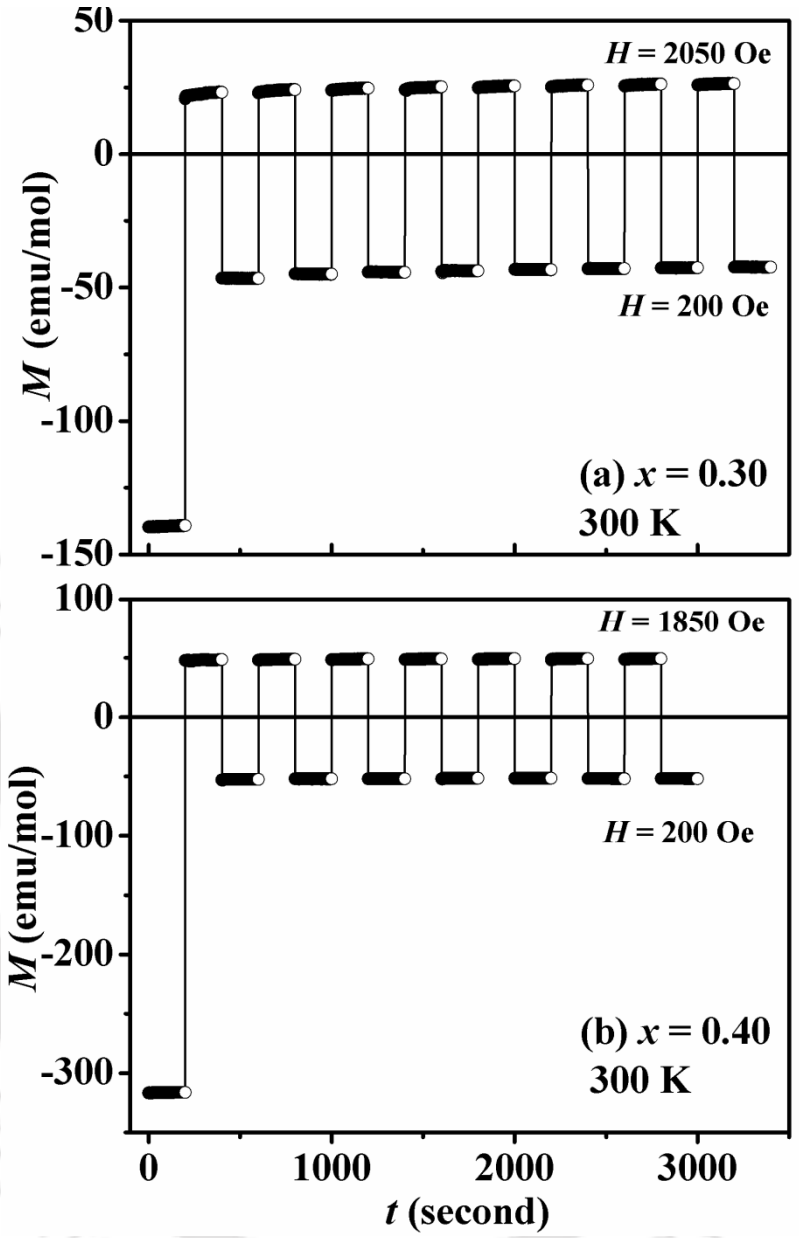


**Figure 3.15:** Bipolar switching of magnetization at 100 K for (a) $x$ = 0.30 and (b) $x$ = 0.40 samples at room temperature.

## 3.6 Exchange Bias Behavior

Many systems showing MR are reported to exhibit sign reversal in the EB field also [26, 85, 89, 91, 107, 108, 110]. Therefore it is of great interest to explore the EB effect in the present series of samples, especially in those samples showing magnetic compensation

behavior. Since $x$ = 0.30, 0.40 and 0.50 samples exhibit $T_{comp}$ above room temperature, therefore study of EB behavior around the $T_{comp}$ of these samples may provide an additional degree of freedom at room temperature for technological applications. Moreover, presence of EB phenomenon in multiferroic compounds itself provides an additional degree of freedom in technological applications [4, 5]. Therefore, in the present work we have explored the temperature dependent EB effect in Ni($Cr_{1-x}Fe_x$)$_2$O$_4$ system with $x$ = 0 – 0.50. For this purpose $M$–$H$ loops of each sample at different temperatures were recorded after cooling the samples in a field of 3000 Oe from above $T_C$ to the required temperature.

Fig. 3.16 shows the $M$–$H$ loops for $x$ = 0, 0.02, 0.04 and 0.10 samples at some selected temperatures in an expanded scale. For these samples the loops are found to shift towards negative $H$-axis with decrease in temperature with enhanced coercivity. However for $x$ = 0.02 and 0.04 samples, for $T$ < 70 K and 90 K respectively, only minor loops could be observed due to the presence of strong AFM and the limitation of maximum applied field in the present set up and hence the measurement of EB field and vertical shift in magnetization were limited down to 70 K and 90 K, respectively for these samples. The value of EB field ($H_{EB}$), effective coercive field ($H_C^{eff}$) and the shift in magnetization ($M_{EB}$) were determined using the relations,

$$H_{EB} = (H_+ + H_-)/2 \tag{3.3}$$

$$H_C^{eff} = (H_+ - H_-)/2 \tag{3.4}$$

$$M_{EB} = (M_+ + M_-)/2 \tag{3.5}$$

where $H_+$ and $H_-$ are two magnetic fields values corresponding to $M$ = 0, during the ascending and the descending branches of $M$–$H$ loop and $M_+$ and $M_-$ are two magnetization values corresponding to $H$ = 0, during the descending and the ascending branches of $M$–$H$ loop [176].

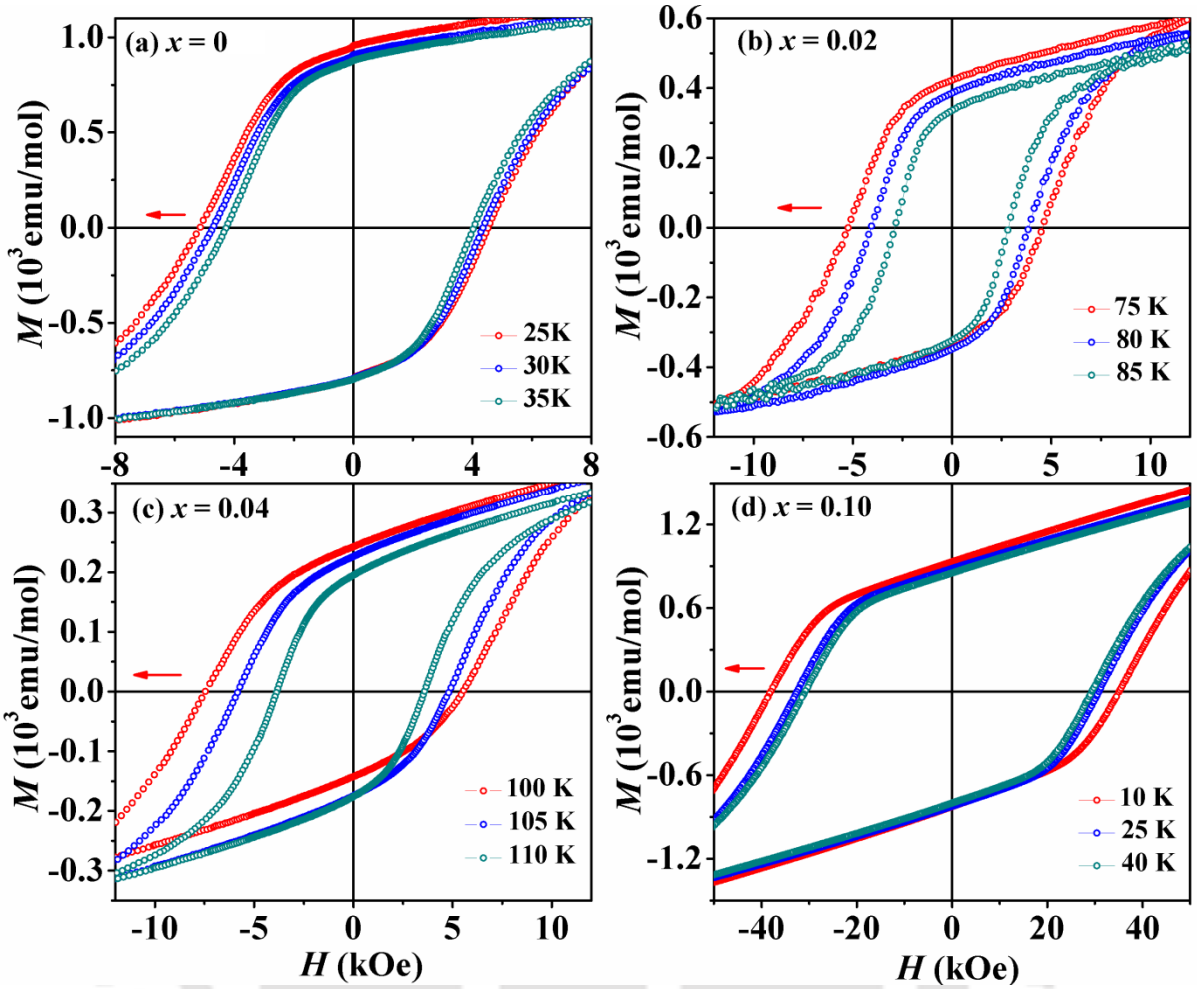


**Figure 3.16:** *M–H* loops for (a) $x = 0$, (b) $x = 0.02$, (c) $x = 0.04$ and (d) $x = 0.10$ samples at different temperatures after cooling the samples under a field of 3000 Oe.

Temperature variations of both $H_{EB}$ and $M_{EB}$ for $x = 0$, 0.02 and 0.04 samples show an exponential rise in magnitude with decrease in temperature as illustrated in Fig. 3.17(a), (b), (d), (e), (g), (h) (black circles). In these systems presence of EB effect can be understood in terms of exchange anisotropy between the FIM and the AFM components. Presence of both FIM and the AFM components and observed EB can also be qualitatively compared with the nature of *M–H* curves [Fig. 3.8(a), (b), (c)] in the low temperature region. In case of $x = 0$ sample, the initial *M–H* loop exhibits a slow variation of initial magnetization almost linearly up to $H \sim 3000$ Oe and beyond which it rises rather sharply. On the other hand, when the temperature is raised close to $T_C$ the initial magnetization increases sharply with increase in $H$. It depicts the presence of competing magnetic interactions like the FIM/ FM component

and the AFM component at low temperature. The competition between such interactions is also consistent with the earlier report by Tomiyasu and Kagomiya [54]; according to which magnetic structure of $NiCr_2O_4$ comprises of both FIM and AFM components at low temperature. In the doped samples also such behavior is observed in *M–H* loop recorded at low temperature as discussed in earlier section. So when these samples are field cooled, the exchange anisotropy between the FIM and the rigid AFM phase gives rise to EB at low temperature. Even though, the long range AFM ordering is expected to appear at low temperature there is a possibility of such ordering taking place in a short range scale at higher temperatures. So in these samples the EB is observed quite close to the $T_C$. For $x = 0$, EB is observed in the temperature range $T \leq 55$ K with a maximum $H_{EB}$ of 312 Oe. For $x = 0.02$, EB is observed for T ≤ 92 K with maximum $H_{EB}$ of 807 Oe and for $x = 0.04$ it is observed up to 125 K with maximum $H_{EB}$ of 6.85 kOe. Therefore the magnitude of $H_{EB}$ increases and it is observed for a wide temperature range in case of the doped samples. This is due to the enhanced magnetic interaction in Fe doped samples and the corresponding increase in $T_C$ and exchange anisotropy.

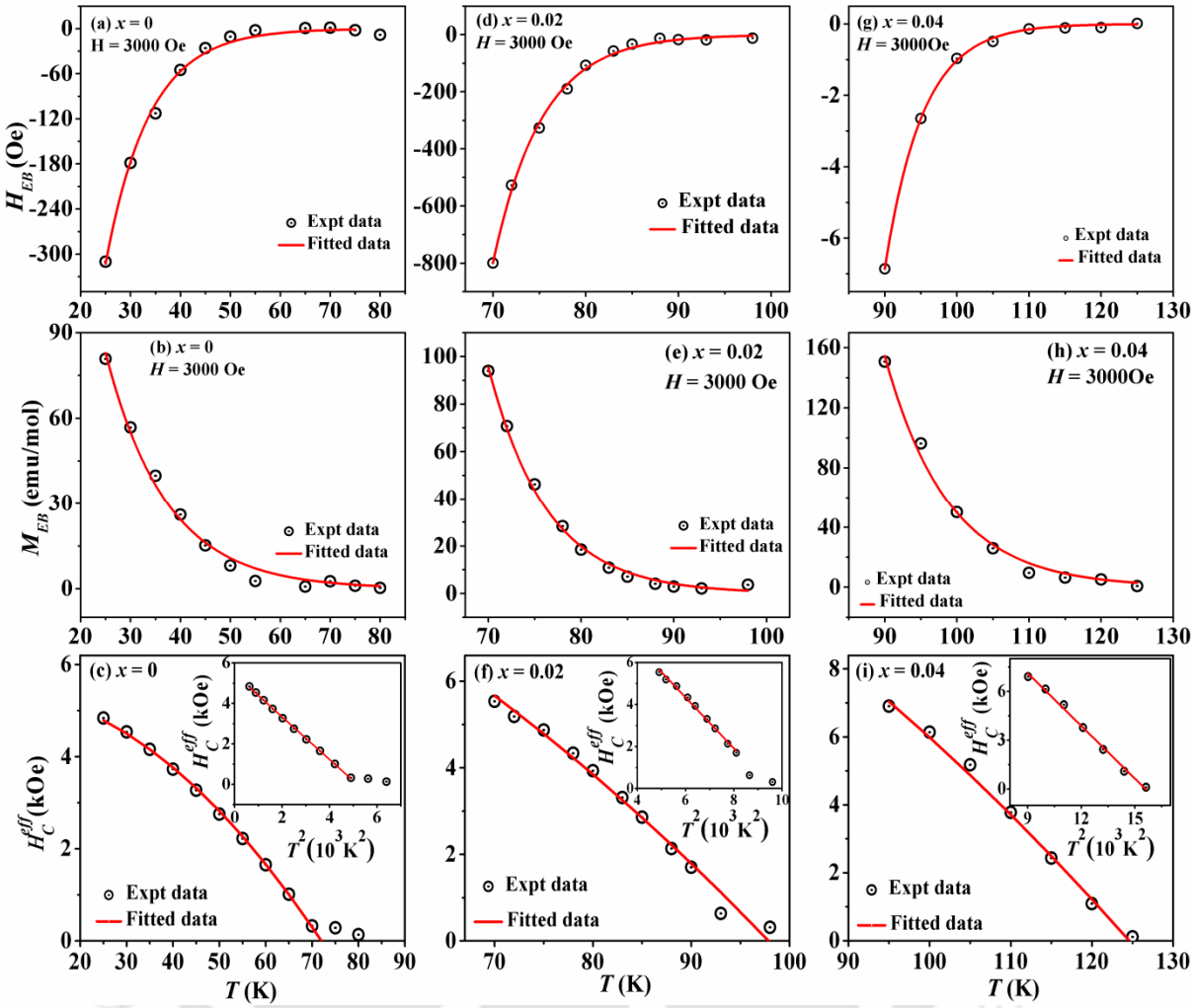


**Figure 3.17:** Temperature variation of $H_{EB}$, $M_{EB}$ and $H_C^{eff}$ for (a) – (c) $x = 0$, (d) – (f) $x = 0.02$ and (g) – (i) $x = 0.04$, respectively along with the theoretical fit. Insets of (c), (f) and (i) show the linear behavior of $H_C^{eff}$ versus $T^2$ plot for $x = 0$, 0.02 and 0.04, respectively.

The temperature dependences of $H_{EB}$ and $M_{EB}$ of $x = 0$, 0.02 and 0.04 samples can be fitted to the following exponential functions,

$$H_{EB} = H_{EB}(0)\exp(-T/T_1) \tag{3.6}$$

$$M_{EB} = M_{EB}(0)\exp(-T/T_2) \tag{3.7}$$

where, $H_{EB}$ (0) and $M_{EB}$ (0) are the values of $H_{EB}$ and $M_{EB}$ at $T = 0$ K and, $T_1$ and $T_2$ are constants. The fitted data are shown as red solid line in Fig. 3.17 and they perfectly follow

the experimental data (black circle). The best fitted parameters for $x = 0$ sample are found to be: $H_{EB}$ (0) = 5.27 ± 0.58 kOe, $T_1$ = 8.84 ± 0.31 K, and $M_{EB}$ (0) = 641.50 ± 50 emu/mol, $T_2$ = 12.22 ± 0.57 K. For $x = 0.02$ and 0.04 samples, we get unreasonably large value of $H_{EB}$ (0) and $M_{EB}$ (0). For these samples the EB measurement is limited down to only 70 K and 90 K, respectively and hence it is very difficult to predict the exact trend of $H_{EB}$ and $M_{EB}$ at low temperature down to 0 K. This fact along with some associated measurement error may lead to unreasonably high value of $H_{EB}$ (0) and $M_{EB}$ (0) in these samples. However, the fitting results give further support to the scenario that the EB in these samples can be attributed to the competing interaction between the FM and AFM components. One possible explanation for the exponential rise of $H_{EB}$ with decrease in temperature is the growth of long range AFM ordering and the corresponding increase in exchange anisotropy between FIM and AFM components at low temperature. Tian *et al.* [177] have reported EB in FIM $NiFe_2O_4$ nanoparticles embedded in AFM NiO matrix with a typical $H_{EB}$ = 500 Oe at 100 K. It was interpreted in terms of exchange interaction between FIM phase and a spin glass (SG) like phase at the interface. The coexistence of FIM and surface spin effect in $NiCr_2O_4$ nanoparticles is reported to contribute EB field of the order of 50 Oe at 100 K [100]. $NiCr_2O_4/Cr_2O_4$ [98] show EB behavior due to the exchange coupling between the FIM and the AFM phases. Unlike the above cases, we are dealing with single phase bulk samples and the $H_{EB}$ value is found to be quite large. Rrecently, Zhu *et al*. [144] have observed similar exponential decay of both $H_{EB}$ and $M_{EB}$ in $NiCr_{1.9}Mn_{0.1}O_4$ with maximum $H_{EB}$ value of 3316 Oe. The particle size of their sample is within nanoscale and EB effect was attributed to the coupling interactions between FM and AFM ordered sublattices with SG like phase. In the present samples, the peak temperature in the ZFC *M–T* curve or the temperature below which the bifurcation between the ZFC and FC magnetization started, do not decrease with increase in applied field. Therefore we can rule out the presence of any SG like phase here [144]. The bifurcation here is only due to the presence of competing AFM in addition to long range FIM. However, the Fe doped sample, $Ni(Cr_{0.96}Fe_{0.04})_2O_4$, in the present study is found to exhibit relatively large $H_{EB}$ compared to that of $NiCr_{1.9}Mn_{0.1}O_4$. The trend of $H_{EB}$ in our samples is also similar to that reported earlier in $La_{0.25}Ca_{0.75}MnO_3$ nanoparticles [176], disordered $R_{0.5}Sr_{0.5}MnO_3$ (R = Y, $Y_{0.5}Sm_{0.5}$, and $Y_{0.5}La_{0.5}$) [178], amorphous/crystalline $NiFe_2O_4$ [179], $La_{1-x}Ca_xMnO_3$ FM/AFM multilayers [180] and

$La_{2/3}Ca_{1/3}MnO_3/La_{1/3}Ca_{2/3}MnO_3$ superlattices [181] and they were mostly interpreted in terms of frustration due to competing magnetic interactions.

The temperature dependence of $H_C^{eff}$ for $x$ = 0, 0.02 and 0.04 samples are shown in Fig. 3.17 (c), (f) and (i), respectively (black circles). Appreciable values of $H_C^{eff}$ are observed for $T \leq 65$ K, 92 K and 125 K for $x$ = 0, 0.02 and 0.04 samples, respectively. Unlike $H_{EB}$, here the temperature dependence could not be fitted to the exponential function. On the other hand, it is found to follow the empirical relation;

$$H_C^{eff} = H_C^{eff}(0)\left[1-\left(T/T_C'\right)^2\right] \tag{3.8}$$

Where, $T_C'$ is a constant and $H_C^{eff}(0)$ is the value of $H_C^{eff}$ at $T$ tends to 0 K. The fitted data are shown as red solid line in the main panel of Fig. 3.17 (c), (f) and (i). Insets show the plot of $H_C^{eff}$ as a function of $T^2$ along with the fitted data for $x$ = 0, 0.02 and 0.04 samples and both exhibit a linear behavior. The value of $H_C^{eff}$ is found to be 5.45 kOe, 11.60 kOe and 16.80 kOe, respectively for the samples with $x$ = 0, 0.02 and 0.04. However, the estimated values of $T_C'$ for the samples are quite close to the experimental $T_C$ value and they are 72 K, 98 K and 125 K for $x$ = 0, 0.02 and 0.04 samples, respectively.

The exponential decay of $H_C^{eff}$ with temperature is familiar and has been reported in many magnetic materials [169, 176, 182, 183]. But the present samples exhibit quadratic temperature dependence of $H_C^{eff}$. The magnetic anisotropy and its temperature dependence are expected to play a major role in controlling the temperature dependence of $H_C^{eff}$. The magnetic anisotropy in turn strongly depends on the nature of domain growth with decrease in temperature. In order to understand the behavior of $H_C^{eff}$, we have investigated the temperature dependence of intensity of (111) peak of neutron powder diffraction pattern reported by Tomiyasu *el al.* [54] for the parent compound $NiCr_2O_4$, because this peak is directly related to the FIM ordering. By taking a few representative (111) peak intensity data from the report, we have replotted the intensity as a function of $T^2$ and also fitted with the empirical relation (3.8) as shown in the inset of Fig. 3.18. For comparison $H_C^{eff}$ as a function

of $T^2$ along with theoretical fit for $NiCr_2O_4$ is also shown in the main panel of Fig. 3.18 and both $H_C^{eff}$ and intensity are found to follow the same linear behavior. So, as the temperature is reduced from $T_C$, the FIM domains grow in size giving rise to increase in magnetic anisotropy and hence increase in $H_C^{eff}$ in the form proportional to $\left[1-\left(T/T_C'\right)^2\right]$. The different temperature dependences of $H_{EB}$ and $H_C^{eff}$ can be understood by probing their actual mechanism. $H_{EB}$ is dictated by the nature of exchange anisotropy between FIM and AFM components and it further depends on how the FIM and AFM components evolve with decrease in temperature. It is attributed to the growth of long range AFM phase with decrease in temperature. On the other hand, $H_C^{eff}$ is mostly dictated by the domain growth and the associated magnetic anisotropy and it is shown to follow the trend of (111) peak intensity of neutron powder diffraction.

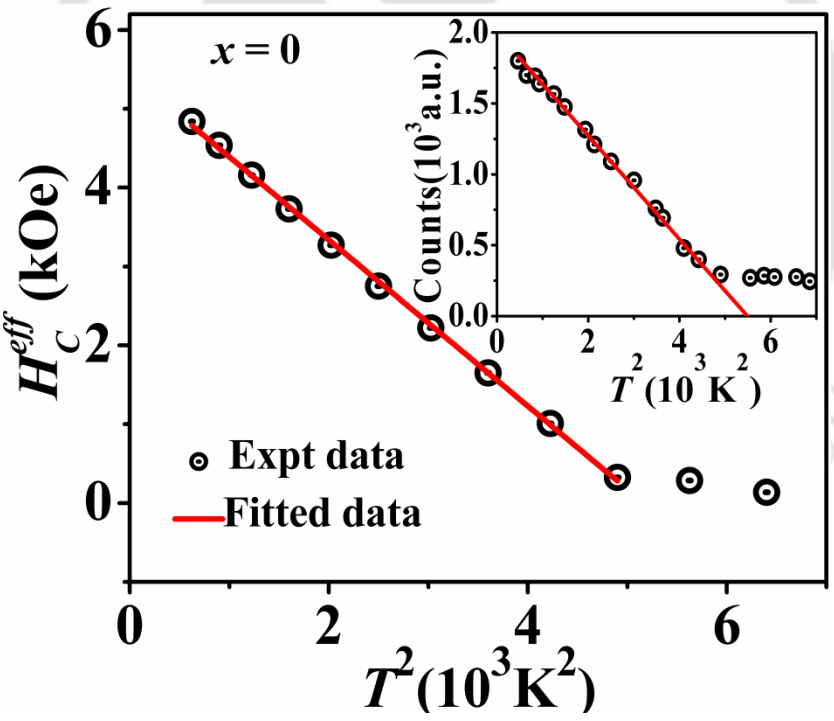


**Figure 3.18:** The linear behavior of $H_C^{eff}$ versus $T^2$ plot. Inset shows the linear behavior of (111) peak intensity of neutron diffraction (obtained from reference [54]) versus $T^2$.

The EB behavior of the $x$ = 0.06 sample, showing MR, exhibits a distinct behavior, where for $T < T_{comp}$ the loops are found to shift towards positive field axis while at higher

temperatures ($T > T_{comp}$), they shift towards negative field axis as shown in Fig. 3.19 in an expanded scale. *M–H* loops shifting towards the positive field axis indicates positive EB field and those shifting to negative field axis indicates negative EB field. Due to compositional compensation region *M–H* loops of $x = 0.06$ sample shows linear behavior. At $T \approx T_{comp}$ (49 K), the loop becomes symmetric about the origin. The maximum EB field value is ~ 5.67 Oe.

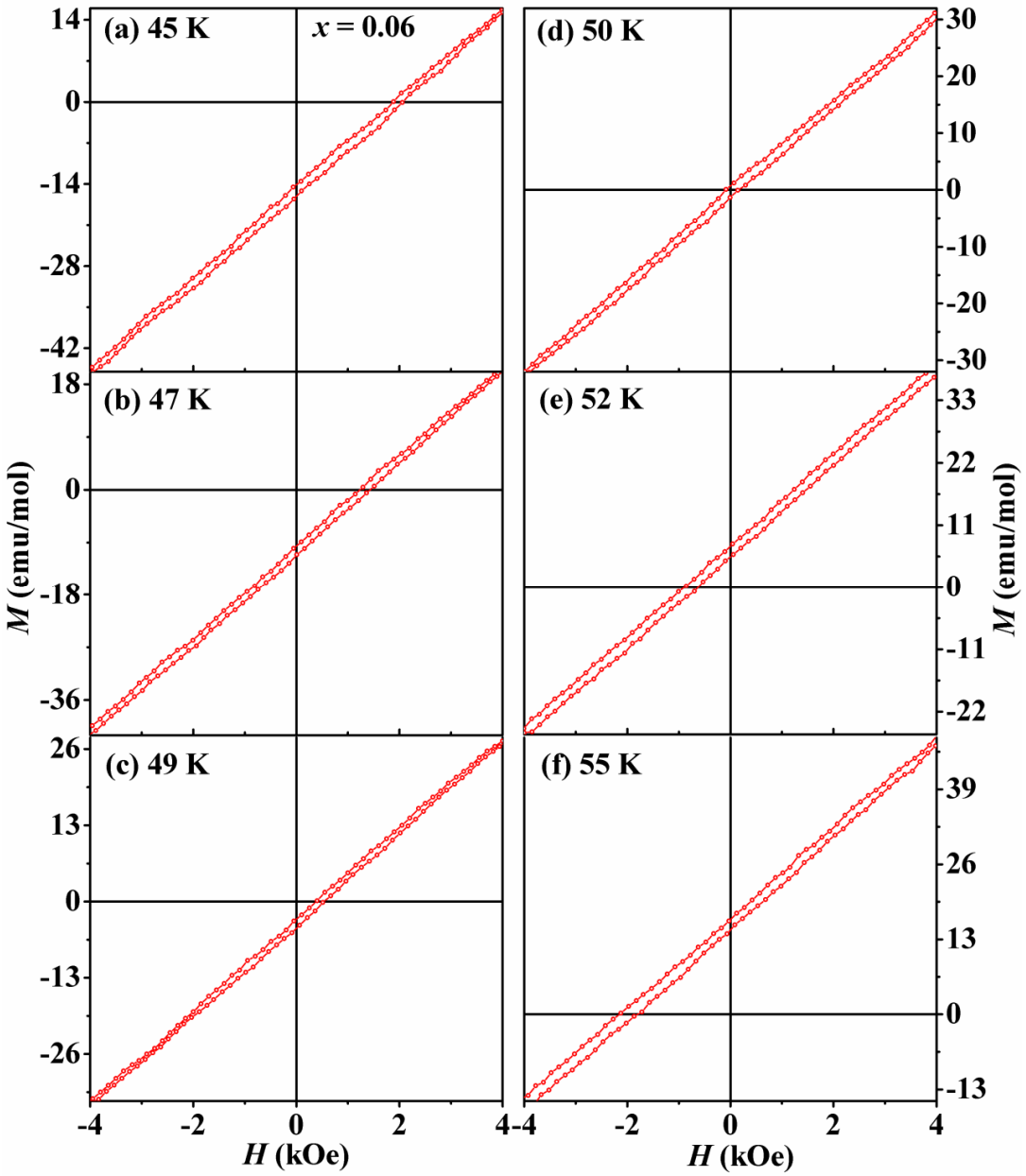


**Figure 3.19:** *M–H* loops for $x = 0.06$ sample at different temperatures after cooling the samples under a field of 3000 Oe.

The temperature variation of $H_{EB}$ and $M_{EB}$ for $x$ = 0.06 sample are shown in Fig. 3.20 (a) and (b). The temperature dependences of $H_{EB}$ and $M_{EB}$ for $x$ = 0.06 are found to exhibit a sign reversal in the vicinity of $T_{comp}$. Even though the FC $M$–$H$ loops of $x$ = 0.10 sample are found to shift only towards the negative $H$-axis as shown in Fig. 3.16(d), the temperature dependence of $H_{EB}$ and $M_{EB}$ exhibits similar behavior as that of $x$ = 0.06 except that they do not undergo any sign reversal [Fig. 3.20(c) and (d)].

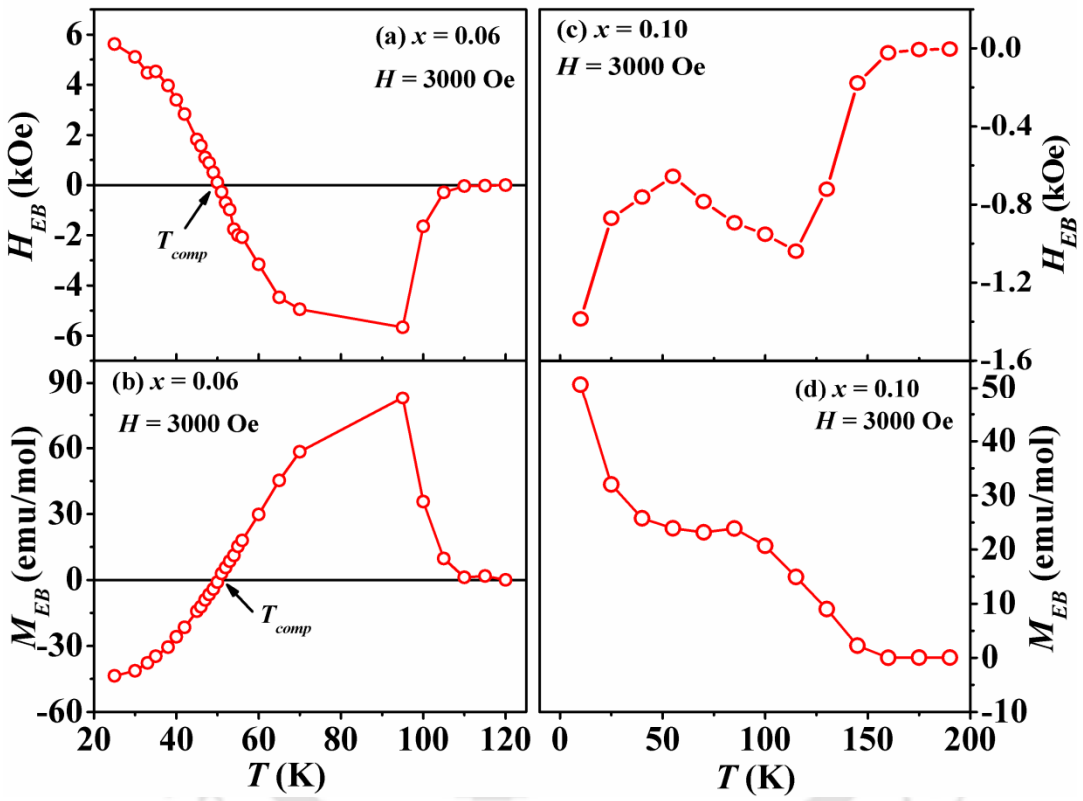


**Figure 3.20:** Temperature variation of $H_{EB}$ for (a) $x$ = 0.06 and (c) $x$ = 0.10 samples. $M_{EB}$ versus temperature plots for these samples are shown in (b) and (d), respectively.

It is quite interesting to study the EB behavior in the $x$ = 0.30, 0.40 and 0.50 samples, showing MR near room temperature. Fig. 3.21 shows the FC $M$–$H$ loops of $x$ = 0.30 sample. At temperature well below the $T_{comp}$ at 323 K the sample exhibits FIM nature but while increasing the temperature it shows a reduction in the magnitude of magnetization as well as opening in the loop. Further increase in the temperature towards $T_{comp}$ (358 K), the behavior of the loop seems to be AFM type with very low opening in the loop. At $T_{comp}$ almost linear loop is observed which is due to the compensated moment of the two sublattices. Again for

temperature well above $T_{comp}$ and below $T_C$ considerable opening and FIM loop is observed due to the uncompensated moment of the two sublattices.

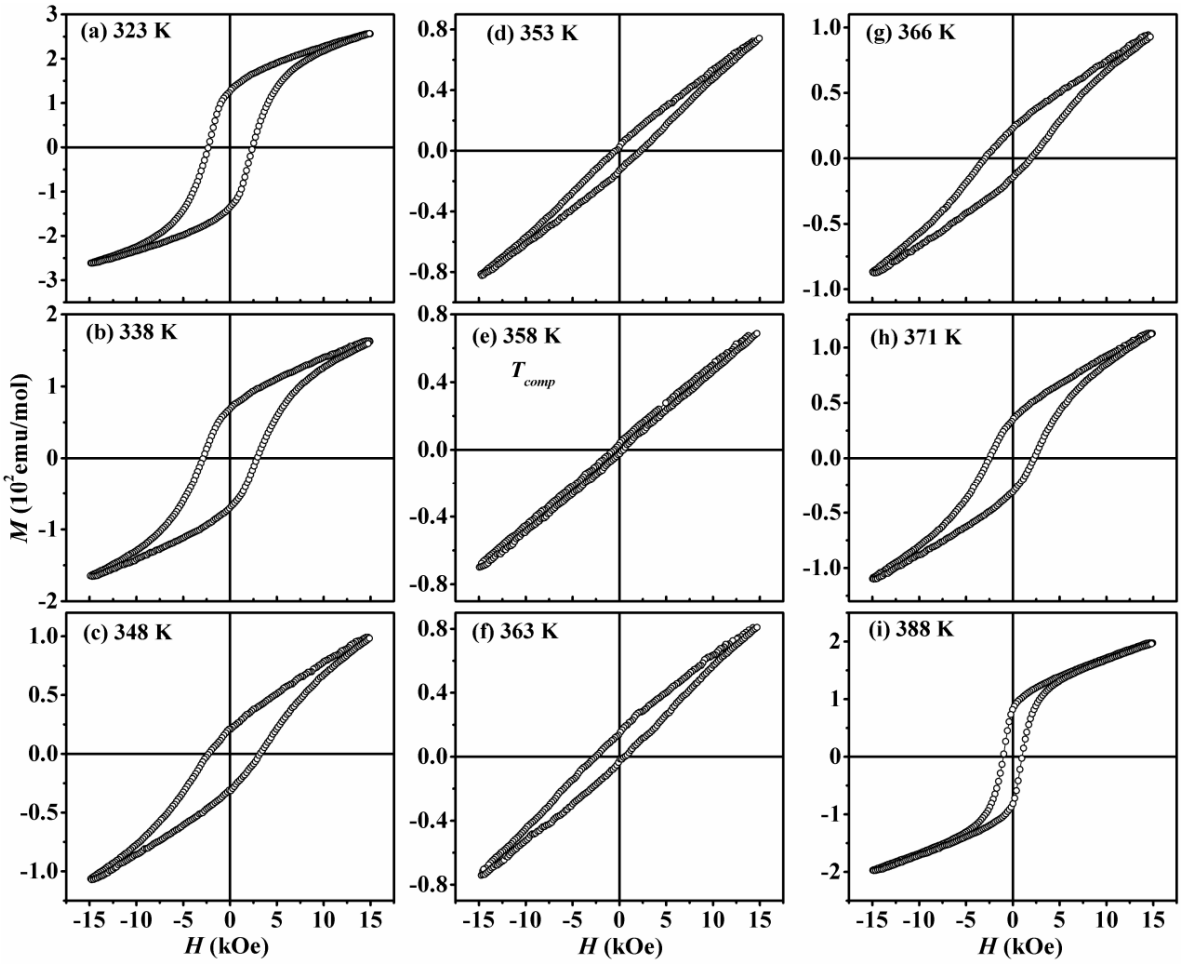


**Figure 3.21:** *M–H* loops for $x$ = 0.30 sample at different temperatures after cooling the samples under a field of 3000 Oe.

Similar to $x$ = 0.06 sample, FC *M–H* loops of these $x$ = 0.30, 0.40 and 0.50 samples also show shifting of the loop towards positive field axis at $T < T_{comp}$ while at higher temperatures ($T > T_{comp}$), they shift towards negative field axis. This behavior for $x$ = 0.30, 0.40 and 0.50 samples is illustrated in Fig. 3.22, 3.23 and 3.24, respectively in an expanded scale. At $T$ close to $T_{comp}$ (358 K, 366 K and 396 K, respectively), symmetric loops with almost linear behavior or with minimum coercivity is observed for all the three samples. However, while increasing or decreasing the temperature on either side of $T_{comp}$, opening in the loop is observed. This behavior implies that close to $T_{comp}$, A and B sublattice moments

are almost compensated. Considerable shifting in the loop is observed only in the temperature range 343 K < $T$ < 373 K for $x$ = 0.30, 348 K < $T$ < 383 K for $x$ = 0.40 and 379 K < $T$ < 409 K for $x$ = 0.50 and beyond that typical symmetric FIM loops are observed. However in case of $x$ = 0.06 sample, considerable shifting is observed for a wide temperature range of 25 K < $T$ < 105 K.

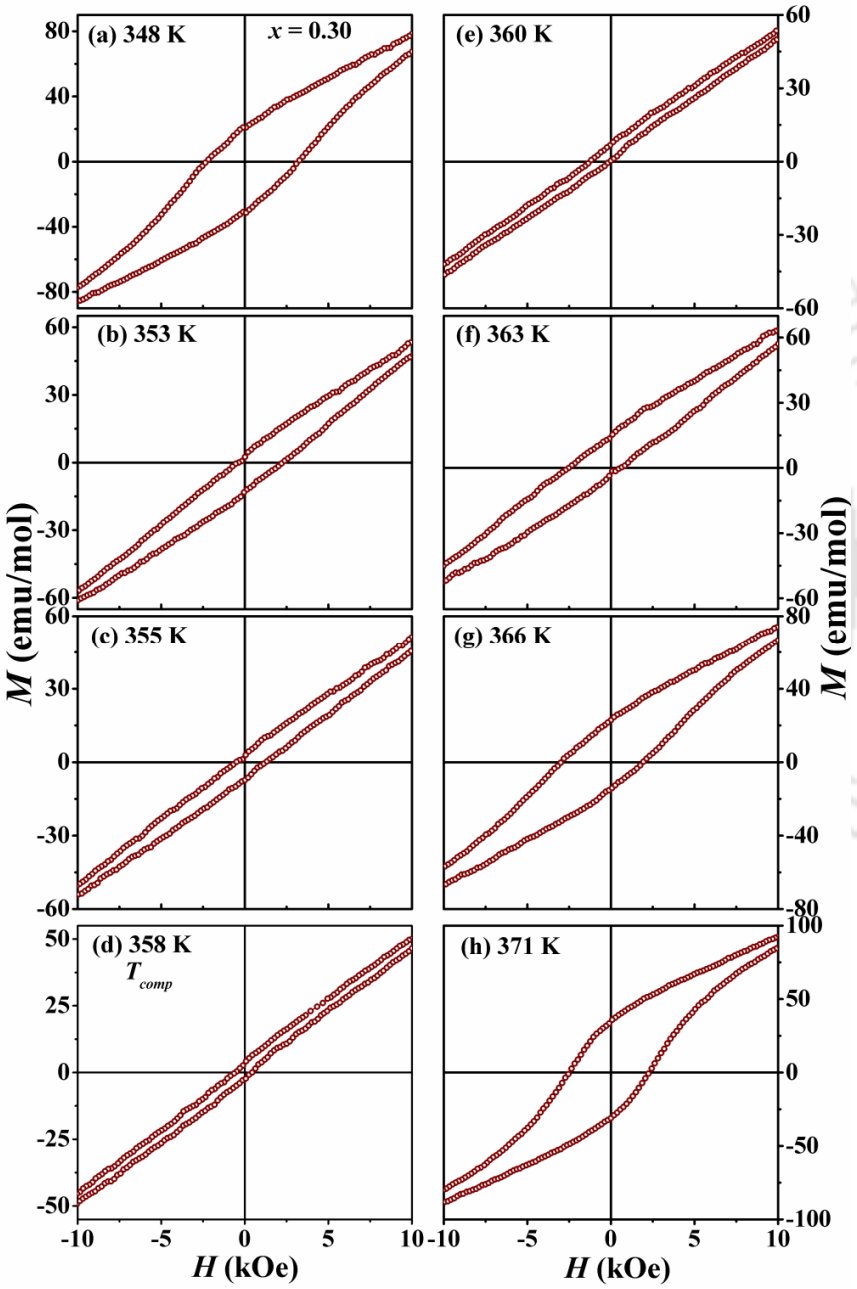


**Figure 3.22:** *M–H* loops for $x$ = 0.30 sample at different temperatures after cooling the samples under a field of 3000 Oe in an expanded scale.

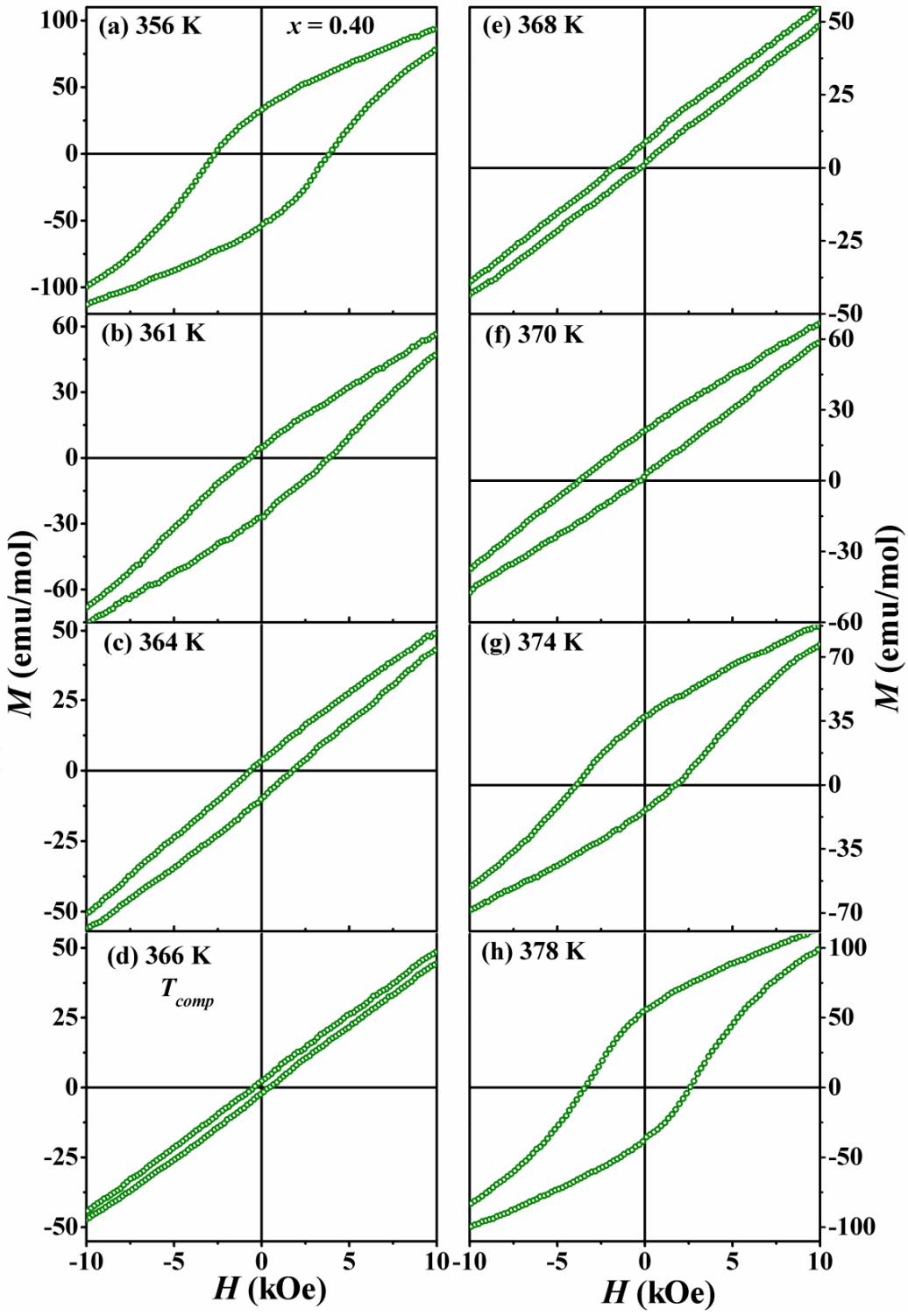


**Figure 3.23:** *M–H* loops for $x$ = 0.40 sample at different temperatures after cooling the samples under a field of 3000 Oe.

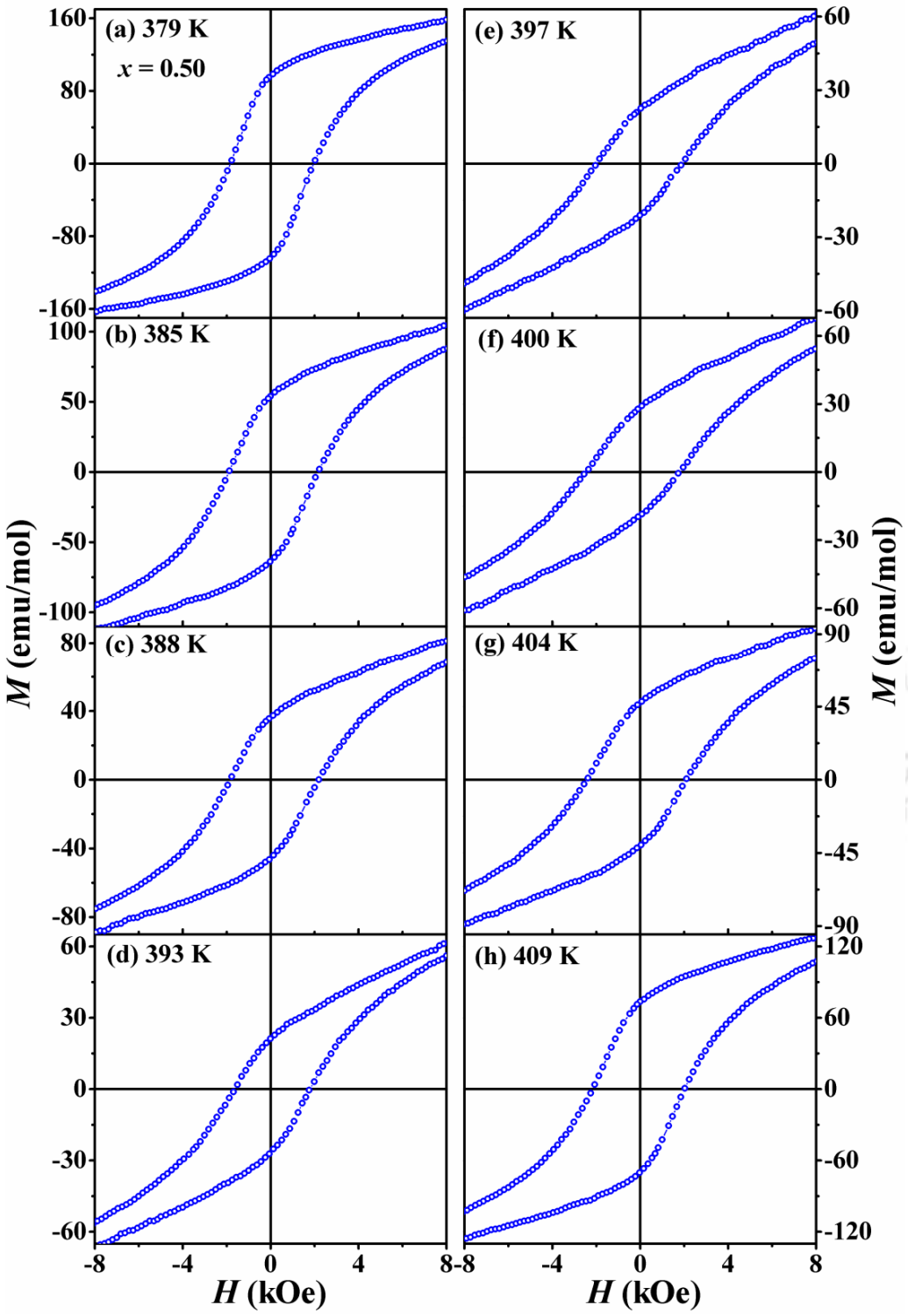


**Figure 3.24:** *M–H* loops for $x$ = 0.50 sample at different temperatures after cooling the samples under a field of 3000 Oe.

Temperature variation of $H_{EB}$ and $H_C^{eff}$ for $x$ = 0.30, 0.40 and 0.50 are shown in Fig. 3.25. As the temperature is increased towards $T_{comp}$, $H_{EB}$ of each sample exhibits sharp increase in magnitude and attain a maximum positive value. This maximum positive value of $H_{EB}$ for $x$ = 0.30 sample is around 0.96 kOe at 353 K. For $x$ = 0.40 and 0.50 sample, this value is 1.59 kOe and 0.18 kOe, respectively at 361 K and 388 K. As the temperature is increased further, $H_{EB}$ decreases and reaches zero at $T_{comp}$. $H_{EB}$ then changes its sign across $T_{comp}$ and start increasing in the negative direction up to a maximum negative value of – 1.01 kOe at 362 K for $x$ = 0.30, – 1.97 kOe at 370 K for $x$ = 0.40 and – 0. 341 kOe at 400 K for $x$ = 0.50 sample and for further higher temperature it approaches zero. The temperature variation of $H_C^{eff}$ of each sample shows a broad twin peak behavior and it drops to a minimum value at temperatures very close to $T_{comp}$. This dramatic drop of $H_C^{eff}$ to a minimum value at $T_{comp}$ is due to the compensated moments at $T_{comp}$. However, the $M_{EB}$ obtained here is too small to be plotted. Such behavior of $H_C^{eff}$ and $H_{EB}$ is observed earlier in similar FIM spinel compound $Co(Cr_{0.95}Fe_{0.05})_2O_4$ [26]. The behavior of both $H_{EB}$ and $H_C^{eff}$ in the vicinity of $T_{comp}$ of the present samples resemble the behavior observed in some other compounds such as in the single crystalline [91] and polycrystalline rare earth intermetallic alloys [107] and in $LaCr_{0.85}Mn_{0.15}O_3$ [86]. Even though their behavior is comparable, the observed $H_{EB}$ in the present compounds is relatively higher. Moreover, here $H_{EB}$ is observed in a wide temperature range and also close to room temperature compared to other spinel and intermetallic alloys. Even though there are a few reports showing room temperature EB, they are mostly in either complicated multilayer system or having a small $H_{EB}$ (only negative) at room temperature [184-186]. So, the important hall mark of the present samples towards potential applications is their large tunable positive and negative EB field in the vicinity of room temperature. This is supported by the MR in the vicinity of room temperature.

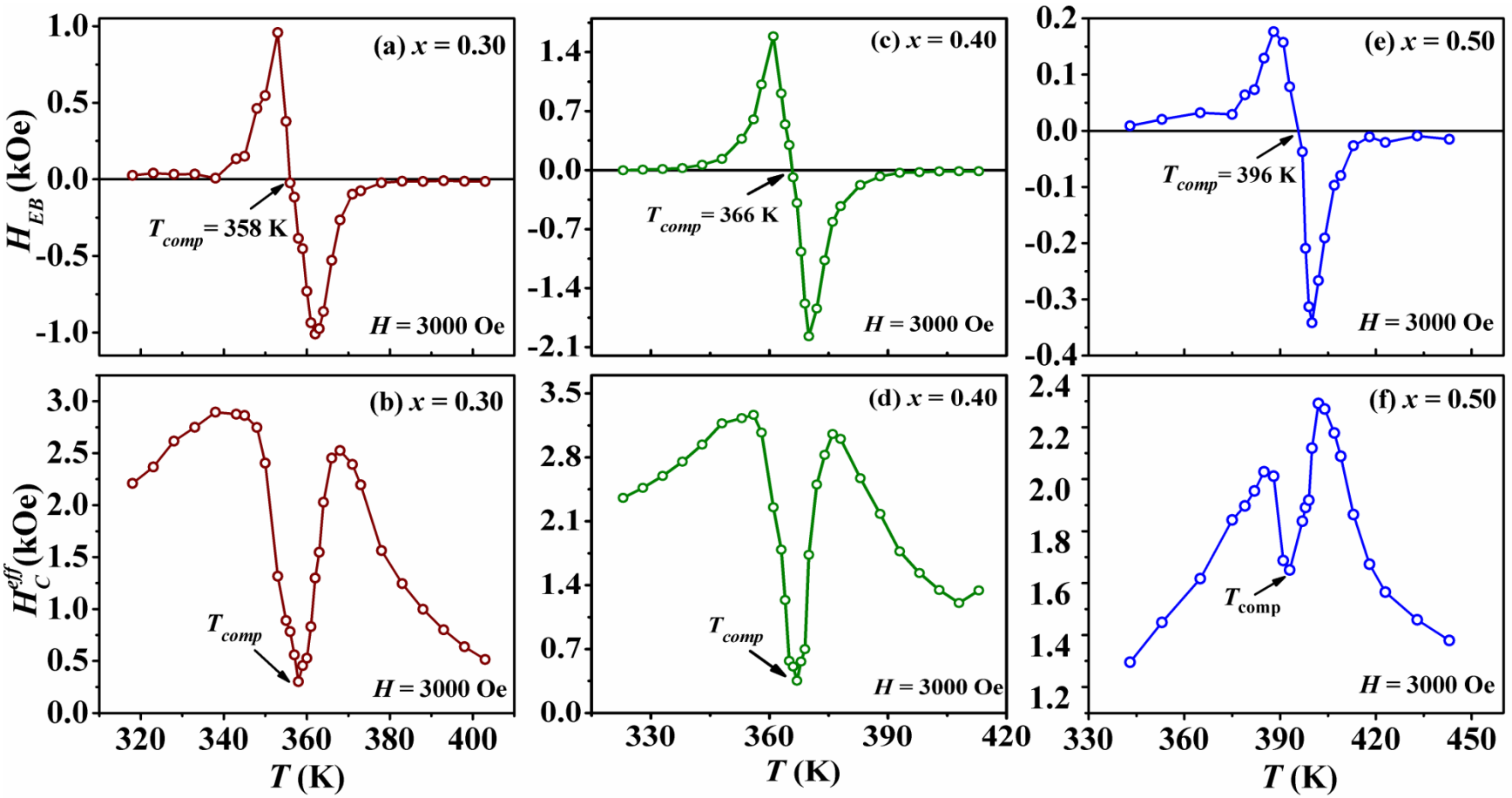


**Figure 3.25:** Temperature variation of $H_{EB}$ for (a) $x$ = 0.30, (c) $x$ = 0.40 and (e) $x$ = 0.50 samples, respectively. Temperature variations of $H_C^{eff}$ for these samples are shown in (b), (d) and (f), respectively.

Eventhough several spinel compounds are reported to show MR as discussed in section 3.4, the observation of tunable EB behavior coupled with MR is quite rare. In some intermetallic alloys such as in $Nd_{0.75}Ho_{0.25}Al_2$ and $Sm_{0.98}Gd_{0.02}Al_2$ [91, 107], sign reversal of both EB and magnetization is explained in terms of the different kinds of exchange coupling between the moments corresponding to CEP and two dissimilar rare-earth ions. In the spinel compound $Co(Cr_{0.95}Fe_{0.05})_2O_4$ [26] it is attributed to the flipping / reorientation of the sign of the spins of Co, Cr and Fe ions in different sublattices without affecting the spin-spin exchange interaction between them. The competition between the canted FM component of $Cr^{3+}$ ions and the PM component of doped ions under the influence of a negative internal field and the change of domination of one component over the other component at above and below $T_{comp}$ give rise to reversal in EB in some orthochromites like $NdCr_{1-x}Fe_xO_3$ ($x$ = 0.15–0.20) [88] and $LaCr_{0.85}Mn_{0.15}O_3$ [86]. In $YFe_{0.5}Cr_{0.5}O_3$[111], it is observed due to competition between DM interaction and single ion anisotropy as explained in case of MR. Moreover, tunable EB along with MR behavior is reported in many other materials like $Sr_2YbRuO_6$ compound [110], nanoparticles [85], perovskites [111, 113], solid solutions of $BiFeO_3$ – $BiMnO_3$ [114], *etc*. and its mechanism differ depending on the nature of material.

In the present compound no CEP or PM moment is expected at $T < T_C$. Since, we are not dealing with nanoparticles, so no core-shell structure is expected. Also our system is not a layered system or a solid solution and so no direct FM/AFM like interfaces are there. Single ion anisotropy is unlikely to play a role due to the cubic nature of the crystal structure. As discussed earlier, the observed MR in our system can be attributed to one sublattice moment overtaking the other sublattice moment due to the temperature variation. Therefore, change of domination of magnetic moment due to one FIM sublattice over the other one with decrease in temperature can be attributed to the sign reversal in $H_{EB}$ and $M_{EB}$ in the systems ($x$ = 0.06, 0.30, 0.40 and 0.50) showing MR. This can be further explained by considering the longitudinal component of magnetic moment of A sublattice ($\mu_A$) and B sublattice ($\mu_B = \mu_{B1\text{-}B3} - \mu_{B2\text{-}B4}$). Here, for simplicity only the longitudinal component of magnetic moment is considered. In spinels, A site and B site ions have strong AFM interaction and as a result the A site and B site moment are antiparallel to each other. For $T_{comp} < T < T_C$, A sublattice moment is aligned along the field direction and dominates over net B sublattice moment *i.e.*, $\mu_A > \mu_B$ ($= \mu_{B1\text{-}B3} - \mu_{B2\text{-}B4}$). Under this condition due to dominant $\mu_A$ along the positive field

direction it is relatively easy to align the net magnetization along the positive field direction during the ascending branches of the *M–H* loop. However, when the field is reversed to complete the *M–H* loop, during the descending branch, it is quite difficult to align $\mu_A$ along field direction and a large negative field is required to orient the net magnetization along filed direction without affecting the original AFM interaction between the two sublattices. On the other hand, when the field is again reversed in the initial direction, net magnetization easily follows it because now $\mu_A$ is forced to align in its ground state direction. So effectively *M–H* loops shift towards the negative field axis or in other words they exhibit negative EB field. This situation is illustrated schematically in Fig. 3.26 for $x = 0.30$ sample at 366 K, *i.e.*, for the temperature range $T_{comp} < T < T_C$. On the otherhand for $T < T_{comp}$, $\mu_B$ $(= \mu_{B1\text{-}B3} - \mu_{B2\text{-}B4}) > \mu_A$, so as per the above argument here large field is needed to align net magnetization during the ascending branches of the *M–H* loop. So in this circumstance, *M–H* loop shifts along the positive field direction and positive EB field is obtained. This situation for $T < T_{comp}$ is expressed schematically in Fig. 3.26 at 348 K. Since at $T = T_{comp}$, $\mu_A = \mu_B$ $(= \mu_{B1\text{-}B3} - \mu_{B2\text{-}B4})$, the EB at $T_{comp}$ is almost zero and also gives rise to a linear hysteresis loop. As a result $H_C^{eff}$ also vanishes close to this temperature. The temperature dependence of $H_{EB}$ and $M_{EB}$ for $x = 0.10$ also tend to show a tunable behavior as shown in Fig. 3.20(c) and (d), however it remains negative down to low temperature due to the possible domination of $\mu_A$ in the entire temperature range.

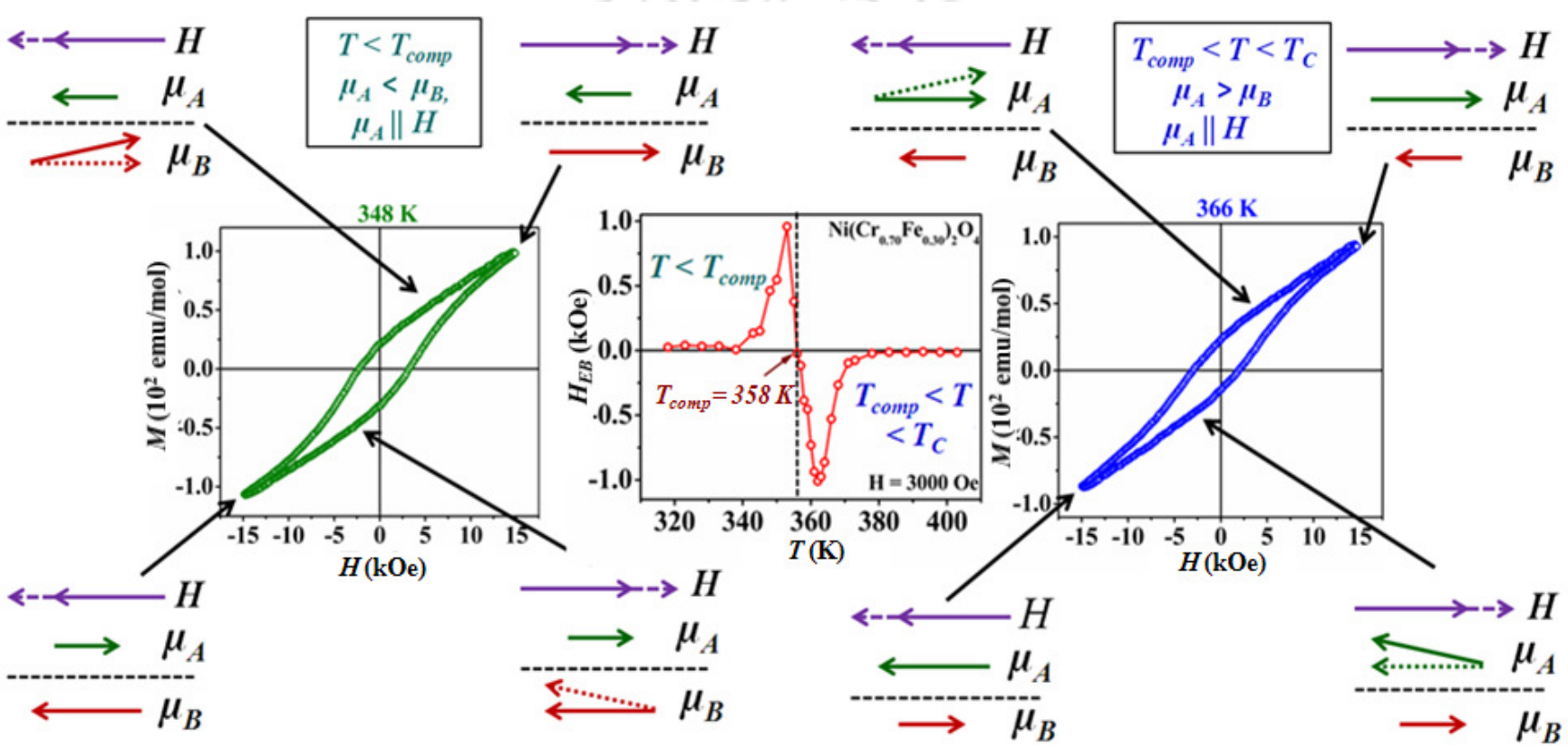


**Figure 3.26:** Schematic block diagram of the magnetic configuration of $x = 0.30$ sample in the two temperature range $T_{comp} < T < T_C$ and $T < T_{comp}$ under the field cooling condition in order to explain the EB behavior.

Moreover, in order to rule out the minor loop effect in the EB field measurement, the *M–H* loops were analyzed by using single point detection (SPD) method as reported recently by Harres *et al*. [187]. According to this method, an *M–H* loop is considered to be a major loop if the first or its higher derivatives of both ascending and descending branches of the *M–H* loop coincide before the maximum field is attained, *i.e.* for the region $|H| \geq H_A$, the anisotropy field. In the present loops for $x$ = 0, 0.02, 0.04 and 0.10 samples, the second derivatives of the descending and the ascending branches were found to overlap for |H| > 7 kOe. Fig. 3.27 shows the typical $d^2M/dH^2$ versus $H$ plots for both descending and ascending branches of *M–H* loops at a given temperature for $x$ = 0, 0.02, 0.04 and 0.10 samples. While for $x$ = 0.30, 0.40 and 0.50 samples the first derivatives of descending and the ascending branches overlap for $|H|$ > 7 kOe and it confirms the major loop behavior. Fig. 3.28 shows the typical *dM/dH* versus *H* plots for both descending and ascending branches of *M–H* loops at two different temperatures for $x$ = 0.30, 0.40 and 0.50 samples, *i.e.* one below and one above the $T_{comp}$ for each sample.

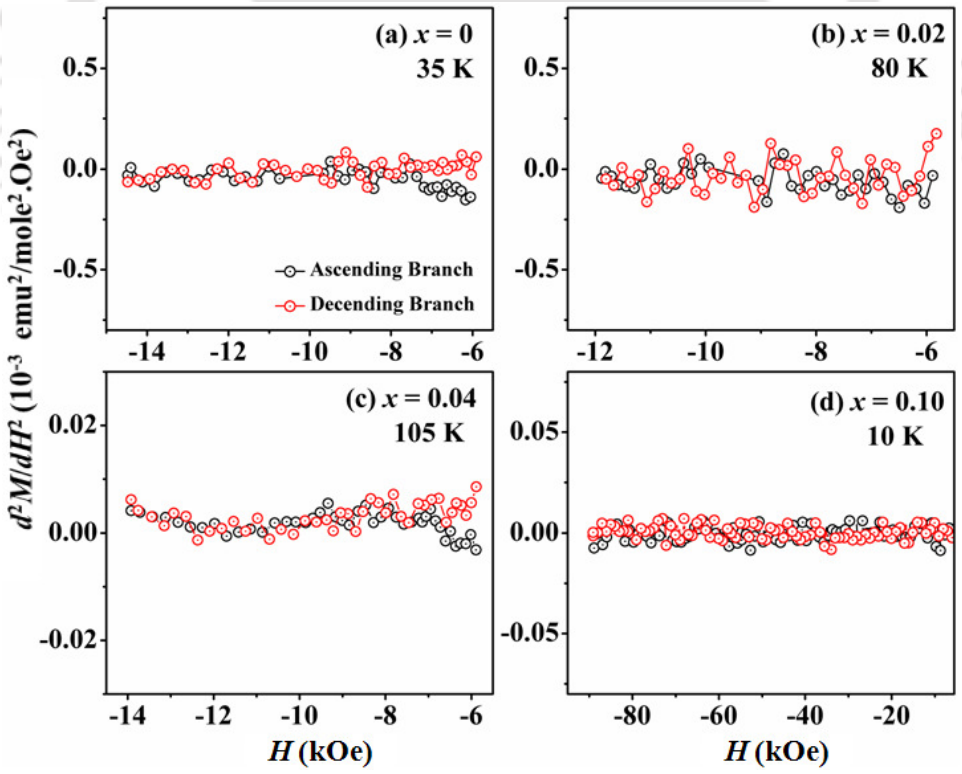


**Figure 3.27:** $d^2M/dH^2$ versus $H$ plots for $x$ = 0, 0.02, 0.04 and 0.10 samples at a particular temperature.

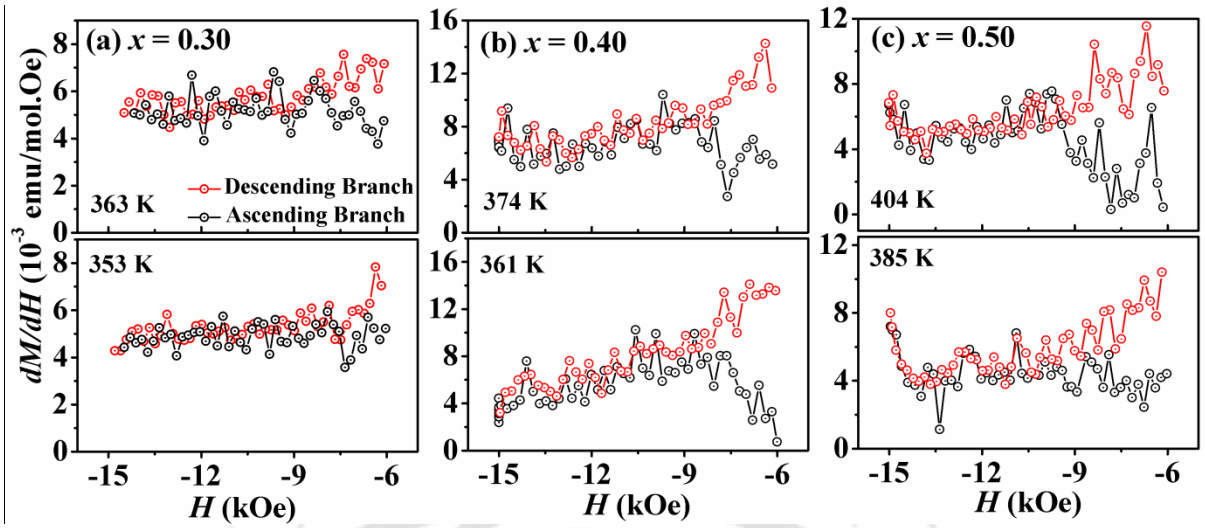


**Figure 3.28:** *dM/dH* versus *H* plots for $x$ = 0.30, 0.40 and 0.50 samples at two particular temperatures above and below $T_{comp}$.

## 3.7 Training Effect

Training effect is an interesting characteristic related to EB phenomenon. It is the most important aging effect of EB systems where, the EB field is found to decrease when the sample is cycled through several consecutive hysteresis loops. Evidence of this effect was first reported by Paccard *et al*. [188] in 1966 in three systems, Co–CoO, NiFe–NiFeMn and NiFe–$Cr_2O_3$ thin films, exhibiting FM-AFM coupling with uniaxial anisotropy. In general, for the commercialization of an EB system, it is necessary to minimize the training effect and EB field should be made as high as possible. Therefore to examine the aging effect of EB in our samples, we have studied the training effect in the parent compound, $NiCr_2O_4$ and for that purpose, consecutive hysteresis loops were recorded at 25 K after FC the sample at $H$ = 3000 Oe. Consecutive hysteresis loops with index $n$ = 1 to $n$ = 9 in an expanded scale are shown in Fig. 3.29 and they highlight the presence of training effect. The shift in the $H_-$ value is found to be larger (descending branch) than that of $H_+$ (ascending branch). Similar type of larger shifting of left side of *M–H* loop with increase in index number $n$ has been reported in $R_{0.5}Sr_{0.5}MnO_3$, bilayer Fe / $KNiF_3$, bilayered FeNi-FeMn and $NiCr_2O_4$/NiO system [134, 178, 189, 190]. Large training is observed from $n$ = 1 to $n$ = 2 and for subsequent loops small training effect is observed. Thus commonly the training effect is separated into two categories, one between $n$ = 1 and $n$ = 2, and the other between consecutive hysteresis loops.

During the first cycle, because of the non-equilibrium state of the AFM layer, the system behaves in irreversible way. The second type of training effect show small decrease in the shifting of loop with the increase of the number of consecutive hysteresis loops [95]. Both $H_{EB}$ and $M_{EB}$ are found to decrease with $n$ as shown in Fig. 3.30 (a) and (b). $H_{EB}$ and $M_{EB}$ for n ≥ 2 could be fitted to simple power law,

$$\mu_0 H_{EB} - \mu_0 H_{EB\infty} = \kappa/\sqrt{n} \tag{3.9}$$

$$\mu_0 M_{EB} - \mu_0 M_{EB\infty} = \kappa/\sqrt{n} \tag{3.10}$$

where, $H_{EB\infty}$ and $M_{EB\infty}$ represent the values of $H_{EB}$ and $M_{EB}$ at $n = \infty$ and, $\kappa$ is the sample dependent constant [178]. The fitted data are shown as red solid line; they closely follow the experimental data. The estimated value of $H_{EB\infty}$ and $M_{EB\infty}$ are 123 Oe and 45.34 emu/mol, respectively. Therefore, it is observed that even at $n \rightarrow \infty$, considerable value of $H_{EB}$ is observed in the sample. The training in our system can be explained by considering the reorientation of the transverse component (AFM) of spin structure towards an equilibrium configuration.

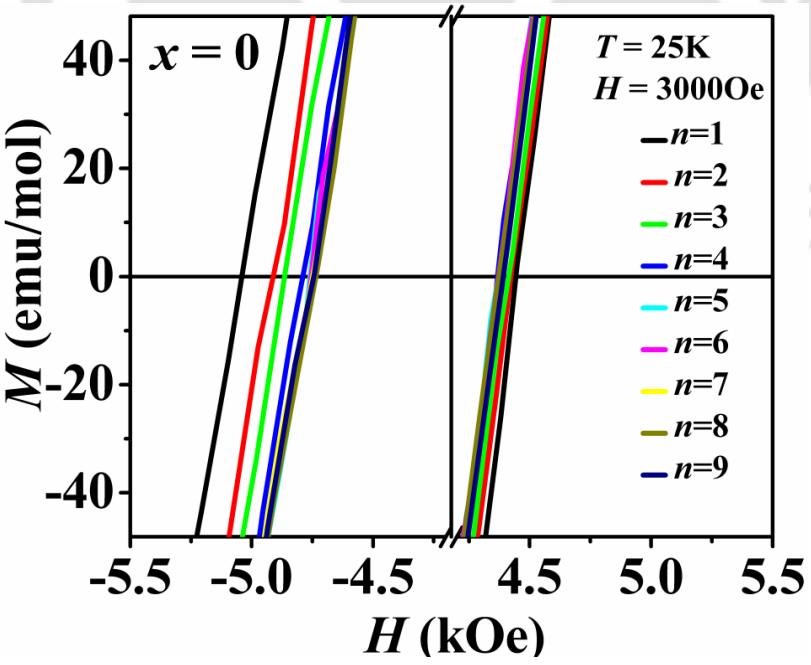


**Figure 3.29:** Consecutive *M-H* loops with index $n$ = 1 to $n$ = 9 in expanded scale for $x$ = 0 sample.

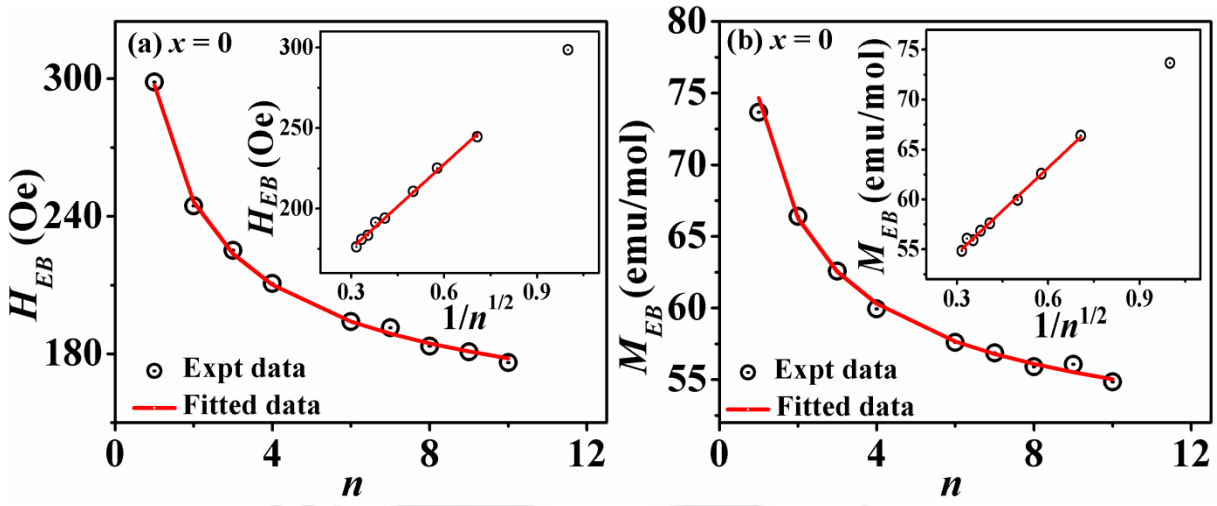


**Figure 3.30:** (a) $H_{EB}$ and (b) $M_{EB}$ as a function of $n$ for $x$ = 0 sample. Insets show the same data as a function of $1/\sqrt{n}$ . The red solid lines represent the fitted data.

## 3.8 Conclusions

To summarize, we have investigated the structural, basic magnetic, EB and MR properties of Ni(Cr$_{1-x}$Fe$_x$)$_2$O$_4$ ($x$ = 0 – 0.60) series in this chapter. We have successfully prepared the single phase samples of Ni(Cr$_{1-x}$Fe$_x$)$_2$O$_4$ using sol-gel route. Rietveld refinement of the XRD pattern of the parent NiCr$_2$O$_4$ at room temperature reveals the tetragonal structure of the sample with $I4_1/amd$ space group. XRD patterns of all the Fe substituted samples can be refined using $Fd\bar{3}m$ space group in cubic structure. Temperature variation of magnetization measurement reveals FIM nature of NiCr$_2$O$_4$ with $T_C$ = 73 K. All the Fe substituted samples are also found to exhibit FIM nature with a systematic increase in $T_C$ with increase in $x$. For $x$ = 0.50 the $T_C$ value is around 574 K. This increase in $T_C$ is due to the strengthening of the super-exchange interaction of the system. Field dependent magnetization measurements at low temperature validates the presence of competing AFM interaction along with long range FIM ordering as reported earlier.

NiCr$_2$O$_4$ itself shows EB behavior and detailed investigation of the EB behavior shows that the EB field decay exponentially with increase in temperature from a maximum value of 312 Oe. Origin of the EB in this sample can be explained by considering the anisotropic exchange interaction between the FIM and the AFM components of magnetic

moment. The temperature dependence of coercive field could be explained based on the empirical relation $H_C^{eff} = H_C^{eff}(0)\left[1-\left(T/T_C'\right)^2\right]$. $NiCr_2O_4$ exhibit small training in the EB field. At the end of infinite consecutive *M–H* loop, the $H_{EB}$ value is estimated to be 123 Oe. The Fe substituted samples with $x$ = 0.02, 0.04 and 0.10 also exhibit negative EB field as observed for the parent compound but with a higher magnitude and in a wide temperature range. This is due to the enhanced magnetic interaction in Fe doped samples and the corresponding increase in $T_C$ and exchange anisotropy.

Fe substitution leads the $NiCr_2O_4$ system to a magnetic compensation behavior (M = 0) for $x$ = 0.06, 0.30 0.40 and 0.50 samples with a sign reversal of magnetization across the compensation temperature. Their magnetic $T_{comp}$ is found to be in the range of 49 K to 396 K, *i.e.* even above room temperature which is observed for the first time. MR is explained by considering different site occupancies (A and B sites) of the Fe ions and the different temperature dependence of the magnetic moments of different sublattices. Study of EB behavior in these samples having MR reveals that the EB field also undergoes a sign reversal across the $T_{comp}$. Most Interestingly such tunable positive and negative EB fields for $x$ = 0.30, 0.40 and 0.50 samples have been observed close to the room temperature. Such tunable EB behavior is explained in terms of change in domination of one sublattice moment over the other as the temperature is varied.

For the first time we have demonstrated the bipolar switching of magnetization at room temperature for $x$ = 0.30 and 0.40 samples by just varying the magnitude of magnetic field without changing its direction.

# Chapter 4

# $Ni(Cr, Al)_2O_4$ Series

## 4.1 Introduction

In the previous chapter, we have seen that substitution of magnetic $Fe^{3+}$ ions with $d^5$ electronic configuration in the $Cr^{3+}$ site of $NiCr_2O_4$ highly influenced its structural and magnetic properties. Fe substitution stabilized the cubic spinel structure. As a result of closely packed oxygen anions in the cubic structure and corresponding decrease in the A – O – B as well as B – O – B bond distance with Fe substitution, we observed enhanced ferrimagnetic (FIM) transition temperature to even above room temperature. Furthermore, due to strengthening of these interactions, Fe substituted samples are found to exhibit higher value of exchange bias (EB) field. Fe substitution disturbs the original normal cation distribution in $NiCr_2O_4$ and leads to a magnetic compensation along with negative magnetization. For higher concentration of Fe, in addition to magnetization reversal (MR) EB field close to room temperature is observed.

In the current chapter we are going to discuss how the structural as well as magnetic properties are altered due to the substitution of non magnetic ions with $d^0$ configuration in the $Cr^{3+}$ site. A few authors have studied these properties on non magnetic $Al^{3+}$ ($d^0$) substituted $CoCr_2O_4$ and $MnCr_2O_4$ [40, 147, 191]. They have found an increase in magnetization up to a particular concentration of $Al^{3+}$ in the $Cr^{3+}$ site of $CoCr_2O_4$. $NiAl_2O_4$ is a cubic spinel at room temperature while $NiCr_2O_4$ is tetragonal [192]. Therefore we can expect a structural transition from tetragonal to cubic as in case of Fe substituted $NiCr_2O_4$ series in Chapter 3. Magnetic properties of spinel compounds strongly depend upon the cations residing in the tetrahedral and the octahedral site. So Al substitution is expected to change the basic

magnetic properties of $NiCr_2O_4$ as well as to initiate MR phenomenon. There are obviously other non magnetic ions in the same group of $Al^{3+}$, like $Ga^{3+}$, $In^{3+}$ and $Ti^{3+}$. But $Ga^{3+}$ has a greater tendency to occupy the tetrahedral site and we want to replace $Cr^{3+}$ by $Al^{3+}$ in the octahedral site only [193]. However, the size of $In^{3+}$ and $Ti^{3+}$ are quite larger compared to $Cr^{3+}$.

Therefore in the present chapter, we have studied the influence of $Al^{3+}$ ($d^0$) ion substitution on the structural, temperature and field dependent magnetic properties of $Ni(Cr_{1-x}Al_x)_2O_4$.

Polycrystalline samples of $Ni(Cr_{1-x}Al_x)_2O_4$ for $x = 0 – 0.50$ were prepared by using sol–gel method. Stoichiometric ratio of high purity (99 %) $Ni(NO_3)_2.6H_2O$, $Al(NO_3)_3.9H_2O$ and $Cr(NO_3)_3.9H_2O$ were taken as the starting compounds. The samples were presintered at 600 °C, 800 °C and 1000 °C for 12 hours each followed by final sintering at 1100 °C for 24 hours in pellet form. X-ray diffraction (XRD) pattern at room temperature was recorded by using Rigaku make TTRAX III X-ray diffractometer using Cu-Kα radiation. Microstructure and composition analyses were carried out using ZEISS make field emission scanning electron microscope (FESEM, ΣIGMA) equipped with energy dispersive X-ray spectroscopy (EDS) facilitiy. Temperature and field dependent magnetization measurements were performed by using a Lakeshore make vibrating sample magnetometer (VSM) of model no. 7410.

## 4.2 Structural Properties

The XRD patterns of $Ni(Cr_{1-x}Al_x)_2O_4$ ($x = 0 – 0.50$) samples recorded at room temperature are shown in Fig. 4.1. Figure shows that all the observed peaks for $x = 0$ sample could be indexed to tetragonal structure and for $x \geq 0.05$, they are indexed to cubic structure. The room temperature XRD pattern of $Ni(Cr_{1-x}Al_x)_2O_4$ ($x = 0 – 0.50$) samples were analyzed by Rietveld refinement method using Fullprof software. Fig. 4.2 and Fig. 4.3 show the typical XRD patterns for $x = 0$, 0.05 and $x = 0.20$, 0.30 samples, respectively, along with Rietveld refinement data. The refinement demonstrates that $x = 0$ sample crystallizes in tetragonal structure with $I4_1/amd$ space group and the Al doped samples crystallize in cubic structure with $Fd\bar{3}m$ space group. Thus like Fe substitution as discussed in Chapter 3, the Al

substitution also strongly suppresses the JTD and the material crystallizes in cubic structure at room temperature. The lattice parameters of $x = 0$ sample are found to be $a = b = 5.828$ Å and $c = 8.415$ Å which are in good agreement with earlier reports [133]. The lattice parameter of the Al substituted samples follow a systematic decreasing trend with increase in the Al concentration '$x$' as depicted in Fig. 4.4. This decreasing trend of lattice parameter confirms the substitution of $Al^{3+}$ ions having smaller ionic radius of 0.535 Å at the $Cr^{3+}$ site (0.615 Å). The lattice parameters, reliability factors and unit cell volume of all the samples at room temperature are displayed in table 4.1.

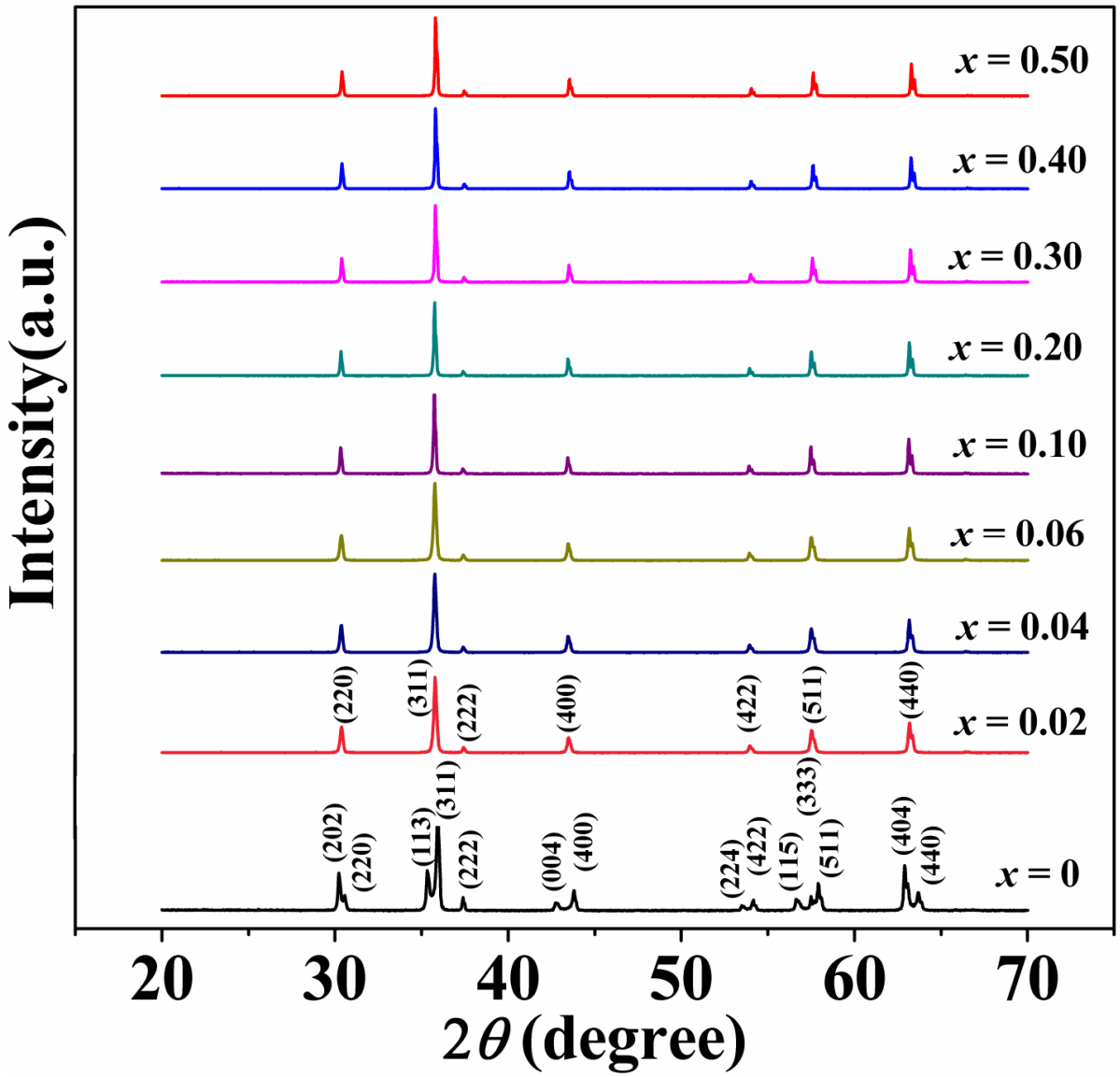


**Figure 4.1:** XRD patterns of $Ni(Cr_{1-x}Al_x)_2O_4$ compounds for $x = 0 – 0.50$.

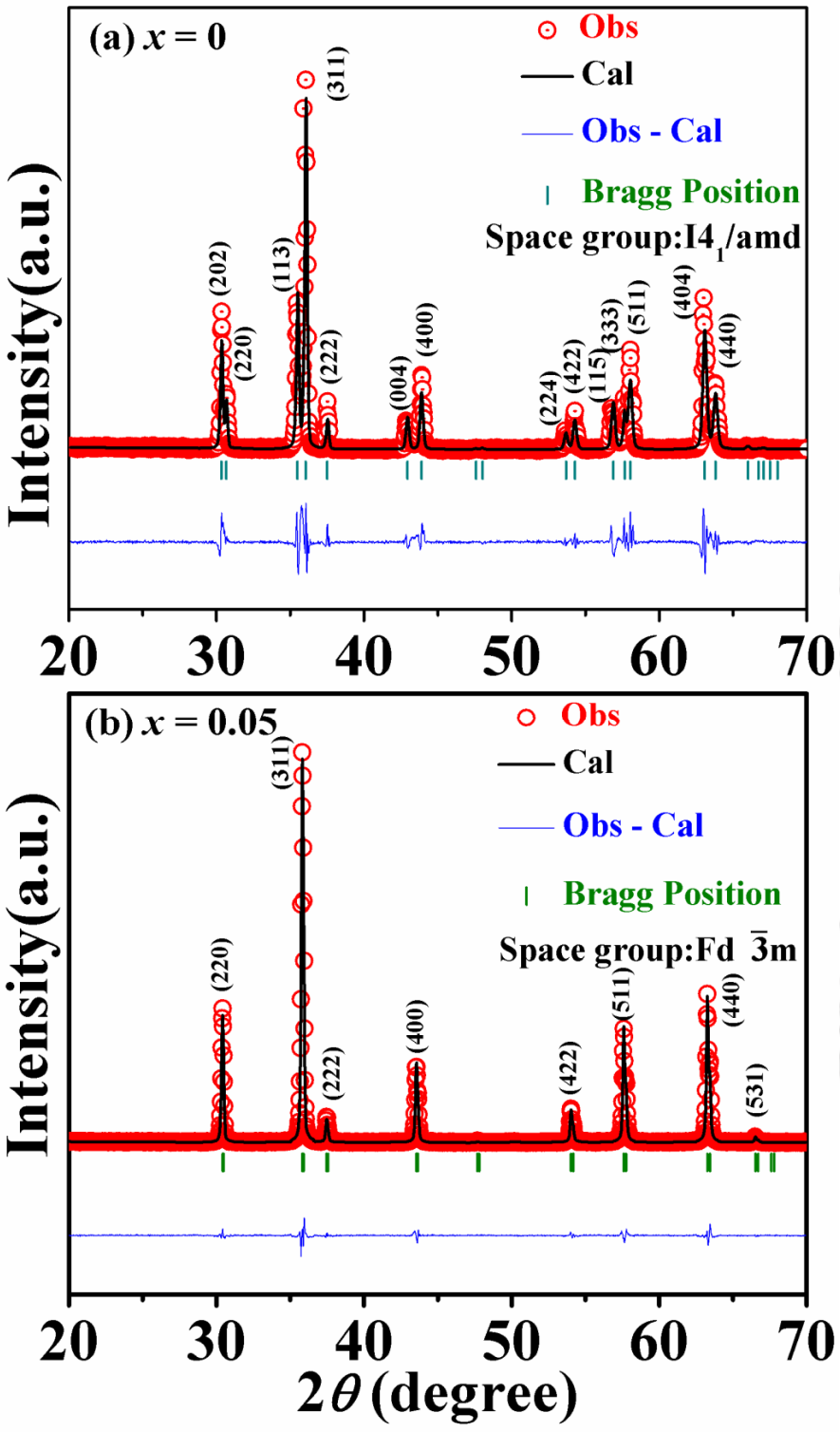


**Figure 4.2:** Rietveld refinement of the XRD patterns of (a) $x$ = 0 and (b) $x$ = 0.05 samples. The red open circles are the experimental data and the black solid lines are the fitted data. The bottom line shows the difference between experimental and refined data.

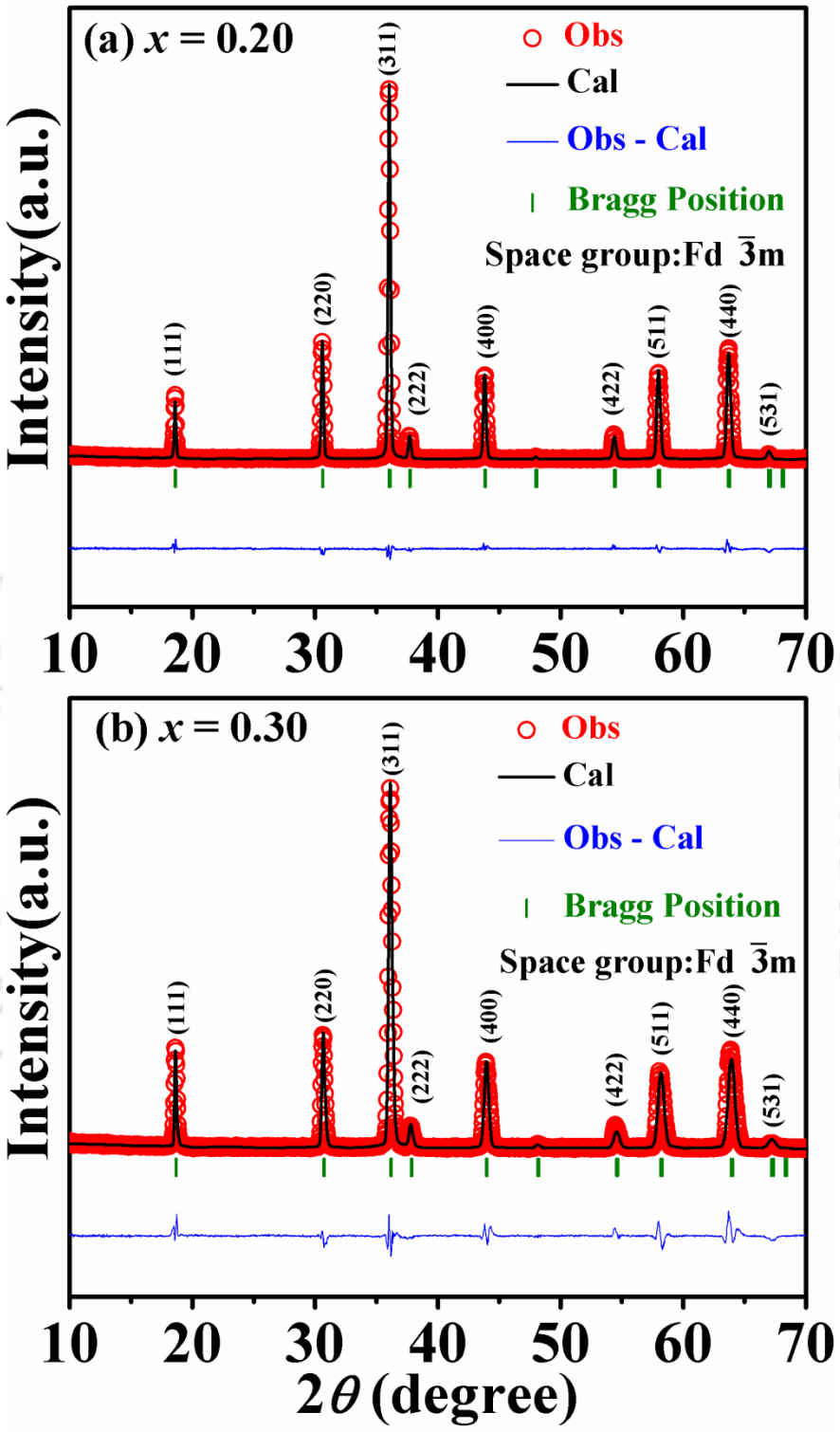


**Figure 4.3:** Rietveld refinement of the XRD patterns of (a) $x$ = 0.20 and (b) $x$ = 0.30 samples. The red open circles are the experimental data and the black solid lines are the fitted data. The bottom line shows the difference between experimental and refined data.

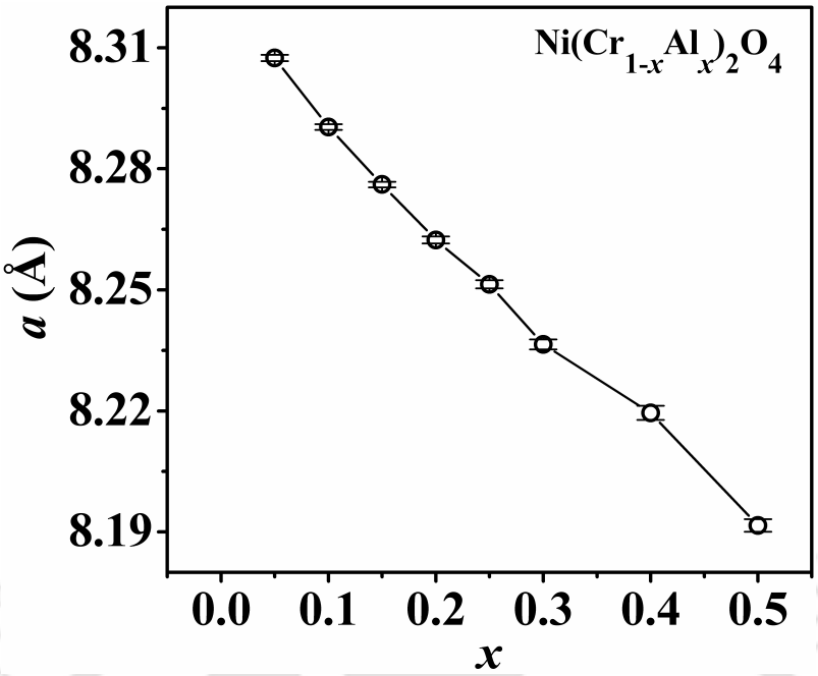


**Figure 4.4:** Variation of lattice parameter '*a*' with Al concentration '*x*'.

**Table 4.1:** Parameters obtained from the Rietveld analysis of XRD patterns for the samples $Ni(Cr_{1-x}Al_x)_2O_4$ (0 – 0.50). $R_F$, $R_{Bragg}$, $R_P$ and $\chi^2$ are the reliability factors.

| **Sample/ Parameters** | ***x* = 0** | ***x* = 0.05** | ***x* = 0.10** | ***x* = 0.15** | ***x* = 0.20** | ***x* = 0.25** | ***x* = 0.30** | ***x* = 0.40** | ***x* = 0.50** |
|---|---|---|---|---|---|---|---|---|---|
| **Space group** | $I4_1/amd$ | $Fd\bar{3}m$ | $Fd\bar{3}m$ | $Fd\bar{3}m$ | $Fd\bar{3}m$ | $Fd\bar{3}m$ | $Fd\bar{3}m$ | $Fd\bar{3}m$ | $Fd\bar{3}m$ |
| ***a* (Å)** | 5.8285 (0.0010) | 8.3075 (0.0007) | 8.2904 (0.0007) | 8.2761 (0.0006) | 8.2624 (0.0008) | 8.2514 (0.0007) | 8.2365 (0.0008) | 8.2195 (0.0007) | 8.1916 (0.0007) |
| ***c* (Å)** | 8.4156 (0.0015) | – | – | – | – | – | – | – | – |
| ***Volume* (Å$^3$)** | 285.89 (0.09) | 573.33 (0.09) | 569.80 (0.08) | 566.86 (0.08) | 564.05 (0.09) | 561.79 (0.09) | 558.76 (0.09) | 555.31 (0.08) | 549.68 (0.08) |
| **$R_F$ (%)** | 4.47 | 2.15 | 2.89 | 2.82 | 3.36 | 3.42 | 5.29 | 3.38 | 7.59 |
| **$R_{Bragg}$ (%)** | 6.25 | 2.21 | 2.70 | 3.31 | 4.03 | 3.51 | 7.02 | 5.83 | 10.5 |
| **$R_P$ (%)** | 16.70 | 7.64 | 7.08 | 7.28 | 7.58 | 9.38 | 10.90 | 13.50 | 11.6 |
| $\chi^2$ | 7.75 | 4.28 | 4.19 | 4.74 | 3.43 | 5.69 | 7.26 | 7.54 | 7.08 |
| **Ni/Cr/Al Occupancy** | 0.959 /2.005 /0.000 | 0.998 /1.902 /0.102 | 0.989 / 1.809 / 0.209 | 0.976 / 1.716 / 0.316 | 0.907 /1.579 /0.379 | 0.850 /1.500 /0.500 | 0.812 /1.367 /0.567 | 0.773 /1.476 /1.076 | 0.707 /1.282 /1.282 |

The microstructural images of $x$ = 0.10 and 0.20 samples are shown in Fig. 4.5 along with the EDS spectrum (right column of the Fig. 4.5). The grain sizes of the samples are found to be distributed in a wide range as shown in Fig. 4.6 for $x$ = 0.10 and 0.20 samples. The average grain size of each sample is obtained by fitting the size distribution histogram to log normal distribution function given by Eq. (3.1) in Chapter 3 [168]. The average grain size of the samples is found to be in the range of 270 – 314 nm with a standard deviation in the range of 0.09 to 0.16 nm. However, the crystallite size estimated from the analysis of XRD patterns is found to be only in the range of 40 to 65 nm and the difference is attributed to the agglomeration of several crystallites into particle. The cation ratios Ni: Cr: Al obtained from EDS analysis for $x$ = 0.10 and 0.20 samples are found to be 0.98: 1.81: 0.19 and 0.99: 1.63: 0.37, respectively which are comparable to the nominal starting compositions.

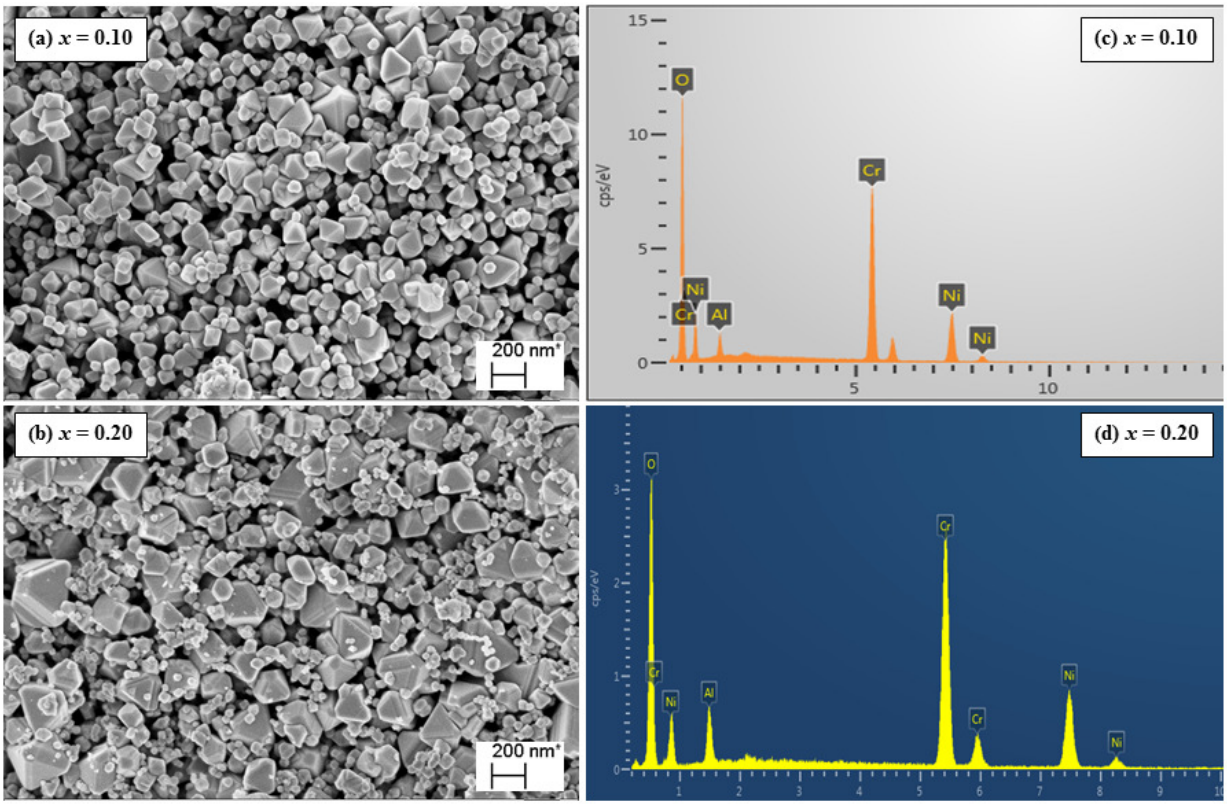


**Figure 4.5:** FESEM images recorded for (a) $x$ = 0.10 and (b) $x$ = 0.20 samples along with EDS spectrum [(c) and (d), respectively].

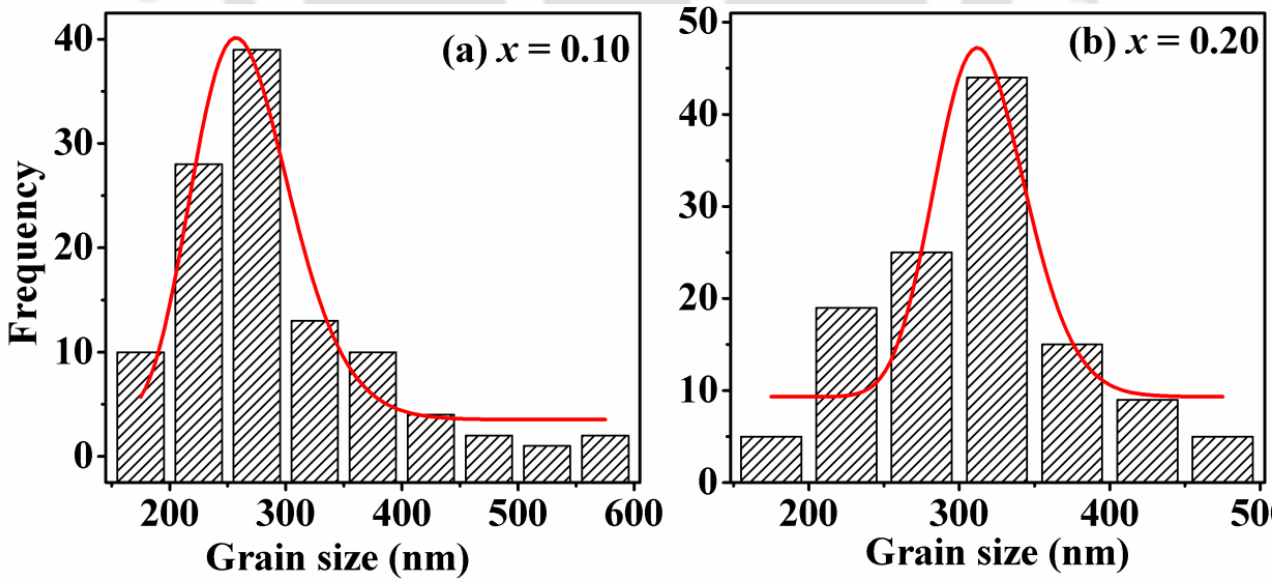


**Figure 4.6:** Grain size distribution of (a) $x$ = 0.10 and (b) $x$ = 0.20 samples.

## 4.3 Temperature and Field Dependent Magnetic Properties

Temperature dependent zero field cooled (ZFC) and field cooled (FC) magnetization ($M$–$T$) for all Ni($Cr_{1-x}Al_x$)$_2$O$_4$ ($x$ = 0 – 0.50) samples were recorded under an applied field of $H$ = 500 Oe. Fig. 4.7 shows the ZFC and FC $M$–$T$ curves of all the samples. A peak observed in the ZFC $M$–$T$ curves of each sample in the series indicates FIM nature of the samples. The FC magnetization is found to be largely enhanced with decrease in temperature as compared to the ZFC magnetization. This huge bifurcation between ZFC and FC curves below FIM transition temperature ($T_C$) is observed due to the presence of competing antiferromagnetic (AFM) interactions along with the long range FIM. The bifurcation appears to be decreased gradually with increase in the Al concentration due to the measured temperature being closed to the $T_C$. The FC $M$–$T$ curves of all the samples show similar behavior with positive magnetization value except that for $x$ = 0.10 sample. For $x$ = 0.10, the FC magnetization below $T_C$ increases first as that of the other samples; but after reaching a maximum value it decreases and becomes zero at 40 K. With further decrease in temperature the magnetization becomes negative. Details of such behavior are discussed in details in section 4.4.

The FIM $T_C$ was determined from $dM$ / $dT$ versus $T$ plot of each sample and for the parent compound ($x$ = 0) it is found to be 73 K which is equivalent to that reported by Ptak *et al.* [133]. With increase in Al concentration, the $T_C$ value is found to decrease from 73 K to 38 K for $x$ = 0.50 sample. The decreasing trend is clearly understood from Fig. 4.8. In the present series, even though the crystal structure at room temperature changes from tetragonal for $x$ = 0 sample to cubic for $x \geq 0.05$ samples, from the figure we have not observed any drastic change in FIM $T_C$. However, a drastic fall in $T_C$ is observed especially when Al concentration is varied from $x$ = 0.10 to 0.15. All samples in the present series have their FIM $T_C$ at quite below room temperature and therefore we cannot rule out the possibility of structural change into tetragonal cell in Al doped samples at low temperatures. Moreover, as per the XRD analysis, the Cr – O – Cr bond angle in both tetragonal and cubic structures is comparable (95.43° and 95.28°, respectively). As a result the superexchange interaction in Cr – O – Cr networks is not expected to be altered drastically rather than being diluted due to

non magnetic Al substitution and accordingly $T_C$ also does not change drastically while moving from $x$ = 0 to 0.05. The decrease in $T_C$ however highlights that substituted non magnetic $Al^{3+}$ ions strongly weaken the superexchange interaction within B sublattice ions ($Cr^{3+}$ – $O^{2-}$ – $Cr^{3+}$/$Al^{3+}$) as well as among A and B sublattice ions ($Ni^{2+}$ – $O^{2-}$ – $Cr^{3+}$/$Al^{3+}$).

The maximum ZFC magnetization value corresponding to the peak temperature can provide information about the occupation of Al ions in different magnetic sublattices. For $x$ = 0 and 0.05 samples the peak values are found to be comparable, however for $x$ = 0.10 sample it is found to be reduced by an order of magnitude. For further increase in Al concentration up to $x$ = 0.30 the peak magnetization value systemically increases and beyond that it decreases. In order to make this increase and decrease in the peak magnetization value evident, the ZFC $M$–$T$ curves are shown separately in Fig. 4.9. According to literature, the total magnetization of $NiCr_2O_4$ per formula unit can be written as $M = |\uparrow \mu_{A1\text{-}A2} + \uparrow \mu_{B1\text{-}B3} - \downarrow \mu_{B2\text{-}B4}|$, where $\uparrow \mu_{A1\text{-}A2}$, $\uparrow \mu_{B1\text{-}B3}$ and $\downarrow \mu_{B2\text{-}B4}$ are the longitudinal components of the magnetic moments of A1-A2, B1-B3 and B2-B4 sublattices, respectively with respect to the field direction [54]. Therefore it is obvious that the decrease in magnitude of magnetization up to $x$ = 0.10 is due to the occupation of the $Al^{3+}$ in the B1-B3 site. While above $x$ = 0.10, $Al^{3+}$ may start occupying the B2-B4 site also, leading to the enhanced net magnetization. However, $T_C$ of the $x$ = 0.40 and $x$ = 0.50 samples are quite small which may cause decrease in magnetization near $T_C$. In the later part we are going to validate this argument by means of the value of saturation magnetization ($M_s$) determined from the $M$–$H$ loops. This distribution of Al ions also explains the sharp fall in $T_C$ from 65 K for $x$ = 0.10 to 45 K for $x$ = 0.15 sample (Fig. 4.8). Since for $x$ > 0.10, $Al^{3+}$ ions occupy both B1-B3 and B2-B4 sites so there is a possibility of sudden decrease in the concentration of $Ni^{2+}$ – $O^{2-}$ – $Cr^{3+}$ and $Cr^{3+}$ – $O^{2-}$ – $Cr^{3+}$ networks. This in turn leads to the rapid decrease of superexchange interaction and hence the $T_C$ value for $x$ = 0.15.

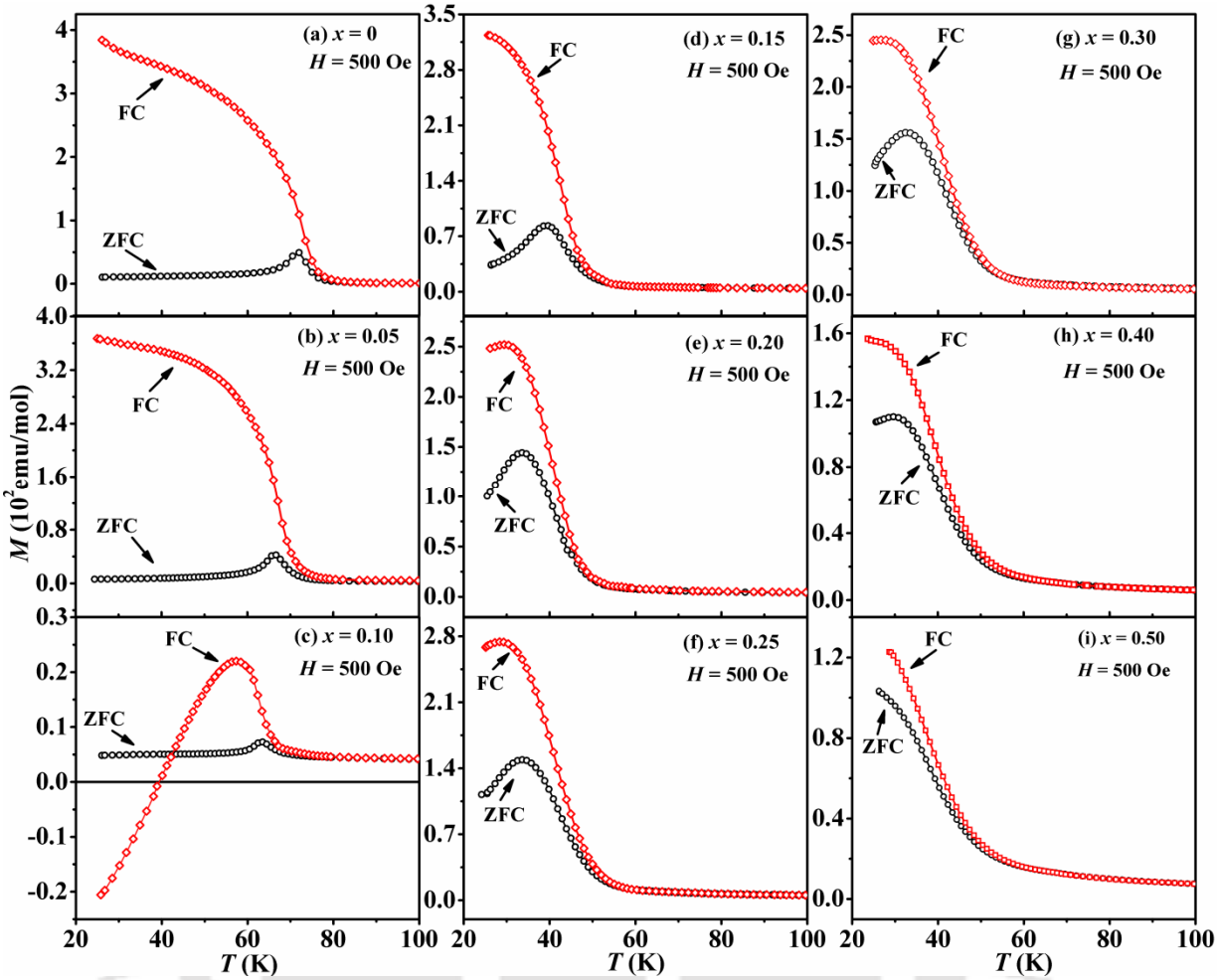


**Figure 4.7:** Temperature dependent magnetization of $Ni(Cr_{1-x}Al_x)_2O_4$ ($x$ = 0 – 0.50) samples under ZFC and FC conditions.

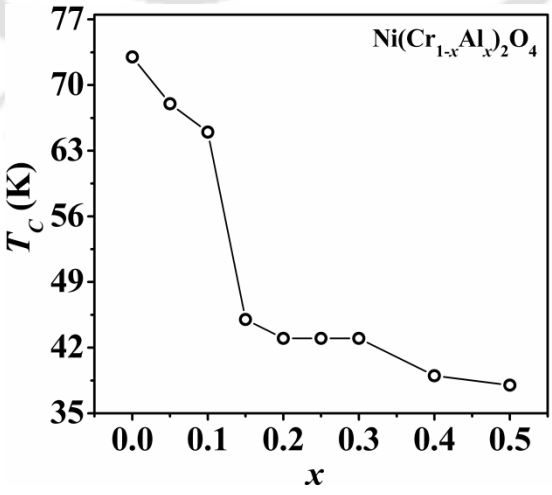


**Figure 4.8:** Variation of $T_C$ with Al concentration '$x$'.

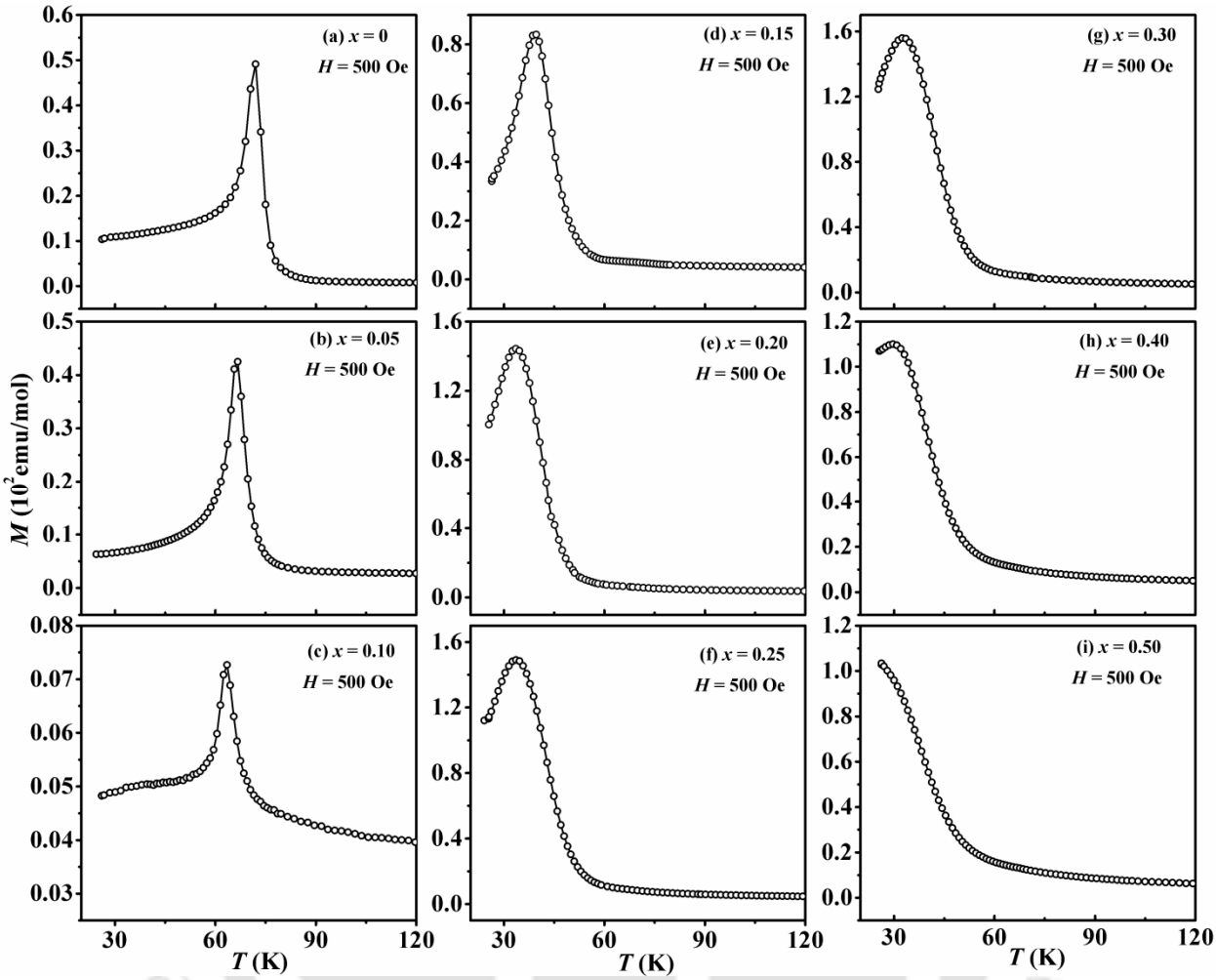


**Figure 4.9:** Temperature dependent magnetization of Ni(Cr$_{1-x}$Al$_x$)$_2$O$_4$ ($x$ = 0 – 0.50) samples under ZFC condition in an expanded scale.

The dc susceptibility ($\chi$) of Ni(Cr$_{1-x}$Al$_x$)$_2$O$_4$ in the paramagnetic (PM) region were fitted by the Curie-Weiss (CW) law $\chi = C/(T - \Theta_C)$, where $C$ and $\Theta_C$ are the curie constant and curie temperature, respectively. Fig. 4.10 shows the CW fit for $x$ = 0 – 0.50 samples. The hyperbolic shape of the inverse $\chi^{-1}$ versus temperature plot confirms the FIM nature of the samples. The negative value of Currie temperature $\Theta_C$ obtained for all the samples indicates that the magnetism in these samples is governed by negative superexchange interaction. The magnitude of $\Theta_C$ value is found to decrease from – 557 K for $x$ = 0 to – 210 K for $x$ = 0.50 sample with increase in Al concentration and is consistent with expected reduction in superexchange interaction. The effective PM moment ($\mu_{eff}$) can be determined from the Curie

constant $C = N\mu_{eff}^2 / 3k_B$, obtained from the CW fit. The theoretical $\mu_{eff}$ values can be calculated from,

$$\mu_{eff} = \sqrt{\mu_{Ni}^2 + 2(1-x)\mu_{Cr}^2} \tag{4.1}$$

where, $\mu_{Ni}$ and $\mu_{Cr}$ are the theoretical moments of $Ni^{2+}$ and $Cr^{3+}$. $Ni^{2+}$ and $Cr^{3+}$ are considered in high spin sate and their spin only magnetic moments are determined using the expression $g\sqrt{s(s+1)}$ and are found to be 2.83 $\mu_B$ and 3.87 $\mu_B$, respectively. The $\mu_{eff}$ values obtained from the experimental data and the theoretical $\mu_{eff}$ values as a function of doping concentration are shown as black circles and red squares, respectively in Fig. 4.11. Both are found to be almost comparable and decreases with increase in Al concentration as expected due to occupation of $Al^{3+}$ with zero magnetic moment in the Cr site. The magnetic frustration can be experimentally estimated from $f = |\Theta_C| / T_C$, known as the frustration index [19]. If magnetic exchange energy is not frustrated by any other sources, the system should suffer long range magnetic ordering exactly at $T \approx |\Theta_C|$ as familiar for bulk FM systems ($f \approx 1$). But this is not true for AFM or FIM materials in which magnetic ordering temperature $T_C$ is always smaller compared to $|\Theta_C|$. In general weak magnetic frustration survives if $2 \leq f \leq 10$ and it leads to stable non-collinear spin configurations. From the CW fit, we found the value of $f$ for $NiCr_2O_4$ to be 7.6 which is comparable to reported value of 7.8 by Suchomel *et al.* [19]. It initially decreases slightly with Al substitution up to $x = 0.10$ ($f = 7.4$) while beyond it increases and reaches a maximum value of around 9. Thus all the samples in the present series exhibit weak magnetic frustration. Value of $f$ is also comparable to $CoCr_2O_4$ ($f = 8$) but it is smaller than $ZnCr_2O_4$ ($f = 16$) with non magnetic Zn in the A site [33].

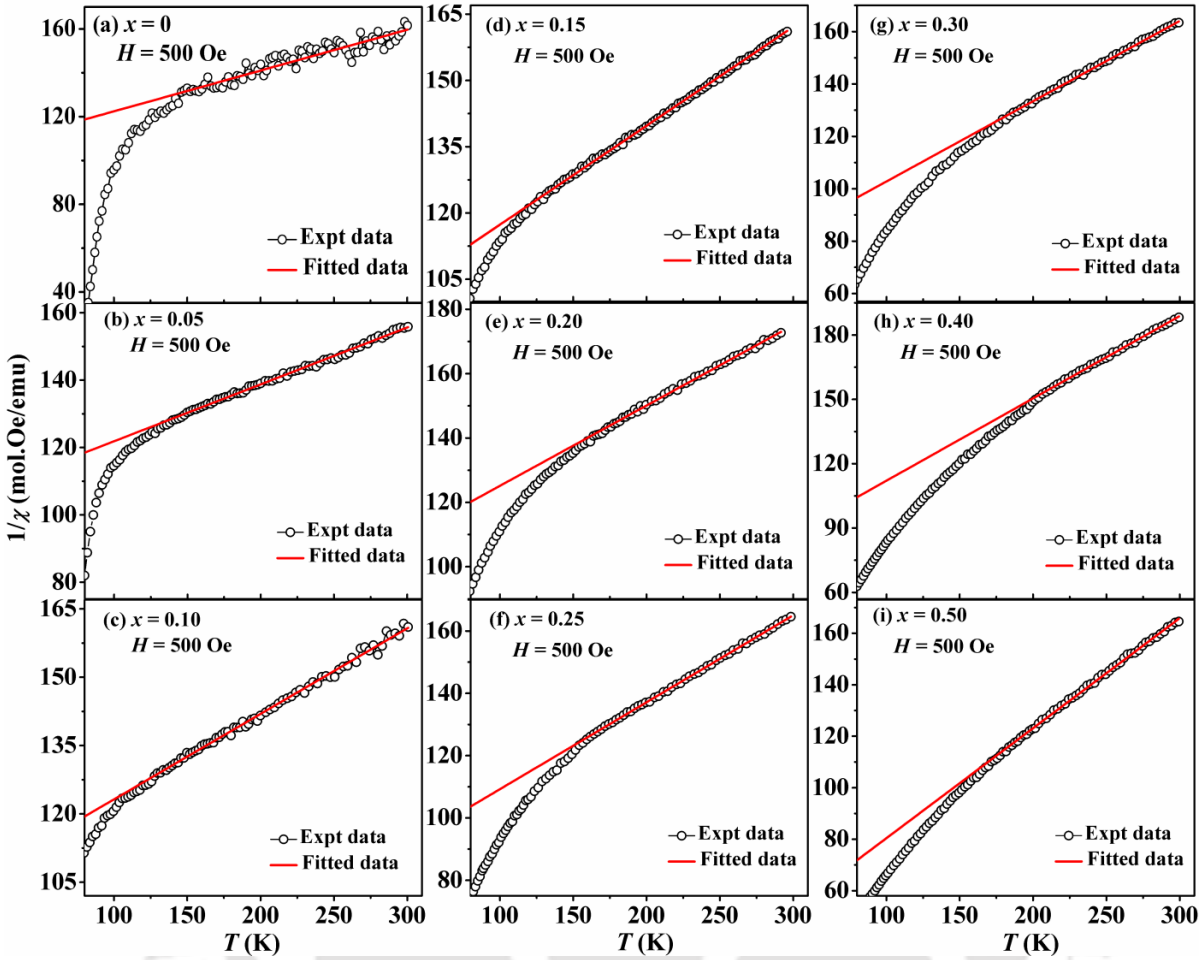


**Figure 4.10:** The Curie-Weiss fit in the PM region of $Ni(Cr_{1-x}Al_x)_2O_4$ ($x$ = 0 – 0.50).

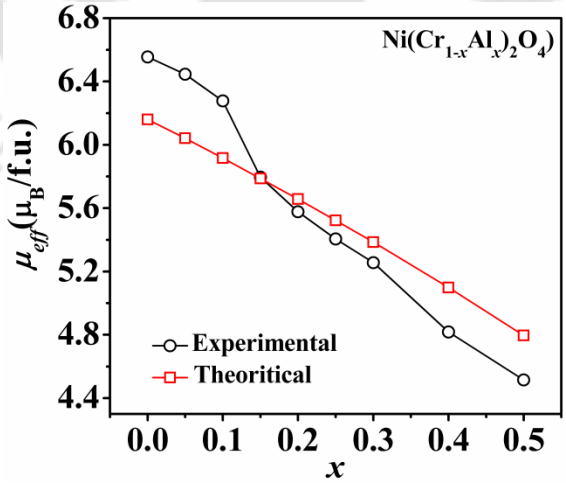


**Figure 4.11:** Variation of experimental (circle) and theoretical (Square) effective magnetic moment '$\mu_{eff}$' with Al concentration '$x$'.

Field dependent magnetization (*M–H*) loops for all the samples were recorded at different temperatures after cooling the samples under zero field. The typical ZFC *M–H* loops recorded at 30 K for all the samples are shown in Fig. 4.12. According to literature $NiCr_2O_4$ exhibits both FIM and AFM ordering [54]. In the present series of samples, large hysteresis loss observed for $NiCr_2O_4$ confirms the presence of competing AFM in addition to the existing long range FIM interaction. The $x = 0.05$ sample also exhibits similar behavior but with a minor loop like behavior due to the presence of large magnetic anisotropy and competing AFM. Almost linear behavior of the *M–H* loop is observed for $x = 0.10$ sample. This may be because of the selection of the temperature which is in the vicinity of magnetic compensation and moreover this sample exhibits lowest ZFC magnetization value as shown in Fig. 4.9(c). However, due to random substitution of Al ions in both the B sites for higher concentration of Al, some of the isolated $Cr^{3+}$ ions may not take part in superexchange interaction and hence remain uncompensated. These uncompensated $Cr^{3+}$ moments may align in the applied field direction and gives rise to additional FM moment. Such additional FM moment results in an increase in the net magnetic moment and coercivity as observed for highly Al doped samples. The saturation magnetization, $M_s$ values were determined by fitting the high field magnetization data to,

$$M(H) = \chi_{AFM}H + M_s \tag{4.2}$$

where, $\chi_{AFM}H$ is the AFM contribution to the magnetization and $M_s$ is the saturation magnetization which is the FM contribution to the total magnetization [194]. $M_s$ values were converted in the unit of Bohr magneton per formula unit of $NiCr_2O_4$ and variation of $M_s$ with increasing $x$ is shown in Fig. 4.13. $M_s$ first decreases up to $x = 0.10$ which can be attributed to the substitution of Al in the B1-B3 site. As discussed from *M–T* data for $x > 0.10$, Al occupies both the B1-B3 and B2-B4 sites causing an increase in $M_s$ up to $x = 0.30$. Some uncompensated $Cr^{3+}$ moments may also supply additional FM moment to the net moment as discussed above. For $x > 0.30$, $T_C$ is quite small and consequently $M_s$ decreases substantially.

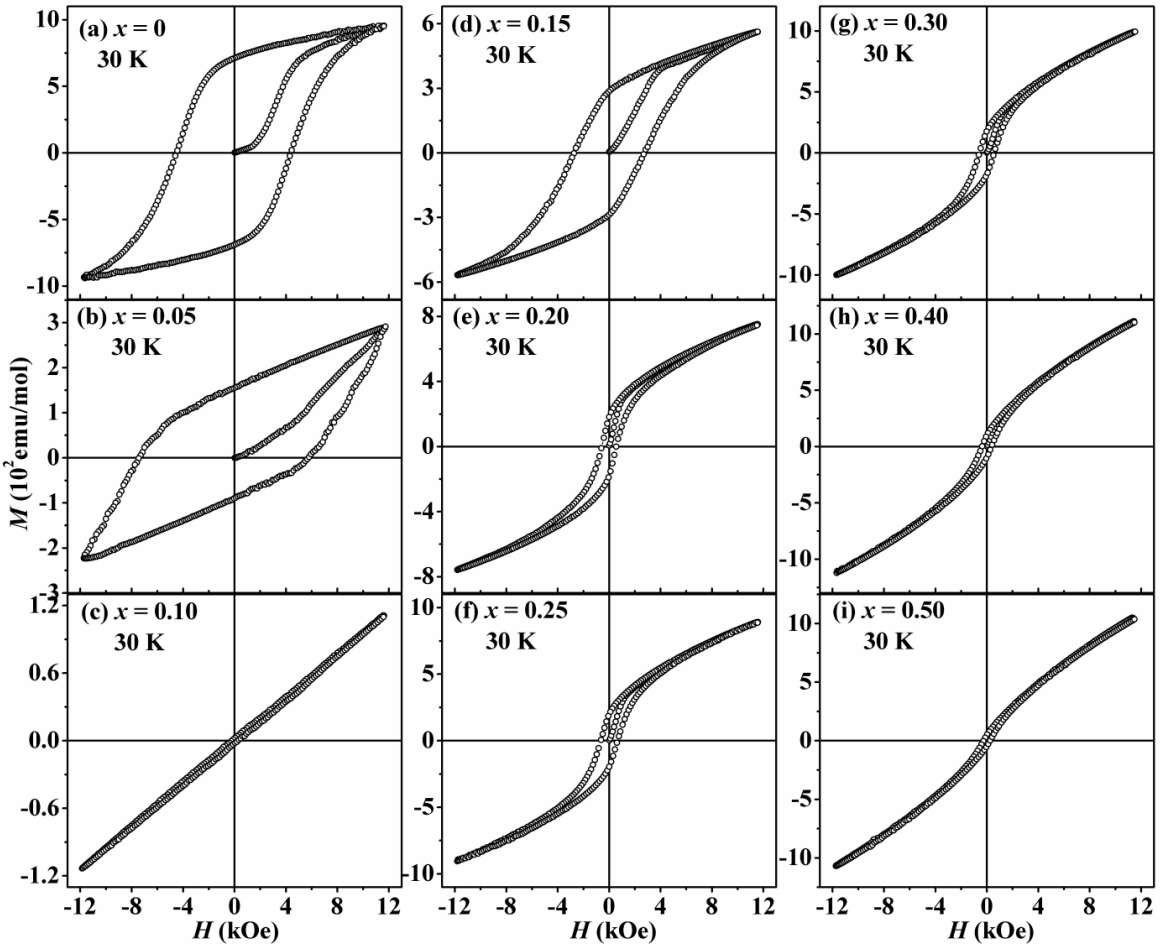


**Figure 4.12:** *M-H* loops at 30 K for Ni(Cr$_{1-x}$Al$_x$)$_2$O$_4$ ($x$ = 0 – 0.50) samples under ZFC condition.

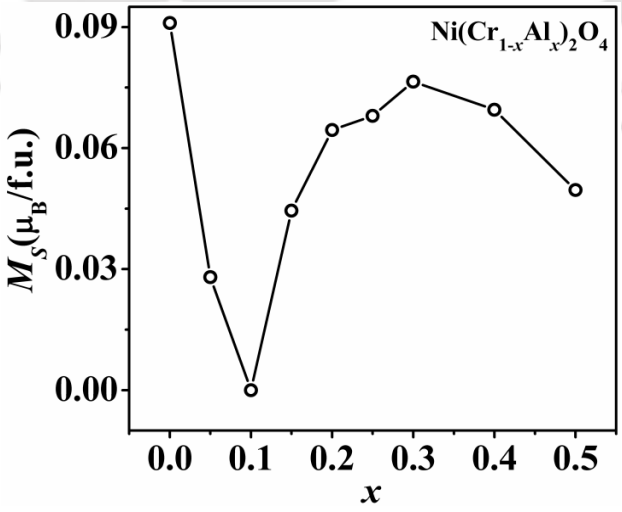


**Figure 4.13:** Variation of saturation magnetization '$M_s$' with Al concentration '$x$'.

## 4.4 Magnetization Reversal

From the variation of ZFC magnetization (Fig. 4.9) and the $M_s$ value (Fig. 4.13) for $Ni(Cr_{1-x}Al_x)_2O_4$ series, we have found that both decreases with increase in Al concentration and attain a minimum value for $x = 0.10$. Thereafter again both of them increase. Therefore, $x = 0.10$ falls at the vicinity of the compositional compensation. Moreover, in Fig. 4.7 we have noticed that the FC magnetization of $x = 0.10$ sample shows a distinguishable behavior. The FC magnetization of $x = 0.10$ sample reverses its sign below a certain temperature. Therefore we have taken the $x = 0.10$ sample for the comprehensive study of the MR behavior.

As shown in Fig. 4.14 (a), below $T_C$ the FC magnetization of $x = 0.10$ sample at $H = 500$ Oe first increases and attains a maximum value at a temperature of around 57 K. For further decrease in temperature, magnetization crosses the $M = 0$ axis at 40 K and then move towards negative value. Thus the magnetic compensation temperature ($T_{comp}$) value for $x = 0.10$ sample is 40 K. When the applied magnetic field is increased, the magnitude of negative magnetization as well as the $T_{comp}$ value decreases. $T_{comp}$ is found to decrease slightly from 40 K for $H = 500$ Oe to 32 K for $H = 2000$ Oe. Finally for an applied field of 2500 Oe the MR completely disappears and the magnetization remains positive in all temperature range as depicted in Fig. 4.14 (b). It is noticeable that the magnetization value becomes positive without changing the trend of $M$–$T$ curves, apart from shifting of the entire $M$–$T$ curve towards positive magnetization. It implies no major change in the mechanism of magnetic interaction rather than field induced increase in canted FIM component. The negative magnetization observed below $T_{comp}$ in this sample can be explained by considering two magnetic sublattices in the framework of Neel's theory [62]. In $NiCr_2O_4$, the net magnetization is positive below $T_C$ because here the A sublattice moment, $\mu_A$ is larger than the B sublattice moment, $\mu_B$ ($= \mu_{B1\text{-}B3} - \mu_{B2\text{-}B4}$) [54]. Replacement of Cr ions in B1-B3 site by non magnetic Al ions causes an increase in net B sublattice moment. It thereby decreases the net magnetic moment leading to the compositional compensation at $x = 0.10$. Hence for $x = 0.10$, B sublattice moment become comparable to that of $\mu_A$ and due to their different temperature dependences negative magnetization is observed for this composition. For $T_{comp} < T < T_C$, for small applied field the A site moment is aligned along the field direction and the resultant B site moment align antiparallel to A site moment. In this arrangement $\mu_A > \mu_B$

(= $\mu_{B1\text{-}B3} - \mu_{B2\text{-}B4}$) and it results in net positive moment. As the temperature decreases, B site moemnt gradually starts rising and at $T = T_{comp}$, it compensates $\mu_A$ and the net magnetization becomes zero. As the sample is cooled below $T_{comp}$, B site moment overcomes $\mu_A$ resulting in a net negative magnetization. However, in this temperature range when a large field is applied, the decrease in magnetic anisotropy of $Cr^{3+}$ sublattice moment and the enhancement in the canted FIM component of $Cr^{3+}$ along field direction lead to the decrease in negative magnetization and finally changes to the positive value. For $x > 0.10$, due to possible substitution of Al ions in both B1-B3 and B2-B4 site, whole B site moment starts diluting and the net B site meoment cannot be dominant over $\mu_A$ at any given temperature. Therefore, no MR is observed for $x > 0.10$.

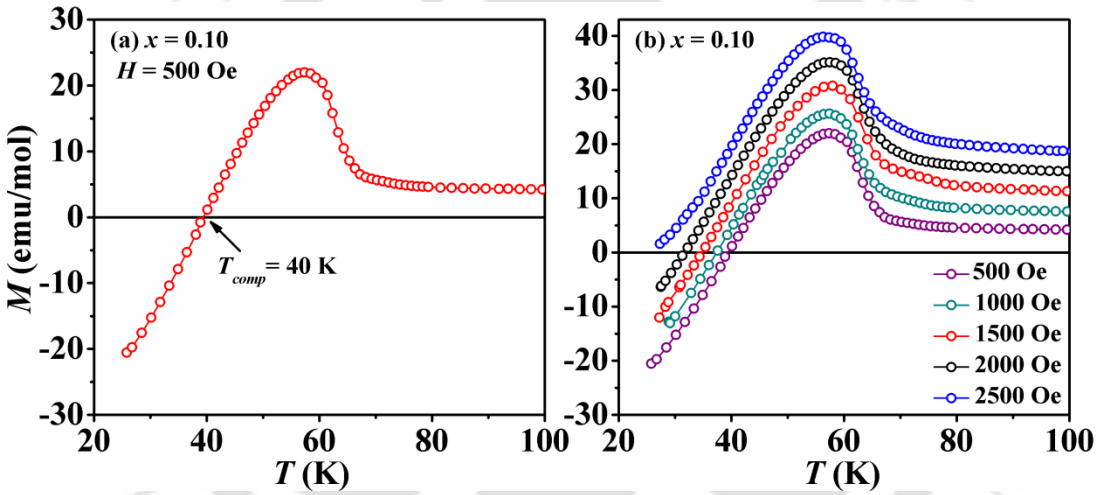


**Figure 4.14:** Temperature dependence of FC magnetization for $x = 0.10$ sample (a) at an applied field of 500 Oe and (b) at different applied fields.

## 4.5 Exchange Bias Behavior

Study of EB behavior was carried out in the present series of samples. With the purpose of examining the EB behavior, *M–H* loops of each sample were recorded at different temperatures after cooling the sample under an applied field of 3000 Oe. The FC *M–H* loops for $x = 0.05$ sample are found to shift towards negative *H*-axis. Although this sample shows signature of negative EB, we could not carry out further analysis because in most of the measured temperatures the *M–H* loops were found to be of minor loop type due to the

presence of large anisotropy and the limitation of maximum applied field in the present set up. So we have excluded this sample from the study of EB field. In contrast to $x$ = 0.05, FC $M$–$H$ loops of $x$ = 0.10 sample are found to shift towards both positive and negative field axis. When the sample is FC through its $T_C$, $M$–$H$ loops at just below $T_C$ are found to shift towards the negative field axis. In the vicinity of $T_{comp}$, the loops are found to be symmetric and for further decrease in temperature ($T < T_{comp}$), the loops are found to shift towards positive field axis. Such behavior of $M$–$H$ loop indicates that for $x$ = 0.10 sample, together with the magnetization the EB field can also be tuned from positive to negative without varying the direction of $H$ but by just varying the temperature. FC $M$–$H$ loops for this sample at different temperatures close to $T_{comp}$ are shown in Fig. 4.15 in expanded scales. Similar to $x$ = 0.05 sample, FC $M$–$H$ loops for $x$ = 0.15 exhibit the shifting towards negative field axis as shown in Fig. 4.16 in expanded scales. However, for samples with $x$ > 0.15, no considerable shift in the $M$–$H$ loop is observed. This may be due to the decrease in magnetic interactions with increasing Al concentration.

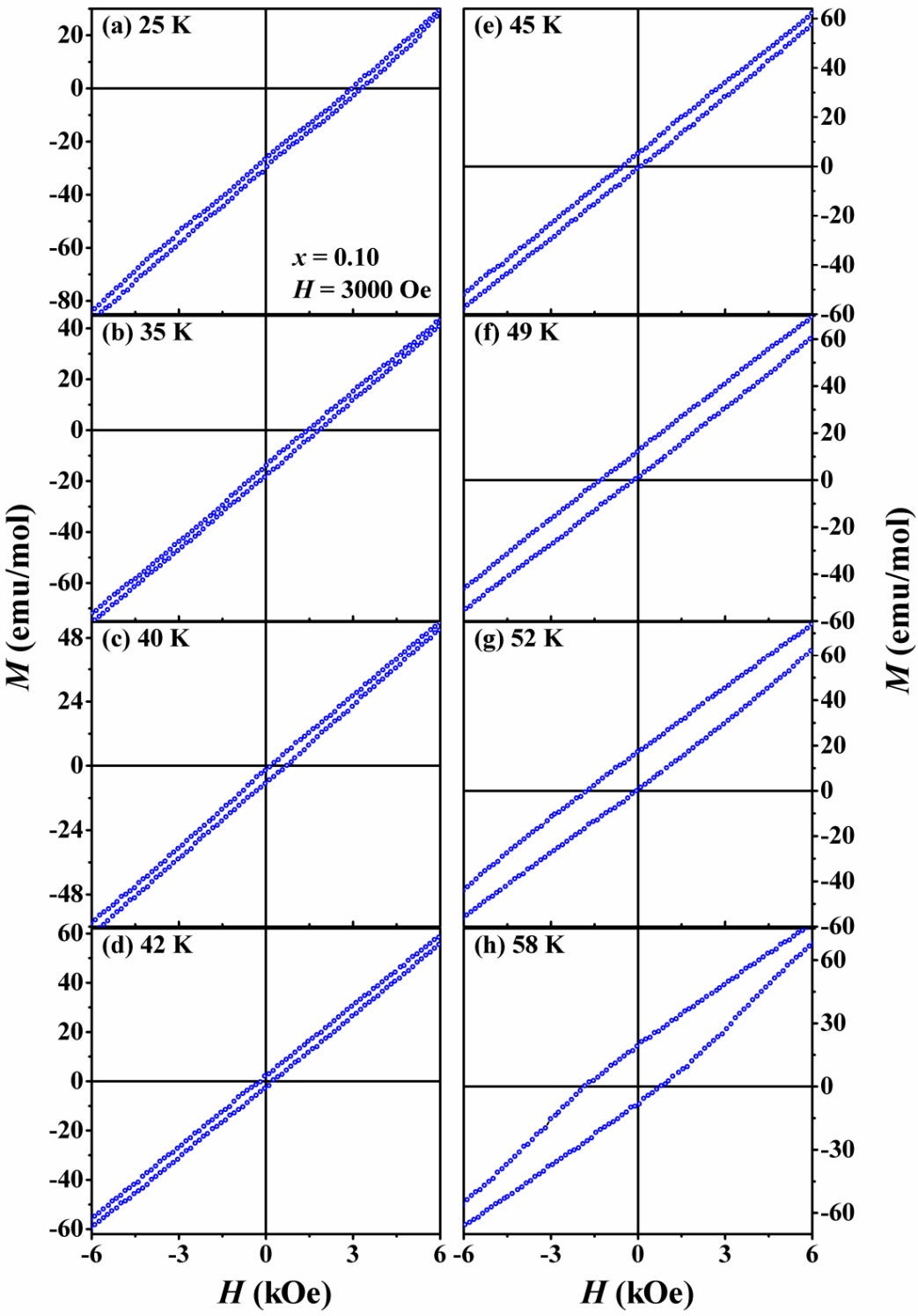


**Figure 4.15:** FC ($H$ = 3000 Oe) $M$–$H$ loops of $x$ = 0.10 at different temperatures in expanded scales.

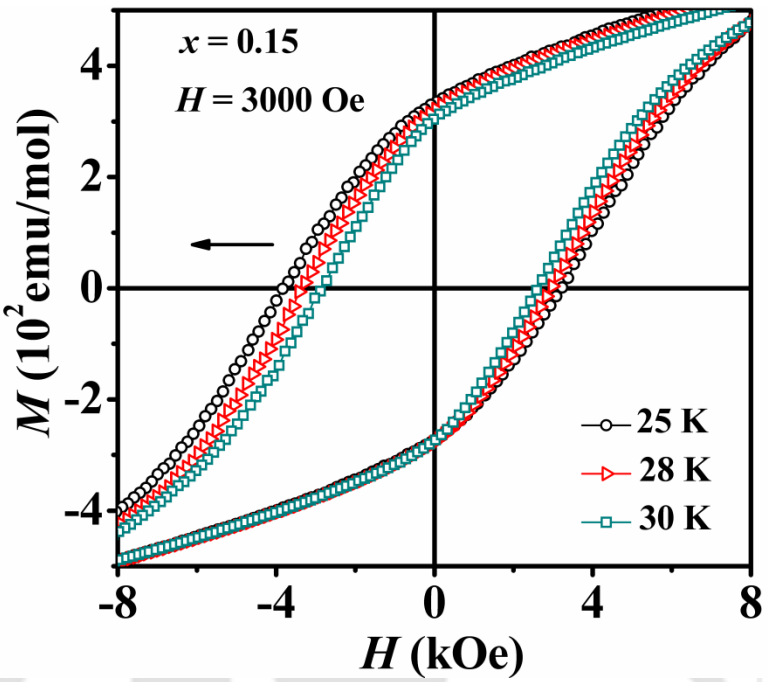


**Figure 4.16:** FC ($H$ = 3000 Oe) $M$–$H$ loops of $x$ = 0.15 at different temperatures in expanded scales.

Using the Eq. (3.3) and Eq. (3.5) in Chapter 3, the value of EB field $H_{EB}$ and the shift in magnetization $M_{EB}$ of the samples were calculated. The $H_{EB}$ and $M_{EB}$ values obtained for $x$ = 0.10 sample are plotted as a function of temperature as shown in Fig. 4.17 (a) and (b), respectively. Just below $T_C$, negative value of $H_{EB}$ is observed and its magnitude increases with decrease in temperature and reaches a maximum negative value of – 0.913 kOe at 52 K. For further decrease in temperature negative $H_{EB}$ decreases and at a temperature $T \approx T_{comp}$ = 40 K, $H_{EB}$ becomes zero. Below $T_{comp}$ it continuously increases in the positive direction and reaches a maximum value of 2.83 kOe at 25 K. After this temperature it may decrease with decrease in temperature for far below $T_{comp}$ showing a peak. But due to minimum temperature limit complete peak like behavior is not observed here. The behavior of $H_{EB}$ is in consistent with the $M$–$H$ loop behavior shown in Fig. 4.15. For this sample the positive $H_{EB}$ value is quite large compared to those of Fe substituted samples with $x$ = 0.30, 0.40 and 0.50 in Chapter 3; which exhibit $T_{comp}$ at above room temperature. In addition to the AFM interaction between the two sublattices and their change in domination with change in temperature, the exchange anisotropy between the FIM and the AFM component at low

temperature may also contribute to the observed EB in Al substituted sample with $x$ = 0.10 and this results in a large $H_{EB}$ at 25 K. This is because at low temperature AFM ordering is present in long range scale as predicted from the nature of *M–T* and *M–H* curve of the sample. However, the sign reversal of $H_{EB}$ is mainly due to the domination of one sublattice moment over the other with decrease in temperature. For convenience, only the longitudinal component of magnetic moment of the two sublattices A ($\mu_A$) and B ($\mu_B = \mu_{B1\text{-}B3} - \mu_{B2\text{-}B4}$) are taken into account to further explain the temperature dependence of $H_{EB}$. The negative $H_{EB}$ observed in the temperature range $T_{comp} < T < T_C$ is due to the domination of $\mu_A$ ($\mu_{Ni}$) which align along the field direction over the antiparallel $\mu_B$ ($\mu_{Cr1} - \mu_{Cr2}$). Due to dominant $\mu_A$ along the positive field direction, in this temperature range it is relatively easy to align the net magnetization along the positive field direction while for the descending branch of *M–H* loop large negative field is required to align the net moment in the negative field direction. As a result *M–H* loops shift towards the negative field axis giving rise to negative $H_{EB}$. However, for $T < T_{comp}$ positive $H_{EB}$ is observed due to the dominant $\mu_B$ compared to $\mu_A$. In this case large positive field is required to rotate the net moment in the positive field direction. At the $T_{comp}$ no $H_{EB}$ is observed since $\mu_A = \mu_B$. In this case also the tunable $H_{EB}$ field for $T_{comp} < T < T_C$ and $T < T_{comp}$ can be schematically understood from the diagram 3.26, given in Chapter 3.

Because of the insulating behavior of the present compound no conduction electron polarization (CEP) is expected at $T < T_C$. Also, the sample is FIM followed by AFM at low temperature and therefore have no possibility of PM moment at $T < T_C$. Since, we are not dealing with nanoparticles no core-shell structure is expected. The present sample is single phase with no direct FM/AFM like interfaces. Possibility of single ion anisotropy can also be ruled out due to the cubic nature of the sample. Therefore, although the sign reversal behavior of magnetization and EB field in the present sample resembles the behavior observed in some intermetallic alloys [91], $NdCr_{1-x}Fe_xO_3$ ($x$ = 0.05 – 0.20) [89], $La_{0.2}Ce_{0.8}CrO_3$ nanoparticles [85], $YFe_{0.5}Cr_{0.5}O_3$ [175], *etc*., the mechanism behind them cannot be explained considering the same argument as for these cases. This part is also discussed earlier in Chapter 3 for Fe substituted samples. Hence, in the present series, the observed MR is solely due to the different temperature dependences of the two sublattices and due to one sublattice moment overtaking the other sublattice moment with change in temperature tunable positive and negative EB field is observed.

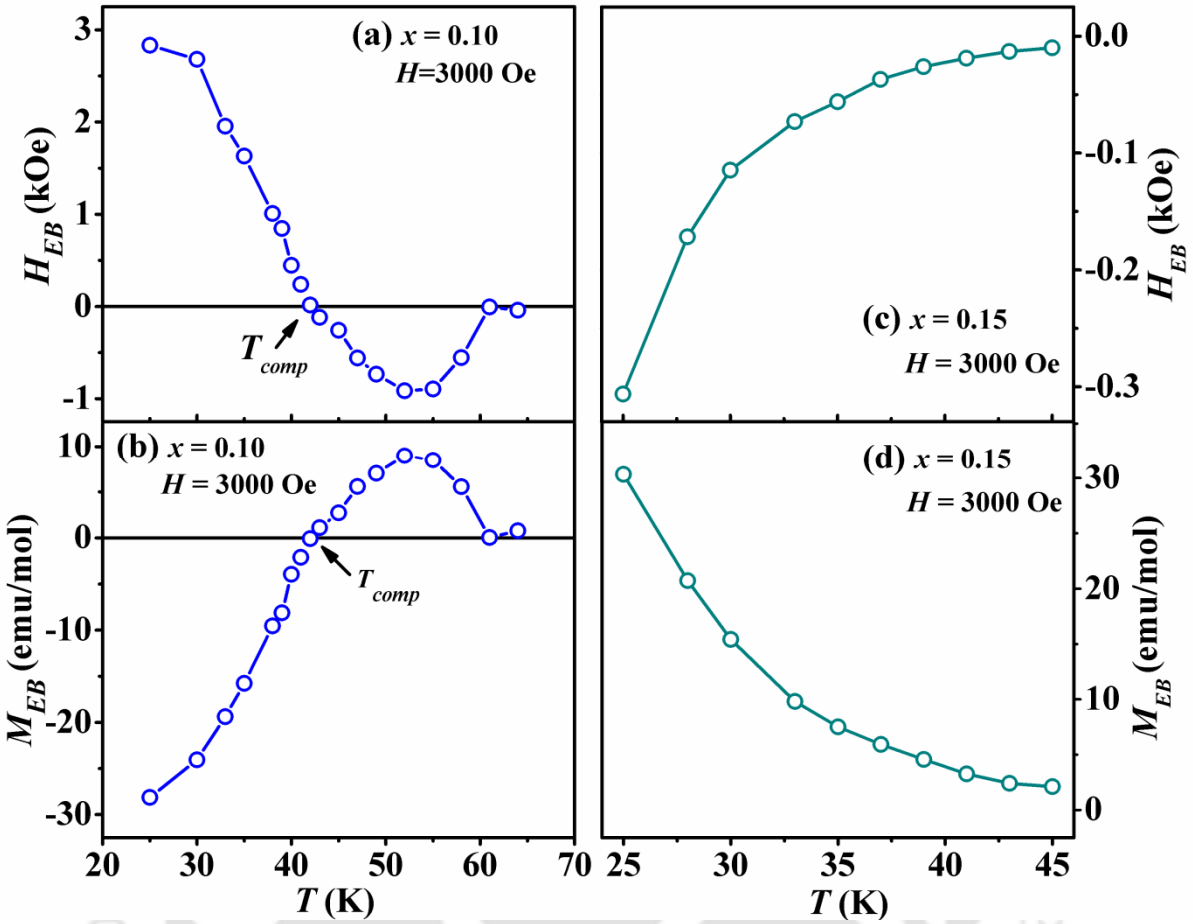


**Figure 4.17:** Temperature variation of $H_{EB}$ and $M_{EB}$ for $x$ = 0.10 (a, b) and $x$ = 0.15 (c, d) samples.

Fig. 4.17 (c) and (d) show the temperature variation of $H_{EB}$ and $M_{EB}$ for $x$ = 0.15 sample. It exhibits a maximum EB field of 306 Oe at 25 K which is comparable to that observed in many other spinel compounds [104]. But the magnitude of $H_{EB}$ is found to decrease exponentially with rise in temperature. $M_{EB}$ also follows the similar behavior with increase in temperature. The EB behavior in these samples can be ascribed to the exchange anisotropy between the FIM and the AFM components of magnetic moment. The ZFC *M–H* loop for these samples at low temperature signifies the presence of both the FIM and AFM component. However, the AFM ordering may also present in short range scale at higher temperatures for which a considerable EB is observed even at temperatures near to $T_C$. The maximum $H_{EB}$ value for this sample is smaller than that of Fe doped samples in the previous chapter. This may be due to the dilution of the exchange interaction due to non magnetic Al

substitution. In order to confirm that the measured EB field for this sample is not due to any minor loop effect, we have carried out single point detection (SPD) method analysis on the FC *M–H* loops as reported by Harres *et al.* [187]. In the present loops, the second derivatives of the descending and the ascending branches were found to overlap for |H| > 7 kOe as shown in Fig. 4.18 at 30 K temperatures.

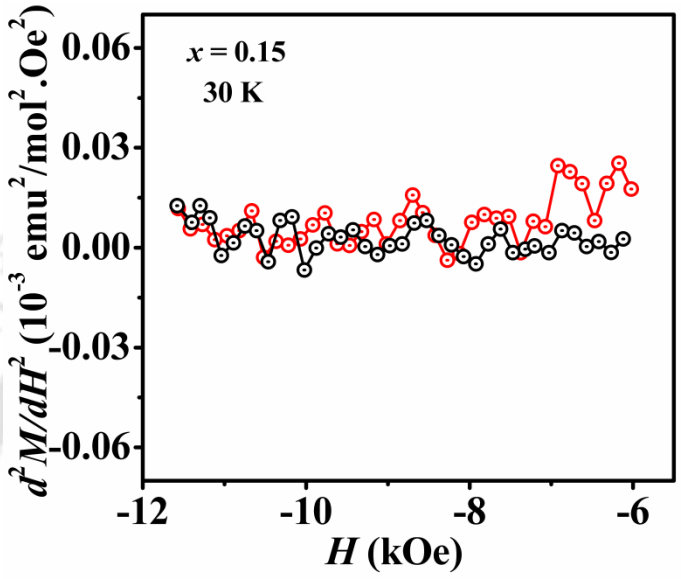


**Figure 4.18:** $d^2M/dH^2$ versus $H$ plots for $x$ = 0.15 sample at 30 K.

## 4.6 Magnetocaloric Effect

The magnetocaloric effect (MCE) is a magneto-thermodynamic phenomenon in which a temperature change of a suitable material is caused by subjecting the material to a magnetic field change. This is also known as adiabatic demagnetization in low temperature physics. It can be quantified as the reversible change in temperature in the material when the field change takes place in an adiabatic process, or the reversible change of magnetic entropy ($\Delta S_M$), if the change in field is brought about in an isothermal process [195]. We have tried to examine the MCE in $x$ = 0.10 sample that exhibits MR. Systems having both normal and inverse MCE can be used to maintain constant temperature bath in solid state refrigeration devices [173]. MCE effect is directly related to the magnetic entropy change $\Delta S_M$ (T) of a material under the application of an external magnetic field. The $\Delta S_M$ of the material can be obtained from[196],

$$\Delta S_M(T,H) = \int_0^H \left(\frac{\partial M}{\partial T}\right)_H dH \tag{4.3}$$

where, $(\partial M/\partial T)_H$ is the first derivative of FC *M–T* curve in magnetic field *H*. From the *M–T* curves at different applied field, $\Delta S_M$ is calculated using the above expression. $-\Delta S_M$ as a function of temperature is shown in Fig. 4.19 and it exhibits a peak ($-\Delta S_M$ = – 0.005 JKg$^{-1}$K$^{-1}$) in the vicinity of $T_C$. For $T < T_C$, it start decreasing towards negative value by crossing over ($-\Delta S_M = 0$) the temperature axis at 57 K and attains a maximum negative value of $-\Delta S_M$ = – 0.0012 JKg$^{-1}$K$^{-1}$ for $H$ = 2 kOe. This polarity reversal of $-\Delta S_M$ is due to the shape of the FC *M–T* curve [Fig. 4.14 (a)] of the sample. As the FC magnetization decreases after reaching a peak value, the first derivative changes sign and as a consequence polarity of $-\Delta S_M$ is also reversed. In general, $-\Delta S_M > 0$ indicates normal MCE and it results in decrease in temperature in the magnetic refrigeration cycle. However, $-\Delta S_M < 0$ indicates inverse MCE and it causes heating in the same refrigeration cycle. The maximum value of $-\Delta S_M$ in the present sample is found to be larger than that observed in perovskite $YFe_{0.5}Cr_{0.5}O_3$ sample and it may be noted that both of these systems exhibit small saturation magnetization [175]. Such coexistence of normal and inverse MCE in the present sample can be used to maintain a constant temperature bath as described by Yusuf *et al*. in $Cu_{0.73}Mn_{0.77}[Fe(CN)_6].zH_2O$ [173] compound and Mao *et al*. in perovskite $YFe_{0.5}Cr_{0.5}O_3$ [175]. The present compound in principle can produce a constant temperature bath of 57 K. Here for the temperature above 57 K, the normal MCE causes decrease in the temperature of the system while for the temperature below 57 K, the temperature of the system increases as a result of inverse MCE. In this way, a constant temperature of 57 K is maintained by the two opposite MCEs. However, the magnitude of $-\Delta S_M$ is quite small for practical application. Small $-\Delta S_M$ may be due to small saturation magnetization of the sample and also due to small applied magnetic field. Therefore further work is needed to improve the magnitude of $-\Delta S_M$ to meet the practical application.

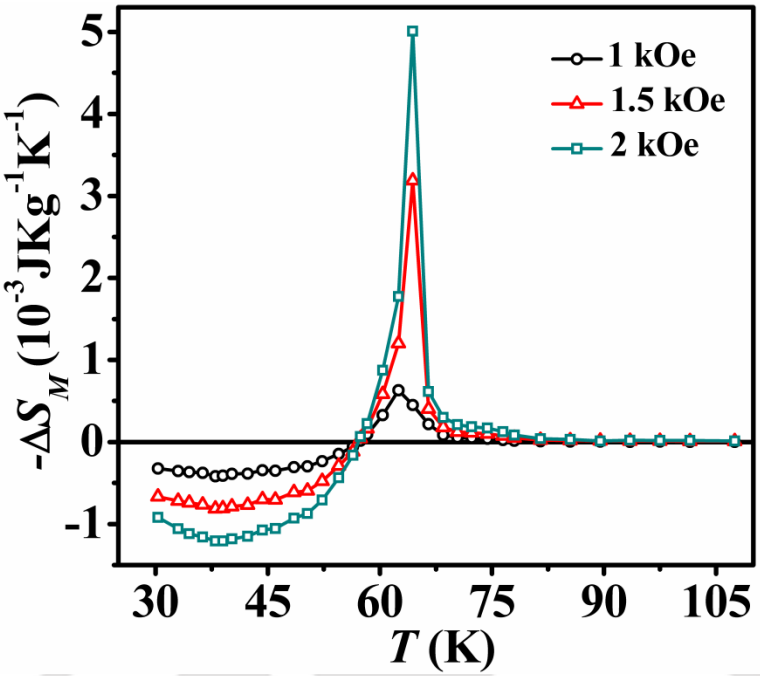


**Figure 4.19:** Temperature variation of magnetic entropy change ($-\Delta S_M$) for $x$ = 0.10 sample.

## 4.7 Conclusions

To summarize, we have studied the temperature and field induced basic magnetic, EB and MR properties of Ni(Cr$_{1-x}$Al$_x$)$_2$O$_4$ ($x$ = 0 – 0.50) samples. We have prepared the single phase samples of Ni(Cr$_{1-x}$Al$_x$)$_2$O$_4$ by using sol-gel route. Rietveld refinement of the room temperature XRD patterns confirm phase purity of the samples and reveals a structural transformation from tetragonal ($I4_1/amd$ space group) to cubic ($Fd\bar{3}m$ space group) with Al doping. The lattice parameter of Al doped samples is found to decrease with increase in Al concentration. All the samples show FIM behavior and the transition temperature is found to decrease with increase in Al concentration due to the weakening of the superexchange interaction. Bifurcation between ZFC and FC $M$–$T$ curves and the behavior of low temperature $M$–$H$ loop show the presence of competing AFM interaction in the samples.

Interesting property of MR is observed for $x$ = 0.10 sample with a compensation temperature of 40 K. This phenomenon is explained considering different temperature dependences of the two sublattices of the sample. Considerable EB field is observed for $x$ = 0.15 sample which can be explained by considering the anisotropic exchange interaction

between the FIM and the AFM components of magnetic moment. The EB field of $x$ = 0.15 sample is found to be only negative while tunable positive and negative EB field is observed across $T_{comp}$ = 40 K for $x$ = 0.10 sample which is due to the change in domination of magnetic moment of one magnetic sublattice over the other with variation in temperature. Both normal and inverse MCEs are observed for $x$ = 0.10 sample.

# Chapter 5

# *Fe and Al Substituted $MnCr_2O_4$ Series*

## 5.1 Introduction

In Chapters 3 and 4, we have seen the interesting magnetic properties of $NiCr_2O_4$ due to the Fe and Al substitution at Cr site. Fe and Al substitution stimulates the magnetization reversal (MR) and tunable exchange bias (EB) behavior across the compensation temperature ($T_{comp}$). Also, Fe substitution leads to the increase in ferrimagnetic (FIM) transition temperature as well as the $T_{comp}$ close to room temperature. Similar to $NiCr_2O_4$, $MnCr_2O_4$ also exhibits non collinear FIM behavior below 45 K. However, in addition to that it undergoes a short range spiral magnetic ordering at $T_S$ = 14 – 18 K due to magnetic frustration as discussed in Chapter 1 [23, 38, 154-156]. The spin canting angles of Mn, Cr1 and Cr2 were reported to be 28°, 85° and 11°, respectively [118] with a net macroscopic axial (FIM) moment of 1.2 $\mu_B$/f.u. Such complex spin configuration leads to ferroelectric polarization and due to correlation between its magnetic, electric and structural properties, $MnCr_2O_4$ has drawn considerable research interest [13, 24].

As discussed in Chapter 1, there are several reports available on the magnetic, magnetodielectric and magnetoelastic properties of pristine $MnCr_2O_4$ [21, 23-25, 38, 155, 156, 161]. Effect of substitution of magnetic and nonmagnetic ions at the A site on the structural and magnetic properties has been studied by a few authors [39, 159, 160] but the report on the substitution of magnetic and nonmagnetic element at Cr site is limitted. The magnetic structure of $MnFe_{2-x}Cr_xO_4$ series by recording Mössbauer spectra and powder neutron diffraction pattern with a special emphasize in ferrite rich samples has been carried out by a few authors [162, 163] and the non collinear alignment of the moments in the B

sublattice was identified. Dmitrieva *et al.* [162] have explained the structural and the magnetic compensation like behavior of ferrite-chromite series assuming canting of B sublattice moments. The observed magnetic properties of $MnCr_{2-t}Al_tO_4$ were also explained assuming canting of the B site moments only [147]. On the other hand, Tomiyasu *et al.* [118] have reported the presence of such canting both in A and B sublattices. Therefore the study of magnetic properties on Fe and Al substituted $MnCr_2O_4$ will be quite interesting. Furthermore, interesting results observed for Fe and Al substitution in Cr site of $NiCr_2O_4$ series as discussed in Chapters 3 and 4 reveal that it would be also interesting to carry out such substitution at B site of $MnCr_2O_4$. The investigation of magnetic properties of Fe and Al substituted $MnCr_2O_4$ compounds would be of interest in studying the effect of spin canting in tuning the magnetic compensation. As per a few earlier reports in $CoCr_2O_4$ sample with similar magnetic and crystal structure as $MnCr_2O_4$, MR and tunable EB behavior have been observed by Mn and Fe substitution in the Cr site [26, 27]. Therefore it is quite interesting to see the effect of Fe and Al substitution for Cr site in the magnetic properties of $MnCr_2O_4$.

## 5.2 Fe Substituted $MnCr_2O_4$ Series

The present section deals with the preparation of Fe doped $MnCr_2O_4$ [$Mn(Cr_{1-x}Fe_x)_2O_4$ ($x$ = 0 – 0.50)] samples and study of their structural properties at room temperature and, temperature and field dependent magnetic properties.

We have prepared the bulk polycrystalline samples of $Mn(Cr_{1-x}Fe_x)_2O_4$ ($x$ = 0 – 0.50) by using sol–gel method. High purity (99 %) $C_4H_6MnO_4.4H_2O$, $Cr(NO_3)_3.9H_2O$ and $Fe(NO_3)_3.9H_2O$ were used as the starting compounds. The precursors were obtained by sol-gel method as discussed in Chapter 2. The precursors were presintered at 600 °C, 800 °C and 1000 °C for 12 hours. Final sintering was carried out at 1200 °C for 24 hours in pellet form. Room temperature X-ray diffraction (XRD) patterns, Raman spectra, microstructural images, composition analysis and, temperature and field variations of magnetization data were obtained as per the details given in Chapter 2.

## 5.2.1 Structural Properties

XRD patterns of $Mn(Cr_{1-x}Fe_x)_2O_4$ samples were recorded at room temperature. XRD patterns of all the samples at room temperature are shown in Fig. 5.1. In contrast to the Fe substituted $NiCr_2O_4$ series as given in Chapter 3, here no structural transition is observed and all the Fe substituted samples are found to exhibit similar XRD pattern confirming the phase purity of the samples. For further confirmation, the XRD patterns were analyzed by Rietveld refinement method and found that all Fe substituted samples including the parent compound are in single phase form with cubic structure. The XRD patterns for $x$ = 0 and 0.40 samples along with Rietveld refinement by choosing $Fd\bar{3}m$ space group in cubic structure are shown in Fig. 5.2 (a & b). The lattice parameter of $MnCr_2O_4$ is found to be $a$ = 8.4396 Å and it is comparable to the reported values [23, 38, 39]. The low values of the reliability factors such as Bragg factor $(R_{Bragg})$ = 3.24 %, crystallographic $R_f$ factor = 2.61 %, profile factor ($R_p$) = 7.33 % and goodness of fit ($\chi^2$) = 4.52 for $MnCr_2O_4$ highlight the good quality of the refinement. The lattice parameters, reliability factors and unit cell volume of all the samples are given in table5.1.

The main XRD peak observed around $2\theta \approx 35.3°$ corresponding to the *hkl* value of (311) for each sample is shown in Fig. 5.3(a) in an enlarged scale. From the figure we can clearly see the shifting of the peak towards lower 2θ value with increase in $x$ up to 0.3 and beyond that no appreciable variation is seen. The observed shift in $2\theta$ position signifies the increase of lattice parameter with increase in Fe concentration up to $x$ = 0.30. The lattice constant obtained from the Rietveld refinement as a function of $x$ is shown in Fig. 5.3(b) and it shows the systematic increase in lattice constant up to $x$ = 0.30, *i.e.* in consistent with the shifting of (311) peak. The increase in the lattice parameter with increase in $x$ can be understood in two ways: (i) The substitution of larger $Fe^{3+}$ (0.645 Å) ions in place of $Cr^{3+}$ (0.615 Å) ions at octahedral site (ii) The preferential occupation of $Fe^{3+}$ (0.49 Å) ions at tetrahedral site replacing $Mn^{2+}$ (0.66 Å) ions and the corresponding $Mn^{2+}$ (0.83 Å) ions moving to the octahedral site, *i.e.* at $Cr^{3+}$ site (0.615 Å) site. This process is expected to result in net increase in lattice constant. However, such possibility can be ruled out as per detailed magnetic studies discussed in section 5.2.2. However, the small reduction in the lattice parameter for $x \geq 0.40$ may be due to the occupation of small amount of Fe ions in $Fe^{2+}$ state

in the A site and hence corresponding transfer of same amount of Mn ions in $Mn^{3+}$ state to the B site. In this case decrease in lattice parameter is obvious because ionic radius of $Fe^{2+}$ in A site (~ 0.64 Å) is less than $Mn^{2+}$ (~ 0.66 Å) while $Mn^{3+}$ in B site is comparable to that of $Cr^{3+}$. Such possibility of occupation of small concentration of $Fe^{2+}$ ions in the A site has been reported earlier [162, 163].

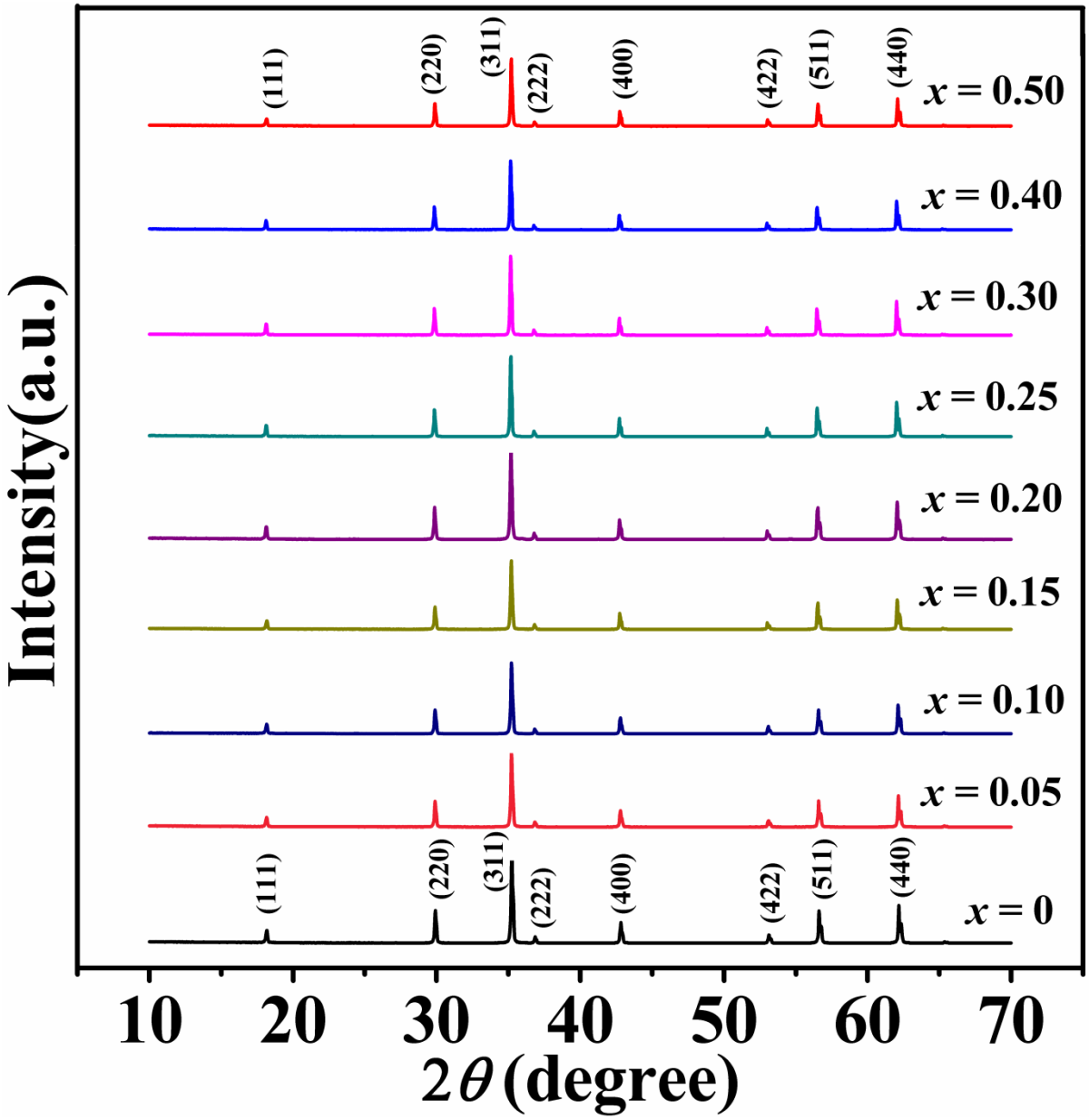


**Figure 5.1:** XRD patterns of $Mn(Cr_{1-x}Fe_x)_2O_4$ compounds for $x = 0 – 0.50$.

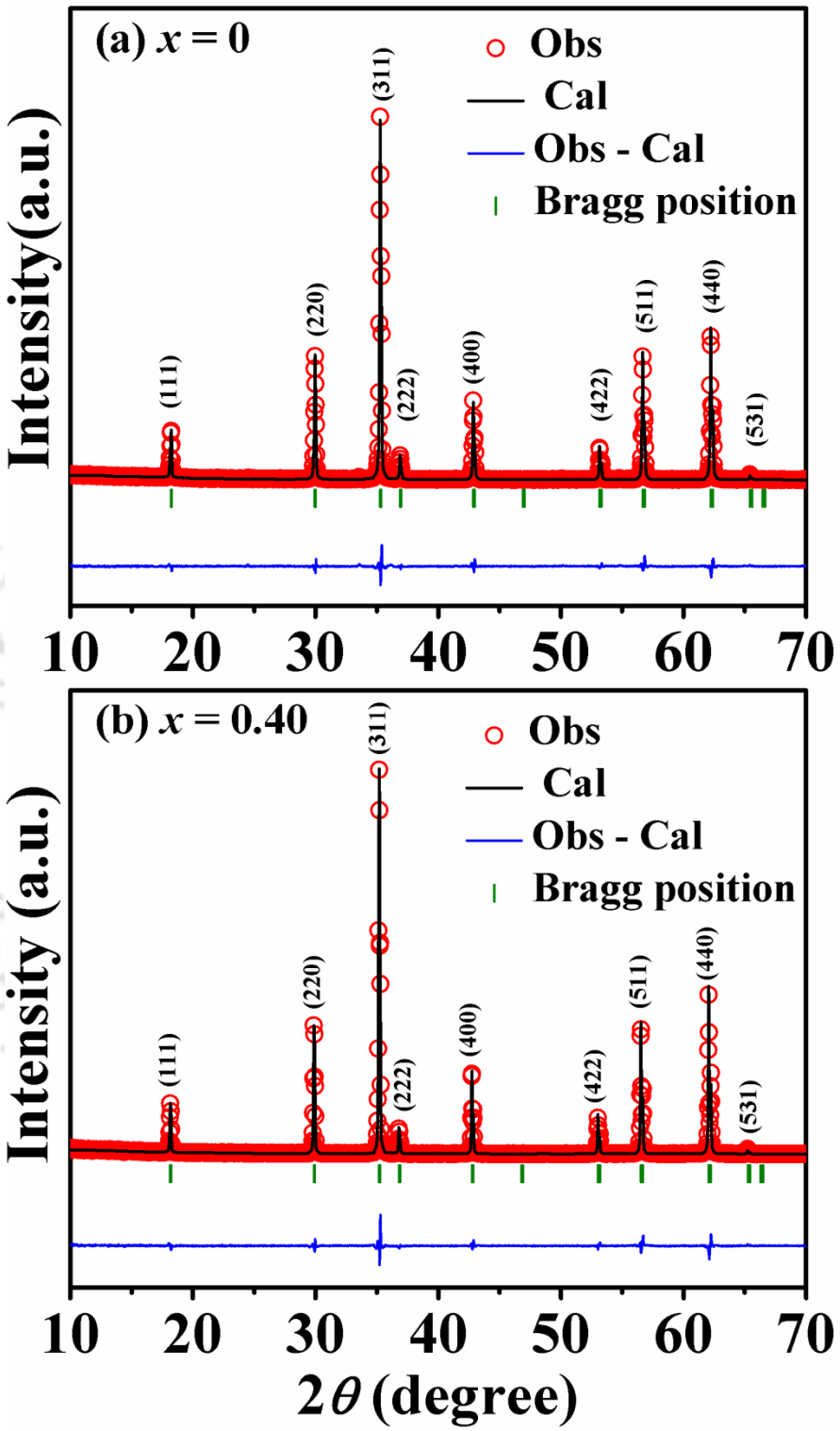


**Figure 5.2:** Rietveld refinement of the XRD patterns of (a) $x = 0$ and (b) $x = 0.40$ samples. The red open circles are the experimental data and the black solid lines are the fitted data. The bottom line shows the difference between the experimental and the fitted data.

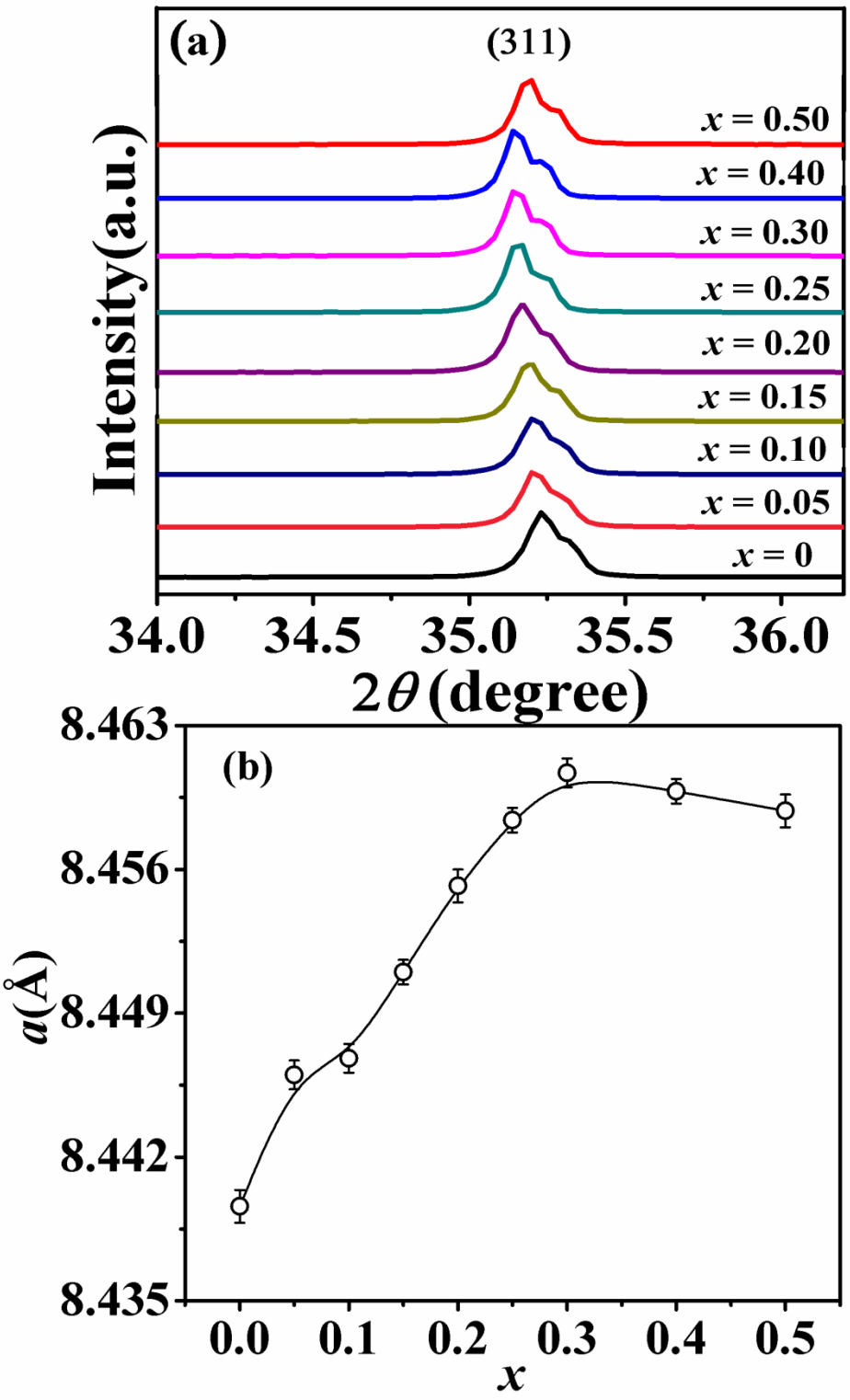


**Figure 5.3:** (a) Enlarged view of the high intense (311) peak for $x = 0 – 0.50$ samples and (b) Variation of lattice parameter with Fe concentration '$x$'.

**Table 5.1:** Parameters obtained from the Rietveld analysis of XRD patterns for the samples $Mn(Cr_{1-x}Fe_x)_2O_4$ (0 – 0.50). $R_F$, $R_{Bragg}$, $R_P$ and $\chi^2$ are the reliability factors.

| **Sample/ Parameters** | ***x* = 0** | ***x* = 0.05** | ***x* = 0.10** | ***x* = 0.15** | ***x* = 0.20** | ***x* = 0.25** | ***x* = 0.30** | ***x* = 0.40** | ***x* = 0.50** |
|---|---|---|---|---|---|---|---|---|---|
| **Space group** | $Fd\bar{3}m$ | $Fd\bar{3}m$ | $Fd\bar{3}m$ | $Fd\bar{3}m$ | $Fd\bar{3}m$ | $Fd\bar{3}m$ | $Fd\bar{3}m$ | $Fd\bar{3}m$ | $Fd\bar{3}m$ |
| ***a* (Å)** | 8.4396 (0.0008) | 8.4460 (0.0008) | 8.4468 (0.0007) | 8.4510 (0.0007) | 8.4552 (0.0007) | 8.4584 (0.0007) | 8.4607 (0.0008) | 8.4598 (0.0007) | 8.4589 (0.0007) |
| ***Volume* (Å$^3$)** | 601.13 (0.09) | 602.49 (0.01) | 602.67 (0.09) | 603.57 (0.09) | 604.47 (0.08) | 605.15 (0.09) | 605.65 (0.09) | 605.45 (0.08) | 605.26 (0.08) |
| **$R_F$ (%)** | 2.61 | 3.76 | 3.69 | 4.33 | 3.39 | 3.42 | 3.25 | 3.78 | 3.78 |
| **$R_{Bragg}$ (%)** | 3.24 | 3.59 | 3.55 | 4.10 | 3.32 | 4.27 | 4.42 | 4.61 | 4.56 |
| **$R_P$ (%)** | 7.33 | 8.12 | 7.82 | 8.32 | 7.35 | 8.39 | 8.62 | 8.64 | 8.94 |
| $\chi^2$ | 4.52 | 5.06 | 4.71 | 5.88 | 4.51 | 4.25 | 5.72 | 5.14 | 5.20 |
| **Mn/Cr/Fe Occupancy** | 1.011 / 1.990 /0.000 | 1.014 / 1.894 / 0.094 | 1.012 / 1.795 / 0.195 | 1.013 / 1.693 / 0.293 | 1.012 / 1.597 / 0.397 | 1.008 / 1.495 / 0.495 | 1.016 / 1.397 / 0.597 | 1.021 / 1.197 / 0.797 | 1.023 / 0.997 / 0.997 |

Bond angles corresponding to the A – O – B and B – O – B superexchange networks are calculated using the value of refined fractional coordinates and lattice parameters by using Fullprof software. Variation of A – O – B and B – O – B bond angles as a function of *x* is depicted in Fig. 5.4(a). The B – O – B bond angle decreases and that of A – O – B increases with increase in Fe concentration. The bond length A – O decreases whereas B – O increases slightly with increase in Fe concentration [Fig. 5.4(b)]. The contraction of A – O distance is sharp compared to the elongation of B – O distance for *x* = 0.40 and 0.50 sample which support the argument of occupation of $Fe^{2+}$ in the tetrahedral site.

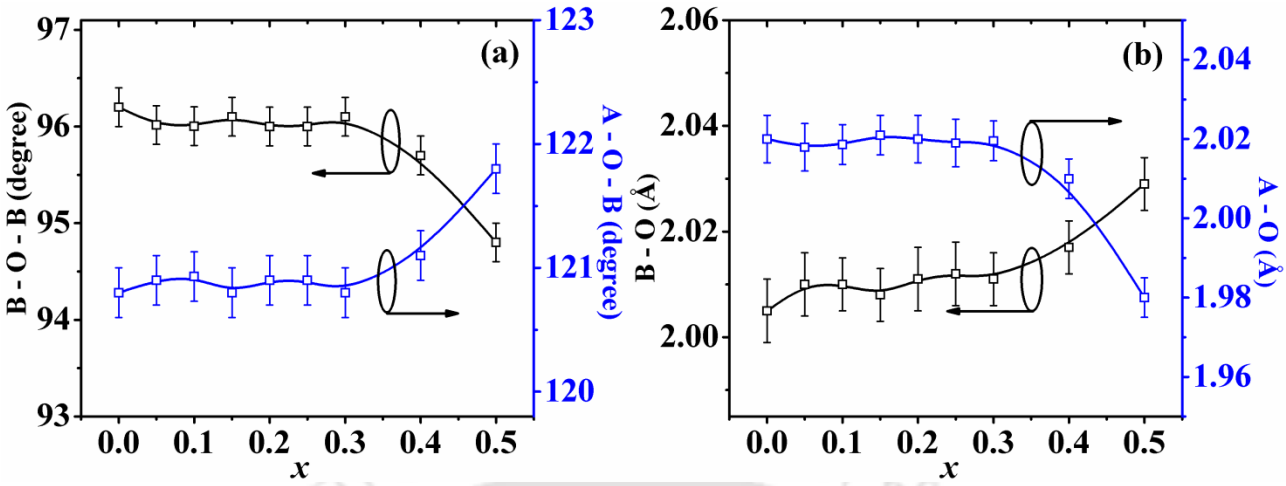


**Figure 5.4:** (a) Variation of B – O – B and A – O – B bond angles and (b) variation of B – O and A – O bond lengths as a function of *x*, the concentration of Fe.

In order to confirm the cation distribution estimated from the XRD analysis and to understand the magnetic properties, we carried out Raman spectroscopic study of all the samples. As per the XRD analysis, $MnCr_2O_4$ exhibits a cubic spinel structure with $Fd\bar{3}m$ ($O_h^7$) space group. A unit cell of cubic spinel compound contains 8 tetrahedral cations, 16 octahedral cations and 32 oxygen anions with a total of 56 atoms (Z = 8). But the smallest Bravais cell consists of only 14 atoms (Z = 2). Therefore 42 vibrational modes are expected for cubic spinel with $Fd\bar{3}m$ space group among which 39 bands correspond to optical modes and three bands correspond to acoustic modes. According to the group theory analysis the optical modes for spinel are $A_{1g} + E_g + F_{1g} + 3F_{2g} + 2A_{2u} + 2E_u + 4F_{1u} + 2F_{2u}$ and there is one triply degenerate $F_{1u}$ acoustic mode. The selection rules yields that $F_{1u}$ modes are infra red active while $A_{1g}$, $E_g$ and $F_{2g}$ modes are Raman active. Hence, there are five Raman active modes ($A_{1g} + E_g + 3F_{2g}$) for cubic spinel compounds [197-199]. Fig. 5.5 shows the Raman spectra of $Mn(Cr_{1-x}Fe_x)_2O_4$ ($x = 0 – 0.50$) samples (open circles). The positions and full width at half maximum (FWHM) of the Raman peaks were estimated by fitting the peaks (green solid lines in Fig. 5.5) by Lorentz profile and are depicted in Fig. 5.6 as a function of *x*. The Raman spectrum of the pristine $MnCr_2O_4$ contains four peaks at 683 $cm^{-1}$, 638 $cm^{-1}$, 509 $cm^{-1}$ and 197 $cm^{-1}$. These peak positions are consistent with the earlier observed modes for $MnCr_2O_4$ and $CoCr_2O_4$ [198, 200, 201]. The strongest peak observed at 683 $cm^{-1}$ is ascribed

to the $A_{1g}$ mode and the other three peaks at 638 $cm^{-1}$, 509 $cm^{-1}$ and 197 $cm^{-1}$ are assigned to $F_{2g}$ (1), $F_{2g}$ (2) and $F_{2g}$ (3) modes, respectively [198].

Normally, it is difficult to distinguish an inverse spinel structure from a normal spinel structure because selection rules are same for both normal and fully inverted and partially inverted structures. Yet, some authors distinguish the inverse spinel structure from the broadening and shifting of the bands compared to the normal structure and also from the appearance of some additional bands, not estimated by the group theory [202, 203]. In the present series of samples, the strongest peak at 683 $cm^{-1}$ for $x = 0$ is found to broaden and shift towards lower wave number with increase in Fe concentration and this behavior is highly pronounced for $x \geq 0.30$. It is clearly observable in Fig. 5.6. Such behavior of the bands is related to the change in mass, bond length, charge, *etc*. The $A_{1g}$ mode at 683 $cm^{-1}$ originates from $CrO_6$ octahedra and the shifting of this peak towards lower wavenumber and its broadening can be thus easily interpreted in terms of heavier $Fe^{3+}$ ions occupying the octahedral $Cr^{3+}$ site. The rather large broadening of this peak for $x = 0.40$ and 0.50 samples can be also attributed to the development of inverse spinel structure [200, 202]. $F_{2g}$ (2) mode observed at 509 $cm^{-1}$ is dependent on the tetrahedral cations [204]. We do not see appreciable change in the peak position of $F_{2g}$ (2) mode up to a concentration of $x = 0.30$ (Fig. 5.6); however for $x > 0.30$, this mode is found to broaden and shift towards higher wave number. If the tetrahedral site is partially substituted by $Fe^{2+}$ ions having smaller ionic size compared to $Mn^{2+}$, the structural disorderness increases as compared to the normal $MnCr_2O_4$ spinel and this leads to the peak broadening. Thus, the shift and broadening of $F_{2g}$ (2) mode towards higher wavenumbers for $x > 0.30$ samples is caused by the presence of $Fe^{2+}$ ions in the A site. It is also noteworthy that such changes in Raman modes have a good correlation with the XRD results discussed above. The significant decrease in the A – O bond length for $x = 0.40$ and 0.50 sample [Fig. 5.4(b)] may be related to the shift of $F_{2g}$ (2) mode to higher wavenumbners. In addition to that we have observed an additional Raman mode peak at 574 $cm^{-1}$ for $x = 0.40$ and 0.50 samples which was not predicted by group theory. This can be attributed to the presence of considerable Fe – O bond in tetrahedral and octahedral networks. It may also be attributed to the inverse spinel structure induced local distortions in the tetrahedral as well as octahedral coordination which would not be detected by XRD. This

local distortion may relax the usual selection rules for cubic spinel structures and may activate Raman forbidden modes and hence leading to the splitting of the Raman modes.

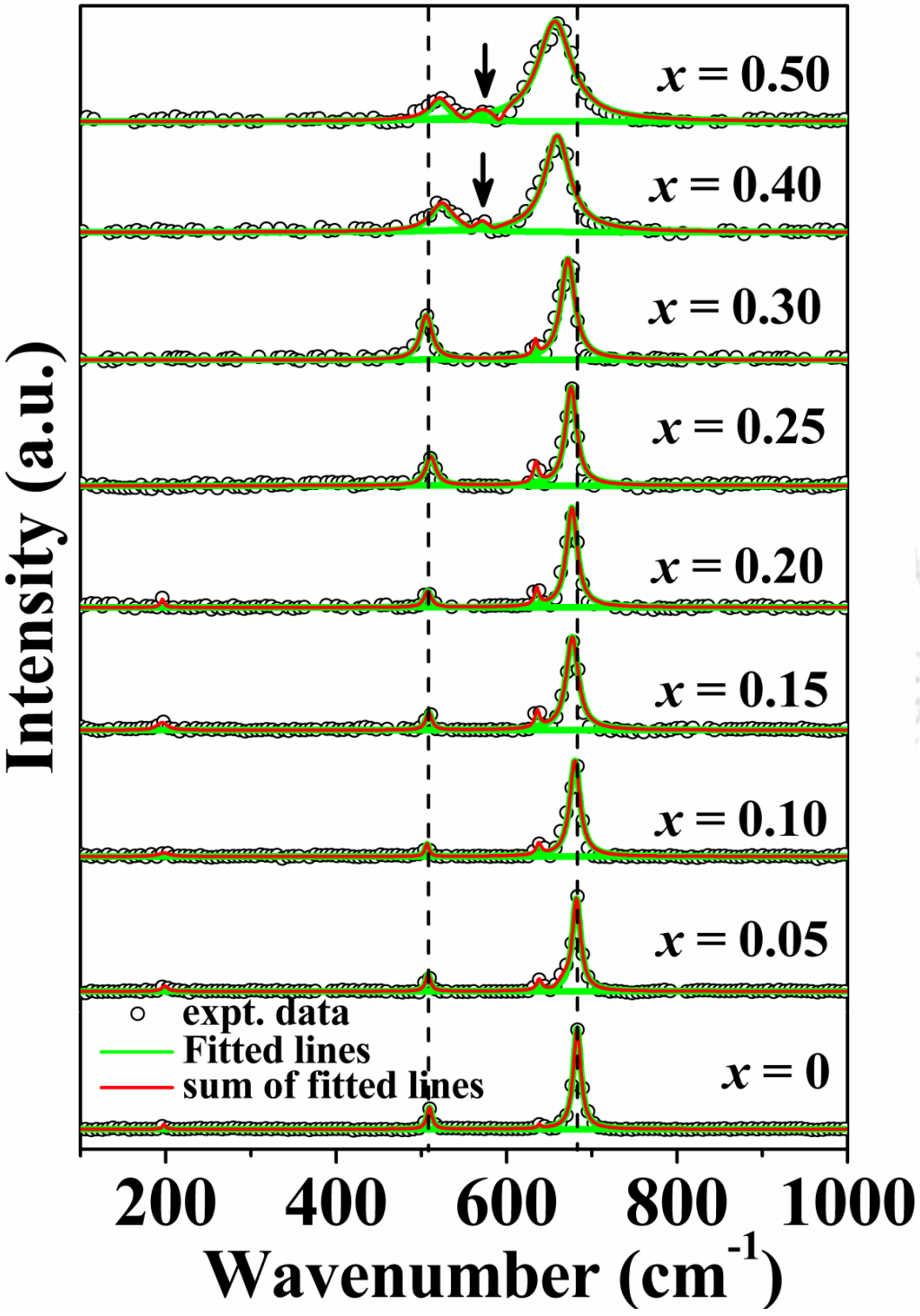


**Figure 5.5:** Raman spectra of $Mn(Cr_{1-x}Fe_x)_2O_4$ samples at room temperature along with the fitted data.

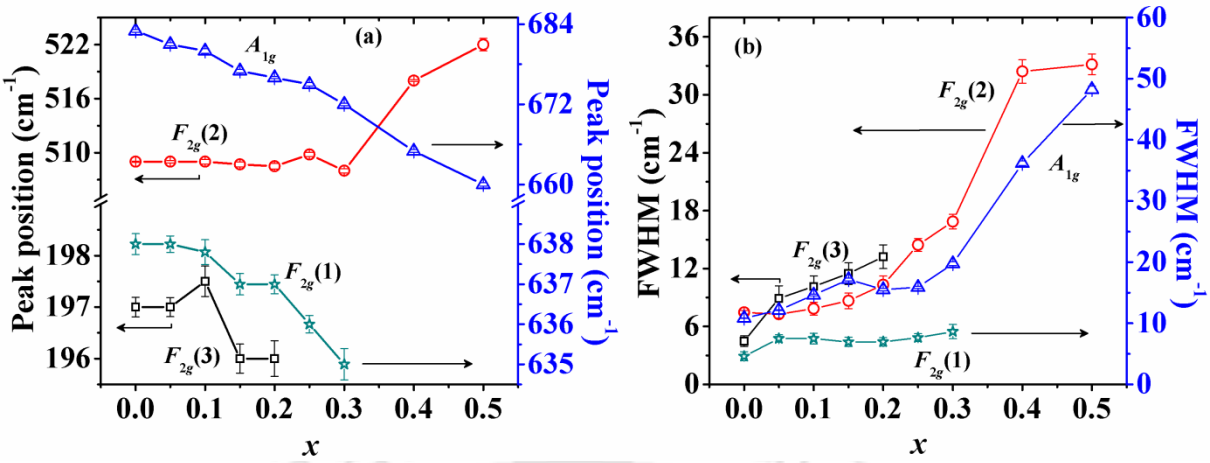


**Figure 5.6:** (a) Peak position and (b) FWHM of various Raman modes of $Mn(Cr_{1-x}Fe_x)_2O_4$ samples at room temperature as a function of Fe concentration '*x*'.

Fig. 5.7 (a) – (d) show the FESEM micrographs of $x = 0$, 0.20, 0.40 and 0.50 samples. The grain sizes of the samples were determined from the micrographs by using ImageJ software. The grain sizes are found to be distributed in a wide range as depicted in Fig. 5.7 ((e) – (h)) for the above samples. The average grain size of each sample is obtained by fitting the size distribution histogram to log normal distribution function [Eq. (3.1)] [168] as reproduced below,

$$f(d,\mu,\sigma) = \frac{1}{d\sigma\sqrt{2\pi}} \exp\left(-\frac{(\ln d - \mu)^2}{2\sigma^2}\right) \qquad (5.1)$$

where, $d$ is the cross-sectional length of the particle, $\mu$ is the logarithmic mean and $\sigma$ represents the standard deviation. The average grain size of $x = 0$ sample is found to be 0.33 µm with a standard deviation of 0.11 µm and it is found to increase up to 0.95 µm (standard deviation = 0.22 µm) for $x = 0.50$ sample. However, the crystallite size estimated from the analysis of XRD patterns of the samples is found to be in the range of 75 to 95 nm which is smaller than that of grain size. The EDS spectra for $x = 0$, 0.20, 0.40 and 0.50 samples are shown in Fig. 5.8. The cation ratios Mn: Cr: Fe obtained from EDS analysis for $x = 0$, 0.20, 0.40 and 0.50 samples are given in table 5.2 which are comparable to the nominal starting compositions.

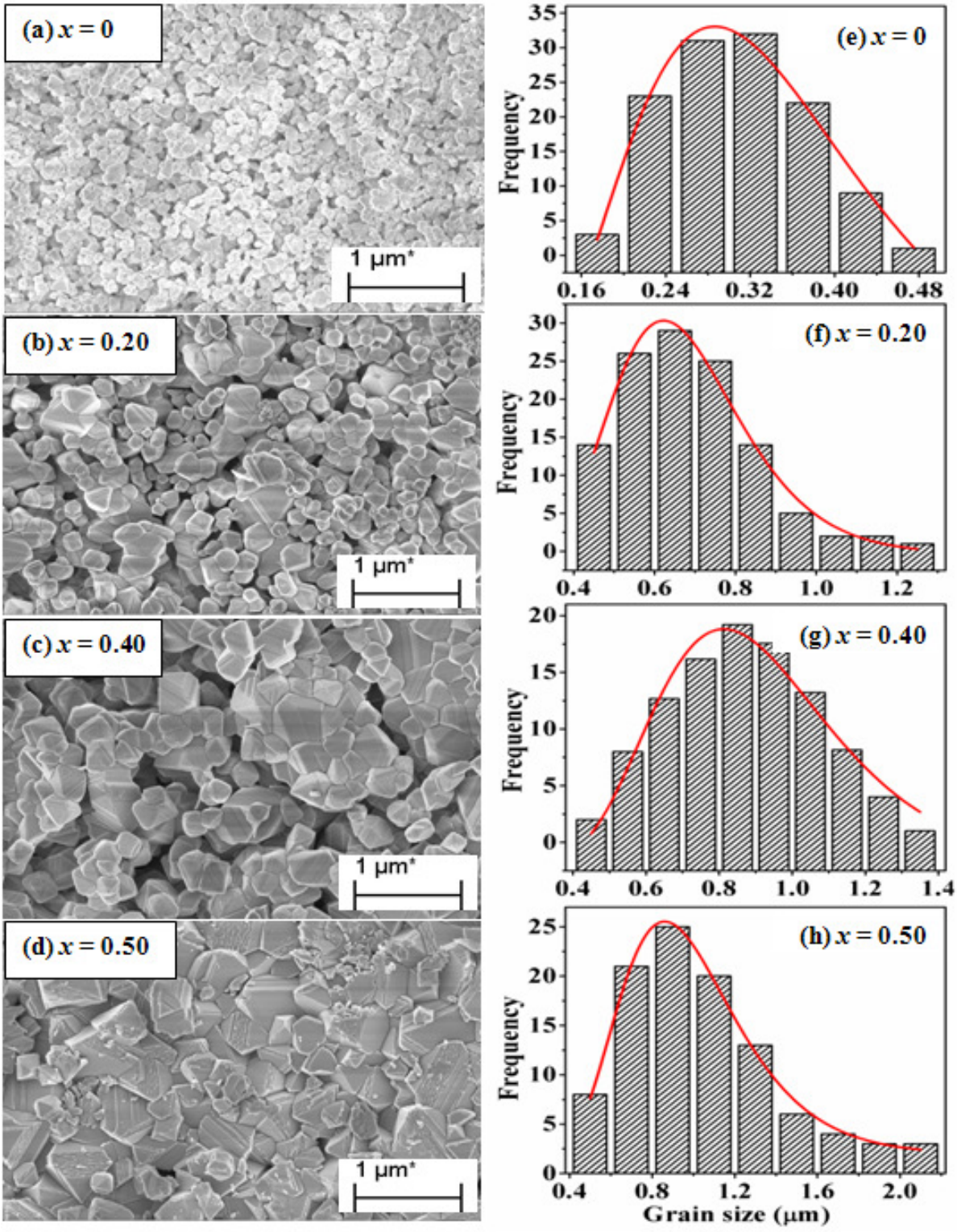


**Figure 5.7:** (a) **–** (d) FESEM images and (e) – (h) grain size distribution of $x$ = 0, 0.20, 0.40 and 0.50 samples of $Mn(Cr_{1-x}Fe_x)_2O_4$.

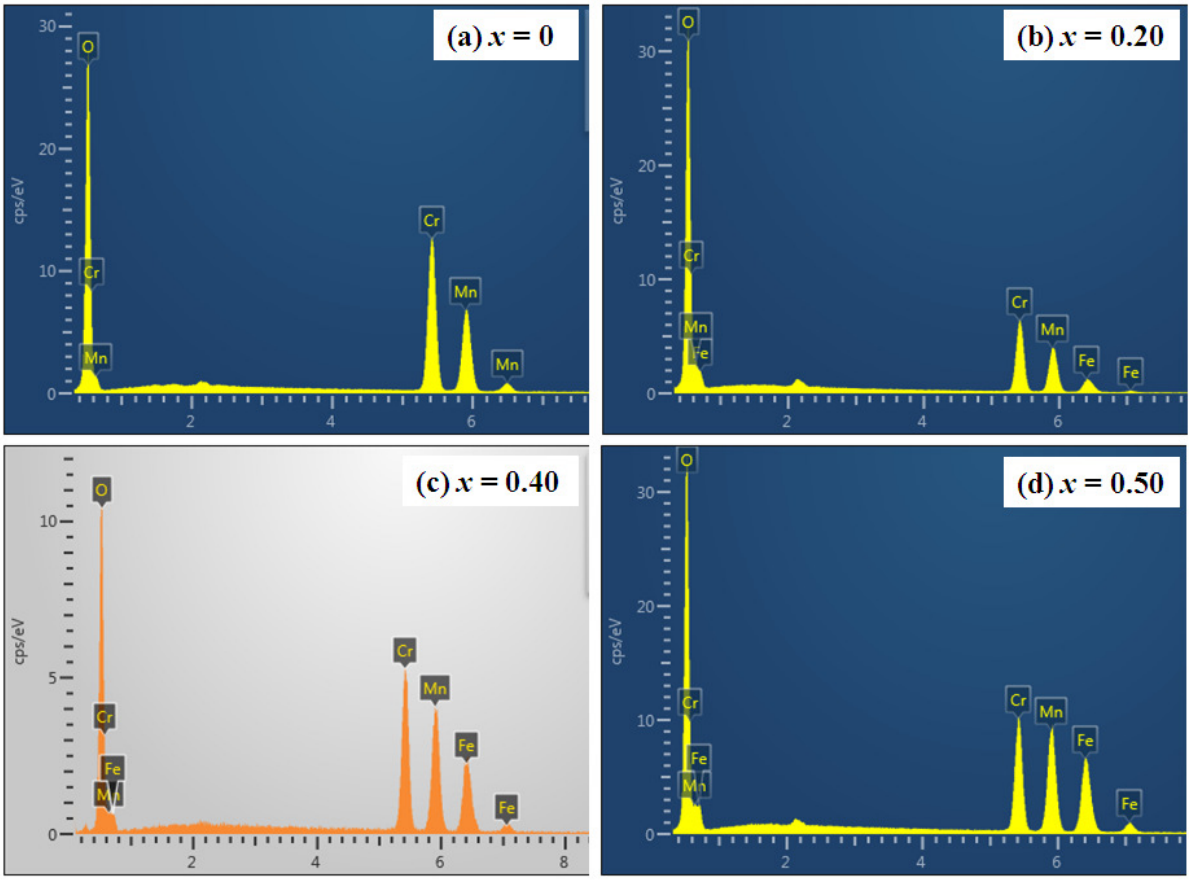


**Figure 5.8:** EDS spectrum of $x$ = 0, 0.20, 0.40 and 0.50 samples.

**Table 5.2:** The cationic ratio determined from EDS analysis for $x$ = 0, 0.20, 0.40 and 0.50 samples.

| Samples | Calculated Cationic Ratio from EDS Analysis | | |
|---|---|---|---|
| | **Mn** | **Cr** | **Fe** |
| ***x* = 0** | 0.98 | 2.01 | 0.00 |
| ***x* = 0.20** | 0.98 | 1.62 | 0.38 |
| ***x* = 0.40** | 1.00 | 1.17 | 0.77 |
| ***x* = 0.50** | 1.00 | 1.01 | 0.95 |

## 5.2.2 Magnetic Properties of $Mn(Cr_{1-x}Fe_x)_2O_4$

Magnetization as a function of temperature (*M–T*) were recorded under both zero field cooled (ZFC) and field cooled (FC) conditions for all the $Mn(Cr_{1-x}Fe_x)_2O_4$ samples for an applied field of 100 Oe. Fig. 5.9 shows the magnetization versus temperature plots for $x$ = 0 – 0.50 samples. All the samples exhibit the FIM behavior and the FIM transition temperature ($T_C$) is determined from the $dM/dT$ versus $T$ plot. $T_C$ for $x = 0$ sample is found to be 46 K and it is comparable to the earlier reports [38, 154]. For $x = 0.05$, the $T_C$ becomes 72 K. Thus with increase in the Fe concentration the FIM $T_C$ increases systematically and reaches 402 K for $x$ = 0.50 from 46 K for $x$ = 0. This increase in $T_C$ emphasizes the strengthening of the superexchange interaction between A and B site cations due to the substitution of $Fe^{3+}$ ions with two $e_g$ electrons in place of $Cr^{3+}$ having zero $e_g$ electron. In the present measurement, we have not observed the spiral FIM transition which is expected at 18 K for the pristine $MnCr_2O_4$ because of the limitation of lower temperature limit (25 K) of the present experimental set up. Such ordering is expected to be further shifted to lower temperature due to Fe substitution, as reported in some earlier reports [205, 206]. This may be the reason that we have not observed any additional transition in case of the Fe substituted samples also. On the other hand, the bifurcation between the ZFC and the FC curve indicates non collinear magnetic structure of the samples. The nature of *M–T* plots of $x$ = 0 – 0.25 samples follow the typical FIM transition; however a peculiar behavior is observed for $x \geq$ 0.30. The *M–T* plots of $x = 0.30$ sample under both ZFC and FC conditions show a peak like structure with a large bifurcation between them for $T < T_C$ and this can be attributed to spin glass (SG) like transition. Similar behavior is observed for $x = 0.40$ sample around the same temperature. Similar peak like behavior observed in spinel $CuCrTiS_4$ and $Fe_{1-x}Cu_xAl_2O_4$ compounds is explained in terms of SG behavior [207, 208]. In addition to this peak, $x = 0.40$ sample shows a second peak after crossing a minimum value of magnetization at 267 K and finally it reaches the paramagnetic (PM) region. Hence, the $x$ = 0.40 sample undergoes magnetic compensation around 267 K followed by FIM transition at $T_C$ = 320 K. The $T_C$ is found to further increased to 402 K for $x$ = 0.50 with a large irreversibility for $T < T_C$. $x$ = 0.50 also shows a partial magnetic compensation like behavior. Detailed analysis and discussion of the compensation like behavior is given in section 5.2.3.

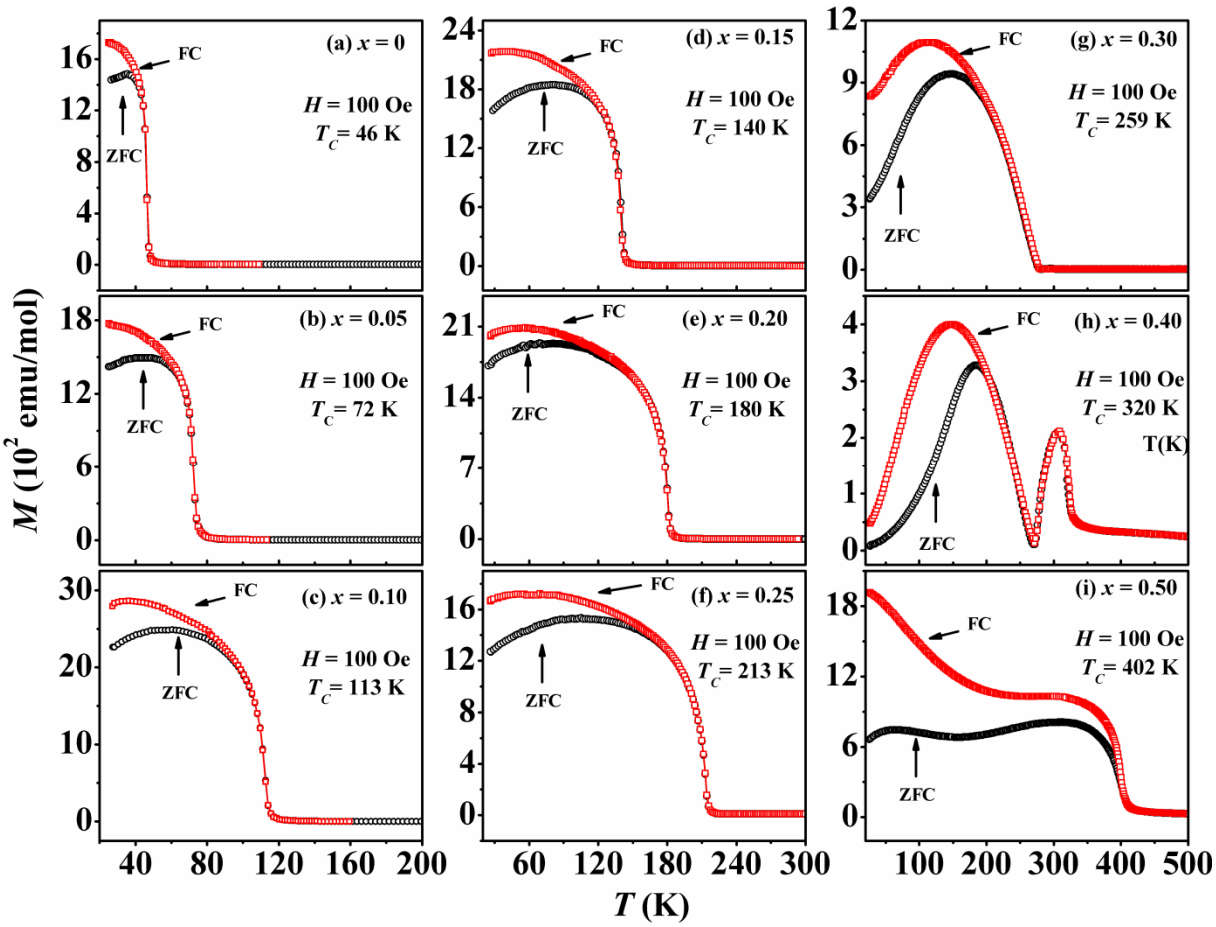


**Figure 5.9:** Temperature dependent magnetization of $Mn(Cr_{1-x}Fe_x)_2O_4$ ($x = 0 – 0.50$) samples under ZFC and FC conditions.

Further elucidation of the magnetic properties was carried out by recording the magnetic hysteresis ($M–H$) loops of $Mn(Cr_{1-x}Fe_x)_2O_4$ samples at different temperatures starting from 25 K to 300 K. $M–H$ loops of all the samples recorded at 25 K are shown in Fig. 5.10. The magnetization of $x = 0$, 0.05 and 0.10 samples are found to remain almost constant and the $M–H$ loops of the samples almost overlap each other; but the magnitude of magnetization decreases with increase in Fe concentration beyond $x = 0.10$. The $x = 0.40$ sample shows a minimum magnetization with largest coercivity (Fig. 5.11) and again for $x = 0.50$, the magnetization is found to increase. According to earlier reports [38, 150], the spiral component observed in $MnCr_2O_4$ does not contribute to the saturation magnetization ($M_s$) of the sample and hence the $M_s$ stays close to 1.2 $\mu_B$ for both $T < T_S$ and for $T > T_S$. Therefore,

in the present study we have used the *M–H* loops recorded at 25 K for the comparison of the $M_s$ values of various samples.

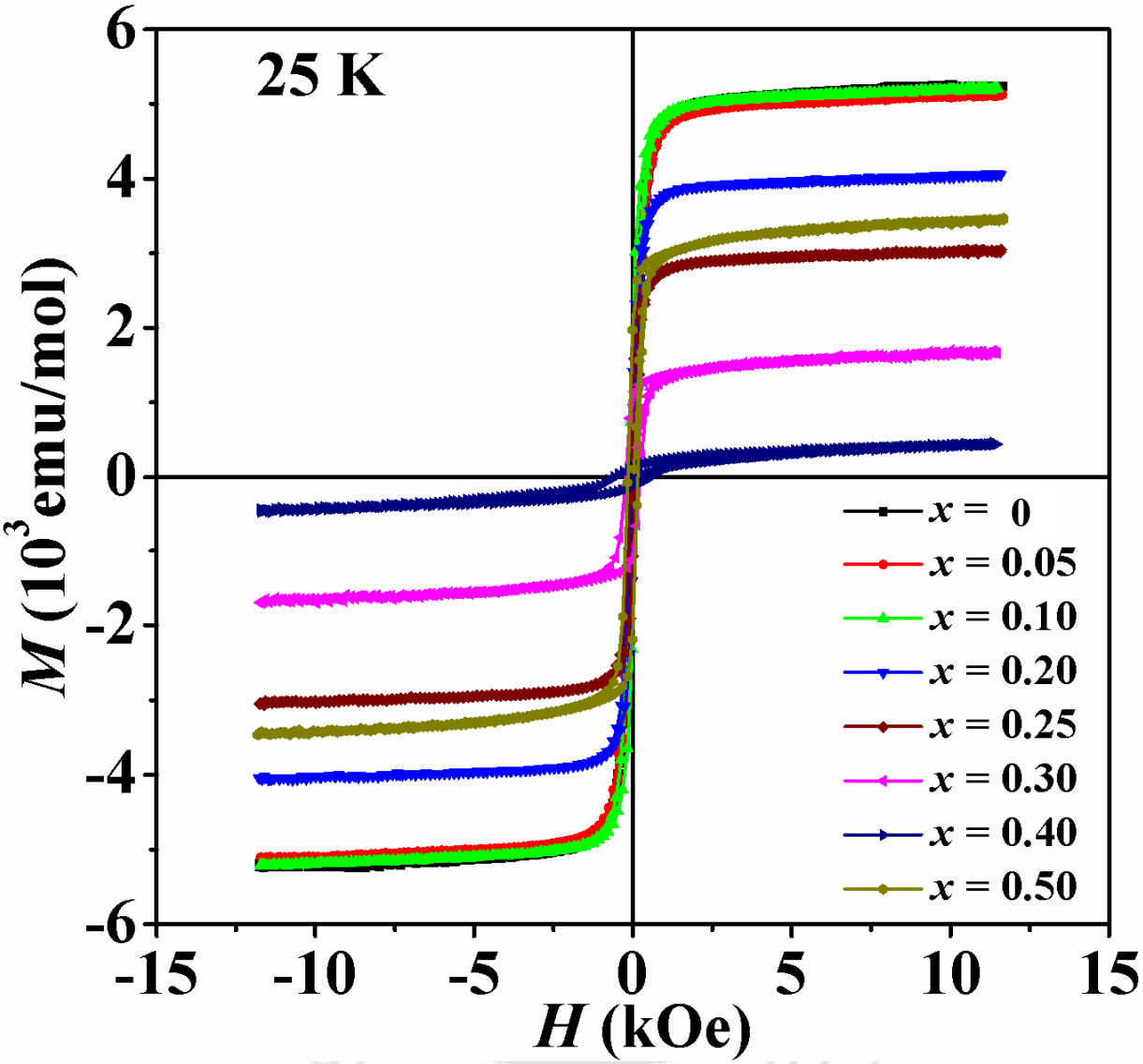


**Figure 5.10:** *M-H* loops of $Mn(Cr_{1-x}Fe_x)_2O_4$ compounds at 25 K.

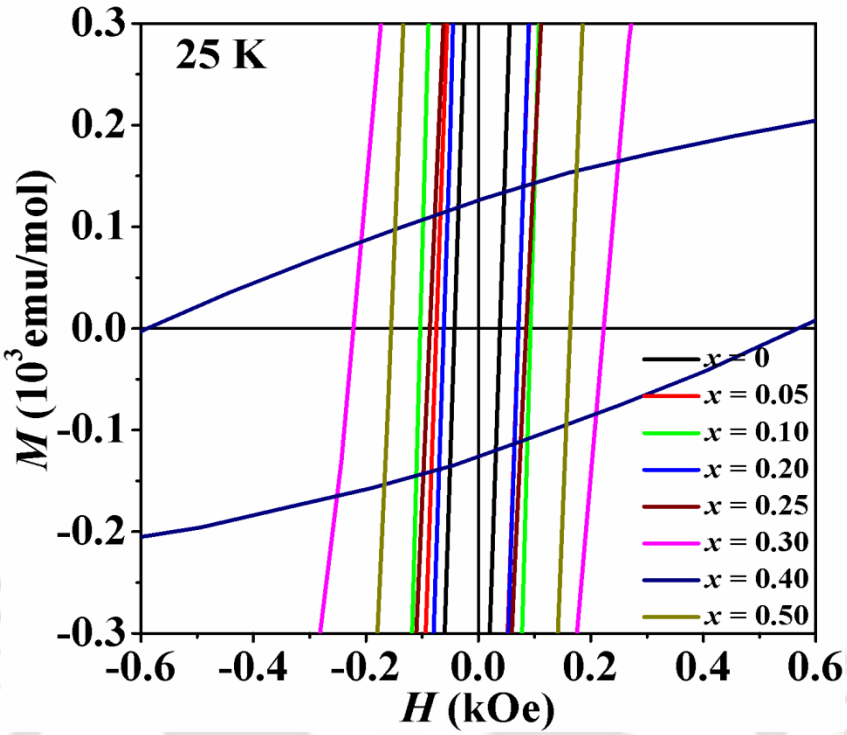


**Figure 5.11:** Expanded scale view in the sign reversal region of the *M-H* loops of $Mn(Cr_{1-x}Fe_x)_2O_4$ compounds at 25 K.

The experimental values of $M_s$ were determined by using the law of approach to saturation (LAS) model [209-211]. In general, the LAS method is used to analyze the magnetization curves of polycrystalline soft magnetic materials. The LAS describes the dependence of magnetization on the applied magnetic field for $H >> H_C$, where only the rotation process of magnetic domains against anisotropy occurs [209-211]. The expression for LAS can be written as

$$M(H) = M_s [1 - (a/H) - (b/H^2)] + \kappa H \qquad (5.2)$$

Where, $\kappa$ is the forced magnetization representing the linear increase in spontaneous magnetization at high applied field and at high temperature. The experimental $M_s$ value obtained from the fitting of the initial magnetization curve by LAS model thus gives the actual saturation magnetization of the samples excluding the linear forced magnetization part. The second term $(b/H^2)$ is due to the uniform magnetocrystalline anisotropy and the first term $(a/H)$ arises due to the structural defects and nonmagnetic inclusions [209-211]. In the present series, we have tried to fit the initial magnetization curves at different temperatures

by using the above expression (5.2) and also by neglecting the first term ($a/H$). We have not found any appreciable change in the quality of the fit and the respective parameters, so the term $a/H$ was neglected. Hence for fitting the initial curves, the following expression is used,

$$M(H) = M_s\,[1 - (b/H^2)] + \kappa H \qquad (5.3)$$

The initial curves of all the samples from $x = 0$ to 0.50 were fitted by Eq. (5.3) in the high field region and the fitted data are reproduced in the entire field range. The experimental (open circles) data along with the fitted curves (solid line) for $x = 0$, 0.10, 0.20, 0.30, 0.40 and 0.50 samples are shown in Fig. 5.12.

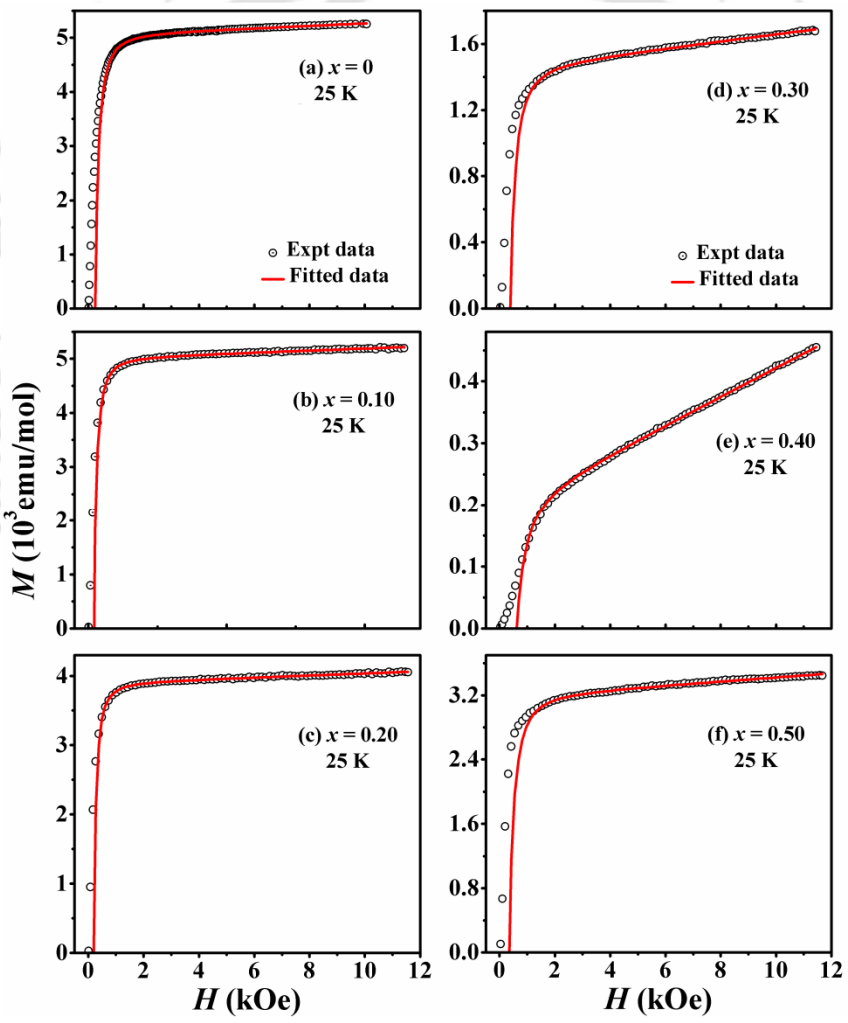


**Figure 5.12:** Initial magnetization curves for (a) $x = 0$, (b) $x = 0.10$, (c) $x = 0.20$, (d) $x = 0.30$, (e) $x = 0.40$ and (f) $x = 0.50$ samples along with the fitted data to the law of approach to saturation.

The experimental $M_s$ values of the samples were obtained at 25 K from the above fit and are given in table 5.3. The $M_s$ values of the samples were converted into Bohr magneton per formula unit and are plotted as a function of Fe concentration in Fig. 5.13. The plot shows three characteristic regions: (i) independent of $x$ up to 0.10, (ii) monotonous decrease in $M_s$ for $x$ = 0.10 to 0.40 and (iii) increase in $M_s$ for $x$ > 0.40. According to the magnetic structure of $MnCr_2O_4$ given by Tomiyasu *et al.* [118], the magnetic moments of A, B1 and B2 sublattices are conically ordered and their cone axes corresponds to FIM components inducing a net macroscopic FIM moment in $[1\bar{1}0]$ direction. The A site moment is antiparallel to the net B site moment. Therefore, in accordance with the magnetic structure given by Tomiyasu *et al.* [118], the total magnetization per formula unit of $MnCr_2O_4$ can be written as,

$$M = | \uparrow \mu_A - \downarrow \mu_{B1} - \downarrow \mu_{B2} | \qquad (5.4)$$

as discussed in Chapter 1. Where $\uparrow \mu_A$, $\downarrow \mu_{B1}$ and $\downarrow \mu_{B2}$ are the longitudinal components of the magnetic moments of A, B1 and B2 sublattices, respectively along the magnetic field direction. Considering the canting angles of A, B1 and B2 site moments, we have considered the spin only moments of $Mn^{2+}$, $Cr^{3+}(1)$ and $Cr^{3+}(2)$ as 4.41 $\mu_B$, 0.26 $\mu_B$ and 2.94 $\mu_B$, respectively. Therefore, the almost constant $M_s$ values observed upon Fe doping up to $x$ = 0.10 can be attributed to substitution of $Fe^{3+}$ ions at Cr1 sites. For $x$ > 0.10, the systematic decrease in the $M_s$ value is due to the dominant occupation of substituted $Fe^{3+}$ ions in the Cr2 site. The occupation of $Fe^{3+}$ ions in the Cr2 sites gradually enhances the net B site moment and hence the net magnetization decreases leading to a composition induced magnetic compensation at $x$ = 0.40. Thus in the composition range from $x$ = 0 – 0.30, A sublattice is the dominant magnetic contributor and for $x$ = 0.40, both the sublattice moments are almost compensated. However, A sublattice moment may be slightly greater than that of the B sublattice moment because of which complete zero magnetization is not observed at the compensation point. For further increase in the doping concentration beyond $x$ = 0.40, B sublattice moment dominates over the A sublattice moment and hence the magnetization increases beyond the compensation point. However, as per the XRD results discussed earlier we have assumed a small amount of Fe ions in the A site in $Fe^{2+}$ state and hence transfer of same amount of Mn ions to the B site in $Mn^{3+}$ state. Such substitution would not affect the

above argument of B sublattice moment dominating over the A sublattice moment. In order to justify this cation distribution obtained on the basis of experimental $M_s$ value, the theoretical $M_s$ value of $Mn(Cr_{1-x}Fe_x)_2O_4$ is estimated as a function of Fe concentration using the Eq. (5.4). The theoretical $M_s$ here describes the net magnetization per formula unit according to different sublattice moment. The calculated $M_s$ values as a function of Fe concentration is shown in Fig. 5.13 (solid line) along with the experimental data. It is found that the trend of experimental and the calculated $M_s$ values are comparable. However, relatively large difference is observed between the experimental and theoretical data for $x = 0$ to 0.10 samples. It could be due to their smaller $T_C$ values and hence considerable difference between the theoretical magnetic structure at 5 K (which was used for calculation) and the experimental data at 25 K. As Fe concentration increases, the superexchange interaction between the A and B site increases and as a result a stable magnetic structure is expected at 25 K. From the inset of Fig. 5.13, it is observed that the $M_s$ values obtained at 30 K, 35 K and 40 K also follow the similar trend as that of at 25 K.

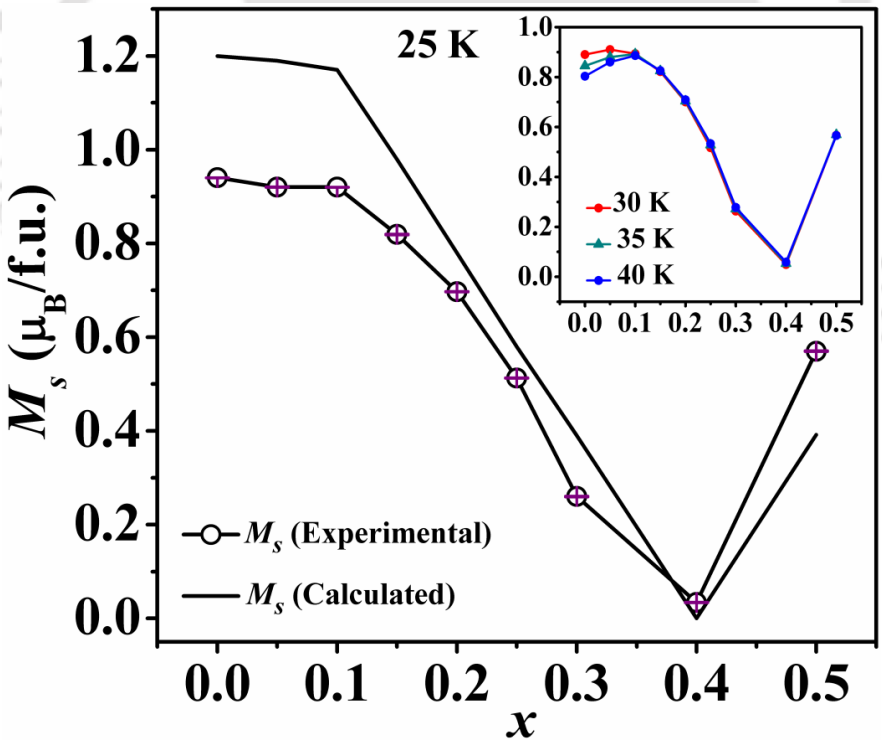


**Figure 5.13:** Variation of experimental (at 25 K) and calculated saturation magnetization ($M_s$) as a function of Fe concentration. Inset shows variation of $M_s$ with Fe concentration at 30, 35 and 40 K.

Magnetic anisotropy is a very important parameter for magnetic materials. The constant *b* in Eq. (5.2) is related to the effective magnetic anisotropy. Hence the effective magnetic anisotropy is calculated from the LAS by employing the following formula [210, 211],

$$b = (8/105)K^2 / M_s^2 \tag{5.5}$$

where, *K* is the effective anisotropy constant. Fig. 5.14(a) shows the variation of anisotropy constant as a function of Fe concentration at 25 K, 30 K, 35 K and 40 K. The anisotropy constant *K* varies in a similar manner as that of the saturation magnetization. It decreases with increase in Fe concentration and become minimum for $x = 0.40$ sample. The error in the estimated values of *K* from fitting is less than 1 %. The origin of the magnetocrystalline anisotropy is due to the spin orbit coupling at the crystal lattice. Large magnetocrystalline anisotropy observed in some ferrites like $CoFe_2O_4$, is attributed to the strong spin orbit coupling in $Co^{2+}$ ions at the octahedral sites. In this case the crystal field is not capable of removing the orbital degeneracy of $Co^{2+}$ at the octahedral site and thus the orbital moment is not quenched leading to strong spin orbit coupling [212]. In $MnCr_2O_4$, the anisotropy cannot be observed due to the $Mn^{2+}$ in tetrahedral site having zero orbital moment. Due to quenched orbital moment, $Cr^{3+}$ in the octahedral site also cannot give rise to anisotropy [213]. But from the neutron diffraction study of $MnCr_2O_4$ it was observed that magnetic moment of $Mn^{2+}$ deviates from their expected moment of 5 $\mu_B$ [118]. Therefore orbital moment may also present which gives rise to the small magnetocrystalline anisotropy in the sample. A uniaxial crystal field acting on $Cr^{3+}$ may also contribute to the magnetocrystalline anisotropy [214]. Due to the random substitution of $Fe^{3+}$, with zero orbital moment, in the two octahedral sites and reduction in the saturation magnetsation may causes the reduction of anisotropy in the doped samples. However slight increase in anisotropy for $x = 0.50$ sample may be due to the presence of $Fe^{2+}$ ions in the tetrahedral site, which is reported to contribute to the anisotropy [215]. However in the present case the anisotropy constant value is small (of the order of $10^4$ erg/cm$^3$) compared to other cobalt ferrite (of the order of $10^6$ erg/cm$^3$) [212].

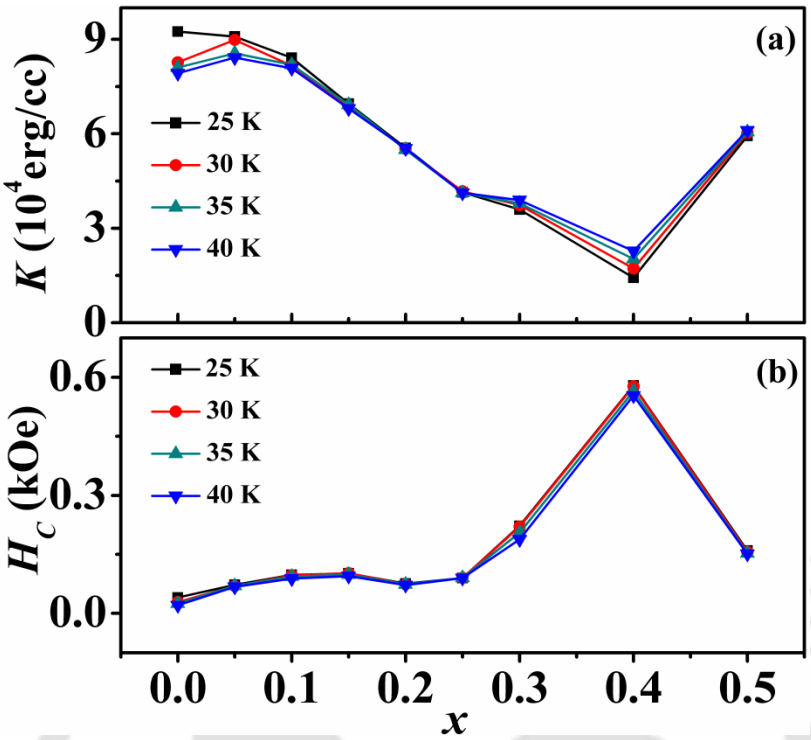


**Figure 5.14:** (a) Variation of anisotropy constant and (b) coercivity at 25, 30, 35 and 40 K as a function of Fe concentration '*x*'.

The coercivity ($H_C$) of the samples was calculated by using the Eq. (3.4) as reproduced below,

$$H_C = \left(H_+ - H_-\right)/2 \tag{5.6}$$

where, $H_+$ and $H_-$ are two magnetic fields values corresponding to $M$ = 0, during the ascending and the descending branches of $M$–$H$ loop. On contrary to $M_s$ and $K$, the coercivity at the compositional compensation point ($x$ = 0.40) is found to be maximum [Fig. 5.14(b)]. In general, the coercivity becomes minimum at the compensation point due to the compensated magnetic moments of the two sublattices of the sample and moreover, coercivity is expected to be smaller whenever the anisotropy is small. The rather large $H_C$ value of $x$ = 0.40 sample can be understood by closely looking at the $M$–$H$ loop and $M$–$T$ plots of the sample. The $x$ = 0.40 sample is at the verge of composition induced magnetic compensation; where the A site and B site moments are almost equal and opposite to each other mimicking the typical antiferromagnetic (AFM) interaction. In AFM like interaction, the net moment is zero and

hence the magnetic energy induced by the applied field *M.H* is close to zero. Thus even to saturate a small uncompensated $M_s$ value, a very large field is required. This can be seen in Fig. 5.12(e) as a rather small variation of *M* as a function of *H* rather than sharp rise in *M* with *H* as seen for other samples. The *M–T* plot of $x = 0.40$ shows magnetic compensation at 267 K [Fig. 5.9(h)] and for $T < T_{comp}$, the magnetization increases down to the peak temperature $T_P = 184$ K and for $T < T_P$, the magnetization decreases towards zero. Such decrease in *M* for $T < T_P$ can be understood in terms of consolidation of magnetic domains to keep the net magnetization and magnetic energy to be minimum. At 25 K far below the $T_P$, *M–H* loop was recorded which is expected to show a large $H_C$ due to the rather poor response of magnetic field as a result of rather small magnetization of each domain. The observed SG like behavior for $x = 0.40$ sample for $T < 184$ K is also expected to contribute to the large $H_C$ value at 25 K.

**Table 5.3:** Saturation magnetization ($M_s$), coercivity ($H_C$) and effective anisotropy constant ($K$) of the samples $Mn(Cr_{1-x}Fe_x)_2O_4$ at 25 K.

| Samples | $M_s$ (emu/g) | $M_s$ ($\mu_B$/f.u.) | $H_C$ (Oe) | $K$ (erg/cm$^3$) |
|---|---|---|---|---|
| $x = 0$ | 23.54 | 0.94 | 40.41 | $9.25 \times 10^4$ |
| $x = 0.05$ | 23.00 | 0.92 | 72.83 | $9.09 \times 10^4$ |
| $x = 0.10$ | 22.96 | 0.92 | 98.15 | $8.41 \times 10^4$ |
| $x = 0.15$ | 20.43 | 0.82 | 102.00 | $6.95 \times 10^4$ |
| $x = 0.20$ | 17.41 | 0.70 | 75.67 | $5.55 \times 10^4$ |
| $x = 0.25$ | 12.66 | 0.51 | 89.95 | $4.14 \times 10^4$ |
| $x = 0.30$ | 6.44 | 0.26 | 222.45 | $3.59 \times 10^4$ |
| $x = 0.40$ | 0.84 | 0.034 | 578.51 | $1.43 \times 10^4$ |
| $x = 0.50$ | 14.03 | 0.57 | 159.23 | $5.93 \times 10^4$ |

Fig. 5.15 shows the variation of $M_s$ and $H_C$ as a function of temperature for different samples. The temperature variation of $M_s$ shows that mostly $M_s$ decreases with increase in temperature and at low temperature they tend to saturate. Such behavior is generally expected due to increase in thermal energy at higher temperature that tends to disorder magnetic correlation. However for $x = 0.40$ and 0.50 samples, a broad peak like behavior is seen due to

tendency towards inverse spinel structure and their competing sublattice moments. The $H_C$ value mostly decreases with increase in temperature due to thermal excitation and decrease in anisotropy constant.

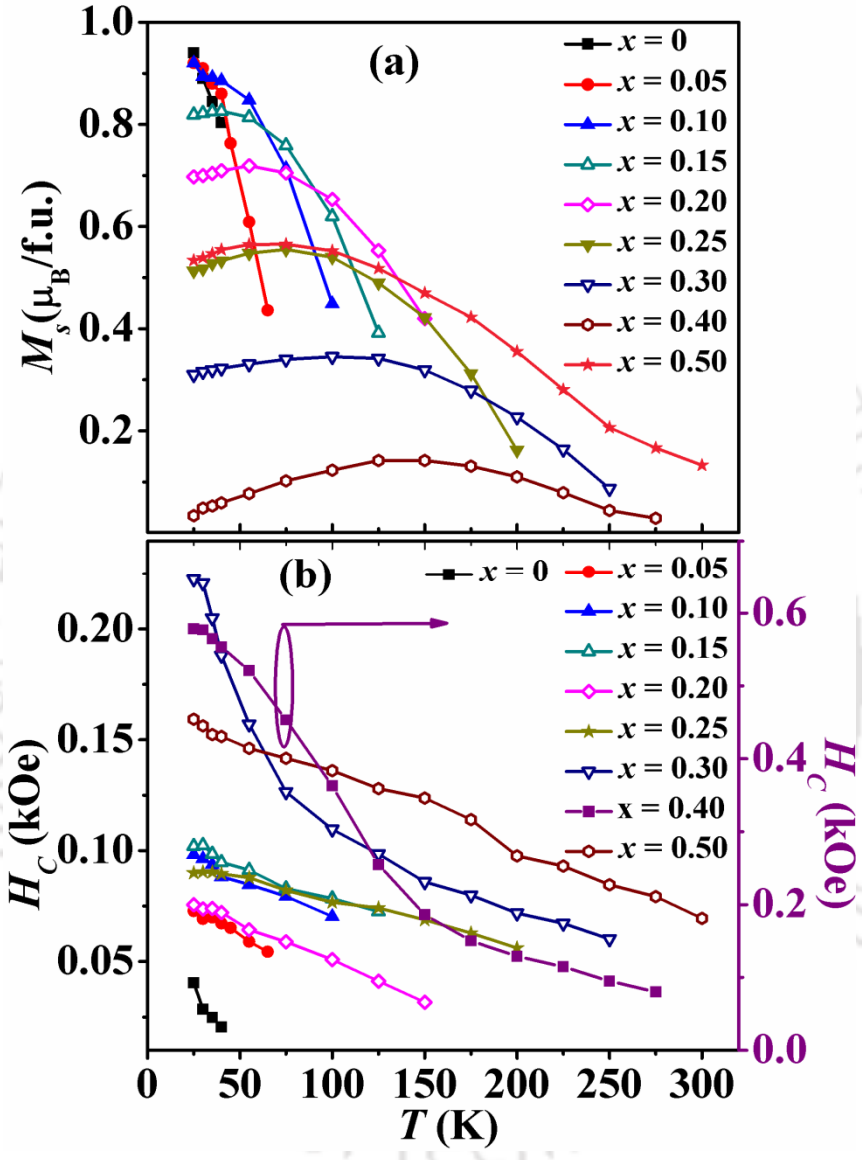


**Figure 5.15:** Variation of (a) saturation magnetization and (b) coercivity with temperature.

## 5.2.3 Temperature Induced Magnetic Compensation

Above results on the magnetic properties of Fe substituted $MnCr_2O_4$ samples reveal that the $x$ = 0.40 sample shows an interesting composition induced as well as temperature induced magnetic compensation. In order to confirm and further understand the temperature

induced compensation behavior we have carried out *M–T* measurements of $x = 0.40$ samples by cooling under different magnetic fields in the range of $H_{FC} = 0.1$ kOe to 3kOe. These plots are shown in Fig. 5.16(a), where the magnetic compensation is observed at 267 K irrespective of the $H_{FC}$ value. All the *M–T* curves of the samples show similar trend. But, with increase in $H_{FC}$ value, the entire *M–T* curve is found to shift upwards due to enhanced field induced magnetization. This magnetic compensation behavior is observed due to different temperature dependences of the magnetic moment of the two sublattices of the sample. As discussed in earlier section, it can be understood in terms of preferential substitution of doped $Fe^{3+}$ions at Cr2 site which increases the net B site moment and is opposite to A site moment. Under the above condition, different temperature dependence of sublattice moments give rise to magnetic compensation at $T_{comp}$ = 267 K. Unlike other magnetic materials (like $Co(Cr_{0.95}Fe_{0.05})_2O_4$ [26], $LaCr_{0.85}Mn_{0.15}O_3$ [86], *etc*.) here no negative magnetization is observed for $T < T_{comp}$. This can be understood in terms of relatively low anisotropy constant and hence complete rotation of A site and B site moments by 180° without changing their FIM interaction for $T < T_{comp}$. So for $T < T_{comp}$ the dominant B sublattice moments orient along the field direction. Such compensation effect without any MR is observed in other compounds also [62, 69]. The $x = 0.50$ sample also shows some partial compensation like behavior [Fig. 5.9(i)], but due to dominant B sublattice moment for $x > 0.40$, this behavior is not prominent here. For all other samples one sublattice moment is completely dominant over the other and therefore no magnetic compensation is observed. The schematic diagram in order to explain the compensation behavior in $x = 0.40$ sample in terms of different sublattice moments is shown in Fig. 5.16(b) and (c).

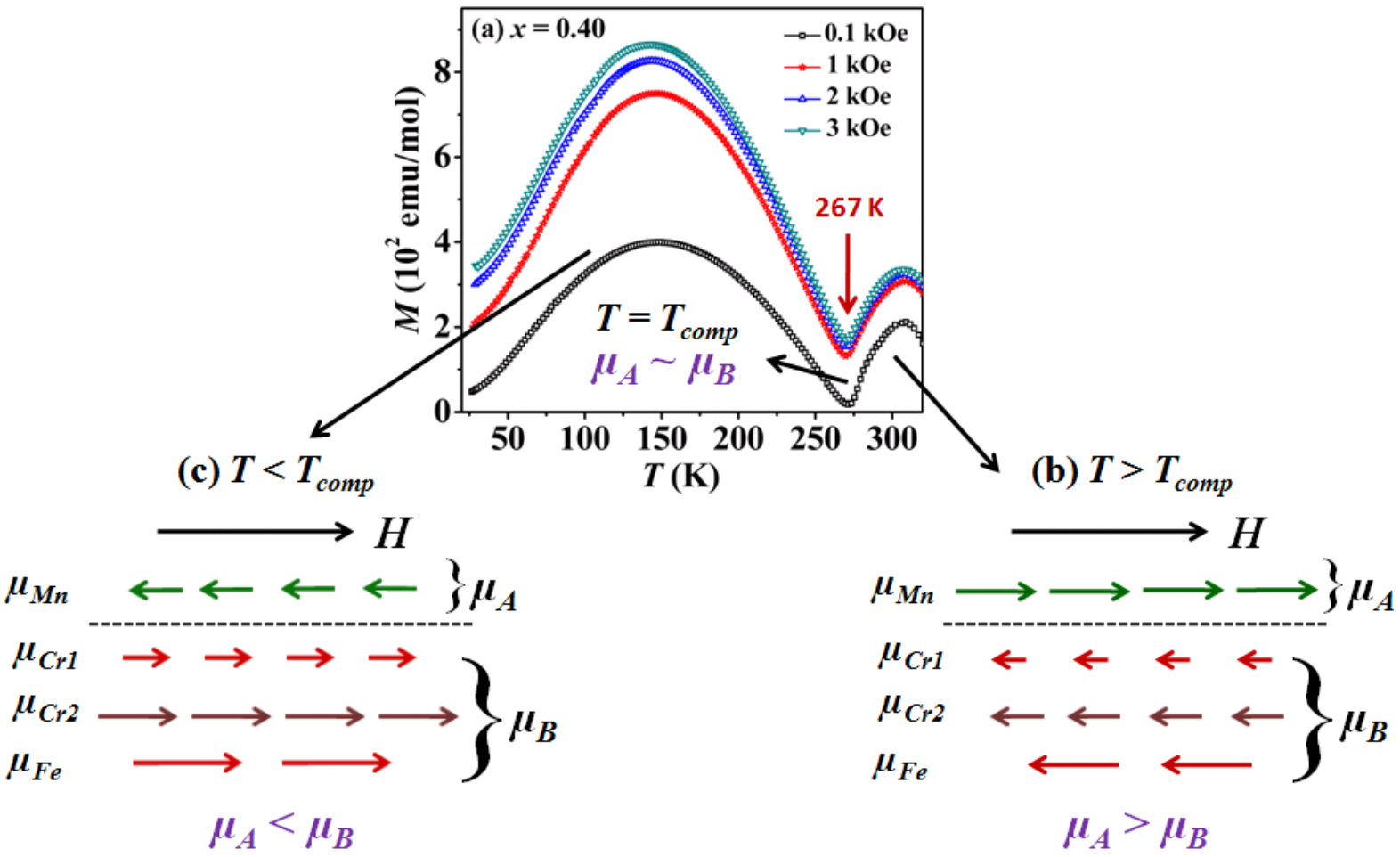


**Figure 5.16:** (a) Magnetization as a function of temperature for $x$ = 0.40 sample under FC condition for different cooling fields. Schematic block diagram of the magnetic configurations in two temperature regions (b) $T > T_{comp}$ and (c) $T < T_{comp}$.

In order to further understand the magnetic properties of $x$ = 0.40 sample and to investigate the presence of EB behavior, we have recorded $M$–$H$ loops at different temperatures in the vicinity of $T_{comp}$ by cooling the sample under a field of $H_{FC}$ = 3000 Oe. These $M$–$H$ loops in expanded scale are shown in Fig. 5.17. All loops are found to be symmetric and hence no signature of EB behavior is seen. As the temperature is increased towards $T_{comp}$ both $M_s$ and remanent magnetization ($M_r$) values are found to decrease with a minimum value at $T_{comp}$ and for further increase in temperature beyond $T_{comp}$, these values are found to increase again. The plots of obtained $M_s$ and $M_r$ values as a function of temperature are shown in Fig. 5.18, where minimum values are seen for $M_s$ and $M_r$ around $T_{comp}$. However, $M_s$ does not approache zero at $T_{comp}$ and it signifies that perfect compensation is not achieved due to small mismatch between net A and B sublattice moments under FC condition. The temperature dependence of $H_C$ shows a peculiar behavior with a maximum $H_C$ value at $T_{comp}$ which is in contrary to the earlier reports [26, 91]. In these reports the coercivity shows a divergence behavior on the both sides of the $T_{comp}$ (twin peak like behavior) while dropping to almost zero at the compensation temperature. They have attributed such drop in $H_C$ at $T_{comp}$ to the fully compensated moments of both the sublattices and observed linear loop at this temperature. This means that at the compensation temperature the FIM compound behaves as an AFM. But at this temperature, the two sublattice magnetizations of the present sample are not fully compensated and a very small net magnetization of each domain exists rather than be zero. As a result of this the external magnetic field induces very low magnetic energy $M.H$ on each domain. As a result of this each domain responds very weakly to increase in applied field and as a result of this relatively large field is needed to saturate the magnetization. This process leads to rather large $H_C$ value. This argument is consistent with large $H_C$ observed for $x$ = 0.40 sample [Fig. 5.14(b)] even at 25 K compared to rest of the samples. Such divergence of coercivity at the compensation point has also been observed in GdCo films and in some homogeneous ferrimagnet [109, 216].

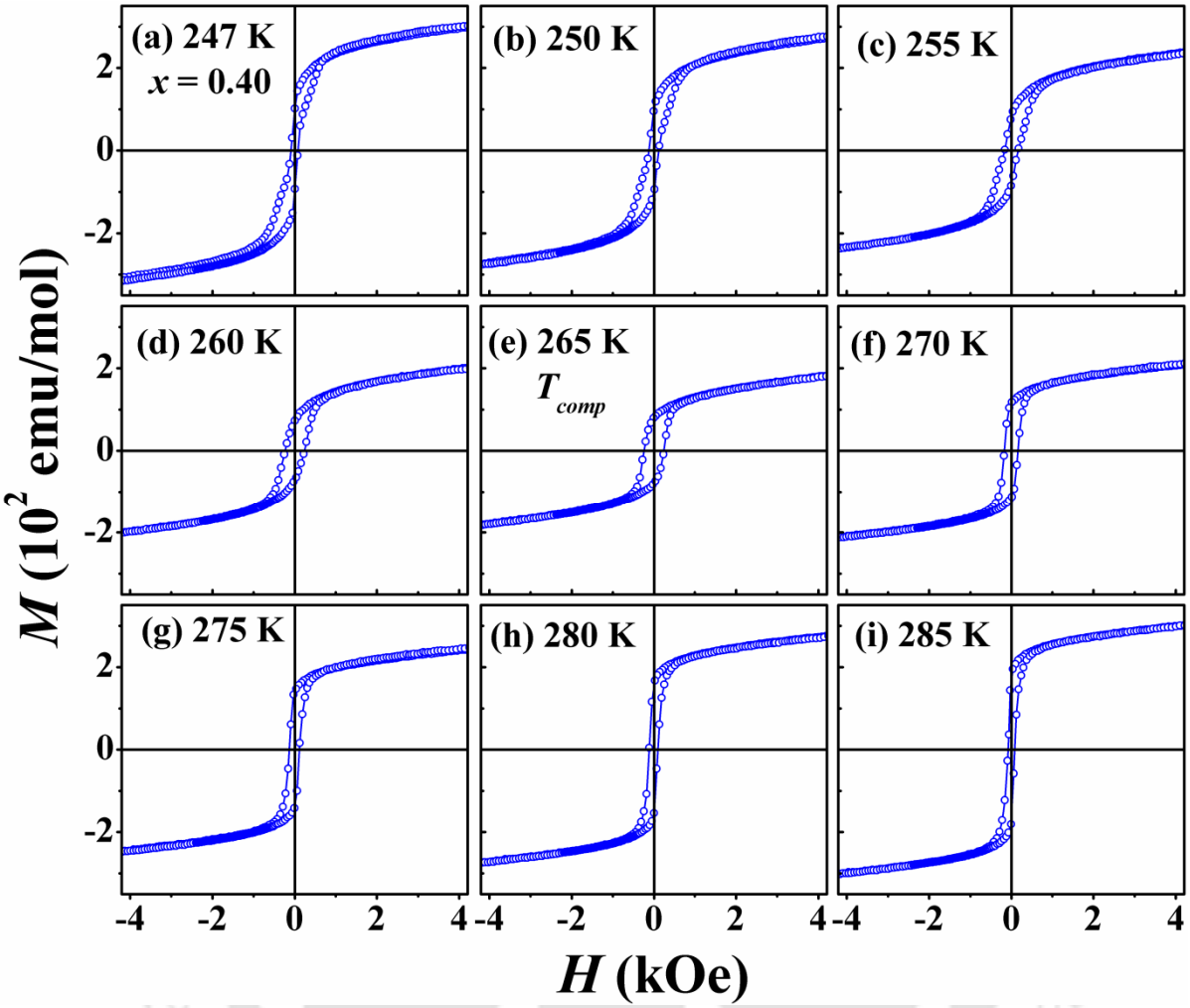


**Figure 5.17:** FC (H = 3000 Oe) *M–H* loops of $x$ = 0.40 sample at different temperatures in an expanded scale.

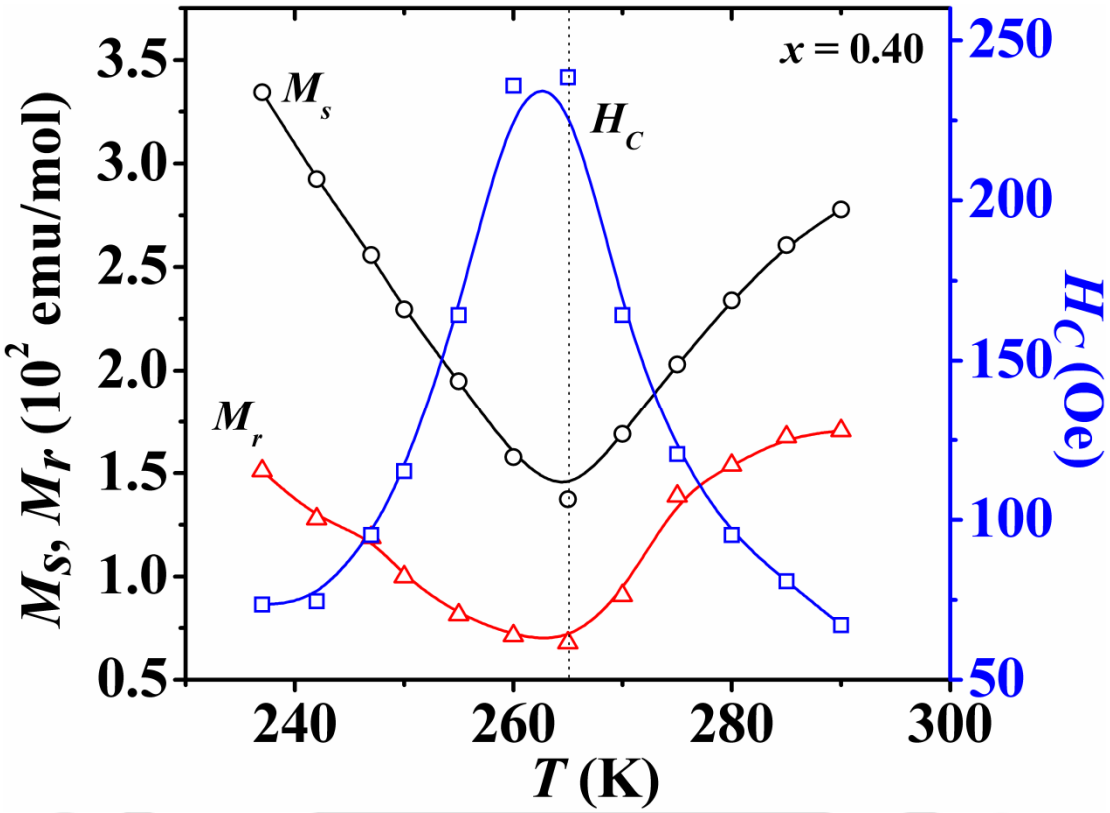


**Figure 5.18:** Variation of saturation magnetization ($M_s$), remanent magnetization ($M_r$) and coercive field ($H_C$) with temperature for $x = 0.40$ sample.

# 5.3 Al Substituted $MnCr_2O_4$ Series

This section deals with the effect of Al substitution at the Cr site of $MnCr_2O_4$. The preparation of $Mn(Cr_{1-x}Al_x)_2O_4$ ($x$ = 0 – 0.30) samples and study of their structural, temperature and field dependent magnetic properties are presented.

Bulk polycrystalline samples of $Mn(Cr_{1-x}Al_x)_2O_4$ ($x$ = 0 – 0.30) were prepared by using sol–gel method. Stoichiometric ratio of high purity (99 %) $C_4H_6MnO_4.4H_2O$, $Cr(NO_3)_3.9H_2O$ and $Al(NO_3)_3.9H_2O$ were used as the starting materials. The samples were presintered at 600 °C, 800 °C and 1000 °C for 12 hours with intermediate grinding. Final sintering was carried out at 1200 °C for 24 hours in pellet form. XRD patterns at room temperature were recorded by using Rigaku make TTRAX III X-ray diffractometer using Cu-Kα radiation and the patterns obtained were analyzed by Rietveld refinement using Fullprof program. Microstructural and composition analyses were carried out using ZEISS make FESEM (ΣIGMA). Magnetic field and temperature dependent magnetization measurements were carried out by using a Lakeshore make VSM of model no. 7410. Raman spectra at room temperature were recorded using micro-Raman spectrometer (LabRam HR800, Horiba Jobin Vyon) in the wave number range of 100 to 1000 $cm^{-1}$ with excitation wavelength of 514 nm.

## 5.3.1 Structural Properties

Room temperature XRD patterns recorded for all the above samples are shown in Fig. 5.19. Similar to Fe doped samples, here also no signature of structural transition is observed. These patterns were Rietveld refined by choosing $Fd\bar{3}m$ space group in cubic structure and found that all the samples including parent compound are well fitted to this space group. Thus all the samples are in single phase form. Rietveld refinement of $x$ = 0 and 0.30 samples are shown in Fig. 5.20. The XRD peaks are found to shift towards the higher 2θ value with increase in $x$, as shown in the enlarged view of the high intense (311) peak for different samples [Fig. 5.21(a)] and it signifies the decrease of lattice parameter as $x$ is increased. The lattice constant obtained from Rietveld refinement as a function of $x$ is shown in Fig. 5.21(b), where it is found to decrease linearly with increase in $x$. It is due to the smaller $Al^{3+}$ ions (~ 0.535 Å) substituting the $Cr^{3+}$ ions (~ 0.615 Å) at octahedral site. Similar reduction in lattice

constant is expected if $Al^{3+}$ ions (0.39 Å) are substituted at tetrahedral site, *i.e.* by partially replacing $Mn^{2+}$ ions (0.66 Å). The possible distribution of $Al^{3+}$ ions in both A and B sites is discussed later in the context of magnetic properties. The lattice parameter of all the samples and the reliability factors of the Rietveld refinement are displayed in table 5.4.

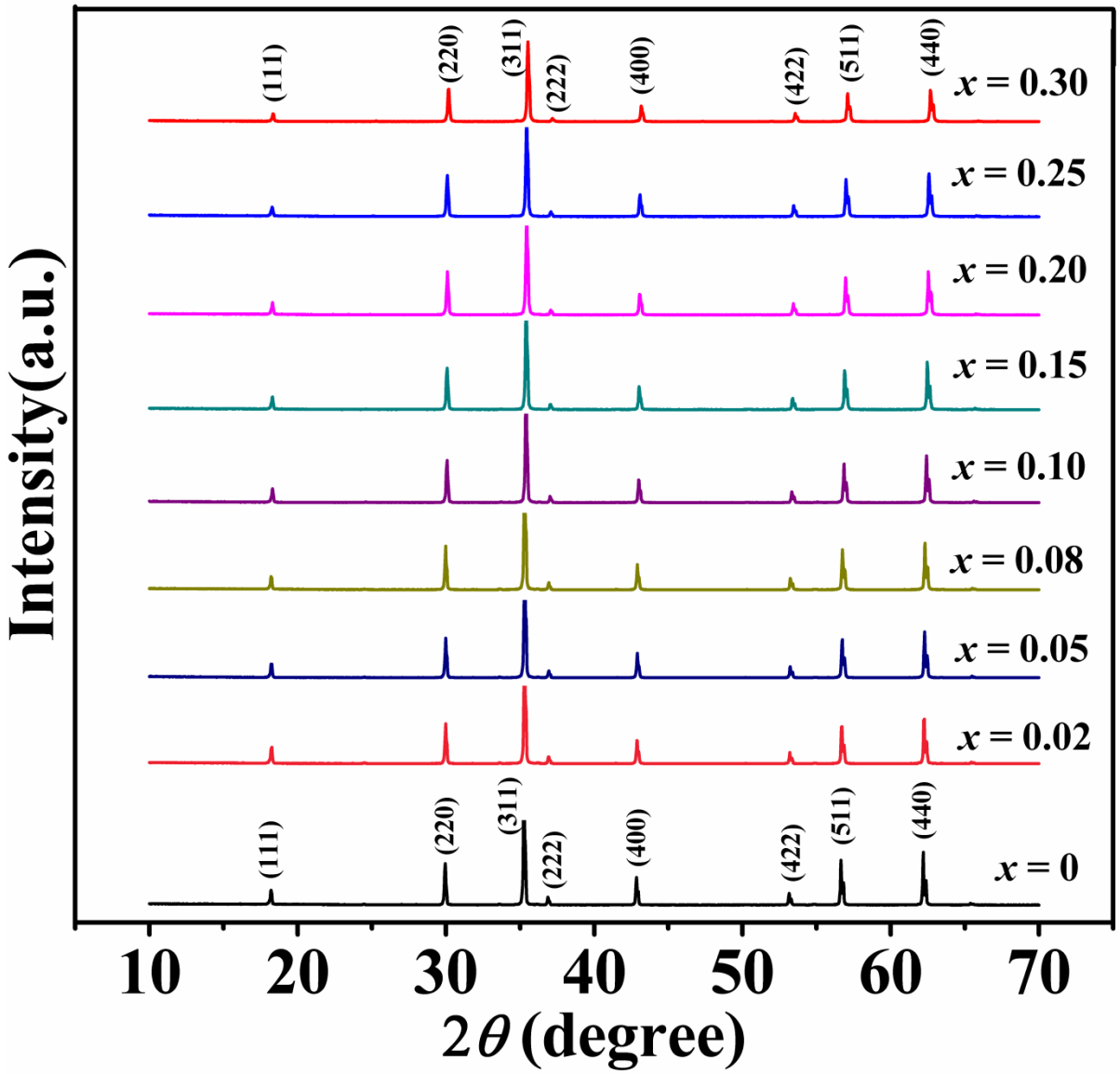


**Figure 5.19:** XRD patterns of $Mn(Cr_{1-x}Al_x)_2O_4$ compounds for $x = 0 – 0.30$.

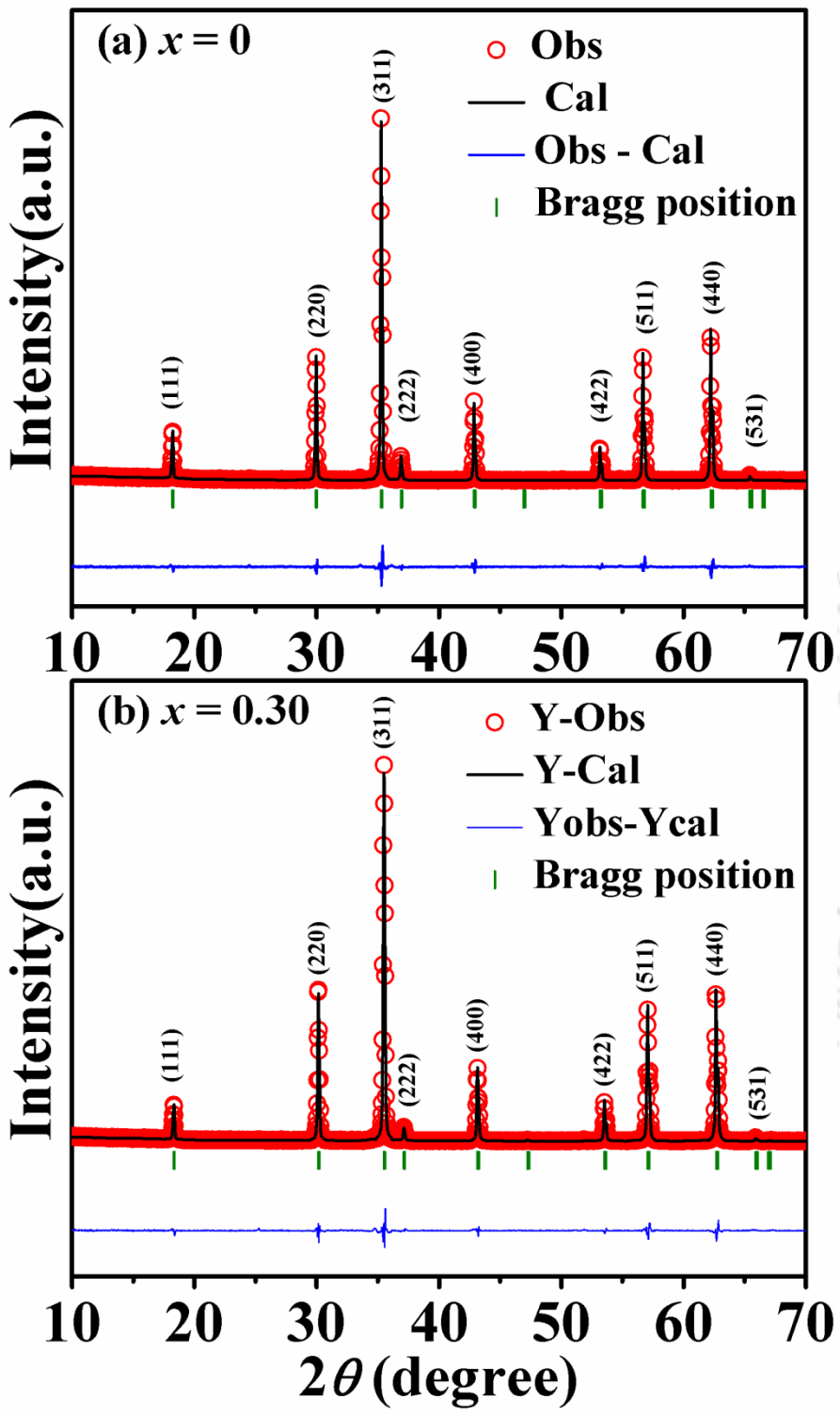


**Figure 5.20:** Rietveld refinement of the XRD patterns of (a) $x = 0$ and (b) $x = 0.30$ samples. The red open circles are the experimental data and the black solid lines are the fitted data. The bottom line gives the difference between experimental and theoretical data.

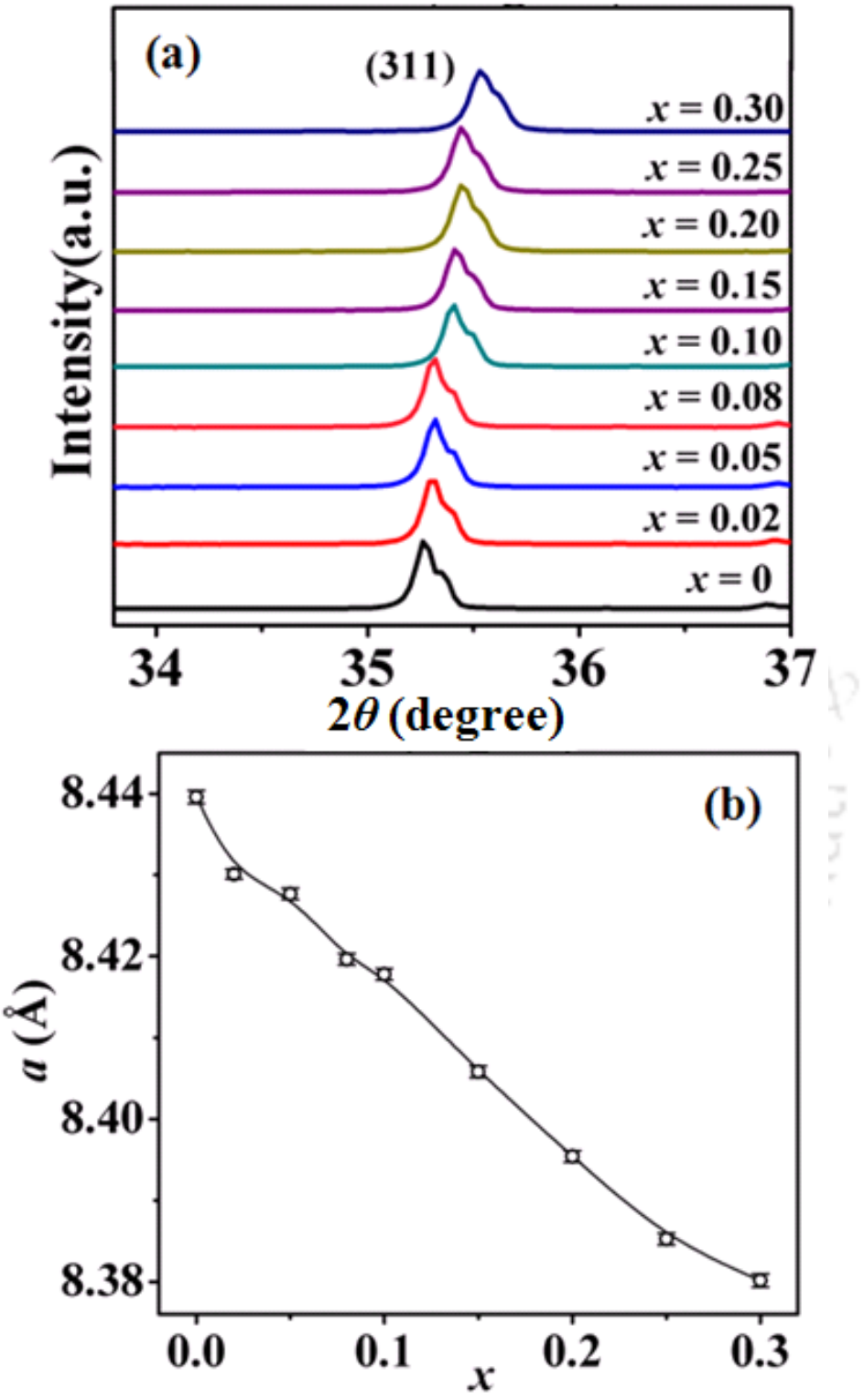


**Figure 5.21:** (a) Enlarged view of the high intense (311) peak for $x = 0 – 0.30$ samples and (b) Variation of lattice parameter with Al concentration. The solid line is just for guidance.

**Table 5.4:** Parameters obtained from the Rietveld analysis of XRD patterns for the samples $Mn(Cr_{1-x}Al_x)_2O_4$ (0 – 0.30). $R_F$, $R_{Bragg}$, $R_P$ and $\chi^2$ are the reliability factors.

| Sample/ Parameters | $x = 0$ | $x = 0.02$ | $x = 0.05$ | $x = 0.08$ | $x = 0.10$ | $x = 0.15$ | $x = 0.20$ | $x = 0.25$ | $x = 0.30$ |
|---|---|---|---|---|---|---|---|---|---|
| Space group | $Fd\bar{3}m$ | $Fd\bar{3}m$ | $Fd\bar{3}m$ | $Fd\bar{3}m$ | $Fd\bar{3}m$ | $Fd\bar{3}m$ | $Fd\bar{3}m$ | $Fd\bar{3}m$ | $Fd\bar{3}m$ |
| $a$ (Å) | 8.4396 (0.0008) | 8.4301 (0.0006) | 8.4277 (0.0007) | 8.4196 (0.0007) | 8.4178 (0.0007) | 8.4058 (0.0007) | 8.3954 (0.0007) | 8.3852 (0.0007) | 8.3802 (0.0008) |
| *Volume* (Å$^3$) | 601.126 (0.09) | 600.199 (0.01) | 598.581 (0.08) | 596.869 (0.09) | 596.482 (0.08) | 593.937 (0.09) | 591.733 (0.09) | 589.586 (0.09) | 588.515 (0.08) |
| $R_F$ (%) | 2.61 | 2.37 | 2.69 | 3.13 | 2.64 | 2.79 | 2.91 | 2.96 | 3.26 |
| $R_{Bragg}$ (%) | 3.24 | 3.39 | 3.50 | 3.57 | 3.24 | 3.11 | 3.02 | 2.92 | 2.91 |
| $R_P$ (%) | 7.33 | 7.69 | 7.87 | 7.29 | 7.56 | 7.08 | 7.56 | 7.48 | 8.04 |
| $\chi^2$ | 4.52 | 5.03 | 5.04 | 4.95 | 4.52 | 4.37 | 3.94 | 3.83 | 4.50 |
| Mn/Cr/Al Occupancy | 1.011 / 1.990 /0.000 | 1.004 / 1.957 / 0.037 | 1.009 / 1.897 / 0.097 | 1.011 / 1.833 / 0.153 | 1.010 / 1.797 / 0.197 | 1.009/ 1.697 / 0.297 | 1.008 / 1.598 / 0.398 | 1.005 / 1.499 / 0.499 | 0.996 / 1.405 / 0.605 |

Raman spectroscopic study of all the samples was carried out in order to further understand the structural properties. Raman spectra of $Mn(Cr_{1-x}Al_x)_2O_4$ ($x$ = 0 – 0.30) samples (open circles) are shown in Fig. 5.22. The position and FWHM of the Raman peaks were estimated by fitting the peaks (green solid lines) by Lorentz profile. The Raman spectrum of the parent compound, *i.e.* $MnCr_2O_4$ contains four peaks at 683 cm$^{-1}$, 638 cm$^{-1}$, 509 cm$^{-1}$ and 197 cm$^{-1}$. These peak positions are consistent with the earlier observed modes for $MnCr_2O_4$ and $CoCr_2O_4$ [198, 200, 201]. As discussed in section 5.2, the strongest peak observed at 683 cm$^{-1}$ is ascribed to the $A_{1g}$ mode and the other three peaks at 638 cm$^{-1}$, 509 cm$^{-1}$ and 197 cm$^{-1}$ are assigned to $F_{2g}$ (1), $F_{2g}$ (2) and $F_{2g}$ (3) modes, respectively [198]. With increase in Al concentration, the strongest peak observed at 683 cm$^{-1}$ for $x$ = 0 is found to shift towards higher wave number especially for $x$ > 0.05. The $A_{1g}$ mode at 683 cm$^{-1}$ originates from $CrO_6$ octahedra and therefore the shifting of this peak towards higher wavenumber for $x$ > 0.05 can be attributed to the occupation of lighter $Al^{3+}$ ions in the

octahedral $Cr^{3+}$ site. The peak position of $F_{2g}$ (2) mode observed at 509 $cm^{-1}$ is related to tetrahedral cations [204] and the shift of this peak towards higher wavenumber with increase in Al concentration illustrates that some of the substituted $Al^{3+}$ ions occupy the tetrahedral (Mn) site also rather than occupying only the Cr site. The broadening of peaks corresponding to both $A_{1g}$ and $F_{2g}$ (2) modes compared to the pristine $MnCr_2O_4$ indicates the development of a mixed spinel structure with some of the doped $Al^{3+}$ ions entering into the tetrahedral site [200, 202]. In addition to that we have observed an additional Raman mode peak at around 588 $cm^{-1}$ for all the doped samples which was not predicted by the group theory. This can be attributed to the activation of Raman mode due to the inverse spinel structure induced lattice distortion. Therefore as per the Raman study and from the study of magnetic properties as discussed in the later section we can conclude that upto $x$ = 0.05, $Al^{3+}$ ions occupy only the tetrahedral A site and beyond that they occupy both A and B sites forming a mixed spinel.

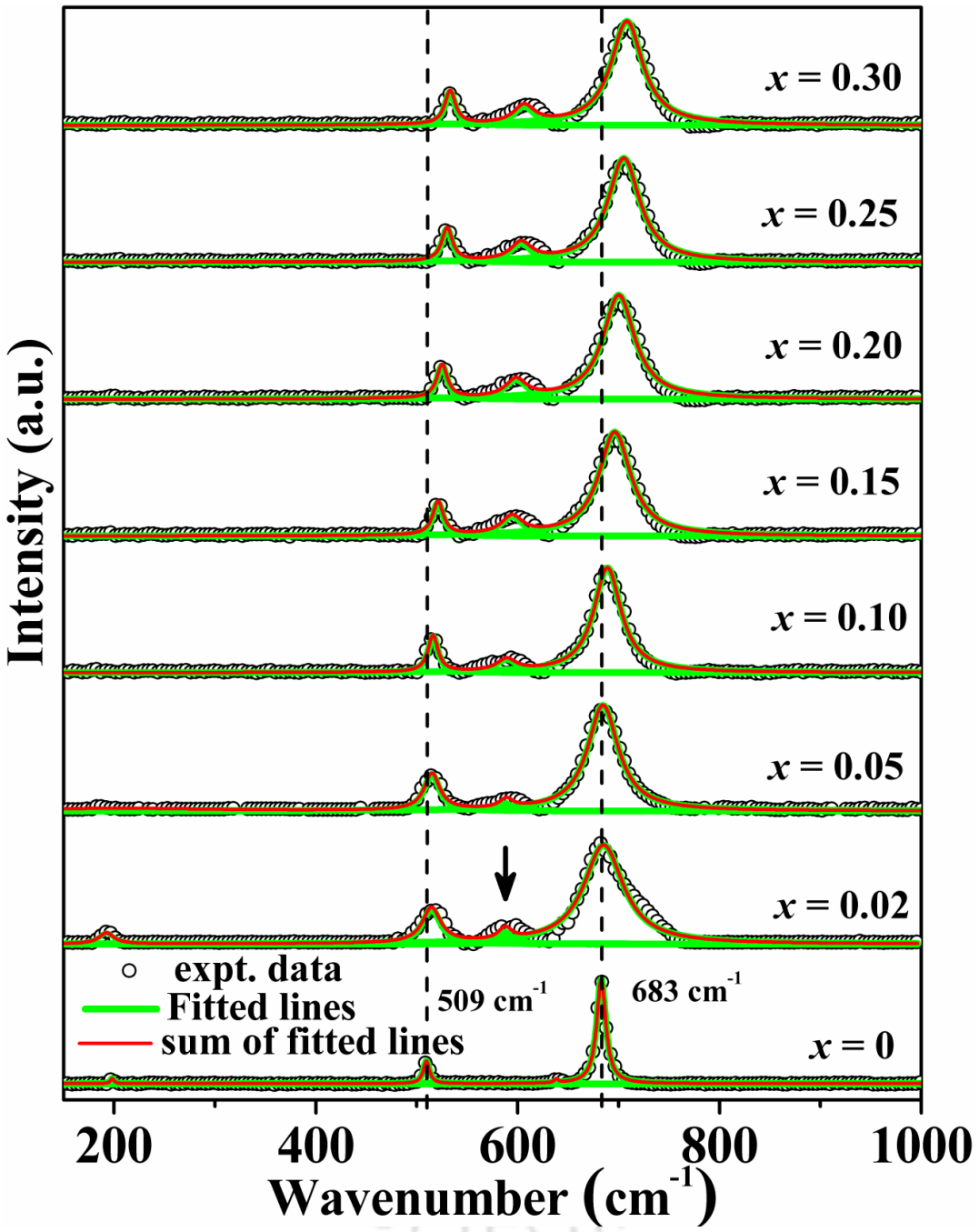


**Figure 5.22:** Raman spectra of $Mn(Cr_{1-x}Al_x)_2O_4$ samples at room temperature along with the fitted data.

The FESEM micrographs of $x$ = 0.10 and 0.30 samples are shown in Fig. 5.23 (a) and (b), respectively. Reduction in the grain size is observed with Al doping. The grain sizes are found to be distributed in a wide range as illustrated in Fig. 5.23 (c) and (d) for $x$ = 0.10 and

0.30 samples, respectively. The average grain size of each sample is obtained by fitting the size distribution histogram to Eq. (5.1). The average grain size of $x = 0.10$ sample is found to be 0.37 µm with a standard deviation of 0.15 µm. With increasing Al concentration the grain size decreases and for $x = 0.30$ sample it is found to be 0.21 µm with a standard deviation of 0.09 µm. The EDS spectra for $x = 0.10$ and 0.30 samples are shown in Fig. 5.24. The cation ratios Mn: Cr: Al obtained from EDS analysis for $x = 0.10$ and 0.30 samples are found to be 1 : 1.78 : 0.22 and 1 : 1.37 : 0.63 which are comparable to the nominal starting compositions.

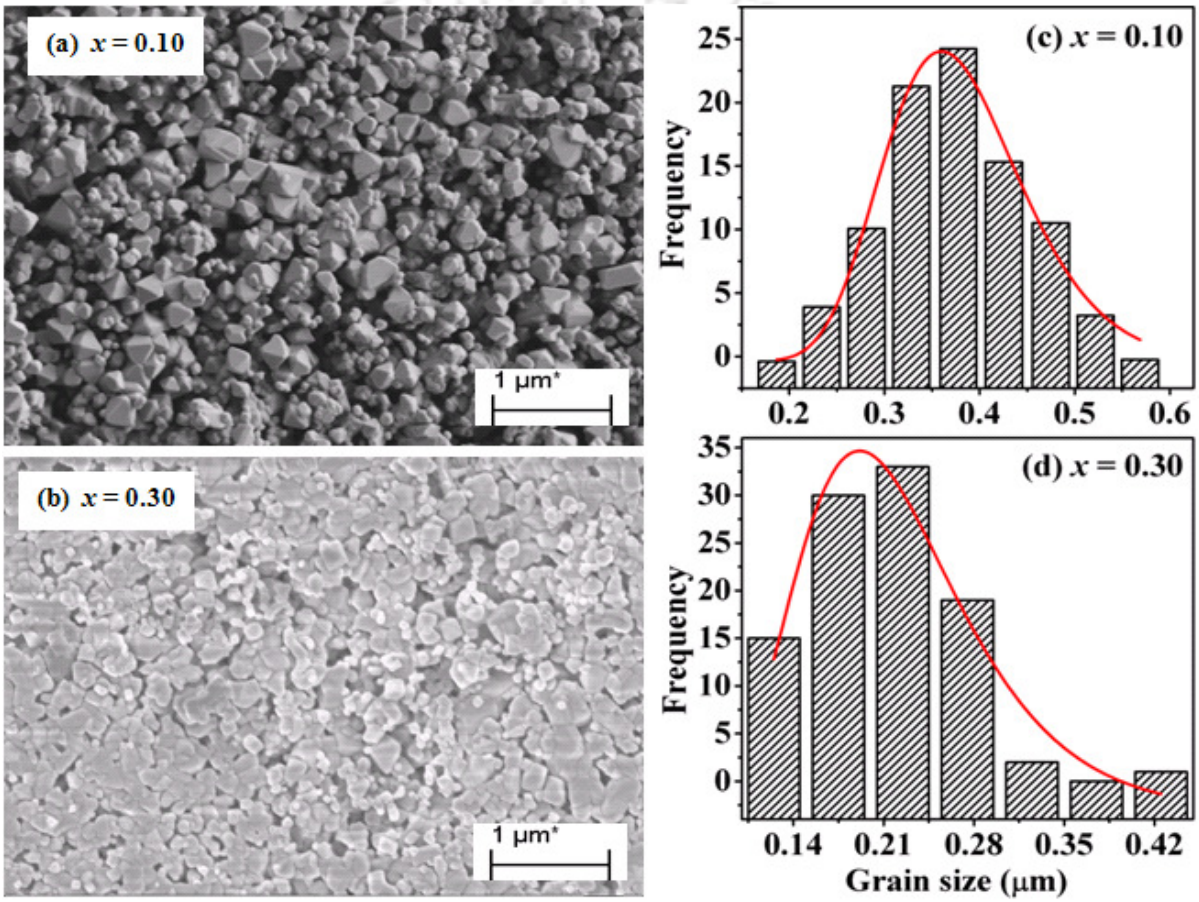


**Figure 5.23:** (a) & (b) FESEM images and (c) & (d) grain size distribution of $x = 0.10$ and 0.30 samples.

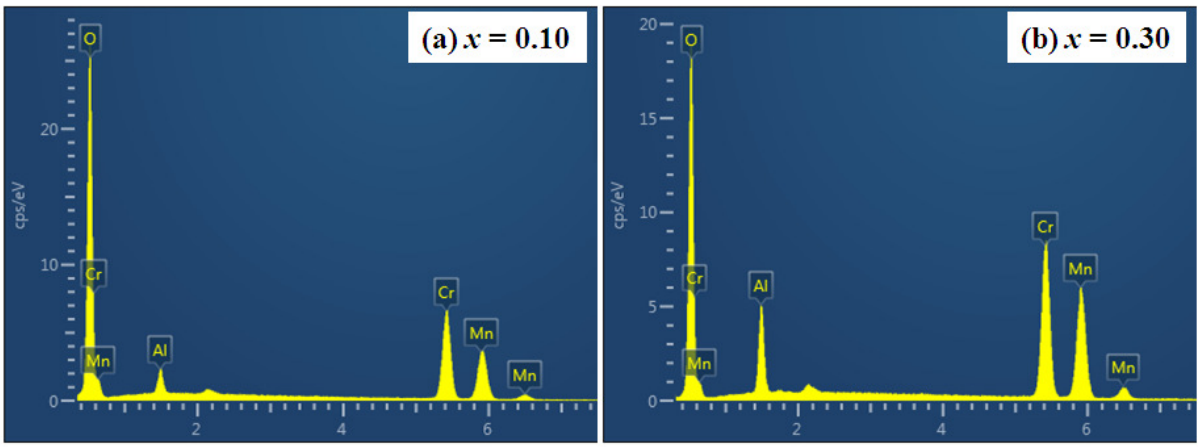


**Figure 5.24:** EDS spectrum of $x$ = 0.10 and 0.30 samples.

## 5.3.2 Magnetic Properties of $Mn(Cr_{1-x}Al_x)_2O_4$

Magnetization as a function of temperature is measured under both ZFC and FC conditions for an applied magnetic field of 100 Oe. Fig. 5.25 shows the magnetization versus temperature plots of $x$ = 0 to 0.30 samples and they all exhibit FIM transition. For $x$ = 0, the FIM $T_C$ is found to be 46 K and it is comparable to the earlier reports [38, 154]. The FIM $T_C$ decreases systematically with increase in Al concentration and reaches 33 K for $x$ = 0.30 sample. This decrease in $T_C$ highlights the weakening of the superexchange interaction between A and B site cations due to the substitution of nonmagnetic $Al^{3+}$ ($d^0$) ions in place of $Cr^{3+}$ ($d^3$). We have not observed any spiral magnetic ordering in the present series of samples due to the limitation of low temperature limit (25 K) of the experimental set up. Such spiral ordering is expected to be quite weak due to Al substitution [191].

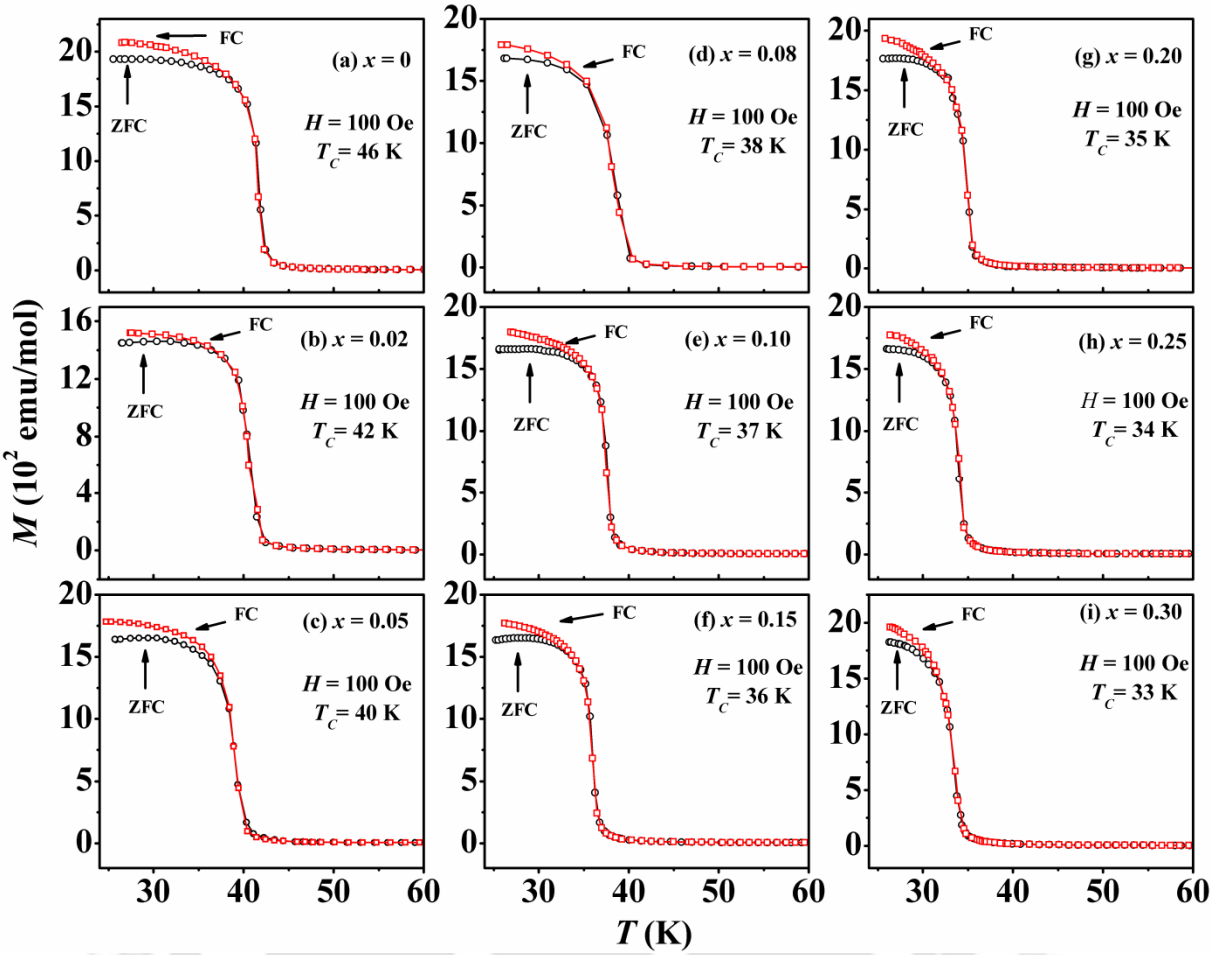


**Figure 5.25:** Temperature dependent magnetization of $Mn(Cr_{1-x}Al_x)_2O_4$ ($x$ = 0 – 0.30) samples under zero ZFC and FC conditions.

In order to further study the magnetic properties, we have recorded the magnetic hysteresis loops of $Mn(Cr_{1-x}Al_x)_2O_4$ samples at different temperatures. Fig. 5.26 shows the *M–H* loops of all the samples recorded at 25 K. The magnitude of magnetization decreases with increase in Al concentration, however in the composition range $x$ = 0.05 to $x$ = 0.10, it is found to increase.

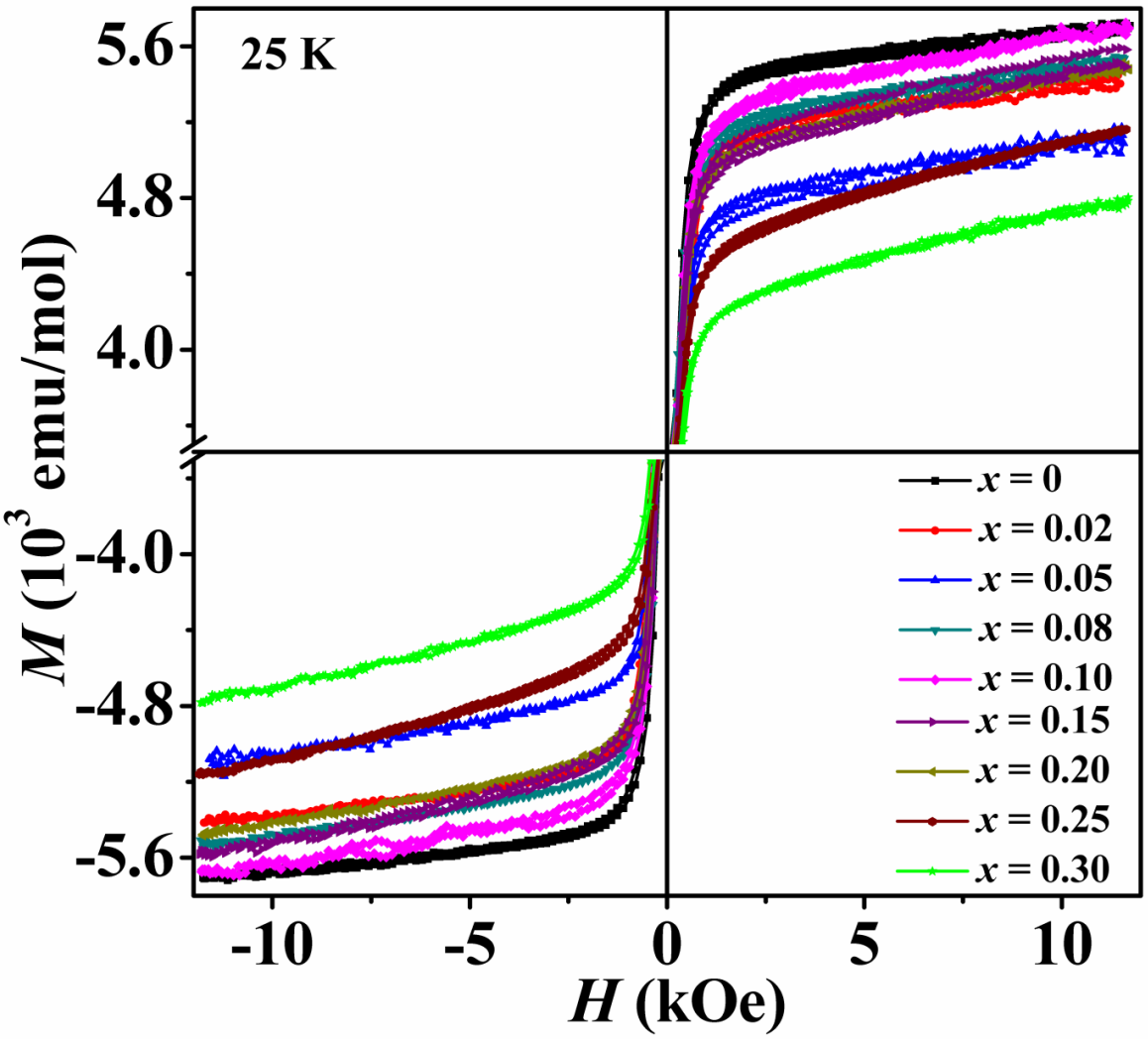


**Figure 5.26:** *M-H* loops of $Mn(Cr_{1-x}Al_x)_2O_4$ compounds at 25 K (for clearly distinguishing different plots, *M* values are restricted close to their saturation).

The experimental $M_s$ values at 25 K were determined by fitting the initial magnetization curves to the LAS model [Eq. (5.3)]. Fig. 5.27 shows the initial experimental (open circles) data along with the fitted data (solid line) for $x$ = 0, 0.10, 0.20 and 0.30 sample. The experimental $M_s$ values obtained at 25 K from the above fit were converted into Bohr magneton per formula unit and are plotted as a function of the Fe concentration in Fig. 5.28(a). $M_s$ decreases with increase in $x$ values and however in the composition range $x$ = 0.05 to $x$ = 0.10, it is found to increase. According to the magnetic structure given by Tomiyasu *et al.* [118], the total magnetization per formula unit of $MnCr_2O_4$ can be expressed by Eq. (5.4). Therefore, the decrease in the $M_s$ values up to $x$ = 0.05 is due to the occupation

of the $Al^{3+}$ ions in the A site. For $x > 0.05$, $Al^{3+}$ ions start occupying the B site also which leads to an increase in the $M_s$ value. The monotonous decrease in $M_s$ value with increase in the Al concentration beyond $x = 0.10$ is due to the dilution of both A and B site moments due to the larger concentration of non-magnetic $Al^{3+}$ ions. In order to check the consistency of our assumption, we have estimated the theoretical $M_s$ value of $Mn(Cr_{1-x}Al_x)_2O_4$ as a function of Al concentration considering the magnetic structure of $MnCr_2O_4$ [Eq. (5.4)]. The theoretical $M_s$ values as a function of Fe concentration is shown in Fig. 5.28(a) (solid line) along with the experimental data. The trend of experimental and the theoretical $M_s$ values are found to be comparable. The relatively large difference between experimental and theoretical data for $x = 0$ could be due to the considerable difference between the cone angles predicted in the theoretical magnetic structure at 5 K which was used for calculation and that of the presently prepared sample at 25 K.

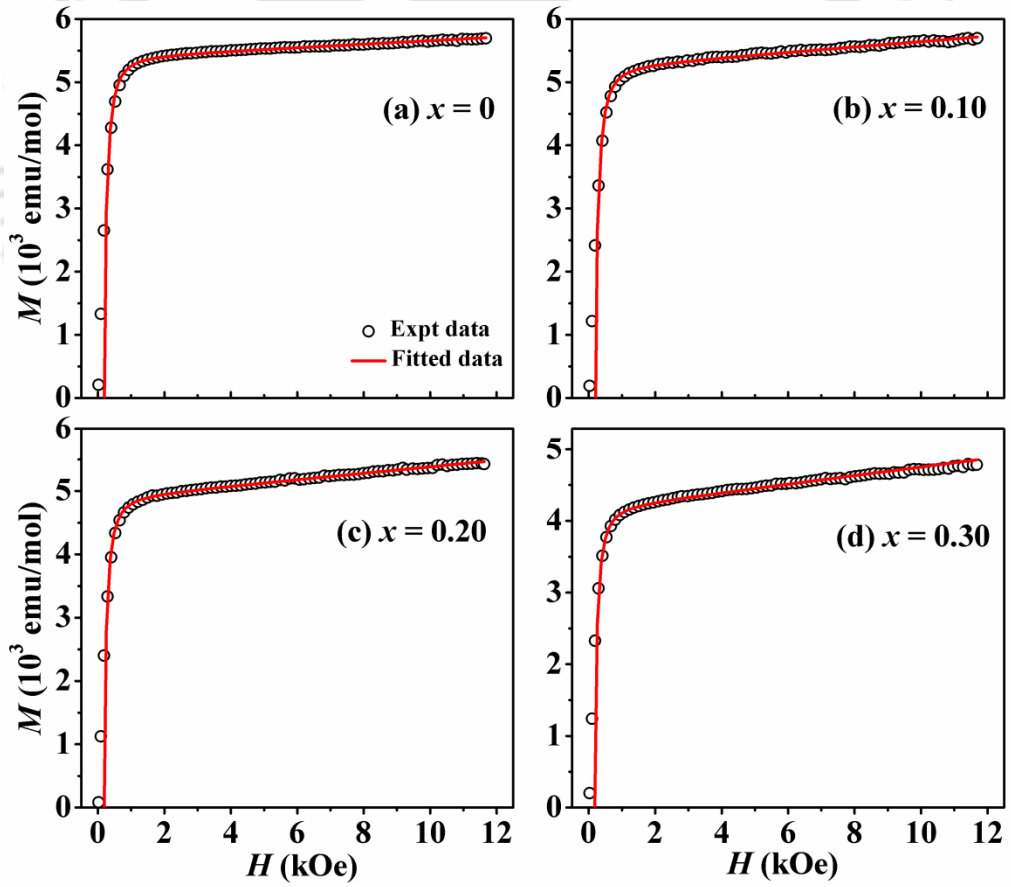


**Figure 5.27:** Initial magnetization curves for (a) $x = 0$, (b) $x = 0.10$, (c) $x = 0.20$ and (d) $x = 0.30$ samples along with the fitted data to the law of approach to saturation.

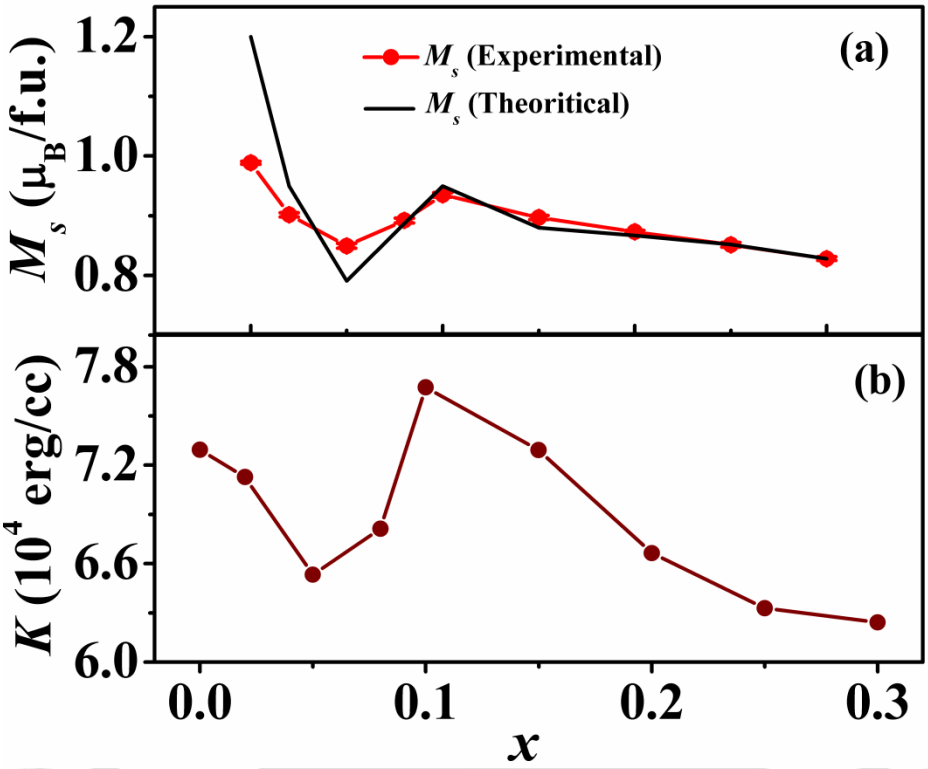


**Figure 5.28:** (a) variation of experimental (at 25 K) and theoretical saturation magnetization ($M_s$) and (b) variation of anisotropy constant at 25 K as a function of Fe concentration.

The effective magnetic anisotropy constant can be determined from the value of constant *b* by using Eq. (5.5). Fig. 5.28(b) shows the variation of anisotropy constant as a function of Al concentration at 25 K. The anisotropy constant *K* follows similar trend as that of the saturation magnetization. As discussed earlier the presence of some orbital moment of $Mn^{2+}$ ions or the crystal field on $Cr^{3+}$ ions may give rise to magnetocrystalline anisotropy in $MnCr_2O_4$. Due to substitution of non magnetic $Al^{3+}$ ($d^0$) ions and the corresponding reduction in the $M_s$ values may contribute to the reduction of anisotropy constant in the doped samples. However slight increase in anisotropy for $x$= 0.08 and 0.10 samples may be due to the beginning of the occupation of the $Al^{3+}$ ions in the B site which makes the A site moment larger compared to the B site resulting in net increase in $M_s$ value.

The susceptibility ($\chi$) data in the PM region of $Mn(Cr_{1-x}Al_x)_2O_4$ were fitted to the Curie-Weiss (CW) law $\chi = C/(T - \Theta_C)$, where $C$ and $\Theta_C$ are the curie constant and curie temperature, respectively. Fig. 5.29 (a) and (b) shows the CW fit for $x$ = 0 and 0.30 samples.

The effective PM moment ($\mu_{eff}$) can be determined from the Curie constant $C = N\mu_{eff}^2/3k_B$, obtained from the CW fit. The theoretical $\mu_{eff}$ values were calculated considering the above cation distribution by using the expression $\mu_{eff} = \sqrt{\mu_{Mn}^2 + 2(1-x)\mu_{Cr}^2}$, where $\mu_{Mn}$ and $\mu_{Cr}$ are the theoretical moments of $Mn^{2+}$ and $Cr^{3+}$ in high spin state calculated by considering spin only contribution. The $\mu_{eff}$ value for $MnCr_2O_4$ is found to be 8.06 $\mu_B$/f.u. which is comparable to the theoretical value of 8.062 $\mu_B$/f.u. For the Al substituted samples $\mu_{eff}$ values decrease systematically as expected and are almost comparable to the theoretical values. The experimental $\mu_{eff}$ values (solid spheres) and the theoretical $\mu_{eff}$ values (solid line) as a function of doping concentration are shown in Fig. 5.29(c). The negative value of Currie temperature $\Theta_C$ obtained for all the samples and the nature of $1/\chi$ versus $T$ plots confirm that these materials undergo FIM transition.

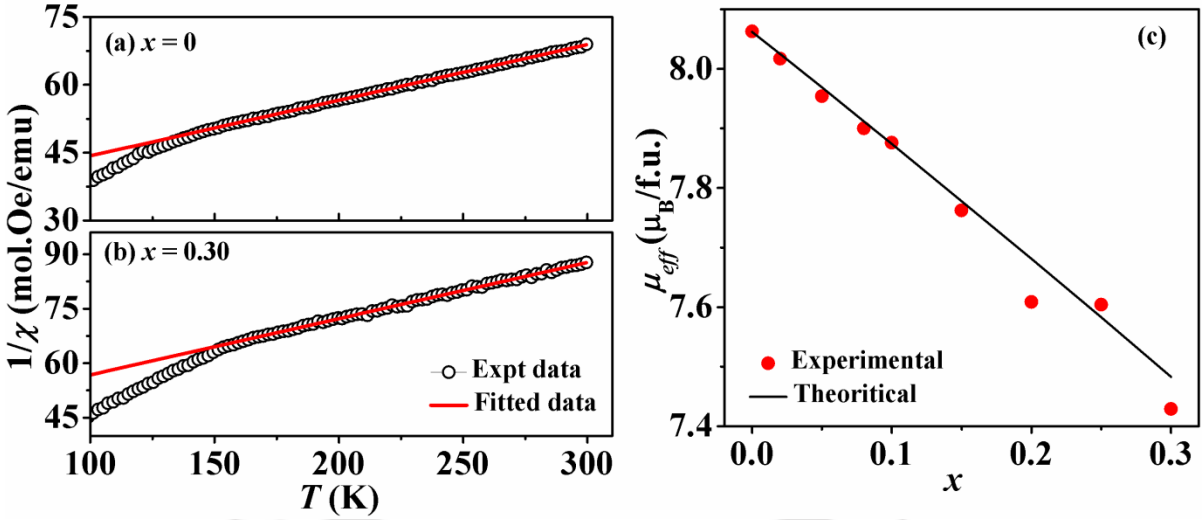


**Figure 5.29:** Curie-Weiss law fit along with experimental data in the PM region of (a) $x = 0$ and (b) $x = 0.30$ samples. (c) Experimental (solid sphere) and theoretical effective magnetic moment '$\mu_{eff}$' (solid line) as a function of Al concentration '$x$'.

# 5.4 Conclusions

The effect of both magnetic (Fe) and non magnetic (Al) ions substitution in Cr site of $MnCr_2O_4$ has been studied in this chapter.

We have successfully prepared the single phase samples of Fe substituted $MnCr_2O_4$ [$Mn(Cr_{1-x}Fe_x)_2O_4$ with $x$ = 0 – 0.50] and investigated the structural as well as detailed magnetic properties of the samples. All the samples are found to crystallize in cubic structure with $Fd\bar{3}m$ space group and the lattice constant is found to increase with increase in Fe concentration up to $x$ = 0.30 sample and beyond that no appreciable variation is seen. Such variation of lattice parameter and the Raman peak broadening as well as shifting indicates the formation of inverse type of structure for $x$ > 0.30 samples. The FIM transition temperature is found to increase from 46 K for $x$ = 0 to 402 K for $x$ = 0.50 due to the strengthening of the superexchange interaction between A and B site ions. Saturation magnetization values were determined by using the LAS model and they are found to decrease with increase in Fe concentration and approach the magnetic compensation at $x$ = 0.40. This composition driven compensation behavior is explained by considering the substitution of $Fe^{3+}$ ions in one of the $Cr^{3+}$ sites. The higher value of coercivity at the compensation point is observed due to poor response of magnetic energy with applied field as a result of very small magnetization of each domain. In addition to composition induced magnetic compensation, we have also observed temperature induced magnetic compensation for $x$ = 0.40 with a compensation temperature of 267 K. This is explained by considering different temperature dependence of the two sublattice moments.

$Mn(Cr_{1-x}Al_x)_2O_4$ ($x$ = 0 – 0.50) samples are also prepared by using sol-gel route and all the samples are found to crystallize in cubic structure with $Fd\bar{3}m$ space group. Lattice constant of $MnCr_2O_4$ is found to be $a$ = 8.4396 Å and it is found to decrease linearly with increase in Al concentration. Magnetic measurements as a function of temperature show FIM nature of the samples and the FIM transition temperature is found to decrease from 46 K for $x$ = 0 to 33 K for $x$ = 0.30 sample. Saturation magnetization values were determined by using the LAS model and they are found to decrease with increase in Al concentration, however in the composition range $x$ = 0.05 to $x$ = 0.10 increasing trend is observed. Such behavior of saturation magnetization with Al concentration is explained by considering different site preferences of $Al^{3+}$ ions at different concentrations. Considering such cation distribution we have determined the theoretical effective magnetic moment of the samples and are found to be comparable to that of the experimental values determined from Curie-Weiss fit of the PM

susceptibility. The Raman spectroscopic study also supports the cation distribution estimated from the magnetic properties.

Composition as well as temperature induced magnetic compensation was observed for Fe substituted $MnCr_2O_4$ while for Al doped series no such behavior was realized. Being a magnetic ion, Fe causes an increase in the FIM transition temperature; making it suitable for practical applications. The compensation temperature (267 K) obtained is also quite close to the room temperature. Non magnetic Al in Cr site of $MnCr_2O_4$ leads to the decrease of FIM transition temperature. So exploring of magnetic properties far below $T_C$ was not possible since the low temperature limit of our experimental set up is 25 K only. Therefore presence of any temperature induced compensation effect below this temperature was not detected.

# Chapter 6

# Conclusions

This chapter concludes the present thesis by summarizing the overall results obtained in Chapters 3, 4 and 5 from magnetic/nonmagnetic (Fe/Al) ion substituted two spinel chromites namely, $NiCr_2O_4$ and $MnCr_2O_4$. The detailed study of structural, magnetic, exchange bias and magnetization reversal properties in $Ni(Cr_{1-x}M_x)_2O_4$ and $Mn(Cr_{1-x}M_x)_2O_4$ series with M = Fe and Al brings about the following conclusions.

$Ni(Cr_{1-x}Fe_x)_2O_4$ ($x$ = 0 – 0.60) samples have been successfully prepared in single phase form by using the sol-gel route and the parent compound $NiCr_2O_4$ is found to crystallize in tetragonal structure with $I4_1/amd$ space group. Fe substitution is found to suppress the Jahn-Teller distortion in $NiCr_2O_4$ and leads to a structural transition from tetragonal to cubic with $Fd\bar{3}m$ space group, even for 2 at % of Fe substitution. This is mainly due to the occupation of some of the $Fe^{3+}$ ions in the A site, rather than occupying only the B site. It is because $Fe^{3+}$ ion in the A site is not Jahn-Teller active. Lattice parameter of samples for $x \geq 0.02$ decreases gradually with increasing of Fe concentration '$x$' which supports the above argument about the occupation of Fe ions in the A site also.

Temperature variation of magnetization measurements reveal ferrimagnetic nature of all the samples with an increase in transition temperature ($T_C$) from 73 K of $x$ = 0 to 574 K of $x$ = 0.50 sample. Thus Fe substitution enhances the $T_C$ even above room temperature due to the strengthening of the super-exchange interaction of the system. Field dependent magnetization measurements at low temperature validates the presence of competing antiferromagnetic interaction along with long range ferrimagnetic ordering as reported earlier [54].

The parent $NiCr_2O_4$ itself shows negative exchange bias (EB) behavior with an exponentially decaying behavior of the EB field ($H_{EB}$) from its maximum magnitude of 312 Oe. EB in this sample arises due to the anisotropic exchange interaction between the ferrimagnetic and the antiferromagnetic components of magnetic moment present in the sample. The temperature dependence of effective coercive field $H_C^{eff}$ however does not follow the similar behavior with the $H_{EB}$ and it could be explained based on the empirical relation $H_C^{eff} = H_C^{eff}(0)\left[1-\left(T/T_C'\right)^2\right]$. $NiCr_2O_4$ exhibit small training in the EB field. At the end of infinite number of loops it exhibits a considerable value of $H_{EB}$ of 123 Oe. The Fe substituted samples with $x$ = 0.02, 0.04 and 0.10 also exhibit negative EB field as observed for the parent compound but with a higher magnitude and in a wider temperature range. This is due to the enhanced magnetic interaction in Fe doped samples and the corresponding increase in transition temperature, $T_C$ and exchange anisotropy.

As per the analysis of temperature ($M$–$T$) and field ($M$–$H$) variation of magnetization and the data of these samples we found that initially up to $x$ = 0.06, $Fe^{3+}$ ions occupy the B2-B4 (Cr2) site while for $x$ > 0.06, relatively larger concentration of $Fe^{3+}$ in the A site compared to B site could be expected. Such substitution kicks off the magnetic compensation behavior ($M$ = 0) in $x$ = 0.06 with a magnetization reversal (MR) across the compensation temperature, $T_{comp}$ = 49 K and no MR for 0.06 < $x$ ≤ 0.20. Further increase in $x$ reduces the magnetic frustration in the B site leading to an increase in the ferrimagnetic moment of B2-B4 site. Thus due to the net B site moment being comparable to A site in $x$ = 0.30, 0.40 and 0.50 samples, MR is again observed for these samples. Their $T_{comp}$ value is found to be near room temperature, *i.e.* 358, 366 and 396 K, respectively. This temperature induced MR is explained by considering the different temperature dependence of the magnetic moments of the two sublattices. Study of exchange bias (EB) behavior in these samples having MR reveals that the EB field also undergoes a sign reversal across the $T_{comp}$. The magnitude of EB field in the present samples is larger and also observed for wider temperature range compared to some other reports showing similar behavior [26, 91]. Most interestingly such tunable positive and negative EB fields for $x$ = 0.30, 0.40 and 0.50 samples have been observed close to the room temperature and as per our knowledge it is the first time that coexistence of MR and EB is observed at the vicinity of room temperature. Such tunable EB

behavior is explained in terms of change in domination of one sublattice moment over the other as the temperature is varied.

For the first time we have demonstrated the bipolar switching of magnetization at room temperature for $x$ = 0.30 and 0.40 samples by just varying the magnitude of magnetic field without changing its direction. Therefore the Fe substituted $NiCr_2O_4$ series have been proved to be a very rich material with exchange bias, magnetization reversal and bipolar switching of magnetization behavior near room temperature. Therefore the Fe substituted series with these interesting behaviors may become a suitable candidate for applications in magnetic data storage (memory) and switches.

Similar to Fe substituted series, $Ni(Cr_{1-x}Al_x)_2O_4$ ($x$ = 0 – 0.50) samples also exhibit a structural transition from tetragonal ($I4_1/amd$ space group) phase for of $x$ = 0 to cubic ($Fd\bar{3}m$ space group) phase in of Al doped samples. The decrease in lattice parameter with increase in Al concentration confirms the occupation of Al in the Cr site. All the samples show ferrimagnetic behavior and the transition temperature, $T_C$ is found to decrease with increase in Al concentration due to the weakening of the superexchange interaction. Bifurcation between zero field cooled and Field cooled temperature variation of magnetization ($M$–$T$) curves and the behavior of low temperature hysteresis ($M$−$H$) loop show the presence of competing antiferromagnetic interaction in the samples.

Here initially the Al ions occupy the B1-B3 site and for $x$ > 0.10 it occupy both B1-B3 and B2-B4 site. This results in the interesting property of magnetization reversal (MR) for $x$ = 0.10 sample with a compensation temperature of 40 K. No MR is observed above $x$ = 0.10 due to the dilution of B site moment and thus completely dominant A sublattice moment. The compensation temperature, $T_{comp}$ here is much lower compared to Fe doped samples due to corresponding low transition temperature, $T_C$ (65 K) of the sample. Exchange bias (EB) field can also be tuned from positive to negative across $T_{comp}$ and similar to Fe doped samples this is explained in terms of the change in domination of magnetic moment of one magnetic sublattice over the other with variation in temperature. While $x$ = 0.15 sample shows only negative EB with a maximum EB field of 306 Oe at 25 K which is smaller compared to the Fe doped samples. Relatively weak anisotropic exchange interaction

between the ferrimagnetic and the antiferromagnetic components of magnetic moment due to non magnetic Al inclusion may cause the reduction of EB field.

$Mn(Cr_{1-x}Fe_x)_2O_4$ with $x = 0 – 0.50$ samples are also prepared by using sol-gel route. Unlike the above two $NiCr_2O_4$ series, $Mn(Cr_{1-x}Fe_x)_2O_4$ samples do not show any structural transition and all the samples exhibit cubic structure with $Fd\bar{3}m$ space group. The lattice constant is found to increase with increase in Fe concentration up to $x = 0.30$ sample and beyond that no appreciable variation is seen. Such variation of lattice parameter and the Raman peak broadening as well as shifting indicates the formation of inverse type of structure for $x > 0.30$ samples. All the samples exhibit ferrimagnetic transition and the transition temperature, $T_C$ is found to increase from 46 K for $x = 0$ to 402 K for $x = 0.50$ due to the Fe substitution induced strengthening of the superexchange interaction between A and B site ions, as observed for the Fe substituted $NiCr_2O_4$ series. Saturation magnetization of the samples is found to decrease with increase in Fe concentration and approach the magnetic compensation at $x = 0.40$. This composition driven compensation behavior is explained by considering the substitution of $Fe^{3+}$ ions in the Cr2 site. The higher value of coercivity at the compensation point is observed due to poor response of magnetic energy as a result of very small magnetization of each domain. In addition to composition induced magnetic compensation, we have also observed temperature induced magnetic compensation for $x = 0.40$ with a compensation temperature of 267 K. This is explained by considering different temperature dependence of the two sublattice moments. Contrary to the Fe substituted samples, here compensation behavior is observed without any magnetization reversal (MR). Low anisotropy of the samples prevents the MR to occur here.

All the $Mn(Cr_{1-x}Al_x)_2O_4$ ($x = 0 – 0.30$) samples are also found to crystallize in cubic structure with $Fd\bar{3}m$ space group. Lattice constant is found to decrease linearly with increase in Al concentration. All the samples exhibit ferrimagnetic nature with a decrease in the transition temperature, $T_C$ from 46 K for $x = 0$ to 33 K for $x = 0.30$ sample. Variation of saturation magnetization ($M_s$) with Al concentration yields that up to $x = 0.05$ $Al^{3+}$ ions occupy the A site and for $x > 0.05$ $Al^{3+}$ ions start occupying the B site also. Beyond $x = 0.10$, due to the dilution of both A and B site moments with larger concentration of non-magnetic $Al^{3+}$ ions, monotonous decrease in $M_s$ value with increase in the Al concentration is

observed. Considering such cation distribution we have determined the theoretical effective magnetic moment of the samples and are found to be comparable to that of the experimental values determined from Curie-Weiss fit of the paramagnetic susceptibility. The Raman spectroscopic study also supports the cation distribution estimated from the magnetic properties. Temperature induced magnetic compensation was not realized in Al substituted series. Decrease in $T_C$ due to non magnetic Al in the Cr site of $MnCr_2O_4$ makes it difficult to explore the magnetic properties far below $T_C$ because of the low temperature limit (25 K) of our experimental set up. Therefore presence of any temperature induced compensation effect below this temperature was not detected. However, exchange bias (EB) behavior is absent in both Fe and Al substituted $MnCr_2O_4$ samples. The lack of exchange anisotropy between the FIM and the AFM components may be the reason of not exhibiting the EB behavior. Also, no tunable behavior of EB is observed for Fe substituted sample with magnetic compensation ($x$ = 0.40) due to the low effective anisotropy of the samples.

Thus in the present thesis work we have studied the magnetic properties of Fe and Al substituted $NiCr_2O_4$ and $MnCr_2O_4$ series and found that Cr site substitution with magnetic Fe ions in both the chromites show rich magnetic properties compared to that of the non magnetic Al substitution. Fe substitution gives rise to interesting magnetic compensation as well as tunable exchange bias (EB) behavior with compensation temperature in the vicinity of room temperature; making them suitable for practical applications. Fe substituted $NiCr_2O_4$ shows enhanced EB field compared to the parent compound.

# Future Scope of Studies

Following are the future scope of research in these types of materials which can be taken up for further studies.

- Neutron powder diffraction studies at different temperature under both zero field cooled and field cooled condition will help to get deep insight into the magnetic structure of the Fe and Al substituted $NiCr_2O_4$ and $MnCr_2O_4$ samples. Especially it will help in identifying the exact magnetic structure above and below $T_{comp}$ of the samples showing magnetization reversal.

- Study of the magnetic properties by extending the maximum applied field upto ~ 5 T for the samples based on $NiCr_2O_4$ will help to further understand their magnetic properties and also may enhance the accuracy of the obtained exchange bias field values. Moreover, magnetic measurement up to 4 K is needful for exploring various low temperature transitions and to understand their underlying mechanisms of both the series.
- It is necessary to carry out the magnetoelectric/dielectric measurement to look for possible multiferroic behavior which is yet to be understood in both the series.
- Study of magnetocaloric effect in those samples with compensation temperature, $T_{comp}$ near room temperature, in order to search for new materials for magnetic refrigeration.
- Preparation of the samples in thin film form, especially the magnetically compensated samples with $T_{comp}$ near room temperature, to study the effect of lattice strain in magnetization reversal and exchange bias phenomenon and to make them practically applicable as well.
- Preparation of Fe doped $NiCr_2O_4$ and $MnCr_2O_4$ samples choosing proper concentration of Fe so that $T_{comp}$ is observed exactly at the room temperature and tunable exchange bias field is observed across it.
- Similar studies of exchange bias and magnetization reversal can be extended in the Mn substitution for Cr in $NiCr_2O_4$ and $MnCr_2O_4$. Because $Mn^{3+}$ is also a transition metal ion with higher magnetic moment of 4 $\mu_B$ compared to $Cr^{3+}$ (3 $\mu_B$).

# References


[1] B. Dieny, V.S. Speriosu, S.S.P. Parkin, B.A. Gurney, D.R. Wilhoit, D. Mauri, Phys. Rev. B 43 (1991) 1297.

[2] J.C.S. Kools, IEEE Trans. Magn. 32 (1996) 3165.

[3] J. Nogués, V. Skumryev, J. Sort, S. Stoyanov, D. Givord, Phys. Rev. Lett. 97 (2006) 157203.

[4] S.M. Wu, S.A. Cybart, D. Yi, J.M. Parker, R. Ramesh, R.C. Dynes, Phys. Rev. Lett. 110 (2013) 067202.

[5] S.M. Wu, S.A. Cybart, P. Yu, M.D. Rossell, J.X. Zhang, R. Ramesh, R.C. Dynes, Nat. Mater. 9 (2010) 756.

[6] W.H. Bragg, Philos. Mag. 30 (1915) 305.

[7] S. Nishikawa, Proc. Tokyo Math.-Phys. SOC. 8 (1915) 199.

[8] A.P. Ramirez, R.J. Cava, J. Krajewski, Nature 386 (1997) 156.

[9] R. Basu, C. Felser, A. Maignan, R. Seshadri, J. Mater. Chem. 10 (2000) 1921.

[10] E.G. Moshopoulou, J. Am. Ceram. Soc. 82 (1999) 3317.

[11] K. Ohgushi, Y. Okimoto, T. Ogasawara, S. Miyasaka, Y. Tokura, J. Phys. Soc. Jpn. 77 (2008) 034713.

[12] E.J.W. Verwey, P.W. Haayman, Physica 8 (1941) 979.

[13] Y. Yamasaki, S. Miyasaka, Y. Kaneko, J.P. He, T. Arima, Y. Tokura, Phys. Rev. Lett. 96 (2006) 207204.

[14] N. Sakamoto, J. Phys. Soc. Jpn. 17 (1962) 99.

[15] K. Maaz, W. Khalid, A. Mumtaz, S.K. Hasanain, J. Liu, J.L. Duan, Physica E: Low Dimens. Syst. Nanostruct. 41 (2009) 593.

[16] N. Menyuk, K. Dwight, D.G. Wickham, Phys. Rev. Lett. 4 (1960) 119.

[17] O. Crottaz, F. Kubel, H. Schmid, J. Mater. Chem. 7 (1997) 143.

[18] S. Klemme, J.C. van Miltenburg, Phys. Chem. Minerals 29 (2002) 663.

[19] M.R. Suchomel, D.P. Shoemaker, L. Ribaud, M.C. Kemei, R. Seshadri, Phys. Rev. B 86 (2012) 054406.

[20] K. Singh, A. Maignan, C. Simon, C. Martin, Appl. Phys. Lett. 99 (2011) 172903.

[21] V. Kocsis, S. Bordacs, D. Varjas, K. Penc, A. Abouelsayed, C.A. Kuntscher, K. Ohgushi, Y. Tokura, I. Kezsmarki, Phys. Rev. B 87 (2013) 064416.

[22] A. Maignan, C. Martin, K. Singh, C. Simon, O.I. Lebedev, S. Turner, J. Solid State Chem. 195 (2012) 41.

[23] N. Mufti, A.A. Nugroho, G.R. Blake, T.T.M. Palstra, J. Phys.: Condens. Matter 22 (2010) 075902.

[24] K. Dey, S. Majumdar, S. Giri, Phys. Rev. B 90 (2014) 184424.

[25] T. Suzuki, K. Adachi, T. Katsufuji, J. Magn. Magn. Mater. 310 (2007) 780.

[26] R. Padam, S. Pandya, S. Ravi, A.K. Nigam, S. Ramakrishnan, A.K. Grover, D. Pal, Appl. Phys. Lett. 102 (2013) 112412.

[27] H.G. Zhang, Z. Wang, E.K. Liu, W.H. Wang, M. Yue, G.H. Wu, J. Appl. Phys. 117 (2015) 17B735.

[28] H.G. Zhang, W.H. Wang, E.K. Liu, X.D. Tang, G.J. Li, H.W. Zhang, G.H. Wu, Phys. Status Solidi (b) 250 (2013) 1287.

[29] L.G. Wang, C.M. Zhu, Z.M. Tian, H. Luo, D.L.G.C. Bao, S.L. Yuan, Appl. Phys. Lett. 107 (2015) 152406.

[30] L.Q. Yan, W. Ren, J. Shen, Z.H. Sun, F.W. Wang, J. Appl. Phys. 105 (2009) 07A719.

[31] K.E. Sickafus, J.M. Wills, N.W. Grimes, J. Am. Ceram. Soc. 82 (1999) 3279.

[32] R.W. Grimes, A.B. Anderson, A.H. Heuer, J. Am. Ceram. Soc. 111 (1989) 1.

[33] C.M. Brent, E.D. Jennifer, S. Ram, E.M. Stoudenmire, P.R. Arthur, J. Phys.: Condens. Matter 21 (2009) 216007.

[34] G.A. Sawatzky, F. Van Der Woude, A.H. Morrish, Phys. Rev. 187 (1969) 747.

[35] J.D. Dunitz, L.E. Orgel, J. Phys. Chem. Solids 3 (1957) 20.

[36] K. Siratori, J. Phys. Soc. Jpn. 23 (1967) 948.

[37] M. Tanaka, T. Tokoro, Y. Aiyama, J. Phys. Soc. Jpn. 21 (1966) 262.

[38] Y.H. Zhou, Z.R. Yang, L. Li, Y.M. Xie, S. Lin, Y.P. Sun, Y.H. Zhang, J. Magn. Magn. Mater. 324 (2012) 3799.

[39] G.T. Lin, X. Luo, Q.L. Pei, F.C. Chen, C. Yang, J.Y. Song, L.H. Yin, W.H. Song, Y.P. Sun, RSC Adv. 6 (2016) 56839.

[40] R. Padam, D. Pal, S. Ravi, A.K. Grover, S. Ramakrishnan, J. Supercond. Nov. Magn. 26 (2013) 1607.

[41] G. Lawes, B. Melot, K. Page, C. Ederer, M.A. Hayward, T. Proffen, R. Seshadri, Phys. Rev. B 74 (2006) 024413.

[42] B.D. Hosterman, J.W. Farley, A.L. Johnson, J. Phys. Chem. Solids 74 (2013) 985.

[43] G. Shirane, D.E. Cox, S.J. Pickart, J. Appl. Phys. 35 (1964) 954.

[44] R.C. O'Handley, Modern Magnetic Materials: Principles and Applications, Wiley Press, New york (2000).

[45] B.D. Cullity, C.D. Graham, Introduction to Magnetic Materials, IEEE Press (2009).

[46] S. Blundell, Magnetism in Condensed Matter, Oxford University Press (2001).

[47] Y. Tokura, N. Nagaosa, Science 288 (2000) 462.

[48] B.J. Kennedy, Q. Zhou, J. Solid State Chem. 181 (2008) 2227.

[49] H.A. Kramers, Physica 1 (1934) 182.

[50] J.C. Slater, Quart. Progr. Rep. M. I. T. July 15,1; Oct. 15 1 (1953).

[51] J.B. Goodenough, A.L. Loeb, Phys. Rev. 98 (1955) 391.

[52] J.B. Goodenough, Phys. Rev. 100 (1955) 564.

[53] N.A. Spaldin, Magnetic Materilas: Fundamental and Applications, Cambridge University Press (2010).

[54] K. Tomiyasu, I. Kagomiya, J. Phys. Soc. Jpn. 73 (2004) 2539.

[55] C. Zener, Phys. Rev. 81 (1951) 440.

[56] C. Zener, Phys. Rev. 82 (1951) 403.

[57] P.W. Anderson, H. Hasegawa, Phys. Rev. 100 (1955) 675.

[58] I. Dzyaloshinsky, J. Phys. Chem. Solids 4 (1958) 241.

[59] T. Moriya, Phys. Rev. 120 (1960) 91.

[60] A.H. Morrish, The Physical principle of Magnetism, IEEE Press (2001).

[61] C. Kittel, Introduction to Solid State Physics, Wiley Press, Singapore (2004).

[62] A. Kumar, S.M. Yusuf, Phys. Rep. 556 (2015) 1.

[63] L.G. Antoshina, A.N. Goryaga, V.V. San'kov, Phys. Solid State 42 (2000) 1488.

[64] W.H. Meiklejohn, C.P. Bean, Phys. Rev. 102 (1956) 1413.

[65] L. Neel, Ann. Phys. 3 (1948) 137.

[66] K. Yoshii, J. Solid State Chem. 159 (2001) 204.

[67] H. Adachi, H. Ino, Nature 401 (1999) 148.

[68] J. Nogues, I.K. Schuller, J. Magn. Magn. Mater. 192 (1999) 203.

[69] H. Young Jun, K. Jun Sig, S. In-Bo, K. Chul Sung, IEEE Trans. Magn. 40 (2004) 2808.

[70] J.S. McCloy, B. Walsh, IEEE Trans. Magn. 49 (2013) 4253.

[71] J. Ostoréro, M. Guillot, J. Appl. Phys. 81 (1997) 4797.

[72] A. Rais, A.M. Gismelseed, I.A. Al-Omari, Phys. Status Solidi (b) 242 (2005) 2949.

[73] E.W. Gorter, J.A. Schulkes, Phys. Rev. 90 (1953) 487.

[74] M. Abe, M. Kawachi, S.i. Nomura, J. Phys. Soc. Jpn. 31 (1971) 940.

[75] Z. Yang, S. Tan, Y. Zhang, J. Phys.: Condens. Matter 15 (2003) 7411.

[76] A. Rais, A.M. Gismelseed, I.A. Al-Omari, Phys. Status Solidi (b) 242 (2005) 1497.

[77] S. Nayak, S. Thota, D.C. Joshi, M. Krautz, A. Waske, A. Behler, J. Eckert, T. Sarkar, M.S. Andersson, R. Mathieu, V. Narang, M.S. Seehra, Phys. Rev. B 92 (2015) 214434.

[78] R. Padam, P. Swati, S. Ravi, S. Ramakrishnan, A.K. Nigam, A.K. Grover, D. Pal, J. Phys.: Condens. Matter 29 (2017) 055803.

[79] H.C. Nguyen, J.B. Goodenough, Phys. Rev. B 52 (1995) 324.

[80] Y. Ren, T.T.M. Palstra, D.I. Khomskii, E. Pellegrin, A.A. Nugroho, A.A. Menovsky, G.A. Sawatzky, Nature 396 (1998) 441.

[81] Y. Kimishima, M. Uehara, T. Saitoh, Solid State Commun. 133 (2005) 559.

[82] J. Hemberger, S. Lobina, H.A. Krug von Nidda, N. Tristan, V.Y. Ivanov, A.A. Mukhin, A.M. Balbashov, A. Loidl, Phys. Rev. B 70 (2004) 024414.

[83] S. Zhang, L. Luan, S. Tan, Y. Zhang, Appl. Phys. Lett. 84 (2004) 3100.

[84] J.S. Jung, A. Iyama, H. Nakamura, M. Mizumaki, N. Kawamura, Y. Wakabayashi, T. Kimura, Phys. Rev. B 82 (2010) 212403.

[85] P.K. Manna, S.M. Yusuf, R. Shukla, A.K. Tyagi, Appl. Phys. Lett. 96 (2010) 242508.

[86] T. Bora, S. Ravi, J. Appl. Phys. 114 (2013) 183902.

[87] T. Bora, S. Ravi, J. Magn. Magn. Mater. 358 (2014) 208.

[88] T. Bora, S. Ravi, J. Appl. Phys. 116 (2014) 063901.

[89] T. Bora, S. Ravi, J. Magn. Magn. Mater. 386 (2015) 85.

[90] X.H. Chen, K.Q. Wang, P.H. Hor, Y.Y. Xue, C.W. Chu, Phys. Rev. B 72 (2005) 054436.

[91] P.D. Kulkarni, A. Thamizhavel, V.C. Rakhecha, A.K. Nigam, P.L. Paulose, S. Ramakrishnan, A.K. Grover, EPL 86 (2009) 47003.

[92] P. Kumar, R. Kumar, S. Pandey, K.G. Suresh, A.K. Nigam, Physica B: Condens. Matter 448 (2014) 6.

[93] L. He, Solid State Commun. 151 (2011) 985.

[94] J. Nogues, J. Sort, V. Langlais, V. Skumryev, S. Surinach, J.S. Munoz, M.D. Baro, Phys. Rep. 422 (2005) 65.

[95] S. Giri, M. Patra, S. Majumdar, J. Phys.: Condens. Matter 23 (2011) 073201.

[96] A.J. Freitas Cabral, J. Peña Serna, B. Rache Salles, M.A. Novak, A.L. Pinto, C.M. Rocha Remédios, J. Alloys Compd. 630 (2015) 74.

[97] F.L. Zan, Y.Q. Ma, Q. Ma, Y.F. Xu, Z.X. Dai, G.H. Zheng, J. Alloys Compd. 581 (2013) 263.

[98] W. Liguang, Z. Changming, T. Zhaoming, Y. Songliu, J. Mater. Res. 30 (2015) 3252.

[99] C. Zhu, Z. Tian, L.G. Wang, S. Yuan, J. Magn. Magn. Mater. 393 (2015) 116.

[100] H. Singh, T. Chakraborty, K. Srikanth, R. Chandra, C. Mitra, U. Kumar, Physica B 448 (2014) 77.

[101] E.C. Passamani, B.R. Segatto, C. Larica, R. Cohen, J.M. Greneche, J. Magn. Magn. Mater. 322 (2010) 3917.

[102] S.R. Guitarra, A. Caneiro, D. Niebieskikwiat, J. Magn. Magn. Mater. 392 (2015) 63.

[103] Y. Li-qin, M. Ferran, J. Zhong-wei, S. Jun, H. Lun-hua, W. Fang-wei, J. Phys.: Condens. Matter 20 (2008) 255203.

[104] R. Padam, S. Ravi, S. Ramakrishnan, A.K. Grover, D. Pal, J. Magn. Magn. Mater. 371 (2014) 144.

[105] Z.P. Li, J. Eisenmenger, C.W. Miller, I.K. Schuller, Phys. Rev. Lett. 96 (2006) 137201.

[106] J. Nogués, D. Lederman, T.J. Moran, I.K. Schuller, Phys. Rev. Lett. 76 (1996) 4624.

[107] S. Venkatesh, V. Ulhas, R. Veer Chand, S. Ramakrishnan, A.K. Grover, J. Phys.: Condens. Matter 22 (2010) 496002.

[108] P.D. Kulkarni, S.K. Dhar, A. Provino, P. Manfrinetti, A.K. Grover, Phys. Rev. B 82 (2010) 144411.

[109] D.J. Webb, A.F. Marshall, Z. Sun, T.H. Geballe, R.M. White, IEEE Trans. Magn. 24 (1988) 588.

[110] R.P. Singh, C.V. Tomy, A.K. Grover, Appl. Phys. Lett. 97 (2010) 182505.

[111] J. Mao, Y. Sui, X. Zhang, X. Wang, Y. Su, Z. Liu, Y. Wang, R. Zhu, Y. Wang, W. Liu, X. Liu, Solid State Commun. 151 (2011) 1982.

[112] F. Hong, Z. Cheng, J. Wang, X. Wang, S. Dou, Appl. Phys. Lett. 101 (2012) 102411.

[113] K. Yoshii, Appl. Phys. Lett. 99 (2011) 142501.

[114] A.A. Belik, Inorg. Chem. 52 (2013) 2015.

[115] S. Nayak, D.C. Joshi, M. Krautz, A. Waske, J. Eckert, S. Thota, J. Appl. Phys. 119 (2016) 043901.

[116] S. Sachdev, Nat. Phys. 4 (2008) 173.

[117] A.A. Zvyagin, Low Temp. Phys. 39 (2013) 901.

[118] K. Tomiyasu, J. Fukunaga, H. Suzuki, Phys. Rev. B 70 (2004) 214434.

[119] D.H. Lyons, T.A. Kaplan, K. Dwight, N. Menyuk, Phys. Rev. 126 (1962) 540.

[120] S.H. Lee, C. Broholm, W. Ratcliff, G. Gasparovic, Q. Huang, T.H. Kim, S.W. Cheong, Nature 418 (2002) 856.

[121] F.K. Lotgering, Philips Res. Repts. 11 (1956) 190.

[122] I.S. Jacobs, J. Phys. Chem. Solids 15 (1960) 54.

[123] E. Prince, J. Appl. Phys. 32 (1961) S68.

[124] Y. Kino, S. Miyahara, J. Phys. Soc. Jpn. 21 (1966) 2732.

[125] K. Gyoon, S. Junji, K. Yukitomo, Jap. J. Appl. Phys. 15 (1976) 411.

[126] G. Ueno, S. Sato, Y. Kino, Acta. Cryst. Sect. C 55 (1999) 1963.

[127] H. Ishibashi, T. Yasumi, J. Magn. Magn. Mater. 310 (2007) e610.

[128] T.D. Sparks, M.C. Kemei, P.T. Barton, R. Seshadri, E.-D. Mun, V.S. Zapf, Phys. Rev. B 89 (2014) 024405.

[129] T. Kimura, T. Goto, H. Shintani, K. Ishizaka, T. Arima, Y. Tokura, Nature 426 (2003) 55.

[130] Y.J. Choi, J. Okamoto, D.J. Huang, K.S. Chao, H.J. Lin, C.T. Chen, M. van Veenendaal, T.A. Kaplan, S.W. Cheong, Phys. Rev. Lett. 102 (2009) 067601.

[131] H. Katsura, N. Nagaosa, A.V. Balatsky, Phys. Rev. Lett. 95 (2005) 057205.

[132] M. Alice, V. Jana Poltierova, H. Petr, P. Jiri, N. Daniel, IOP Conf. Ser. Mater. Sci. Eng. 18 (2011) 032022.

[133] M. Ptak, M. Maczka, A. Gagor, A. Pikul, L. Macalik, J. Hanuza, J. Solid State Chem. 201 (2013) 270.

[134] L.G. Wang, C.M. Zhu, D.L.G.C. Bao, Z.M. Tian, S.L. Yuan, J. Mater. Sci. 50 (2015) 5904.

[135] M. Kataoka, J. Kanamori, J. Phys. Soc. Jpn. 32 (1972) 113.

[136] M. Lenglet, A. d'Huysser, J. Arsene, J.P. Bonnelle, C.K. Jorgensen, J. Phys. C: Solid State Phys. 19 (1986) L363.

[137] S.E. Ziemniak, A.R. Gaddipati, P.C. Sander, J. Phys. Chem. Solids 66 (2005) 1112.

[138] B.L. Dubey, N. Nath, B.N. Tiwari, A. Tripathi, Bull. Mater. Sci. 5 (1983) 153.

[139] S.I. Park, C.S. Kim, J. Appl. Phys. 101 (2007) 09N511.

[140] S.I. Park, K.R. Choi, T. Kouh, C.S. Kim, J. Magnetics 12 (2007) 137.

[141] M. Reehuis, M. Tovar, D.M. Tobbens, P. Pattison, A. Hoser, B. Lake, Phys. Rev. B 91 (2015) 024407.

[142] A.A. Bush, V.Y. Shkuratov, K.E. Kamentsev, A.S. Prokhorov, E.S. Zhukova, B.P. Gorshunov, V.I. Torgashev, Phys. Rev. B 85 (2012) 214112.

[143] K. Devi Chandrasekhar, J. Krishna Murthy, J.Y. Lin, H.C. Wu, W.J. Tseng, A. Venimadhav, H.D. Yang, Phys. Rev. B 94 (2016) 205143.

[144] C.M. Zhu, L.G. Wang, L. Chen, D.L.G.C. Bao, M.C. Wang, S.L. Yuan, J. Mater. Sci. 51 (2016) 9415.

[145] E.W. Gorter, Philips res. Repts. 9 (1954) 295.

[146] Y. Yafet, C. Kittel, Phys. Rev. 87 (1952) 290.

[147] P.L. Edwards, Phys. Rev. 116 (1959) 294.

[148] D.G. Wickham, J.B. Goodenough, Phys. Rev. 115 (1959) 1156.

[149] D.H. Lyons, T.A. Kaplan, Phys. Rev. 120 (1960) 1580.

[150] J.M. Hastings, L.M. Corliss, Phys. Rev. 126 (1962) 556.

[151] T.W. Houston, A.J. Heeger, J. Phys. Chem. Solids 29 (1968) 1085.

[152] T. Tsuda, A. Hirai, T. Tsushima, Solid State Commun. 9 (1971) 2207.

[153] H. Nagasawa, T. Tsushima, Phys. Lett. 15 (1965) 205.

[154] R.N. Bhowmik, R. Ranganathan, R. Nagarajan, Phys. Rev. B 73 (2006) 144413.

[155] E. Winkler, S. Blanco Canosa, F. Rivadulla, M.A. Lopez-Quintela, J. Rivas, A. Caneiro, M.T. Causa, M. Tovar, Phys. Rev. B 80 (2009) 104418.

[156] T. Dina, M. Julián, C. María Teresa, L.W. Elin, J. Phys.: Condens. Matter 27 (2015) 016003.

[157] F.F. Fava, I. Baraille, A. Lichanot, C. Larrieu, R. Dovesi, J. Phys.: Condens. Matter 9 (1997) 10715.

[158] M.A. Hamad, Process. Appl. Ceramics 10 (2016 ) 33.

[159] S. Ohtani, Y. Watanabe, M. Saito, N. Abe, K. Taniguchi, H. Sagayama, T. Arima, M. Watanabe, Y. Noda, J. Phys.: Condens. Matter 22 (2010) 176003.

[160] F. Leccabue, B.E. Watts, D. Fiorani, A.M. Testa, J. Alvarez, V. Sagredo, G. Bocelli, J. Mater. Sci. 28 (1993) 3945.

[161] R. Masrour, M. Hamedoun, A. Benyoussef, J. Magn. Magn. Mater. 322 (2010) 301.

[162] T.V. Dmitrieva, I.S. Lyubutin, B.I. Pokrovskii, N.D. Bondareva, Sov. Phys.-JETP 36 (1973) 709.

[163] S.J. Pickart, R. Nathans, Phys. Rev. 116 (1959) 317.

[164] S.J.L. Kang, Sintering, Densification, Grain Growth and Microstructure, Elsevier (2005).

[165] R.A. Young, The Rietveld Method" International Union of Crystallography, New York, Oxford University (1996).

[166] R. Kumar, Atomic and Molecular Physics, Campus Book International (2009).

[167] S. Foner, Rev. Sci. Instr. 30 (1959) 548.

[168] E.A. Odo, Nanosci. Nanotechnol. 5 (2015) 57.

[169] T. Bora, P. Saravanan, S. Ravi, J. Supercond. Nov. Magn. 26 (2013) 1645.

[170] L.R. Shi, Z.C. Xia, M. Wei, Z. Jin, C. Shang, J.W. Huang, B.R. Chen, Z.W. Ouyang, S. Huang, G.L. Xiao, Ceram. Int. 41 (2015) 13455.

[171] S.M. Yusuf, A. Kumar, J.V. Yakhmi, J. Phys.:Conf. Ser. 200 (2010) 022073.

[172] P. Mandal, A. Sundaresan, C.N.R. Rao, A. Iyo, P.M. Shirage, Y. Tanaka, C. Simon, V. Pralong, O.I. Lebedev, V. Caignaert, B. Raveau, Phys. Rev. B 82 (2010) 100416.

[173] S.M. Yusuf, A. Kumar, J.V. Yakhmi, Appl. Phys. Lett. 95 (2009) 182506.

[174] L.H. Yin, Y. Liu, S.G. Tan, B.C. Zhao, J.M. Dai, W.H. Song, Y.P. Sun, Mater. Res. Bull. 48 (2013) 4016.

[175] J. Mao, Y. Sui, X. Zhang, Y. Su, X. Wang, Z. Liu, Y. Wang, R. Zhu, Y. Wang, W. Liu, J. Tang, Appl. Phys. Lett. 98 (2011) 192510.

[176] X.H. Huang, J.F. Ding, G.Q. Zhang, Y. Hou, Y.P. Yao, X.G. Li, Phys. Rev. B 78 (2008) 224408.

[177] Z.M. Tian, S.L. Yuan, S.Y. Yin, L. Liu, J.H. He, H.N. Duan, P. Li, C.H. Wang, Appl. Phys. Lett. 93 (2008) 222505.

[178] S. Karmakar, S. Taran, E. Bose, B.K. Chaudhuri, C.P. Sun, C.L. Huang, H.D. Yang, Phys. Rev. B 77 (2008) 144409.

[179] V. Korenivski, R.B. van Dover, Y. Suzuki, E.M. Gyorgy, J.M. Phillips, R.J. Felder, J. Appl. Phys. 79 (1996) 5926.

[180] N. Moutis, C. Christides, I. Panagiotopoulos, D. Niarchos, Phys. Rev. B 64 (2001) 094429.

[181] P. Prieto, M.E. Gómez, G. Campillo, A. Berger, E. Baca, R. Escudero, F. Morales, J. Guimpel, N. Haberkorn, Phys. Status Solidi (a) 201 (2004) 2343.

[182] S.A. Makhlouf, H. Al-Attar, R.H. Kodama, Solid State Commun. 145 (2008) 1.

[183] Y. Melikhov, J.E. Snyder, D.C. Jiles, A.P. Ring, J.A. Paulsen, C.C.H. Lo, K.W. Dennis, J. Appl. Phys. 99 (2006) 08R102.

[184] M.C. He, B. You, H.Q. Tu, Y. Sheng, Q.Y. Xu, W.B. Rui, Y. Gao, Y.Q. Zhang, Y.B. Xu, J. Du, J. Appl. Phys. 117 (2015) 17C745.

[185] M. Meinert, B. Buker, D. Graulich, M. Dunz, Phys. Rev. B 92 (2015) 144408.

[186] J.F. Qian, A.K. Nayak, G. Kreiner, W. Schnelle, C. Felser, J. Phys. D: Appl. Phys. 47 (2014) 305001.

[187] A. Harres, M. Mikhov, V. Skumryev, A.M.H.d. Andrade, J.E. Schmidt, J. Geshev, J. Magn. Magn. Mater. 402 (2016) 76.

[188] D. Paccard, C. Schlenker, O. Massenet, R. Montmory, A. Yelon, Phys. Status Solidi (a) 16 (1966) 301.

[189] L. Wee, R.L. Stamps, L. Malkinski, Z. Celinski, D. Skrzypek, Phys. Rev. B 69 (2004) 134425.

[190] C. Schlenker, S.S.P. Parkin, J.C. Scott, K. Howard, J. Magn. Magn. Mater. 54 (1986) 801.

[191] R. Padam, S. Ravi, D. Pal, J. Magn. Magn. Mater. 418 (2016) 231.

[192] H. Itzhak, D. Danut, Ü. Ersan, F.Y. Alan, H.A. Elizabeth, H. Jingzhu, S.S. Maddury, J. Phys.: Condens. Matter 14 (2002) 10511.

[193] B.C. Melot, K. Page, R. Seshadri, E.M. Stoudenmire, L. Balents, D.L. Bergman, T. Proffen, Phys. Rev. B 80 (2009) 104420.

[194] J. Sannigrahi, S. Bhowal, S. Giri, S. Majumdar, I. Dasgupta, Phys. Rev. B 91 (2015) 220407.

[195] J. Romero Gómez, R. Ferreiro Garcia, A. De Miguel Catoira, M. Romero Gómez, Renew. Sustainable Energy Rev. 17 (2013) 74.

[196] J. Yang, Y.P. Lee, Y. Li, J. Appl. Phys. 102 (2007) 033913.

[197] Z. Wang, P. Lazor, S.K. Saxena, G. Artioli, J. Solid State Chem. 165 (2002) 165.

[198] H.C. Gupta, M.M. Sinha, Balram, B.B. Tripathi, Physica B: Condens. Matter 192 (1993) 343.

[199] M. Ptak, M. Mączka, A. Pikul, P.E. Tomaszewski, J. Hanuza, J. Solid State Chem. 212 (2014) 218.

[200] Y. Chen, Z. Liu, S.P. Ringer, Z. Tong, X. Cui, Y. Chen, Cryst. Growth Des. 7 (2007) 2279.

[201] J. Chen, W. Shi, X. Zhang, H. Arandiyan, D. Li, J. Li, Environ. Sci. Technol. 45 (2011) 8491.

[202] A. Wang, E. Kuebler Karla, L. Jolliff Bradley, A. Haskin Larry, Am. Mineral. 89 (2004) 665.

[203] M.A. Laguna-Bercero, M.L. Sanjuán, R.I. Merino, J. Phys.: Codens. Matter. 19 (2007) 186217.

[204] J. Preudhomme, P. Tarte, Spectrochim. Acta 27A (1971) 1817.

[205] J. Ma, V.O. Garlea, A. Rondinone, A.A. Aczel, S. Calder, C. dela Cruz, R. Sinclair, W. Tian, S. Chi, A. Kiswandhi, J.S. Brooks, H.D. Zhou, M. Matsuda, Phys. Rev. B 89 (2014) 134106.

[206] N. Liu, K.H. Zhao, X.L. Shi, L.W. Zhang, J. Appl. Phys. 111 (2012) 124112.

[207] S. Nagata, N. Koseki, S. Ebisu, Philos. Mag. 92 (2012) 2957.

[208] S. Maiti, A.K. Kundu, O.I. Lebedev, P. Bera, C. Anandan, A. Gayen, M.M. Seikh, RSC Advances 5 (2015) 83809.

[209] J.F. Herbst, F.E. Pinkerton, Phys. Rev. B 57 (1998) 10733.

[210] N. Ranvah, Y. Melikhov, D.C. Jiles, J.E. Snyder, A.J. Moses, P.I. Williams, S.H. Song, J. Appl. Phys. 103 (2008) 07E506.

[211] K. Raju, G. Venkataiah, D.H. Yoon, Ceram. Int. 40 (2014) 9337.

[212] L. Kumar, P. Kumar, M. Kar, Appl. Nanosci. 3 (2013) 75.

[213] V. Tsurkan, M. Mücksch, V. Fritsch, J. Hemberger, M. Klemm, S. Klimm, S. Körner, H.A. Krug von Nidda, D. Samusi, E.W. Scheidt, A. Loidl, S. Horn, R. Tidecks, Phys. Rev. B 68 (2003) 134434.

[214] S. Horiuchi, S. Miyahara, J. Phys. Soc. Jpn. 28 (1970) 529.

[215] K. Yosida, M. Tachiki, Prog. Theor. Phys. 17 (1957) 331.

[216] M. Kryder, H.P. Shieh, D. Hairston, IEEE Trans. Magn. 23 (1987) 165.

# List of Publications in International Journals

1. Effect of Al Substitution in Structural and Magnetic Properties of $MnCr_2O_4$
   **Junmoni Barman** and S. Ravi
   Journal of Superconductivity and Novel Magnetism, DOI: 10.1007/s10948-017-4169-3.
2. Study of Magnetic Compensation Behavior in $Mn(Cr_{1-x}Fe_x)_2O_4$
   **Junmoni Barman** and S. Ravi
   Journal of Magnetism and Magnetic Materials, **437** (2017) 42.
3. Sign Reversal of Magnetization and Exchange Bias in $Ni(Cr_{1-x}Al_x)_2O_4$ ($x$ = 0–0.50)
   **Junmoni Barman** and S. Ravi
   Journal of Magnetism and Magnetic Materials, **426** (2017) 82.
4. Tunable Exchange Bias and Bipolar Switching of Magnetization Near Room Temperature
   **Junmoni Barman** and S. Ravi
   Journal of Superconductivity and Novel Magnetism, **29** (2016) 2859.
5. Exchange Bias and Magnetization Reversal in $Ni(Cr_{1-x}Fe_x)_2O_4$ ($x$ = 0 – 0.20)
   **Junmoni Barman**, P. D. Babu and S. Ravi
   Journal of Magnetism and Magnetic Materials, **418** (2016) 300.
6. Study of Exchange Bias Behavior in $Ni(Cr_{1-x}Fe_x)_2O_4$
   **Junmoni Barman** and S. Ravi
   Solid State Communications, **201** (2015) 59.
7. Study of Exchange Bias and Training Effect in $NiCr_2O_4$
   **Junmoni Barman**, Tribedi Bora and S. Ravi
   Journal of Magnetism and Magnetic Materials, **385** (2015) 93.

# List of Papers Presented in National/International Conferences

1. Effect of Mn Substitution in the Magnetic Properties of $NiCr_2O_4$: A Systematic Study by Using Vibrating Sample Magnetometer (VSM)
   **Junmoni Barman** and S. Ravi
   International Conference on Sophisticated Instruments in Modern Research (ICSIMR 2017), IIT Guwahati, Assam, India.
2. Sign Reversal of Magnetization and Exchange Bias Field in $Ni(Cr_{1-x}Fe_x)_2O_4$ ($x$ = 0.30 & 0.40)
   **Junmoni Barman** and S. Ravi
   Research Conclave 2017, IIT Guwahati, Assam, India.
3. Study of Magnetic Compensation Behavior in $Mn(Cr_{1-x}Fe_x)_2O_4$
   **Junmoni Barman** and S. Ravi
   National Conference in Advances in Material Science (AMS 2017), Gauhati University, Assam, India.
4. Study of Tunable Exchnage Bias Behavior on $Ni(Cr_{1-x}Mn_x)_2O_4$
   **Junmoni Barman** and S. Ravi
   International Conference on Innovative Research In Applied Physics, Material Sciences, Instrumentation, Electronics, Communication, Electrical, Power Control, Computer Science and Information Technology (TECHNOVA 2016), Gauhati University, Assam, India.
5. Sign Reversal of Magnetization and Exchange Bias Field near Room Temperature
   **Junmoni Barman** and S. Ravi
   $X^{th}$ National Conference of Physics Academy of North East (PANE 2016), St. Anthony's College, Meghalaya, India.
6. Study of Exchange Bias effect in $Ni(Cr_{0.85}Al_{0.15})_2O_4$
   **Junmoni Barman** and S. Ravi
   International Conference on Materials Science and Technology (ICMST 2016), St. Thomas College Palai, Kerala, India.

7. Exchange Bias and Magnetization Reversal in $Ni(Cr_{1-x}Fe_x)_2O_4$ ($x$ = 0.02-0.50)
   **Junmoni Barman**, P.D. Babu and S. Ravi
   International Conference on Magnetic Materials and Applications (ICMAGMA 2015), VIT University, Tamil Nadu, India.
8. Structural and Magnetic Properties of $Mn(Co_{1-x}Fe_x)_2O_4$
   **Junmoni Barman** and S. Ravi
   IX$^{th}$ National Conference of Physics Academy of North East (PANE 2014), NERIST, Arunachal Pradesh, India.
9. Structural and Magnetic Properties of $Ni(Cr_{1-x}Fe_x)_2O_4$
   **Junmoni Barman** and S. Ravi
   International Conference on Magnetic Materials and Applications (ICMAGMA 2014), Pondicherry University, Puducherry, India.

# Workshop / School attended

1. The National Workshop on Advanced Probing Techniques in Transmission Electron Microscope (APTTEM 2016), IIT Guwahati, Assam, India.
2. IUCr workshop on X-ray diffraction systems and related applications (2014), IIT Guwahati, Assam, India.